Measurements of OH* and CH* in a Constant Volume Combustion Bomb

Submitted by

Mengchen Hu

Somerville College



A thesis submitted in partial fulfilment of the requirements for the degree of Doctor of Philosophy

Department of Engineering Science

University of Oxford

Trinity Term 2013

Measurements of OH* and CH* in a Constant Volume Combustion Bomb

Mengchen Hu — Doctor of Philosophy
Somerville College, Oxford — Department of Engineering Science

A thesis submitted in partial fulfilment of the requirements for the degree of Doctor of Philosophy at the University of Oxford, Trinity Term 2013

ABSTRACT

Combustion monitoring in internal combustion engine or burners is a difficult task due to the harsh environment for any sensor, therefore optical diagnostics are very attractive for these types of application. Chemiluminescence measurement is one of the most common and most promising ways of implementing optical diagnostics in combustion monitoring applications because the measured signal, emitted naturally with combustion, has potential to be an indirect measure of combustion relevant parameters, such as the equivalence ratio and heat release rate. In hydrocarbon combustion, the most common chemiluminescence emitters are OH*, CH*, C_2* and CO_2*. This thesis focuses on the measurement of OH* and CH* chemiluminescence, whose sensitivities are affected by temperature, pressure, equivalence ratio and stretch rate.

To measure OH* and CH* chemiluminescence, an existing constant volume combustion vessel has been refurbished, along with the sub-systems for fuel delivery, ignition, LabView control, data acquisition, and optical detection using a pair of photo-multiplier tubes (PMTs), interference filters and a series of apertures.

Modelling accurately the optical setup is essential for the CH* and OH* chemiluminescence measurements in the combustion bomb. To achieve this goal, a narrow field of view system has been selected as it enables the elimination of photons scattered from the internal surfaces. A calibration of the PMTs converts the measurements into the absolute OH* and CH* chemiluminescence in terms of watt.

Measurements from a combustion bomb are versatile and accurate since it determines the OH* and CH* chemiluminescence as a function of temperature and pressure from a single experiment. The calculation of the normalised OH* and CH* chemiluminescence (against mass burned rate) was based on a multi-zone combustion model and measured pressure record from the vessel. *NIICS* (Normalised Intensity Integrated Calculation System) has been created to fetch data from the multi-zone model, the optical model, and experimental measurements, to match them up by interpolation and to normalise the OH* and CH* chemiluminescence. *NIICS* also allows the user to select data uncorrupted by the noise and heat transfer.

The chosen data (in this case, CH*/OH* chemiluminescence ratio) have been fitted using a multi-variate fitting and correlation analysis. This formulation can be used to indicate the local equivalence ratio from premixed methane / air and iso-octane / air flames over the local pressure range 0.5 – 20 bar, the unburned gas temperature range 450 – 600 K, and equivalence ratio range 0.8 – 1.1.

The chemical-kinetic mechanisms of the absolute OH* and CH* chemiluminescence have been investigated by studying the influence of the equivalence ratio, unburned gas temperature, and local pressure. It should be pointed out that two confounding observations occur, i.e. a discontinuity in the chemiluminescence along the isentropes, and chemiluminescence continuing after the end of combustion. This led to the further spectroscopic analysis.

This study concluded with spectroscopic measurements using an Ocean Optics spectrometer and a Princeton ICCD spectrometer. It was found that the broadband CO_2* is responsible for the two disconcerting observations. In addition, CH* chemiluminescence has been shown to be very faint from premixed laminar methane / air flames; hence the CH*/OH* formula in essence quantifies the CO_2*/OH* ratio as a function of pressure, temperature, and equivalence ratio. The 'CH* chemiluminescence' can characterise the background CO_2*, so as to provide a practical way to probe the feasibility of absolute OH* as an indicator of combustion relevant parameters in the future.

ACKNOWLEDGEMENTS

This dissertation is improved by constructive guidance and suggestions with a number of people who helped debug it. Particular thanks to my supervisor, Professor Richard Stone, who gave me instructions throughout. In addition, perceptive criticism accorded to me played an important role in results verification.

I would like to thank Dr. Ben Williams for his assistance in the optical bomb modelling and spectroscopic measurements. In particular, I believe that I was highly motivated by his warm discussion with me in which I was enlightened and got nourished so much. I would also like to thank Dr. Martin Davy for his discussions on chemiluminescence.

Many thanks also to my parents not only for their financial support but also for their encouragement and patience, which create a feeling of home.

Dr Steve Marshall helped me to get started with measurements of laminar burning velocities, a particular ‘thank you’ for his assistance.

Finally, I would like to thank my friends from my postgraduate years in Oxford: Huayong Zhao, Fan Xu, Longfei Chen, Kun Liang, Felix Leach, and Nathan Hinton. I cherish our friendship and hope that we will be able to stay in touch despite the large distances between us in the future.

CONTENTS

ABSTRACT ..... **I**
ACKNOWLEDGEMENTS ..... **II**
NOMENCLATURE ..... **VII**
LIST OF FIGURES ..... **X**
LIST OF TABLES ..... **XVII**
Chapter 1 Introduction **1**
1.1 Laminar Premixed Flames 1
1.2 CH* and OH* Chemiluminescence 2
1.2.1 Basics of Flame Chemiluminescence 2
1.2.2 Chemiluminescence Production Mechanisms 4
1.3 Sensitivity of CH* and OH* Emissions to Combustion Conditions 9
1.3.1 Equivalence Ratio, Φ 9
1.3.2 Pressure, P 12
1.3.3 Temperature, T 13
1.3.4 Strain Rate, α 14
1.4 Chemiluminescence as an Indicator of Heat Release Rate 14
1.5 Overview of Present Work 16
Chapter 2 Experimental Apparatus **19**
2.1 Overview of the Test Facility 19
2.2 Combustion Vessel and Heating System 20
2.3 Gaseous Mixture Delivery System based on Theory of Partial Pressures 22
2.3.1 Theoretical Analysis 22
2.3.2 Experimental Procedure 22
2.4 Alternative Gaseous Mixture Preparation Method using Mass Flow Controllers 25
2.4.1 Introduction 25
2.4.2 Principle of Mass Flow Controller Operation 26
2.4.3 Mass Flow Controller Calibration 28
2.4.4 Method Validation 32
2.5 Liquid Fuel Delivery 33
2.5.1 Introduction 33
2.5.2 Volume Calculation 33
2.5.3 Vapour Pressure 35
2.5.4 Syringe Based System 37
2.5.5 Method Validation 39

2.6 Sensors and Data Acquisition 40
Chapter 3 Optical Equipment: Modelling, Validation and Calibration 44
3.1 Overview 44
3.2 Optical System Hardware 45
3.2.1 Photomultiplier 45
3.2.2 PMT Output Circuit 47
3.3 The Optical Model 51
3.3.1 Introduction 51
3.3.2 Assumptions, Geometry and Conventions 52
3.3.3 2D Modelling 54
3.3.4 3D Modelling 60
3.4 Model Validation 63
3.4.1 Introduction 63
3.4.2 Analysis of a Pinhole Centred at the Focal Point of Lens 64
3.4.3 Experimental Validation with a Point Source 65
3.4.3.1 Experimental set up and LED Scan 65
3.4.3.2 LED Scans at Intermediate Distances along the Optical Axis 73
3.4.3.3 LED Scans at Four PMT Orientations 75
3.4.4 Planar Uniform Light Source Calibration 76
3.4.5 Conclusion 79
3.5 Absolute Calibration of the PMT System for OH* and CH* Measurements 80
3.6 Conclusion 88
Chapter 4 Chemiluminescence Analysis Approach 90
4.1 Overview 90
4.2 The BOMB Program 91
4.3 Experimental Summary Spreadsheet 93
4.4 Nical Programme 94
4.4.1 Overview of Nical 94
4.4.2 Calculation of Mass of Fuel 97
4.4.3 Data Filtering 98
4.4.3.1 Introduction 98
4.4.3.2 Filtering the Pressure Trace 99
4.4.3.3 Filtering the OH* / CH* Measurements 101
4.4.4 Interpolation 102
4.4.5 Calculation of Rate of Heat Release 103
4.4.6 Concatenating and Saving the Data 104
4.5 Discussion of Errors 108
4.6 Conclusion 110

Chapter 5 Correlation of the CH*/OH* Chemiluminescence Ratio 111
5.1 Overview 111
5.2 Curve Fitting and Correlation..... 113
5.2.1 Introduction.....113
5.2.2 Choice of Functional Fit 114
5.3 Multi-Variate Minimisation Method 120
5.4 Current Fits for the Fuels of Methane and Iso-octane Mixtures with Air 122
5.5 CH*/OH* Ratio for Sensing Equivalence Ratio 127
5.6 Conclusions 129
Chapter 6 Absolute CH* and OH* Chemiluminescence Data Analysis 130
6.1 Overview 130
6.2 OH* and CH* Kinetic Mechanisms 132
6.3 Methane Results 133
6.3.1 Introduction.....133
6.3.2 Influence of the Equivalence Ratio, Temperature, Pressure and Stretch on the Chemiluminescence Curve Development.....135
6.3.2.1 Effect of Equivalence Ratio, Φ 135
6.3.2.2 Effect of Temperature and Pressure 139
6.3.2.3 Effect of Stretch Rate 144
6.3.3 CH* and OH* as an Indicator of Heat Release Rate 147
6.4 Iso-octane Results..... 148
6.4.1 Introduction.....148
6.4.2 CH* and OH* Chemiluminescence for Equivalence Ratio Sensing 149
6.5 Issues to be Discussed 151
6.5.1 Chemiluminescence Discontinuity along Isentropes.....152
6.5.2 Chemiluminescence after the End of Combustion 158
6.6 Conclusion..... 161
Chapter 7 Spectroscopic Results.....162
7.1 Overview 162
7.2 Optical Equipment..... 163
7.2.1 Ocean Optics USB4000 Fiber Optic Spectrometer 163
7.2.2 Princeton ICCD Kinetic Spectrometer 164
7.2.3 Narrow field of View Optical System 170
7.3 Results 171
7.3.1 Introduction.....171
7.3.2 Chemiluminescence Spectra 173
7.3.2.1 Methane / Air Flame Spectra 173
7.3.2.2 Butane / Air Flame Spectra 181

7.3.3 Interleaved Measurements 184
7.3.4 Absolute OH* Chemiluminescence 189
7.4 Conclusion 191
Chapter 8 Conclusions and Future work 193
8.1 Conclusions 193
8.1.1 Quantitative Modelling of CH*/OH* chemiluminescence ratio (Chapter 5) 195
8.1.2 Dependence of the Absolute CH* and OH* Chemiluminescence on Combustion Conditions (Chapter 6) 196
8.1.3 Spectroscopic Measurements (Chapter 7) 197
8.2 Future Work 198
8.2.1 Absolute Measurements of OH* Chemiluminescence 198
8.2.2 Analysis of Absolute OH* Chemiluminescence 198
8.2.3 Fuel Variability 199
References 200
Appendix A Lambda Sensor Calibration 209
A.1 Overview of Lambda Sensor 209
A.1.1 Working Principle of the Zirconia Sensor 210
A.2 Lambda Sensor Calibration 212
A.2.1 Lambda Sensor Calibration with Gas Mixtures 213
Appendix B Optical Ray Tracing Using Matrices 215
B.1 Ray Transfer Matrix Algorithm 215
B.2 Application in the Optical Model 216

NOMENCLATURE

Acronyms

2D	2-Dimensional
3D	3-Dimensional
a	Anode
atm	Atmospheres
AC	Alternating Current
CCD	Charge Coupled Device
CO	Carbon Monoxide
CO_2	Carbon Dioxide
CWL	Centre Wavelength
det	Detector Size
DAQ	Data Acquisition
DC	Direct Current
FFT	Fast Fourier Transform
fps	Frames per Second
GT	Gas Turbine
HBW	Width of the Pass-band, i.e. the difference between the two wavelengths at which the transmittance is half the peak value
HT	High Tension
IC	Internal Combustion
ICCD	Intensified Charge Coupled Device
k	Cathode
LED	Light Emitting Diode
mfb	Mass Fraction Burned
NA	Numerical Aperture
N_2	Nitrogen
O_2	Oxygen
RoHR	Rate of Heat Release
ROI	Region of Interest
PMT	Photomultiplier Tube
S	Samples
TC	Thermocouple
TIFF	Tagged Image File Format
TTL	Transistor-transistor Logic
UV	Ultraviolet
Vdc	Volts Direct Current

Greek

α	Half Cone Angle / Stretch Rate
α	Thermal Diffusivity
γ	Ratio of Specific Heat (c_p/c_v)
η	Collection Efficiency
θ	Apex Cone Angle
λ	Wavelength of Light / Thermal Conductivity
ν	Wave Frequency
τ	Time Constant / Exposure Duration

Φ Equivalence Ratio
ρ Density
Ω Solid Angle

Roman

A Flame Surface Area / Light Absorbance
c_p Specific Heat at Constant Pressure
c_v Specific Heat at Constant Volume
C Capacitance
D Diameter of the Bomb / Mass Diffusivity
E_a Activation Energy
f Focal Length
I Light Intensity Existing the Interference Filter (in unit of watt)
I_0 Light Intensity Entering the Interference Filter (in unit of watt)
I^+ Normalised Intensity (in unit of J/g)
I^* Absolute Intensity (in unit of watt)
k Rate Coefficient
ld Lens Diameter
lf Focal Length of the Lens
$\dot{m}$ Mass Flow Rate
M Molecular Mass / Magnification
n Index of Refraction
p_0 Initial Pressure
p_c Critical Pressure
p_{vpr} Vapour Pressure
P Pressure
Q Heat
r_b Burned Gas Radius
r_i Radius Prior to Combustion ($t = 0$)
r_f Flame Radius
R Vessel Radius / Resistance
R Pearson's Correlation Coefficient
R_0 Ideal Gas Constant
s Velocity or Speed
S_f Stretched Laminar Flame Speed
S_g unburned gas velocity immediately ahead of flame front
S_s Un-stretched Laminar Flame Speed
S_u Un-stretched Laminar Burning Velocity
t Time
T Temperature / Transmission
T_0 Initial Temperature
T_c Critical Temperature
u Lens-to-Object Distance
U Internal Energy
v Lens-to-Detector Distance
V Voltage
W Work
x_r Molar Fraction of Residuals
Δx Flame Front Thickness

X	Capacitive Reactance
Z	Impedance

Subscripts

b	Burned
f	Fuel
g	Gas
mix	Mixture
r	Residuals
s	Flame Speed
u	Un-stretched / Unburned

LIST OF FIGURES

Figure 1. 1 1D un-stretched laminar burning velocity. From Marshall [3]. 2
Figure 1. 2 The simplified methane oxidation mechanism. The main portion of the carbon follows the marked reaction path. Only a small portion follows the side paths, which yield OH*, CH*, and CO_2* [15]. 8
Figure 1. 3 Variation of mean CH* (in Figure 1.3a) and OH* (in Figure 1.3b) chemiluminescence intensity (normalized against mass flow rate of fuel) with equivalence ratio: premixed natural gas-air flame in a counter-flow burner [16]. 11
Figure 2. 1 Schematic representation of the experimental facility with gaseous mixture delivery system for the introduction of methane. 20
Figure 2. 2 Cross-section of the combustion vessel and its oven. From Saeed (2002) [35].21
Figure 2. 3 A schematic cutaway view of a thermal-type mass flow controller. From [38]. ... .26
Figure 2. 4 Sensor temperature profile. From [37]. 28
Figure 2. 5 Principle of the wet gas meter, based on Hayward (1979) [39]. 29
Figure 2. 6 Mass flow controller (MKS) calibration for air. 30
Figure 2. 7 Mass flow controller (UFC-1200A) calibrated against methane. 31
Figure 2. 8 Selected region of mass flow controller (UFC-1200A) calibration against methane. 31
Figure 2. 9 Φ Given by Lambda Sensor against that Calculated from Mass Flow Controller Voltages. 33
Figure 2. 10 Vapour pressure of iso-octane using the Wagner correlation equation. 36
Figure 2. 11 KDS Model 310 Plus syringe actuator. From [42]. 37
Figure 2. 12 A component fitted to the syringe port which allows the injection of liquid fuel into the bomb. From [3]. 38
Figure 2. 13 Equivalence ratio measured by lambda sensor against target at T_0 = 380 K..39
Figure 2. 14 Equivalence ratio measured by lambda sensor against target at T_0 = 450 K..40
Figure 2. 15 The LABVIEW mixture preparation tab. 41
Figure 2. 16 The LABVIEW combustion tab. 42
Figure 3. 1 Schematic of a photomultiplier tube. 46
Figure 3. 2 PMT output buffering system. 48
Figure 3. 3 Circuit diagram of the PMT output buffering and amplifier system. 49
Figure 3. 4 Comparison of ‘narrow field of view’ sensitive area and ‘wide field of view’ sensitive area. 51
Figure 3. 5 Arrangements of the combustion bomb and photo-multiplier tube (PMT). 53
Figure 3. 6 The 2D spatial collection efficiency map. The *x* and *y* readings in the map are elemental indices rather than actual length in mm. (Conversion factor is 0.7076 mm). 56
Figure 3. 7 Plot of a slice through the collection efficiency map at the far window for the 2D calculation. η_{coll} in the insert denotes the spatial collection efficiency.. 57

Figure 3. 8 The PMT signal for constant chemiluminescence strength as a function of flame radius r_f. Although collection efficiency map was generated in 2D, this analysis takes advantage of axial symmetry to give the 3D solution.....59
Figure 3. 9 The 3D spatial collection efficiency map. The *x* and *y* readings in the map are elemental indices rather than actual length in mm. (Conversion factor is 0.7076 mm). 61
Figure 3. 10 Plot of a slice through the collection efficiency map at the far window for the 3D calculation (in Figure 3.10a, 401 steps in θ discretization; in Figure 3.10b, 10001 steps in θ discretization).....62
Figure 3. 11 Variation of total photon collection with radius for a spherical flame with a constant photon flux (#/(m^2·s)).. 63
Figure 3. 12 The 3D spatial collection efficiency map in the case of a pinhole centred at the focal point of the lens. 64
Figure 3. 13 PMT with a black paper mask wrapped around it. 66
Figure 3. 14 Arrangement of the point source (LED) calibration experiment. A mask with 3 mm width was attached to the acrylic circle. 66
Figure 3. 15 PMT measurements using 7 mm aperture wrapped around the detector. 67
Figure 3. 16 Normalised uniformity contour plot, showing the region of high and comparatively uniform sensitivity of photocathode.....68
Figure 3. 17 (Figure 3.17a, b) Far-slice collection efficiency comparisons by changing detector size: (a) *det* = 4; (b) *det* = 24 (*v* = 48). (Figure 3.17c, d) Far-slice collection efficiency comparisons by modifying lens-to-detector distance: (c) *v* = 46; (b) *v* = 50 (*det* = 24). 69
Figure 3. 18 Comparison of the LED scan results with the model results for both PMTs and orientations. The dip with width of 7 mm results from the LED being scanned across the 3 mm wide alignment mask. In the optical model, the detector diameters are varying, from 4 mm (effective sensitive region) to 24 mm (largest detector dimension). While the diameter of aperture 2 (wrapped around the PMT) is set to be 3.5 mm, the position of aperture 2 is considered to be 8 mm away from the detector......72
Figure 3. 19 Comparison of the model to experiments at intermediate locations using a scanned point light source. .....**Error! Bookmark not defined.**
Figure 3. 20 Comparison of model to experiments with four PMT orientations.....76
Figure 3. 21 Arrangement of planar uniform light source for calibration of the PMT optics. 77
Figure 3. 22 Comparison between the model and the experiment (broken line) when moving a uniformly illuminated screen along the optical axis. 78
Figure 3. 23 OH* signal collected with radius with a constant photon flux (#/(m^2·s)). 79
Figure 3. 24 General arrangement of the calibration system. 80
Figure 3. 25 Use of an Ocean Optics USB spectrometer (with an absolute calibration) for calibration of PMT for OH* Chemiluminescence measurement. 81
Figure 3. 26 Image of the red dot on the tracing film (the visible diameter is 3.2 mm, corresponding to a length of 188.235 pixels)...**Error! Bookmark not defined.**

Figure 3. 27 Screenshot of the Photron FASTCAM Viewer showing the cursors that were used for checking the position on the image of the spark electrodes (the inset shows a natural light photograph of the electrodes).....83
Figure 3. 28 Output of the photomultiplier tube (PMT, in Figure 3.28a) and the corresponding OH* energy from the Ocean Optics USB spectrometer (in Figure 3.28b). 85
Figure 3. 29 Use of an Ocean Optics USB spectrometer (with an absolute calibration) for calibration of PMT for CH* Chemiluminescence measurement. 86
Figure 3. 30 CH* power from the USB spectrometer. 86
Figure 3. 31 Interference filters' transmission. 88
Figure 4. 1 Overview of Normalised Intensity Integrated Calculation System (*NIICS*) using data from the *BOMB* program, the optical model and experiment. 91
Figure 4. 2 Applying Butterworth filtering to the experimental pressure trace. Pressure 'noise' is obtained by subtracting the filtered pressure data from the original pressure record. 101
Figure 4. 3 Original OH* / CH* traces versus that filtered using the MATLAB *butter* function for a fourth order Butterworth filter. 'Noise' associated with the chemiluminescence is obtained by subtracting the filtered data from the original measurements… 102
Figure 4. 4 Example of a graph of laminar burning velocity. The lower limit and higher limit have been chosen by the user; hence the regions outside of these are grey in Figure 4.4b. 106
Figure 4. 5 Normalised OH* and CH* chemiluminescence (unit: J/g) of interest as a function of mass fraction burned for the data selected in Figure 4.4b. 107
Figure 4. 6 Sensitivity study with an assumed 1% error to illustrate the effect of errors in the pressure measurement for stoichiometric methane / air flames with p_0 = 2 bar and T_0 = 380 K on the computed flame radius (Figure 4.6a) and the normalised chemiluminescence intensities (Figure 4.6b, c). 109
Figure 5. 1 Normalised CH*/OH* ratio of methane-air mixtures for equivalence ratios Φ = 0.9, 1.0, and 1.1, along unburned gas isentropes at T_0 = 380 K and p_0 = 1.0, 2.0, and 4.0 bar. R is Pearson's correlation coefficient to assess how closely different variables are interdependent. 115
Figure 5. 2 Dependence of the normalised CH*/OH* ratio for mixtures of methane with air on the operating pressure for equivalence ratios Φ = 0.8, 0.9, 1.0, and 1.1, along unburned gas isentropes starting at values of T_0 = 380 K or 450 K and p_0 = 1.0, 2.0, and 4.0 bar. The curves show the least square fit of Equation (5.4) to the points. R is a measure of the degree of linear relationship between CH*/OH* ratio and the pressure. 117
Figure 5. 3 Parameters *a*, *b*, and *c* for methane obtained from least squares fits of Equations (5.5) to (5.7) to data in Figure 5.2. 119
Figure 5. 4 Normalised CH*/OH* ratio of methane-air mixtures for equivalence ratios Φ = 0.9, 1.0, and 1.1, along unburned gas isentropes at T_0 = 380 K and p_0 = 1.0,

2.0, and 4.0 bar. The red curves indicate the curve fitting of Equation (5.8) to the measurements. 124
Figure 5. 5 Individual methane / air experimental data points from Figure 5.2 plotted against their corresponding values predicted by Equation (5.8) using the coefficients in Table 5.1. 125
Figure 5. 6 Individual iso-octane / air experimental data points plotted against their corresponding values predicted by Equation (5.8) using the coefficients in Table 5.3. 126
Figure 5. 7 Predicted CH*/OH* ratio (Equation (5.8) using parameters listed in Table 5.1) for varying pressure and equivalence ratios in methane / air flames. 127
Figure 5. 8 Predicted CH*/OH* ratio (Equation (5.8) using parameters listed in Table 5.3) for varying pressure and equivalence ratios in iso-octane / air flames. 128
Figure 6. 1 Repeatability of laminar burning velocities and normalised OH* as a function of pressure (p) with initial conditions of p_0 = 2.77 bar, T_0 = 415 K. 134
Figure 6. 2 Normalised OH* (in Figure 6.2a) and CH* (in Figure 6.2b) chemiluminescence as a function of mass fraction burned in premixed methane / air combustion for different equivalence ratios ranging from 0.8 to 1.1, for two known initial temperatures, i.e. 380 K and 450 K, and for three given initial pressures, i.e. 1, 2, and 4 bar. In each subplot, four different curves indicate normalised chemiluminescence with various equivalence ratios at the same initial temperature and pressure. 136
Figure 6. 3 Normalised OH* (in Figure 6.3a) and CH* (in Figure 6.3b) chemiluminescence as a function of equivalence ratio at three selected mass fraction burned values for two known initial temperatures, i.e. 380 K and 450 K, and for three given initial pressures, i.e. 1, 2, and 4 bar. 138
Figure 6. 4 Effect of current pressure (p_u) and unburned gas temperature (T_u) on normalised OH* (in Figure 6.4a) and CH* (in Figure 6.4b) for stoichiometric methane / air mixtures. Normalised intensities (mJ/g) are shown as 'spot values'. 141
Figure 6. 5 Effect of current pressure (p_u) and unburned gas temperature (T_u) on normalised OH* and CH* at initial temperature $\boldsymbol{T_0}$ = 380 K, and at equivalence ratios 0.8, 0.9, and 1.1 respectively for methane / air mixtures. Normalised intensities (mJ/g) are shown as 'spot values'. 142
Figure 6. 6 Effect of stretch rate (α, in unit of s^{-1}) on the normalized CH*/OH* ratio for stoichiometric methane / air mixtures. The results are for a single isentrope, but with different initial pressures and temperatures of p_0 / T_0 = 2.0 bar/380 K (Δ), 2.77 bar/415 K (+), and 3.75 bar/450 K (*). .....**Error! Bookmark not defined.**
Figure 6. 7 Absolute OH* (Figure 6.7a) and CH* (Figure 6.7b) chemiluminescence as a function of heat release rate (*RoHR*) for stoichiometric methane / air mixtures with different initial conditions that were chosen to follow an isentrope. 148
Figure 6. 8 Normalised OH* and CH* chemiluminescence as a function of mass fraction burned in premixed iso-octane / air combustion for different equivalence ratios ranging from 0.8 to 1.1, for a known initial temperature (450 K), and for three given initial pressures, i.e. 0.75, 1.5, and 3 bar. In each subplot, four different

curves indicate normalised chemiluminescence with various equivalence ratios at the same initial temperature and pressure. 150
Figure 6. 9 Absolute OH* (Figure 6.9a) and CH* (Figure 6.9b) chemiluminescence as a function of heat release rate (*RoHR*) for stoichiometric iso-octane / air mixtures with different initial conditions, under which the isentropes are close to overlapping.....151
Figure 6. 10 Chemiluminescence from OH* (in Figure 6.10a) and CH* (in Figure 6.10b) with discontinuities along the isentropes for stoichiometric methane / air mixtures. Normalised chemiluminescence intensities (mJ/g) are shown as 'spot values'. 153
Figure 6. 11 (a) Three stoichiometric methane / air mixtures with different initial conditions of p_0 / T_0 = 2.0 bar/380 K, 2.77 bar/415 K, and 3.75 bar/450 K, chosen to follow an isentrope. Normalised OH* (mJ/g) are shown as 'spot values'. (b) The same data as Figure 6.11a, plotted to show the different normalised OH* chemiluminescence (mJ/g) at the same pressures (as the unburned gas is compressed isentropically, then the same pressure means the same unburned gas temperature); the unburned gas temperatures (K) are shown as 'spot values'. 154
Figure 6. 12 Chemiluminescence from CH* with discontinuities along isentropes for weak methane / air mixtures (Φ = 0.9, in Figure 6.12a) and stoichiometric iso-octane / air mixtures (in Figure 6.12b). Normalised intensities (mJ/g) are shown as 'spot values'. 155
Figure 6. 13 (a) the top-left picture shows the instantaneous temperature profile, (b) the top-right picture shows the mass fractions of the stable species CH_4, CO_2, H_2O and O_2, (c & d) and the two bottom pictures show the mass fraction profiles of H and OH. (Modelled by Professor Bernd Rogg).....156
Figure 6. 14 OH* and CH* chemiluminescence continue after the maximum pressure for methane / air (in Figure 6.14a) and iso-octane / air (in Figure 6.14b) flames..159
Figure 7. 1 Example of a spectroscopic measurement using the Ocean Optics USB4000 spectrometer. The left plot shows radiation (in terms of # of counts per pixel) as a function of wavelength, the right one converts the data to spectral intensity (in units of watts) as a function of wavelength using its calibration data. 163
Figure 7. 2 Example of an image from the Princeton ICCD kinetics spectrometer (with 600 lines/mm diffraction grating with centre wavelength at 430 nm). 165
Figure 7. 3 Single trigger kinetics mode (window shift size is set to be 1). The exposure duration (τ) is set to be 3.8 ms. A surprisingly short readout time is shown (by the notscan pulse being low) at the end. The shutter is open for entire exposure, and the shutter open duration is 255 × 3.8 ms = 969 ms.....167
Figure 7. 4 Zoomed in version of Figure 7.3. Time between norm3 pulses is 3.8 ms. Negative pulses on norm3 are 16 μs wide, indicating the time taken to move the charge one row. The negative-going sync pulse (i.e. external sync pulse) is 1 ms wide, which was set by a function generator. 167

Figure 7. 5 Single trigger kinetics mode (window shift size is set to be 10). The exposure duration (τ) is set to be 3.8 ms. The shutter is open for entire exposure, and the shutter duration is for (255/10) × 3.8 ms = 95 ms.....168
Figure 7. 6 Zoomed in version of Figure 7.5. Negative pulses on norm3 are 160 µs wide, indicating time taken to move charge ten rows. The time between the norm3 pulses is 3.8 ms. 168
Figure 7. 7 Multiple trigger kinetics mode (window shift size is set to be 5). The exposure duration (τ) is set to 3.8 ms. External sync pulses arrive every 20ms. 51 (i.e. 255/5) exposures mean that the total experiment time is just over 1 s (i.e. 51 × 20 ms = 1020 ms). The readout duration is 600 ms as can be seen from the notscan pulse. 169
Figure 7. 8 Zoomed in version of Figure 7.7. The negative pulses on norm3 are 80 µs wide, indicating the time taken to move the charge five rows. Each external sync pulse is followed by a 3.8 ms shutter exposure.....169
Figure 7. 9 Geometric arrangement for the Princeton optical system. 171
Figure 7. 10 (a) Pressure and mass fraction burned as a function of time, and (b, c) chemiluminescent emission spectra from combustion bomb for stoichiometric methane / air flames with p_0 = 2 bar and T_0 = 380 K measured by the Ocean Optics USB4000 spectrometer. Figure 7.10b shows the detected signal in terms of counts, and Figure 7.10c illustrates the wavelength-dependent emission intensity. 174
Figure 7. 11 Time history of the spectral intensities at 308, 431, 450, and 589 nm. Emission spectra were measured from stoichiometric methane / air flames with p_0 = 2 bar and T_0 = 380 K.....175
Figure 7. 12 Time history of CH* and background CO_2* 'line spectrum' from the stoichiometric methane/air flame with p_0 = 2 bar and T_0 = 380 K detected by USB4000 spectrometer. In this plot, either the CH* or CO_2* 'line spectrum' is obtained by averaging values at the upper (i.e. 435 nm and 425 nm) and lower (i.e. 425 nm and 415 nm) boundaries.....176
Figure 7. 13 The same methane / air combustion event as in Figure 7.10 (Φ = 1, p_0 = 2 bar, and T_0 = 380 K), recorded by the Princeton ICCD spectrometer. The colour bar included in Figure 7.13a is to interpret the false colouring scale (i.e. chemiluminescence spectra in terms of # of counts) of the image.....177
Figure 7. 14 Time history of CH* and background CO_2* 'line spectrum' from stoichiometric methane / air flame (p_0 = 2 bar, T_0 = 380 K) detected by the Princeton ICCD spectrometer. In this plot, either CH* or CO_2* 'line spectrum' (in terms of # of counts) is obtained by averaging values at the upper (i.e. 435 nm and 425 nm) and lower (i.e. 425 nm and 415 nm) boundaries. 179
Figure 7. 15 (a) Time history of CH* and background CO_2* 'line spectrum' from the rich methane/air (Φ=1.2, p_0 = 2 bar, and T_0 = 380 K) flame detected by the USB4000 spectrometer; (b) Spatially and spectrally resolved flame spectra measured by the Princeton ICCD spectrometer. 180

Figure 7. 16 (a) Pressure and mass fraction burned as a function of time, and (b, c) CH* chemiluminescence emission from a rich butane/air flame (Φ=1.2, p_0 = 2 bar, and T_0 = 380 K) measured by the Ocean Optics USB4000 spectrometer.....182
Figure 7. 17 Time history of CH* and background CO_2* 'line spectra' from rich butane/air (Φ=1.2, p_0 = 2 bar, and T_0 = 380 K) flame detected by the USB4000 spectrometer. In Figure 7.17, the CH* chemiluminescence has been characterised by averaging the spectral values at 435 nm and 425 nm, and the CO_2* chemiluminescence has been characterised as the mean of the intensities at 425 nm and 415 nm. 182
Figure 7. 18 Spatially and spectrally resolved rich butane/air flame spectra (Φ=1.2, p_0 = 2 bar, and T_0 = 380 K) measured by the Princeton ICCD spectrometer (with 600 lines/mm diffraction grating with centre wavelength at 430 nm)..183
Figure 7. 19 The same data as Figure 7.15. Pressure and mass fraction burned traces (Figure 7.19a) and spatially and spectrally resolved flame spectra (Figure 7.19b) measured by the Ocean Optics USB4000 spectrometer. It can be seen that both maxima are achieved approximately at the same time (~65 ms). ...186
Figure 7. 20 Repeatability of the PMT measurements from PMT measurements of rich butane/air combustions with equivalence ratio of 1.2, initial temperatures of 380 K (Figure 7.20a) and 450 K (Figure 7.20b), initial pressure of 2 bar. The solid curves represent V_{CH*} (in unit of volts), and the dashed curves denote the pressure traces. 187
Figure 7. 21 Comparison of integral CH* chemiluminescence (without background correction) and global chemiluminescence profiles from the interleaved measurements of rich butane/air combustion with equivalence ratio of 1.2, initial temperatures of 380 K (Figure 7.21a) and 450 K (Figure 7.21b), initial pressure of 2 bar. The circle markers represent data collected by the Ocean Optics USB4000 spectrometer; the cross markers denote sampled PMT signals. The marker colour denotes measurements from a particular experiment. 188
Figure 7. 22 A fifth-order polynomial fit for the estimation of the broadband CO_2* emission.....190
Figure 7. 23 Global (band-pass filtered) chemiluminescence profiles for the absolute OH* and broadband CO_2* from measurements of rich methane/air combustions with equivalence ratio of 1.2, initial temperatures of 380 K, and initial pressure of 2 bar. 191
Figure A. 1 A schematic cutaway view of a Zirconia sensor. From NTK online resource [81]. 210
Figure A. 2 Zirconia sensor output signal. From NTK online resource [81]. 211
Figure A. 3 The wide band sensor structure and operation. From Stone [84]. 212
Figure B. 1 Simplified 2D arrangement of the optical elements. 216
Figure B. 2 Simplified 3D geometric arrangement of the optical elements. 218
Figure B. 3 Collection-area subtends at a point. 219

LIST OF TABLES

Table 1. 1 Rate constants summarised by Nori et al. [7] for CH*. Rate coefficients are expressed as $k = A \cdot T^b \cdot \exp(-E_a/RT)$ with E_a in units of cal·mol^{-1} and $A \cdot T^b$ in cm^{3}mol^{-1}s^{-1} for two body reactions (with T in Kelvin) 5

Table 1. 2 Rate constants summarised by Nori et al. [71] for OH*. Rate coefficients are expressed as $k = A \cdot T^b \cdot \exp(-E_a/RT)$ with E_a in units of cal·mol^{-1} and $A \cdot T^b$ in cm^{3}mol^{-1}s^{-1} for two body reactions or cm^{6}mol^{-2}s^{-1} for three body reactions (with T in *K*) 6

Table 3. 1 Illustration of optical elements properties 55

Table 3. 2 Geometry of the optical system and the corresponding values 70

Table 5. 1 Values of Curve Fitting Coefficients for the Methane / Air Mixture 123

Table 5. 2 Values of R-squared for the Methane / Air Mixture Curve Fitting.....123

Table 5. 3 Values of the Equation (5.8) Coefficients for the Iso-octane / Air Mixture 125

Table 8. 1 Values of Curve Fitting Coefficients for the Methane / Air and Iso-octane / Air Mixtures 195

Table A. 1 Specified Accuracy of the ECM AFRecorder Lambda Sensor for Different Lambda Ranges 213

Table A. 2 Comparison of the ECM AFRecorder Lambda Sensor against Four Calibration Gases 214

Chapter 1 Introduction

For laminar premixed flames, the applicability of chemiluminescence as an indirect measure for heat release has been shown in many experimental and theoretical studies. The chemiluminescence spectrum of a hydrocarbon flame consists of emissions from many radicals including OH*, CH*, C_2*, and CO_2*, and the former two radicals are of particular interest. In this chapter, the basics of the different combustion modes and the concept of a laminar premixed flame are introduced in Section 1.1, followed by the basics of OH* and CH* chemiluminescence in Section 1.2. Also investigated is the sensitivity of CH* and OH* to combustion conditions, followed by discussion of CH* and OH* chemiluminescence as an indicator of heat release rate. This chapter ends by presenting an overview of the current work.

1.1 Laminar Premixed Flames

According to Turns [1], a flame can be classified as one of the following two categories: premixed flames and non-premixed flames. While the former denotes that the fuel and oxidant are mixed at a molecular level prior to any significant chemical reaction; the latter, which is also defined as a diffusion flame, signifies a flame where reactants are initially separated. In a diffusion flame, reactions are taking place only at the interface.

Flame structure has been studied in great detail by Fristrom [2] who suggested that a flame consists of four regions: (1) unburned; (2) pre-heat; (3) reaction; and (4) burned gas. Initially, fresh unburned mixture at the ambient conditions is delivered to the flame zone. As the mixture approaches the flame front it is heated by conduction and radiation from the flame zone upstream. Chemical reactions and heat release are negligible at this stage. Once temperatures are hot enough to sustain combustion, chemical reactions take place in the

reaction zone. The gases emerging from this zone enter the burned gas zone where concentration and temperature are once again constant.

Laminar premixed flames have distinct burning velocities. It is the velocity where the flame front is moving relative to the unburned mixture, which is pushed outwards by the expansion of the burned gas. In the 1D case, the case of an un-stretched laminar burning velocity is illustrated as follow:

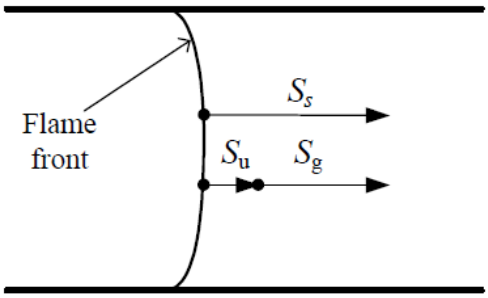


Figure 1. 1 1D un-stretched laminar burning velocity. From Marshall [3].

$$S_u = S_s - S_g \tag{1.1}$$

S_u un-stretched laminar burning velocity

S_s un-stretched laminar flame speed

S_g unburned gas velocity immediately ahead of flame front

1.2 CH* and OH* Chemiluminescence

1.2.1 Basics of Flame Chemiluminescence

Chemiluminescence is light emitted by molecules, that have been created in an electronically excited energy state, when they relax to a lower energy state through the spontaneous emission of a photon. Flame chemiluminescence, which is the chemiluminescence emitted in flames, is of particular interest because the concentrations of the excited state radicals that are observed in flames exceed the equilibrium concentrations of radicals at the same temperature without chemical reactions by orders of magnitude. This means that the flame

chemiluminescence is not only due to thermal excitation, but also closely related to chemical reactions. Hence flame chemiluminescence has been subject to broad attention as a measure of combustion relevant quantities such as equivalence ratio and heat release rate.

The wavelength emitted by the radicals is a characteristic of the molecules that undergo electronic transition from one configuration to another configuration. According to Zizak [67], hydrogen flames, including nitrous oxide-hydrogen flames, have the characteristic of OH* band spectra peaks at 281 nm, 306 nm (strong), and 343 nm, with a weak background emission. With the addition of nitrogen, NO bands occurs in the UV, and a green broadband emission can result from the recombination of NO and O to NO_2. In the hotter oxy-hydrogen flames, there is a weak continuum in the blue and UV regions of the spectrum, which is due to the recombination of OH and H to H_2O; however this broadband emission does not exist in the air-hydrogen flames.

In hydrocarbon flames, the only product of combustion which has an appreciable equilibrium concentration that gives a narrow-band radiation spectra is hydroxyl (OH). Besides, a broadband spectra that extends from below 300 nm to 600 nm is excited CO_2*. Apart from these, many unstable radicals such as CH, C_2 may be formed and give appreciable emission in the visible region. In cooler flames, it is possible to detect CHO radicals between 300 nm and 400 nm; however this is of secondary significance.

Among the mentioned chemiluminescence species, CH* and OH* have been widely investigated numerically and experimentally [7, 13, 16, 20, 22, 47, 48, 49, 51, 52]. While OH* spectra exhibits a peak at 306.4 nm, the strongest CH* chemiluminescence occurs at 431.5 nm.

$$\mathrm{CH}^* \rightarrow \mathrm{CH} + \mathrm{h}\nu \tag{1.2a}$$

$$\mathrm{OH}^* \rightarrow \mathrm{OH} + \mathrm{h}\nu \tag{1.2b}$$

where the superscript * denotes the excited state species, h is Planck's constant, v is the frequency of the emission.

1.2.2 Chemiluminescence Production Mechanisms

Of the various proposed mechanisms for the production of CH* in flames the following have received the most attention within the literature

$$C_2 + OH \rightarrow CH^* + CO \quad (1.3a)$$

$$C_2H + O \rightarrow CH^* + CO \quad (1.3b)$$

$$C_2H + O_2 \rightarrow CH^* + CO_2 \quad (1.3c)$$

where (1.3a) was proposed by Gaydon [5] as the dominant production mechanism for CH* in hydrocarbon flames. The formation of CH* from the reaction of the ground state ethynyl radical (C_2H) with atomic oxygen (1.3b), was originally proposed by Glass [6] in 1965; however, according to Nori and Seitzman [7] this was not confirmed until the later works of Grebe and Homman [8]. The reaction of ethynyl with molecular oxygen, (1.3c), was suggested by Renlund [9] whereby CH* is thought to be produced via a peroxy (O_2C_2H) intermediate.

The literature suggests that the relative importance of reactions (1.3a), (1.3b), and (1.3c) is highly dependent upon the nature of the flame, the stoichiometry of the reaction, and perhaps also the chemical composition of the fuel (although it should be acknowledged that while this latter statement is a logical conclusion to be drawn from a review of previous work it is not well proven). Based upon experimental measurements of C_2H and O concentrations in helium diluted acetylene-air flames, Devriendt and Peters argue that (1.3b) should be the major, if not dominant, source of CH* production in normal hydrocarbon flames [10]. However, this view is not universally accepted. Elsamra et al. [11] for example, contend that (1.3c) dominates (1.3b) under hot, lean conditions.

A number of researchers have attempted to use chemical kinetic computations to identify the dominant CH* production mechanism. In one recent work Nori and Seitzman [7] completed a comparison of the predictive accuracy of four proposed CH* formation models (applied to a 1D laminar flame) against experimental measurements of chemiluminescence in premixed methane-air and pre-vaporised Jet-A-air flames under lean burn conditions. In this case, three models (i.e. Elsamra et al. [11], Smith et al. [58], and Devriendt et al. [75]) are based on formation reactions (1.3b) and (1.3c), while the fourth model (Hall et al. [76]) uses the combination of reactions (1.3a) and (1.3b). The rate constants are summarized in Table 1.1. The results of the study suggest reactions (1.3b) and (1.3c), i.e. the formation of CH* from an ethynyl (C_2H) precursor, as the dominant formation routes in lean flames. This result however, was qualified by the authors with an acknowledgement of concern regarding the C_2 kinetics used in the model and the accuracy of the results at high pressure for validation.

Table 1. 1 Rate constants summarised by Nori et al. [7] for CH*. Rate coefficients are expressed as $k = A \cdot T^b \cdot \exp(-E_a/RT)$ with E_a in units of cal·mol^{-1} and $A \cdot T^b$ in cm^{3}mol^{-1}s^{-1} for two body reactions (with T in Kelvin)

#	Reaction	A	b	E_a	Ref.
(1.3a)	$C_2 + OH \rightarrow CH^* + CO$	2×10^{14}	0	0	Petersen et al. [76]
(1.3b)	$C_2H + O \rightarrow CH^* + CO$	$2.50\ (\pm 0.8) \times 10^{12}$	0	0	Smith et al. [58]
		5.2×10^{11}	0	2600	Petersen et al. [76]
		$1.08\ (\pm 0.4) \times 10^{13}$	0	0	Devriendt et al. [75]
		$6.023\ (\pm 3.0) \times 10^{12}$	0	457	Elsamra et al. [11]
(1.3c)	$C_2H + O_2 \rightarrow CH^* + CO_2$	$3.20\ (\pm 1.0) \times 10^{11}$	0	1599	Smith et al. [58]
		$2.17\ (\pm 0.8) \times 10^{10}$	0	0	Devriendt et al. [75]
		6.023×10^{-4}	4.4	-2285	Elsamra et al. [11]

With regard to OH* formation, a series of investigations has been conducted, from the early suggestions by Gaydon [5] to the latest work of Hall and Petersen [12]. OH* emission measurements from hydrogen mixtures has been studied in shock tubes by Belles et al. [25], Gutman et al. [26], Gardiner et al. [27], and Hidaka et al. [28]. Measurements of OH* formation rates in hydrocarbon mixtures have been reported by Carl et al. [29], Lichtin et al.

[30], and Smith et al. [31, 58]. The conclusion is that the primary OH* formation reaction in hydrocarbon combustion processes is:

$$CH + O_2 \rightarrow OH^* + CO \qquad (1.4a)$$

However, researchers differ in their recommendations for the function of OH* in hydrogen mixtures with some in favour of

$$H + O + M \rightarrow OH^* + M \qquad (1.4b)$$

Based on the recent suggestions of Smith et al. [58] and the support of other sources [33, 34], the possibility of OH* formation through H + 2OH (1.4c) has to be considered as well:

$$H + OH + OH \rightarrow OH^* + H_2O \qquad (1.4c)$$

Kinetic rate constants for reactions (1.4a) to (1.4c) have long been studied and the experiments conducted to determine the dominant OH* formation mechanisms have taken one of two approaches: (1) flame [29, 58, and 49] and (2) shock tube research [12, 78]. Nori et al. [71] have summarized the OH* mechanism and rate constant information, with the rate constants given in an Arrhenius form, and this is shown in Table 2.1. It should be pointed out that these investigations were carried out under particular experimental conditions; therefore the results obtained cannot be always applied to flames.

Table 1. 2 Rate constants summarised by Nori et al. [71] for OH*. Rate coefficients are expressed as $k = A \cdot T^b \cdot \exp(-E_a/RT)$ with E_a in units of cal·mol^{-1} and $A \cdot T^b$ in cm^{3}mol^{-1}s^{-1} for two body reactions or cm^{6}mol^{-2}s^{-1} for three body reactions (with T in K)

#	Reaction	A	b	E_a	Ref.
(1.4a)	$CH + O_2 \rightarrow OH^* + CO$	3.72×10^{10}	0	167.2	Carl et al. [29]
		3.24×10^{14}	-0.4	4150	Hall et al. [12]
(1.4b)	$H + O + M \rightarrow OH^* + M$	1.20×10^{13}	0	6940	Hidaka et al. [78]
		$5.45\ (\pm 2.3) \times 10^{12}$	0	0	Smith et al. [58]
		3.1×10^{14}	0	10000	Hall et al. [12]
(1.4c)	$H + OH + OH \rightarrow OH^* + H_2O$	$1.45\ (\pm 0.6) \times 10^{15}$	0	0	Smith et al. [58]

The origin of the 'blue continuum' CO_2* chemiluminescence has also been investigated. However, its mechanism and emission structure has been debated [67] since it is

least understood compared with CH* and OH*. In early studies, Baulch et al. [32] presented that reaction (1.5) was the primary cause of CO_2* chemiluminescence:

$$CO + O \rightarrow CO_2^* \tag{1.5}$$

According to the later investigation [79], the origin of the CO_2* emission is given by the following mechanisms:

$$CO + {}^3O + M \rightarrow {}^3CO_2^* + M \tag{1.6a}$$

$${}^3CO_2^* \rightarrow CO_2^* \tag{1.6b}$$

$$CO_2^* \rightarrow CO_2 + h\nu \tag{1.6c}$$

$$CO_2^* + M \rightarrow CO_2 + M \tag{1.6d}$$

where ^3O is an O atom in the triplet ground state; $^3CO_2$* denotes a CO_2 molecule in an excited triplet state, which then goes over into a neighbouring excited singlet state CO_2* without radiation (1.6b). Next, the de-excitation of excited state CO_2* occurs through one of the two ways: (1) radiation (1.6c), and (2) collisional quenching (1.6d). M represents a third collisional partner; in reaction (1.6d), M will take up the released energy. Shock tube measurements [79] of the spectral intensity between the wavelength range of 260 nm and 700 nm yielded an overall rate coefficient:

$$k = 6.8\ (\pm 0.6) \times 10^5 \exp(-1960/T) \quad \text{(in unit of } cm^3mol^{-l}s^{-1}) \tag{1.7}$$

for CO_2* formation reaction between 1300 and 2700K.

In hydrocarbon flames, the chemiluminescence during combustion is either emitted from the reaction zone or from the burned gas region. Besides, the chemiluminescence of the OH* transition and the CH* transition is measured with superimposed background emissions that occur at the same wavelengths as the OH* and CH* chemiluminescence. The background observed at these wavelengths is commonly ascribed to emissions from CO_2*, however it may also be due to other sources. According to Tinaut et al. [48], whose work is in some ways similar to the current work, the flame front emissions consist of, mainly, narrow-

band OH*, CH*, and C_2* radicals, while the dominant contribution of emissions from the burned gas region is the broadband CO_2*. As this thesis mainly focuses on the chemiluminescence emission from the flame front, the narrow-band OH* and CH* chemiluminescence are of particular significance.

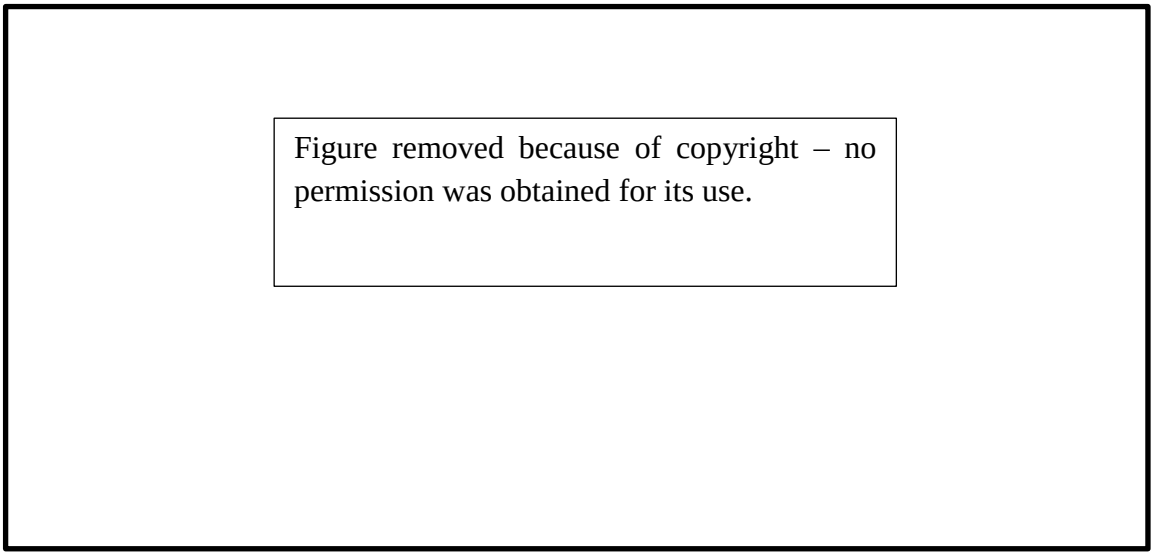


Figure 1. 2 The simplified methane oxidation mechanism. The main portion of the carbon follows the marked reaction path. Only a small portion follows the side paths, which yield OH*, CH*, and CO_2* [15, Fig. 2].

Predictions of CH* and OH* chemiluminescence are necessarily limited by the difficulty of modelling combustion processes, and in particular the formation and consumption of intermediate species such as CH*, in detail. Unsurprisingly then, the majority of published works in this area consider only the combustion of methane (the most simple of the hydrocarbons, CH_4) in air and, typically, use substantially simplified reaction mechanisms [12, 13, 14, 15, 17, 18, 47, 49]. While such models are undoubtedly helpful in explaining experimentally observed phenomena under specific circumstances, the wider interpretation of numerical results should be treated with suspicion. Figure 1.2 is a typical example of the simplified reaction pathways used for the prediction of lean premixed combustion of methane in air [15]. Najm's analysis [13], comes to a conclusion that only a small portion of the carbon follows the side reaction paths, which lead to the chemiluminescent radicals OH*,

CH*, and C_2*, while most of the carbon follows the main reaction path, which has been labelled as the marked reaction path in Figure 1.2. Other researchers have made similar *a priori* selections of the reaction pathways to be included in their models [14].

1.3 Sensitivity of CH* and OH* Emissions to Combustion Conditions

Although the majority of the prior works available within the literature consider 'flows with simultaneous variations of equivalence ratio, strain rate, temperature, and sometimes pressure' [16] significant areas of agreement can be found regarding the behaviour of CH* and OH* chemiluminescence intensity to the effects of equivalence ratio, temperature, pressure and strain.

1.3.1 Equivalence Ratio, Φ

With respect to equivalence ratio, the intensity of CH* chemiluminescence is widely reported to increase with increasing equivalence ratio under lean burn conditions. Higgins et al. [17], in an experimental study of CH* chemiluminescence from lean-burning ($0.66 \leq \Phi \leq 0.86$), premixed, laminar methane-air flames, found that for any fixed pressure, the normalized CH* chemiluminescence intensity (normalized with respect to the fuel mass flow rate, *i.e.* $I_{CH*}/\dot{m}_{CH_4}$) increased with increasing equivalence ratio. Higgins attributed this observed increase in CH* chemiluminescence intensity with increasing Φ to an increased flame temperature as the equivalence ratio moves towards stoichiometric. Taupin et al. [18] reported similar results for the lean-burn combustion of methane-air mixtures in a pressurized, premixed turbulent flame (such as might be found in a gas-turbine (GT) combustion chamber), suggesting a linear relationship between CH* chemiluminescence intensity and Φ for a fixed combustion air temperature and ambient pressure ($293\ \text{K} \leq T_{comb} \leq 673\ \text{K}$, and $0.1\ \text{MPa} \leq P \leq 0.4\ \text{MPa}$) [18]. A linear relationship was also reported for the variation of $\alpha_T = \Delta CH^*/\Delta\Phi$ ($\Delta\Phi$ represents equivalence ratio range between unstable flame detection and

extinction; ΔCH* denotes the normalised CH emission variation, and α_T is the mean slope of the CH* variation versus equivalence ratio) with combustion air temperature. In a numerical study of lean burn combustion in a 1D laminar methane-air flame Nori and Seitzman [7] predicted the CH* chemiluminescence signal (in this case normalized by total heat release per flame area) to increase substantially with increasing equivalence ratio over the range examined ($0.5 \leq \Phi \leq 1.0$).

Uniquely among the prior works reviewed for this report, Hardalupus and Orain show results for the variation of CH* chemiluminescence intensity (again normalized by fuel mass flow rate) for natural gas (94% methane)/air mixtures under both lean and fuel-rich conditions [16]. These results, shown in Figure 1.3a, show CH* intensity to increase (in an apparently linear manner) with increasing equivalence ratio in the range $0.7 \leq \Phi \leq 1.1$ - the deviation of the results for a jet velocity (V_0) of 2 ms^{-1} from this general trend were attributed to instability close to the lean extinction limit of the flame. Peak intensity is shown at an equivalence ratio of 1.1 with CH* chemiluminescence decreasing as Φ is increased further to 1.3. While the coarse sample rate of this work does not allow the position of the CH* peak to be determined with confidence, it is worth noting that the results of Hardalupus and Orain are wholly consistent with Higgins' assertion that CH* chemiluminescence intensity is directly correlated with flame temperature as peak flame temperatures are expected to occur at an equivalence ratio just in excess of 1.0.

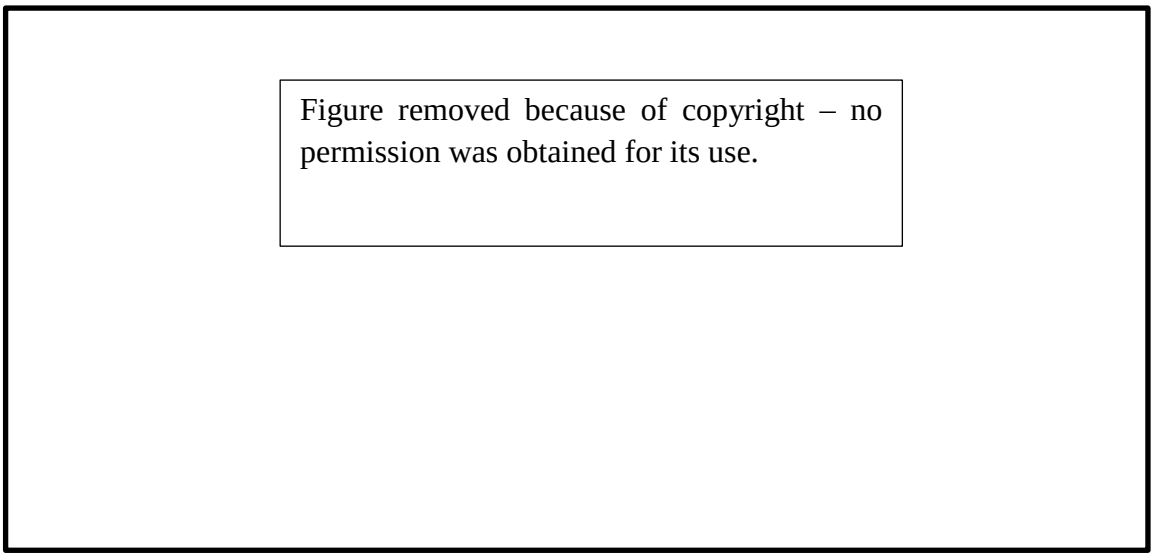


Figure 1. 3 Variation of mean CH* (in Figure 1.3a) and OH* (in Figure 1.3b) chemiluminescence intensity (normalized against mass flow rate of fuel) with equivalence ratio: premixed natural gas-air flame in a counter-flow burner [16, Fig. 10].

The relationship between equivalence ratio and the OH* chemiluminescence has long been studied [14, 16, 47, 48, 49, 70]. Higgins et al. reported systematic measurements of OH* chemiluminescence from a premixed laminar flame at pressures ranging from 0.5 to 2.5 MPa, and equivalence ratios from 0.66 to 0.86 [47]. As with the trend for CH*, the normalised OH* chemiluminescence (against the mass flow rate) increases with increasing equivalence ratio (from 0.65 to 0.85). Higgins attributed this to a temperature effect. Tinaut et al. [48] measured the OH* chemiluminescence in premixed combustion of n-heptane, iso-octane, and a mixture of 50% n-heptane and 50% toluene in a constant volume combustion bomb. They found that a small increase in equivalence ratio (from 0.8 to 1.0) gives a notable increase in OH* intensity, which is associated with an effect of temperature. Meanwhile they deduced that the intensities of OH* and CH* are highly dependent on the fuel species. Hardalupas et al. [16] showed that the maximum normalised OH* chemiluminescence occurs close to stoichiometric; however, the mean intensity of OH* had a less steep profile compared to that of the mean intensity of CH*. This is shown in Figure 1.3b.

In summary, there exists a monotonic behaviour between the OH* and CH* chemiluminescence and the equivalence ratio as it is towards stoichiometric, which indicates the OH* and CH* chemiluminescence to be a useful indicator of equivalence ratio.

1.3.2 Pressure, *P*

With regards to the effects of pressure, Nori and Seitzman's numerical studies predict pressure to have a significant effect of the normalized CH* signal with an increase in pressure from 1 to 15 atm (0.101 to 1.515 MPa) markedly decreasing CH* chemiluminescence intensity [7]. Nori's results are consistent with the experimental observations of Higgins et al. who consider the effects of pressure and strain rate on the CH* chemiluminescence from lean premixed laminar methane-air flames at ambient pressures ranging from 0.5 to 2.5 MPa [17], Taupin et al. [18] who consider similar flames at somewhat lower pressures, up to 0.4 MPa, and Ikeda et al. [24] who investigated a rich premixed methane air flame (Φ = 1.1) at pressure between 0.1 and 1.5 MPa. In this later study, Ikeda and co-workers report the CH* intensity to be more sensitive to the effects of pressure than OH*.

Higgins attributes the decrease in CH* chemiluminescence with pressure for a fixed value of Φ to increased collisional quenching and a decrease in the fraction of carbon that goes through the C_2H reaction pathway at higher pressures. However, it should be noted that Higgins' later statement regarding the fraction of carbon passing through the C_2H path is unsupported by his own experimental work and seems to be based upon the numerical predictions of Najm and co-workers on an unsteady premixed stoichiometric methane-air flame with N_2 dilution [13]. Significantly, with respect to the potential behaviour of CH* chemiluminescence intensity in heavier hydrocarbon flames, Najm et al. [13] do not include the (1.3a) or (1.3c) reaction pathway in their computations. Similarly, as discussed previously,

the (1.3a) reaction pathway is either ignored or modelled with a low degree of confidence in the work of Nori [7].

For OH* chemiluminescence, Higgins et al. [47] studied the pressure effect from lean (0.66 – 0.86) methane / air combustion in the pressure range of 0.5 to 2.5 MPa, and they found the functional relationship to be monotonically decreasing with increasing pressure. The pressure effect is primarily attributed to the increased quenching at high pressures according to Higgins, and their observation is consistent with Docquier's argument. Docquier et al. measured chemiluminescence in premixed methane / air flames using a Bunsen-type burner, and investigated the effect of pressure (1 to 10 bar) and equivalence ratio (0.6 – 1.1) [53]. They have found that for the normalised OH* chemiluminescence (as with CH* and C_2*), there is a clear decay of the signal as pressure increases; meanwhile this behaviour is also observable in their numerical simulations for OH*. Tinaut et al. [48] measured OH* and CH* in a constant volume combustion bomb, and they reported that for a given initial temperature, the OH* chemiluminescence increases as the initial pressure grows, which was striking. However, it is worth mentioning that their OH* (as well as CH*) measurements have not been normalised against mass burned rate. Furthermore, they did not propose a relationship between the absolute OH* and CH* and the local pressure.

1.3.3 Temperature, *T*

As noted previously, CH* and OH* chemiluminescence intensity has been positively correlated with flame temperature [17, 47]. It is then unsurprising that increasing pre-combustion temperatures (initial temperatures) are reported to increase CH* and OH* chemiluminescence intensity in both laminar and turbulent methane-air flames [7, 18, 48].

1.3.4 Strain Rate, α

Hardalupus and Orain [16] measured CH* and OH* (as well as C_2* and CO_2*) chemiluminescence in a natural-gas fuelled, pre-mixed, counter-flow flame for a range of strain rates between 80 and 400 s^{-1}. The measurements, which were performed at atmospheric pressure, showed some variation of mean CH* and OH* intensities with rate of strain related to flame quenching close to the extinction limits. Under more stable conditions, Higgins and co-workers [17], in a study on lean burning methane-air flames ($0.66 \leq \Phi \leq 0.86$), found no dependence of the CH* chemiluminescence intensity on rate of strain ($200 < \alpha < 650$ s^{-1}) in the pressure range of 0.5 to 2.5 MPa. Nori and Seitzman [7], in a numerical study on lean premixed methane-air flames, predict CH* chemiluminescence intensity to either increase or remain roughly constant. Normalized by integrated heat release, which decreases with increasing strain, this results in a normalized CH* chemiluminescence signal that increases with increasing strain rates, although the sensitivity of the heat release normalized signal to strain rate is low at higher (5.05 bar) pressure.

1.4 Chemiluminescence as an Indicator of Heat Release Rate

The heat release rate is an important parameter for the understanding and prediction of unstable combustion states. Until now, most heat release measurements have been based on narrow-band OH*, CH*, C_2* and broadband CO_2* chemiluminescence emissions [4] because these radicals are supposed to correlate with the heat release rate.

The previous section of this review indicates that CH* and OH* chemiluminescence intensities are affected by equivalence ratio (Φ), pressure (p), temperature (T), and strain (α). However, although the literature indicates reasonable consensus regarding the individual effects of each of these four combustion variables, less agreement is found with regard to the suitability of CH* and OH* chemiluminescence intensity measurements as indicators of heat

release rate. Najm and co-workers [13] in a detailed investigation on 'the adequacy of certain experimental observables as measurements of flame burning rate' (defined by Najm as fuel consumption rate) conclude that CH* and OH* chemiluminescence is unreliable as an indicator of heat release since the reaction paths leading to the production of excited state CH* and OH* radicals carry only a small proportion of the carbon flow. It is argued that subtle changes in flame chemistry brought about by, for example, high flame curvature or unsteady strain rate can lead to an extinction of the CH* and OH* chemiluminescence while the flame continues through other, more favoured, chemical pathways [13]. However, Hardalupas and Orain [16] caution against the generalization of Najm's conclusions pointing out that not only is the cited study limited to unsteady premixed nitrogen-diluted methane-air flames with high curvature, but also that no supporting experimental evidence is presented to verify the chemical model used for calculating chemiluminescence. This lack of experimental validation for the chemical model is of particular concern because, as has been mentioned in an earlier section of this review, this model does not include either the (1.3a) or the (1.3c) reaction pathways for CH* production. In their study, Hardalupas and Orain conclude that the chemiluminescence intensity from CH* (and also OH* and CO_2*) is a good indicator of heat release rate for the premixed, counter-flow, natural-gas flame examined. Note that although Aleiferis et al. [19] also state that chemiluminescence from OH*, CH*, and C_2* are good indicators of heat release and reaction rate in premixed flames this is referenced in this case to the much earlier work of Gaydon [5].

The disagreement between the conclusions of [13] and [16] is indicative of the present state of knowledge concerning CH* and OH* production in flames. It should be recognized, as it is by Hardalupas and Orain [16], that the results of these two studies are not necessarily at variance with one another and that, in fact, these two apparently inconsistent conclusions might accurately reflect CH* and OH* production behaviour in what are two significantly

different flame structures (a premixed stoichiometric N_2 diluted methane-air flame in a two dimensional unsteady vortical flow [13], and a steady, premixed, natural-gas flame in a counter-flow burner [16]).

With respect to the measurement of heat release rate in IC engines, Hultqvist et al. [20], in a study of homogeneous charge compression ignition combustion, concluded that the crank-angle resolved broadband chemiluminescence intensity (in this case, integrated along a line-of-sight that allowed approximately 40% of the combustion volume to be imaged, and averaged over 400 cycles) was well correlated with instantaneous heat release rate. However, although Hultqvist's work is cited in several subsequent studies as justification for the use of broadband chemiluminescence measurements as indicators of global heat release rate [21, 22], it should be noted that the correlation presented is without physical significance; a second order polynomial was chosen as providing an acceptable fit to the data for chemiluminescence intensity vs. rate of heat release without reference to, or discussion of, the possible causes of such a relationship. Similarly, and somewhat surprisingly having referenced the work of Hultqvist immediately prior to presenting their own data, Thirouard et al. suggest a linear relationship between total chemiluminescence intensity and heat release rate. Again, no physical justification for this presumed relationship is given [22].

1.5 Overview of Present Work

The primary objective of this thesis is to develop an empirical model for flame chemiluminescence from two radicals, i.e. OH* and CH*, and to evaluate the usefulness of flame chemiluminescence as a combustion diagnostic at various operating conditions for gaseous and liquid fuels of importance: methane and iso-octane.

CH* and OH* have been shown to be dependent on various combustion conditions such as pressure, temperature, equivalence ratio and stretch. Hence there is a clear need for

well controlled experiments that measure CH* and OH* flame chemiluminescence intensity over a wide range of engine relevant air-fuel ratios, residual gas levels, temperatures, and pressures. By using a spherically propagating premixed laminar flame in a combustion bomb it is possible to have careful control of the initial conditions. Furthermore, during the experiment the pressure will rise (thereby increasing the temperature) so that a single experiment will yield a sequence of data. Chapter 2 describes the experimental facilities used in this study, including the constant volume combustion bomb and the subsystems for fuel delivery, ignition, LabView control, data acquisition and the optics necessary for acquiring flame chemiluminescence.

To measure the OH* and CH* chemiluminescence accurately, the optical system needs to be designed with a restricted field of view. In Chapter 3, a model of the optical system is developed, in order to optimise the optical geometry and to quantify the optical system collection efficiency as a function of flame radius. Additionally, this chapter includes the absolute calibration of the PMT systems so as to relate the absolute chemiluminescence as an energy output (in terms of watt).

The normalisation of the OH* and CH* chemiluminescence (against mass of fuel burned rate and collection efficiency) is based on a multi-zone combustion model and the experimental data. By using a multi-zone combustion model, then pressure measurements can be used to define the unburned mixture temperature, the flame radius and the heat release rate. *NIICS* (Normalised Intensity Integrated Calculation System) has been created to combine the data (from the multi-zone model, experimental measurements, and the optical model) and to calculate the normalised OH* and CH* intensities. Details of the chemiluminescence normalisation approach are presented in Chapter 4.

The normalised CH*/OH* ratio data are then fitted using a multi-variate fitting and correlation analysis in Chapter 5, and this mathematical formulation is used to evaluate flame

chemiluminescence from these species, for sensing the equivalence ratio in premixed flames of methane and iso-octane at various operating conditions. It is worth noting that the OH* and CH* chemiluminescence refer to emissions within the band-pass filtered wavelength ranges at which such emissions are observed, i.e. signals are considered without background subtraction. In fact, there are continuous CO_2* emissions that occur at the same band-pass filtered wavelengths as the OH* and CH* chemiluminescence. Besides, the background emission observed within the wavelength band that are commonly ascribed to emissions from CO_2* may be due to other sources but none the less, CO_2* chemiluminescence is used as a label for the background emissions in these bands.

Chapter 6 studies the dependence of the absolute OH* and CH* chemiluminescence on combustion parameters such as pressure, temperature, and equivalence ratio in the above fuels. This chapter also examines the leading chemical kinetic mechanisms of OH* and CH* chemiluminescence, and estimates implications for sensing engine relevant quantities such as equivalence ratio and heat release rate. Again, the OH* and CH* signals are considered without subtraction of the background emissions that occur at the same wavelengths as the OH* and CH* chemiluminescence.

To isolate the background emissions, spectroscopic measurements have been conducted using an Ocean Optics spectrometer and a Princeton ICCD spectrometer, and these results are summarised in Chapter 7. Finally, Chapter 8 concludes the thesis with a summary and recommendations for further studies.

Chapter 2 Experimental Apparatus

The experimental setup used in this work consists of a test facility designed for the study and characterization of the gaseous and liquid fuel combustion processes. The main components are a spherical combustion vessel and heating system, complete with equipment for the introduction of fuels, ignition system, data acquisition system and sensors. Each of these parts is dealt with in more detail below.

2.1 Overview of the Test Facility

By using a combustion 'bomb' it is possible to have accurate control over the initial conditions (equivalence ratio, initial temperature and pressure) under which a premixed laminar flame will spherically propagate. During the combustion event the pressure will rise (thereby increasing the temperature) so that a single experiment will yield a sequence of unburned gas conditions.

Figure 2.1 shows schematic diagram of the experimental configuration used in the current work. The present test facility consists of the following sub-systems:

1. Combustion vessel and heating system
2. Air / fuel mixture delivery system
3. Ignition system, with central ignition
4. Sensors and data acquisition system
5. Optical system

The optical system employed to detect OH* and CH* chemiluminescence from the combustion bomb consists of a pair of fused silica lenses, each with a nominal aperture of 40 mm, using interference filters and photo-multiplier tubes (PMTs). Chapter 3 will discuss the optical system in detail. The ignition system is not discussed in this chapter; more information is found in Marshall [3].

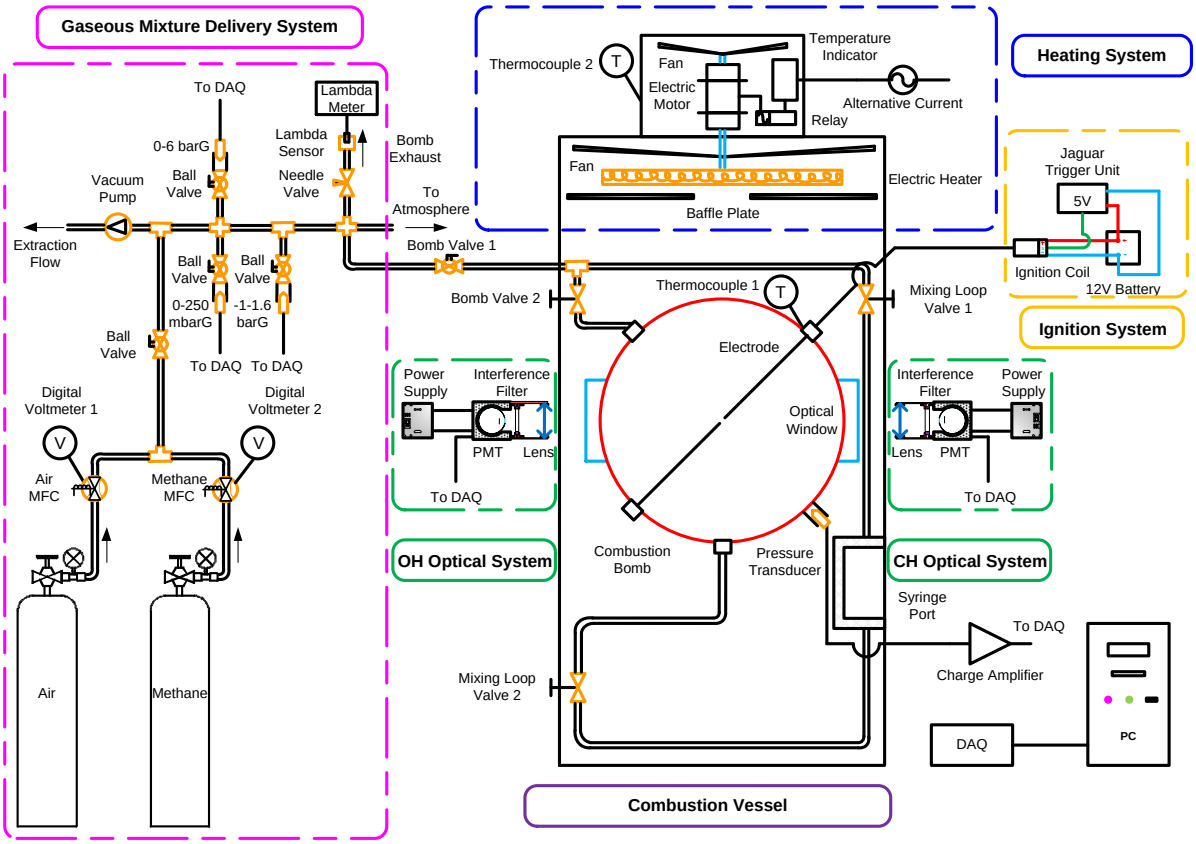


Figure 2. 1 Schematic representation of the experimental facility with gaseous mixture delivery system for the introduction of methane.

2.2 Combustion Vessel and Heating System

The spherical combustion vessel is made of stainless steel, with an internal diameter of 160 mm, and it can withstand a maximum pressure of 34 bar. The vessel is currently resting on a curved base-plate which fitted the curvature of the bomb and was bolted down to the optical bench to secure it. The framework for the optical bench also provides mounting for all the valves, vacuum pump, small gas cylinders, electronics including a PC and shelves for storage. A cross-section of the combustion vessel and its oven is shown in Figure 2.2.

The mixture is ignited by two opposed, co-linear electrodes which form an approximately 1.2 mm spark gap at the centre of the sphere. The spark is triggered by a TTL pulse, the duration of which sets the charging time of the Jaguar HT coil pack.

As shown in Figure 2.2, the bomb is constructed in two halves, each of which can have an optical access window. The two halves are held together by twelve steel bolts and

sealed by a Viton O-ring. The windows are also sealed by O-rings. End caps bolted into flanges in the bomb hold the windows in. A ring of gasket material and a ring of brass are placed between the windows and the end caps to protect the quartz. Although the windows and window end caps can be replaced by a blanking end cap, as seen in Figure 2.2, two photomultiplier tubes mounted outside the vessel for collecting the chemiluminescence signals, meant that both windows were required.

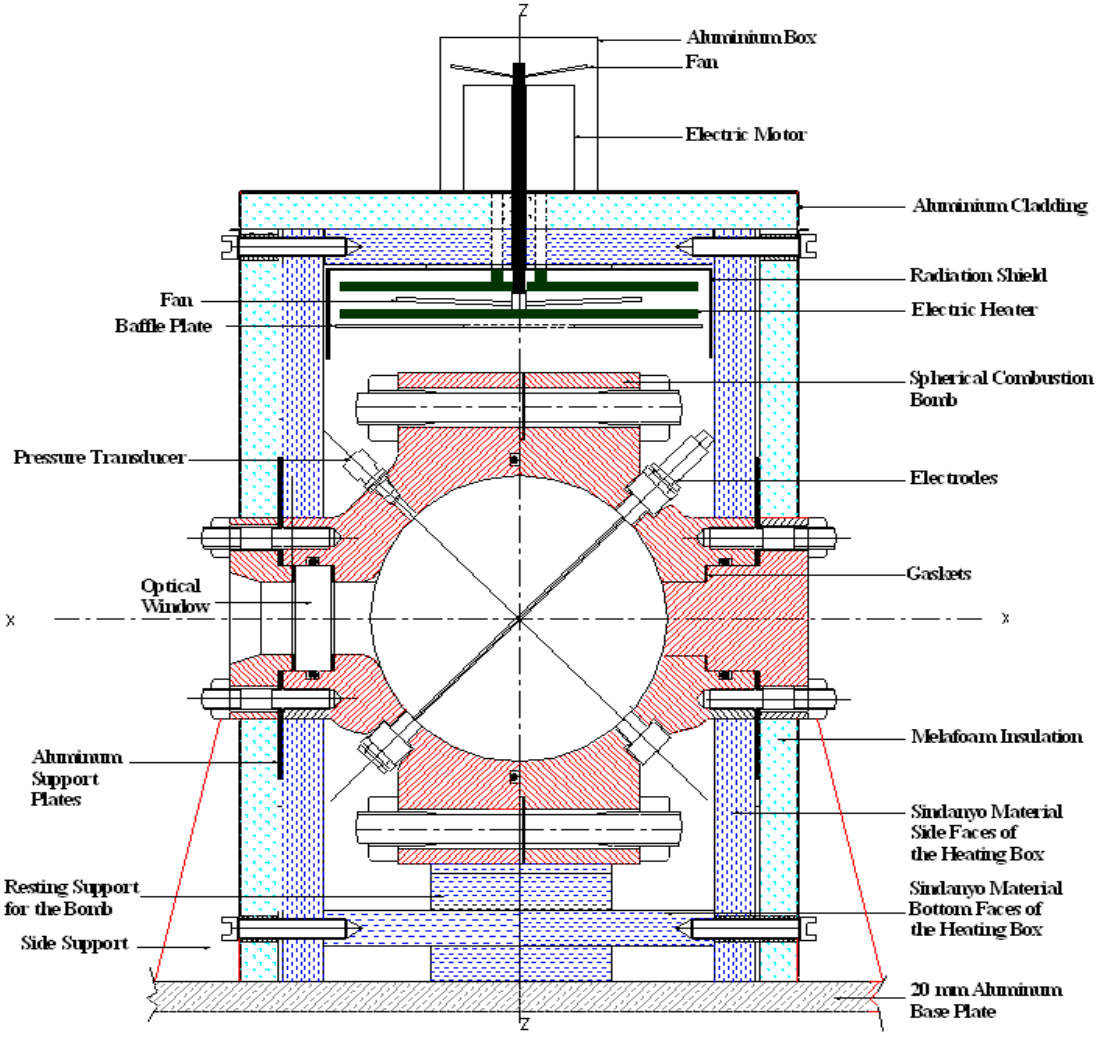


Figure 2. 2 Cross-section of the combustion vessel and its oven. From Saeed (2002) [35].

The combustion vessel has also six openings in the walls of the sphere for two spark plug electrodes, the piezo-electric pressure sensor (Section 2.6), the thermocouple (Section 2.6) and two gaseous flow connections. The bomb is inside a temperature controlled oven

with a circulating fan, a heater and a controller. The maximum rated temperature of the bomb is 200 ℃.

2.3 Gaseous Mixture Delivery System based on Theory of Partial Pressures

2.3.1 Theoretical Analysis

For gaseous fuel and air delivery and mixture preparation, the theory of partial pressures is used to calculate the partial pressures of fuel and air, equivalence ratio and mixture preparation pressure based on the chosen fuel. For a fuel burned stoichiometrically in air:

$$C_xH_y + a\,(O_2 + \frac{79}{21}N_2) \;\rightarrow\; bCO_2 + cH_2O \;+\; a\frac{79}{21}\,N_2 \tag{2.1}$$

The atom balance gives:

$$C_xH_y + \left(x + \frac{y}{4}\right)\left(O_2 + \frac{79}{21}N_2\right) \rightarrow xCO_2 + \frac{y}{2}H_2O + \left(x + \frac{y}{4}\right)\frac{79}{21}N_2 \tag{2.2}$$

Dalton's Law of Partial Pressures indicates that the ratio of the partial pressures of the fuel and the air will be equal to their molar ratio.

$$p_f = \frac{n_f}{n_{air}} \times p_{air} \tag{2.3}$$

$$p_{mix} = p_f + p_{air} \tag{2.4}$$

2.3.2 Experimental Procedure

For the experimental procedure implemented in LABVIEW, each stage uses measurements from the previous stage, rather than the assumption of what should have been done, in order to predict the target in the next stage. Actual equivalence ratio and molar residual fraction (if any) are also calculated based on measurements, Marshall (2010) [3].

To prepare a gaseous mixture, it is worth noting beforehand, that the air is added in two batches: one before fuel addition and one after. Any residuals left in the bomb have air added to them, and then gaseous fuel is injected, followed by the other batch of air. To

increase experimental accuracy, p_{mix} is greater than the initial bomb pressure required so that more fuel has to be added and then some of the mixture removed. Due to the limited gas motion within the combustion chamber during the charging process, a period of not less than five minutes was allowed before ignition to ensure a homogeneous mixture. According to Stone et al. [36], the combustion data from mixtures that were allowed to settle for over two hours showed no difference from those that settled for five minutes. The five-minute settling time also ensured that a quiescent mixture was ignited. Dividing the air addition into two stages allows a sensitive pressure transducer to be used for measuring the fuel addition, thereby reducing the error in the partial pressure of fuel being added, which is far smaller than the pressure of the air being used.

$$n_1 = n_r \tag{2.5}$$

$$n_2 = n_r + n_{air1} \tag{2.6}$$

$$n_3 = n_r + n_{air1} + n_f \tag{2.7}$$

$$n_4 = n_r + n_{air1} + n_f + n_{air2} = n_{mix} \tag{2.8}$$

This analysis has assumed that the gases have been added slowly so there is no temperature change in the bomb during the filling process. In reality, any small temperature changes are taken into account by replacing the number of moles n with the ratio of the pressure to the temperature $\frac{p}{T}$, which is proportional to the former. For example, it is assumed that $T_4 = T_0$, the initial temperature for the experiment, therefore,

$$\frac{p_{mix}}{T_0} = n_4 = n_r + n_{air1} + n_f + n_{air2} \tag{2.9}$$

and the number of moles of residuals is expressed as

$$n_r = x_r n_{mix} = x_r \frac{p_{mix}}{T_0} \tag{2.10}$$

Hence the choice of mixture pressure, initial temperature and residual mole fraction define the number of moles of residuals, which is recorded by LABVIEW. The number of moles of fuel then required can be expressed from equation (2.11) and (2.16):

$$x_r = \frac{n_r}{n_r+n_{air}+n_f} = \frac{n_r}{n_{mix}} \tag{2.11}$$

$$x_r\left(n_r + n_{air} + n_f\right) = n_r \tag{2.12}$$

$$x_r\left(n_{air} + n_f\right) = n_r(1 - x_r) \tag{2.13}$$

$$x_r n_f \left(\frac{n_{air}}{n_f} + 1\right) = n_r(1 - x_r) \tag{2.14}$$

$$x_r n_f \left(1 + \frac{100}{21\Phi}\left(x + \frac{y}{4}\right)\right) = n_r(1 - x_r) \tag{2.15}$$

$$n_f = \frac{n_r(1-x_r)}{x_r\left(1+\frac{100}{21\Phi}\left(x+\frac{y}{4}\right)\right)} = \frac{n_{mix}(1-x_r)}{\left(1+\frac{100}{21\Phi}\left(x+\frac{y}{4}\right)\right)} \tag{2.16}$$

The partial pressure of the fuel is simply obtained by multiplying the current temperature. A similar process is implemented to get the number of moles of air. It is worth mentioning that the partial pressure of the first portion of air is set up to be a bit higher than the current atmosphere pressure in order to eliminate the possible effect caused by ambient air leaking into the bomb vessel.

$$n_{air} = \frac{100}{21\Phi}\left(x + \frac{y}{4}\right) n_f \tag{2.17}$$

$$n_{air2} = \frac{100}{21\Phi}\left(x + \frac{y}{4}\right) n_f - n_{air1} \tag{2.18}$$

Once the second portion of air is injected, the actual equivalence ratio and residual mole fraction can be calculated by:

$$\Phi = \frac{100}{21}\left(x + \frac{y}{4}\right)\frac{n_f}{n_{air}} \tag{2.19}$$

$$x_r = \frac{n_r}{n_r+n_{air1}+n_f+n_{air2}} \tag{2.20}$$

For experiments with residuals, a dummy experiment is carried out before each batch of experiments and some of the combustion products are retained in the vessel; while for

experiments without residuals, the bomb is flushed three times with air between experiments to make sure that no products of combustion are left. The current methane and iso-octane experiments are conducted without residuals.

2.4 Alternative Gaseous Mixture Preparation Method using Mass Flow Controllers

2.4.1 Introduction

The gaseous mixture preparation was previously based on the theory of mole fractions. This method is precise but time consuming. For one thing, the number of moles has been calculated using actually $\frac{p}{T}$, but the thermocouple has a slow response; so to minimise temperature changes in the bomb during the filling process, the gases should be added slowly. For another, it is also necessary to wait for the gases to fully mix, since they have been added sequentially, and any leaks could confound the mixture preparation process.

The recent gaseous experiments to be discussed are from mixtures of methane and air, and were prepared by using a pair of mass flow controllers calibrated respectively for methane and air. This is quicker than admitting each gas separately and measuring the partial pressures, as there is no additional waiting time for the gases to mix uniformly.

The next section gives a description of the principle of mass flow controller operation, the mass flow controller calibration, and the setting up of the mass flow controllers in the test facility. This section ends by validating the mixture preparation method from a series of methane / air lambda measurements at various equivalence ratios using a pair of mass flow controllers.

2.4.2 Principle of Mass Flow Controller Operation

The mass flow controller is a device to measure and control the mass flow rate accurately and reliably. The principles of heat transfer are used to develop a linear output signal of 0 to 5 Vdc over the specific flow range.

The mass flow controller can be separated into 4 main components: a base assembly with gas fittings, a flow sensor, a regulating valve and appropriate electronics to automatically regulate the flow in response to an external command. Figure 2.3 shows a schematic cross-view of a typical thermal mass flow controller.

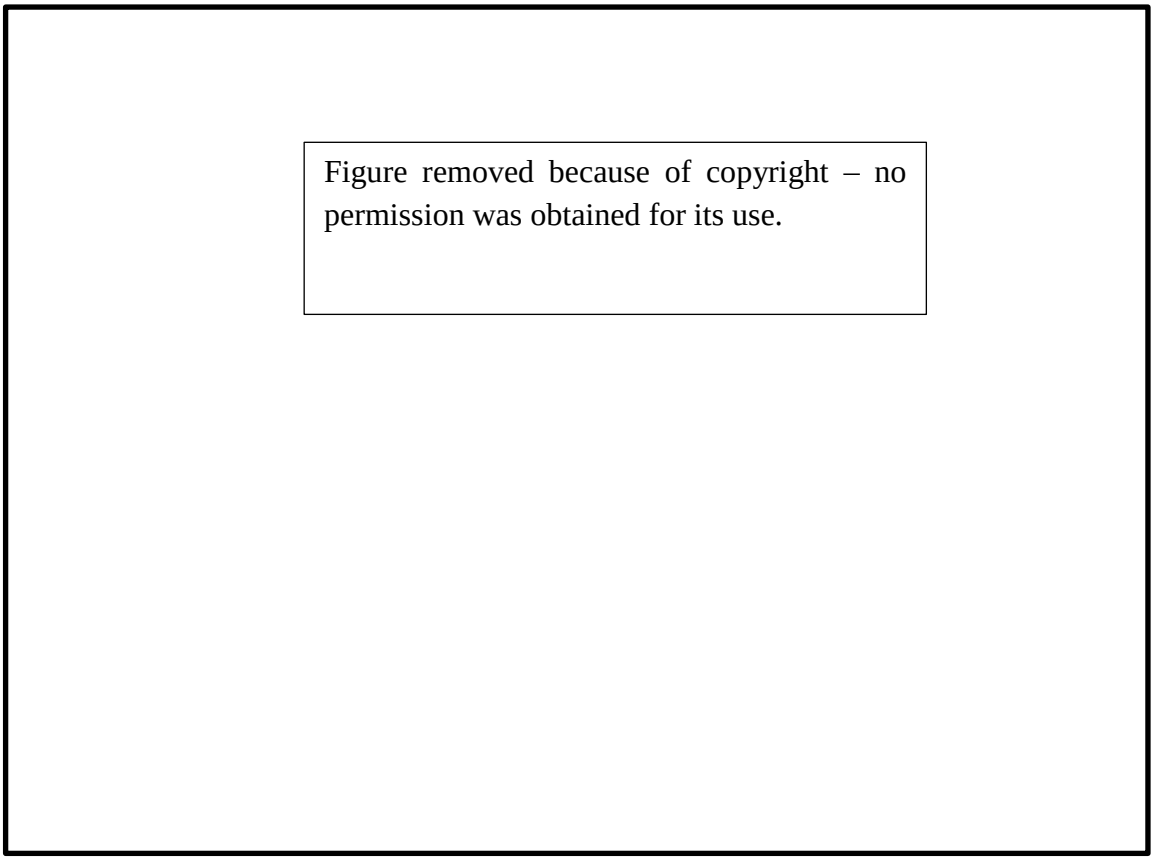


Figure 2. 3 A schematic cutaway view of a thermal-type mass flow controller. From [38, Fig. 2].

The bypass assembly is precisely designed in such a way that a fixed fraction of the gas that flows through the controller always passes the flow sensor, so the bypass is always proportional to the total flow within the range for which the mass-flow controller is built. The

total flow then passes through the control valve. The reason for using a bypass is that the sensor can only measure a small flow, typically 5 sccm (standard cubic centimetre per minute), the bypass system allows the controller to control and measure higher flows. For example, on a 100 sccm full scale mass-flow controller, the bypass is adjusted so that when 100 sccm flows through the controller, 5 sccm will flow through the sensor tube and 95 sccm will flow through the bypass. It is carefully designed to operate under laminar flow conditions, therefore assuring accuracy over the entire range of mass flow for the instrument. A fine mesh (20 micron) screen is permanently installed on the inlet fitting, protecting the sensor tube against particulate contamination.

The heart of the mass flow controller is a two-element sensor, which uses the thermal properties of a gas to directly measure the mass flow rate. To illustrate the sensor principles, take the case of cool gas flowing through a heated tube. Mathematically, the heating can be described by the First Law of Thermodynamics,

$$\dot{Q} = c_p \dot{m} \Delta T \tag{2.21}$$

Where $\dot{Q}$ is the heat rate supplied to the gas flow; $\dot{m}$ represents the mass flow rate; c_p is the specific heat for a constant pressure; ΔT is the net change in gas temperature as it traverses along the tube. If the heat flux is monitored, the amplitude can be converted into an electrical signal. Given that the specific heat is known for the gas, the mass flow rate can then be determined from the electric signal.

The sensor includes a tube externally wound with two heated resistance thermometers, measuring the change in temperature distribution created by the gas flowing inside the tube. For zero flow, the upstream and downstream temperatures will be equal. When the gas is flowing, the upstream region cools down whereas the downstream region heats up causing a temperature gradient along the length of the tube (see Figure 2.4 for details). Since the sensor temperature differences due to flow are converted into resistance changes by the coil of the

heating resistances, the resistance changes are converted to a voltage, i.e. 0 to 5 Vdc by a Wheatstone bridge. Accordingly, for a mass flow controller operating in its working zone the measurement is proportional to the flow with a coefficient.

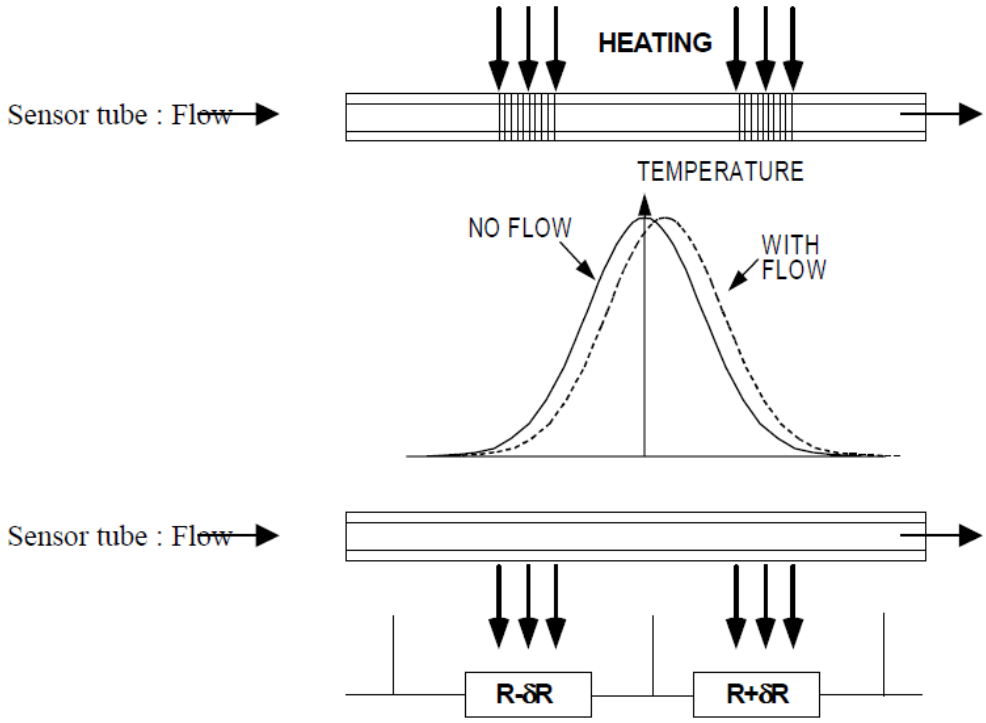


Figure 2. 4 Sensor temperature profile. From [37].

The electronics board contains an amplifier and detector bridge circuits. It compares the amplified detector output (measured by the sensor) to an external command voltage. This comparison generates an error signal which is used to drive the control valve.

The control valve will proportionally open or close until the output is equal to the set-point. The mass flow controller uses a normally closed valve, which is actuated by a solenoid.

2.4.3 Mass Flow Controller Calibration

As discussed in the previous section, the measurement (0 to 5 Vdc) is proportional to the gas flow. High linearity is needed to provide confidence if using a mass flow controller to deliver

mixtures; thus each mass flow controller needs to be calibrated for the known flow range and gases.

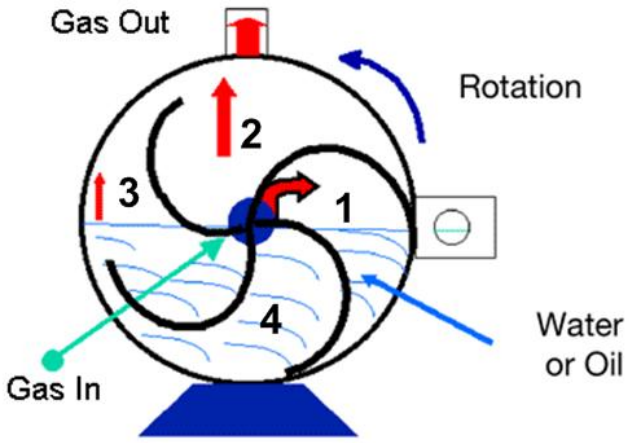


Figure 2. 5 Principle of the wet gas meter, based on Hayward (1979) [39].

The main instrument used for calibrating the mass flow controllers is a wet gas meter, which is a volumetric, positive displacement meter (drum type) that yields high precision and accuracy. As can be seen from Figure 2.5, the cylindrical drum that has a rotating axis is partitioned into several chambers that are sealed by water (or oil). The housing is filled with liquid to a specified level, and has an inlet tube that sticks out above the liquid level. If the gas with a higher pressure than that of the outlet enters through the inlet tube, it is guided into the chamber 1. The pressure of chamber 2 at this time is the same as that of the outlet, which is exposed above the liquid level. And then due to a difference in the gas pressure, the drum rotates counter-clockwise. The gas is fed into and discharged from chambers 1, 2, 3, and 4 in turn. It is worth mentioning that the incoming gas is saturated prior to the meter, since otherwise water would evaporate from the wet gas meter, and this would cause an over-reading. Hence a thermocouple is needed so that the saturation pressure of the water vapour can be found. The mass flow rate of dry gas is eventually derived from the wet gas volume flow rate by considering the ideal gas law, which is shown in Equation (2.22).

$$\dot{m} = \frac{(p_{atm} - p_{sat}) \cdot \dot{V}}{\frac{R}{M} \cdot T} \tag{2.22}$$

Where $\dot{m}$ and $\dot{V}$ stand for mass flow rate and volume flow rate, respectively; p_{atm} and p_{sat} represent atmospheric pressure and saturation pressure respectively.

For the current methane and air experiments, a UFC-1200A mass flow controller is well suited for controlling the methane; while an MKS mass flow controller is used for measuring the air flow rate. Figures 2.6 and 2.7 illustrate the mass flow controller calibrations for methane and air. Additional care needs to be paid to the calibration of the UFC-1200A mass flow controller using methane; this is because methane flow may cause flammable or explosive atmospheres when it is mixing with remaining air. To reduce the potential safety hazard, nitrogen is purged through the mass flow controller before and after calibrating with methane. Besides, ventilation of saturated methane from the outlet of the flow meter needs to be conducted away using the vacuum pump. Moreover, a funnel is placed right in front of the outlet to collect the methane and over-dilute the mixture so that it is not flammable.

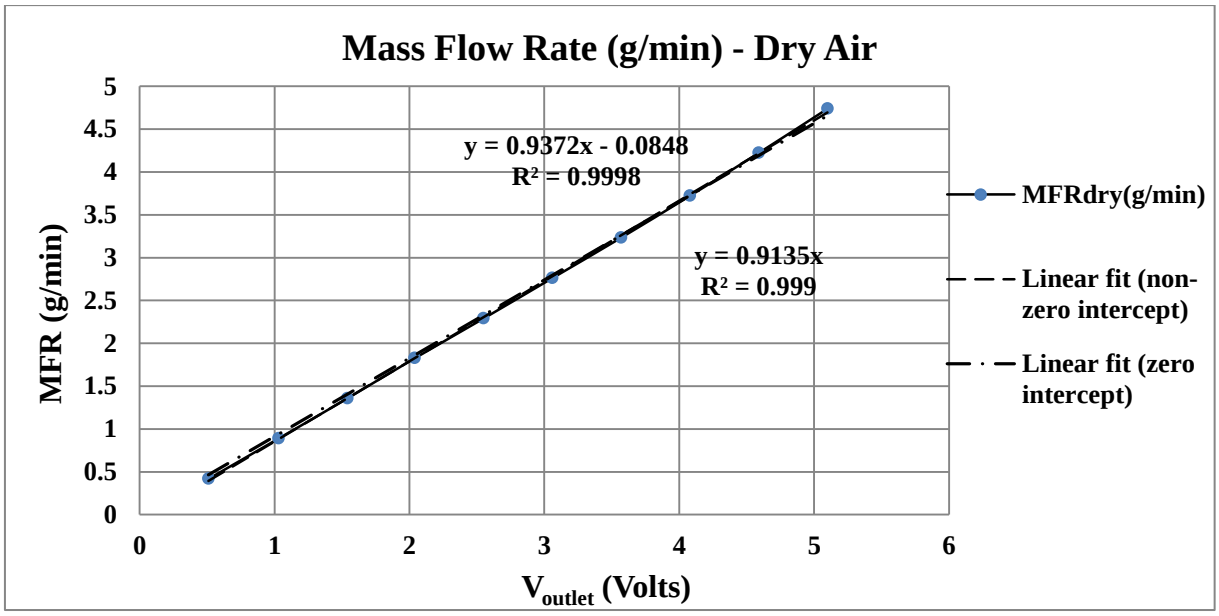


Figure 2. 6 Mass flow controller (MKS) calibration for air.

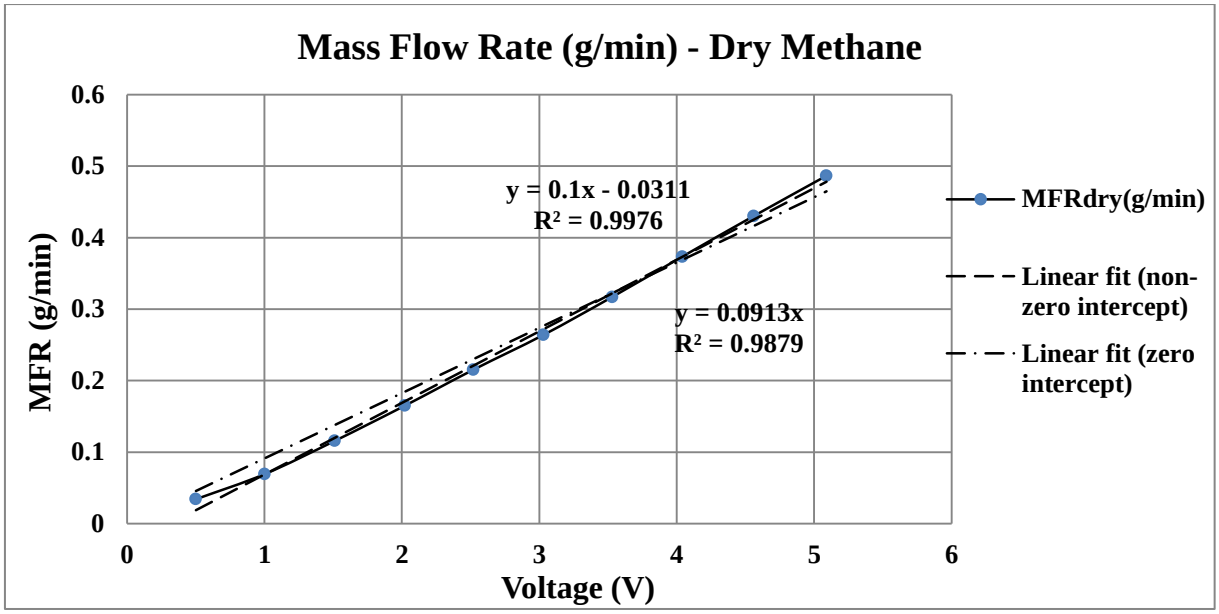


Figure 2. 7 Mass flow controller (UFC-1200A) calibrated against methane.

Figure 2.6 illustrates that the air flow through the controller is proportional to the output voltage; whereas the linearity of methane MFC fit is not as good as the previous, as seen in Figure 2.7. To fully take advantage of linear fitting correlation of methane MFC, attention is paid to looking at a selected region with voltages from 1V to 2.5V, which is illustrated in Figure 2.8.

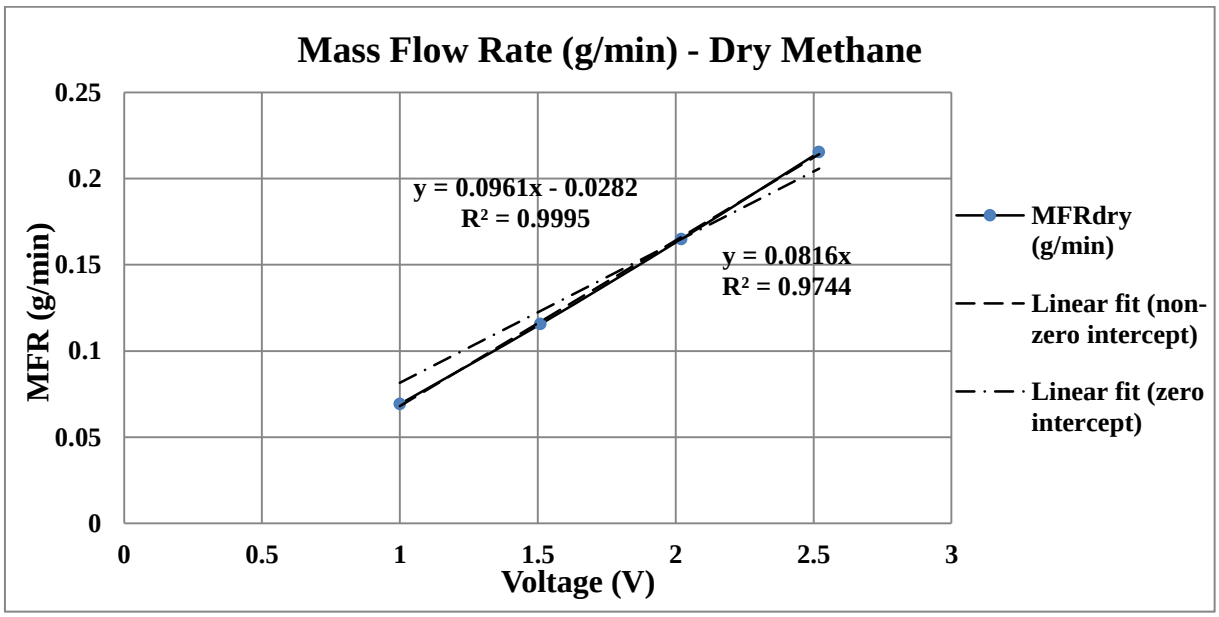


Figure 2. 8 Selected region of mass flow controller (UFC-1200A) calibration against methane.

If the demand voltage for the methane MFC is fixed at 1.76V, then the fitting correlations are:

$$\dot{m}_{CH_4}(g/min) = 0.0961 \cdot V_{CH_4} - 0.0282 \tag{2.23}$$

$$\dot{m}_{air}(g/min) = 0.9372 \cdot V_{air} - 0.0848 \tag{2.24}$$

Thus the target voltage of the air MFC can be found.

As an example, for a stoichiometric mixture of methane (CH_4) and air without residuals, substitution of $M_{CH_4} = 16(\frac{g}{mol})$, and $M_{air} = 29\ (\frac{g}{mol})$ will yield:

$$\dot{m}_{CH_4} = 0.0961 \times 1.76 - 0.0282 = 0.1409\ (^{g}/_{min}) \tag{2.25}$$

$$\dot{n}_{CH_4} = \frac{\dot{m}_{CH_4}}{M_{CH_4}} = 8.8085 \times 10^{-3}\ (^{mol}/_{min}) \tag{2.26}$$

$$\dot{n}_{air} = \dot{n}_{CH_4} \times \frac{2}{O_2\% \cdot \phi} = 8.8085 \times 10^{-3} \times \frac{200}{21} = 0.08389(^{mol}/_{min}) \tag{2.27}$$

$$\dot{m}_{air} = 0.08389 \times 29 = 2.43282(^{g}/_{min}) \tag{2.28}$$

And finally

$$V_{air} = \frac{\dot{m}_{air} + 0.0848}{0.9372} = 2.6863\ (V) \tag{2.29}$$

2.4.4 Method Validation

It is vital to ensure that the methane / air mixture is of the correct equivalence ratio using the above mentioned mass flow controllers. This was validated by using an ECM AFRecorder lambda sensor, which is carefully calibrated (see appendix A for details). A series of experiments was conducted at T_0 = 380 K, P_0 = 4 bar, with various equivalence ratios, ranging from 0.7 to 1.4. Then the output was tested by comparison with the theoretical lambda value. Figure 2.9 shows good agreement. On closer inspection, the slope of linear fitting in lean condition is approaching unity; while the slope of 1.1884 reflects that there is a slight different trend in the rich condition, i.e. the rich mixture is slightly over-predicted by using the lambda sensor.

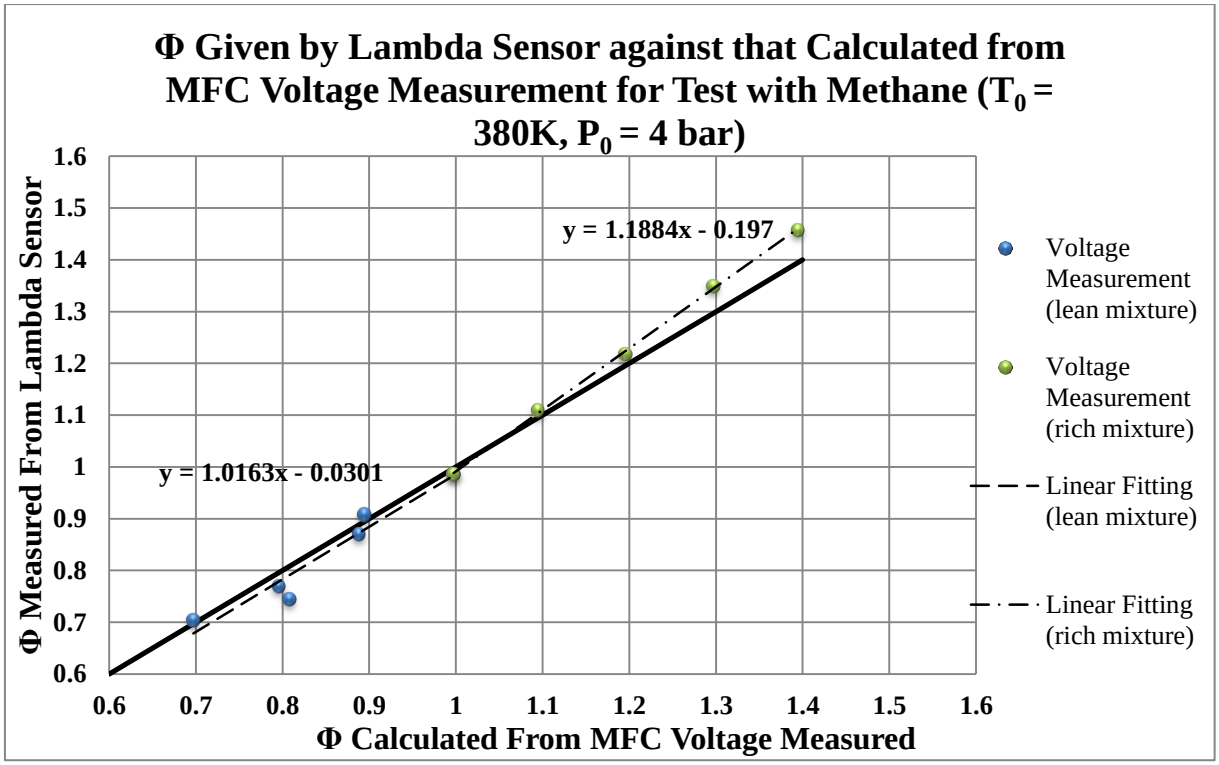


Figure 2. 9 *Φ* Given by Lambda Sensor against that Calculated from Mass Flow Controller Voltages.

2.5 Liquid Fuel Delivery

2.5.1 Introduction

The mole fraction method is sound for liquid fuel delivery on the assumption that the liquid fuel is fully vaporised. The major experimental procedures can be summarised as follows, i.e. injecting fuel, mixing for it to evaporate, observing the resultant pressure rise.

In this section, an experimental analysis of fluid volume is illustrated; followed by an investigation of vapour pressure in order to ensure full evaporation of the liquid fuel. Next, there is a description of the liquid fuel injection hardware used in this study. Finally, the method is validated by comparing the equivalence ratio measurements from a lambda sensor.

2.5.2 Volume Calculation

Assuming the liquid fuel is fully evaporated and acting as an ideal gas, the volume of fuel is calculated from the number of moles. For a fuel burned stoichoimetrically in air:

$$C_xH_yO_z + \left(x + \frac{y}{4} - \frac{z}{2}\right)\left(O_2 + \frac{79}{21}N_2\right) \rightarrow xCO_2 + \frac{y}{2}H_2O + \left(x + \frac{y}{4} - \frac{z}{2}\right)\frac{79}{21}N_2 \quad (2.30)$$

Theoretically, the number of moles of fuel can be expressed similar as equation (2.16):

$$n_f = \frac{n_r(1-x_r)}{x_r\left(1+\frac{100}{21\Phi}\left(x+\frac{y}{4}-\frac{z}{2}\right)\right)} = \frac{n_{mix}(1-x_r)}{1+\frac{100}{21\Phi}\left(x+\frac{y}{4}-\frac{z}{2}\right)} \quad (2.31)$$

Next, assuming the mixture of air-vaporised liquid fuel-residual is an ideal gas, and T_0 is the required temperature for the mixture; the ideal gas law gives the moles of fuel and the liquid volume of fuel (V_f):

$$n_{mix} = \frac{p_{mix} \cdot V_{bomb}}{R_0 \cdot T_0} \quad (2.32)$$

$$n_f = \frac{p_{mix} \cdot V_{bomb} \cdot (1-x_r)}{R_0 \cdot T_0 \cdot \left(1+\frac{100}{21\Phi}\left(x+\frac{y}{4}-\frac{z}{2}\right)\right)} \quad (2.33)$$

$$V_f = \frac{n_f \cdot M_f}{\rho_f} = \frac{p_{mix} \cdot V_{bomb} \cdot (1-x_r) \cdot M_f}{\rho_f \cdot R_0 \cdot T_0 \cdot \left(1+\frac{100}{21\Phi}\left(x+\frac{y}{4}-\frac{z}{2}\right)\right)} \quad (2.34)$$

It is worth noting that the molar number '*n*' that has been calculated in LabView is actually $\frac{p}{T}$. In addition, any slight temperature change in the process is taken into consideration by replacing the required T_0 with the current temperature T from the thermocouple. Assuming a fully evaporated fuel acting as an ideal gas:

$$n_f = \frac{p_f' \cdot V_{bomb}}{R_0 \cdot T} \quad (2.35)$$

$$m_f = n_f \cdot M_f = \frac{p_f' \cdot V_{bomb} \cdot M_f}{R_0 \cdot T} \quad (2.36)$$

where T represents the current bomb temperature, and p_f' denotes the partial pressure of fuel. In the liquid state in the syringe, $\rho_f = \frac{m_f}{V_f}$ yields:

$$V_f = \frac{m_f}{\rho_f} = \frac{p_f' \cdot V_{bomb} \cdot M_f}{R_0 \cdot T \cdot \rho_f} \quad (2.37)$$

Once the density and molar mass of fuel are provided, the volume of liquid fuel can be obtained. For a pure fuel, temperature will often have a marked influence. A physical property called liquid density, $Y = \frac{n}{V} = \frac{\rho}{M}$, is taken into consideration. Accordingly,

$$V_f = \frac{p_f' \cdot V_{bomb}}{R_0 \cdot T \cdot Y_f} \tag{2.38}$$

Sourced from Daubert and Danner (1997) [40], correlations of liquid density are listed and discussed below.

$$Y = \frac{A}{B^{\left(1+\left(1-\frac{T}{C}\right)^D\right)}} \tag{2.39}$$

For a temperature give in Kelvin it gives the liquid density in units of kmol/m^{-3}.

These thermodynamic data and appropriate correlations were then converted into LabView codes, which are easily accessed through a LabView interface program so that they can be used in the model.

The advantage of using liquid density is that the accurate liquid volume can be calculated even when the temperature changes near the syringe port, if a second thermocouple is used near the syringe to measure the local temperature.

2.5.3 Vapour Pressure

Throughout the liquid fuel delivery, the liquid fuel should be vaporized fully. Hence it is essential to ensure that the partial pressure of fuel is smaller than the vapour pressure at a given temperature, otherwise condensation of the fuel could occur. In practice, the real time vapour pressure is calculated by the LabView program.

Vapour pressure is the pressure exerted by a vapour in thermodynamic equilibrium with its condensed phases at a given temperature in a closed system. It increases non-linearly with temperature. According to Reid et al. (1987) [41], the Wagner equation is the most accurate method for vapour pressure estimation and correlation:

$$lnp_{vpr} = \frac{a\tau + b\tau^{1.5} + c\tau^3 + d\tau^6}{T_r} \tag{2.40}$$

$$p_{vpr} = \frac{p_{vp}}{p_c} \tag{2.41}$$

$$T_r = \frac{T}{T_c} \tag{2.42}$$

$$\tau = 1 - T_r \tag{2.43}$$

Where p_c and T_c represent critical pressure and temperature; p_{vpr} and T_r denote the reduced vapour pressure and temperature normalised by their critical point data. Coefficients *a*, *b*, *c* and *d* are fuel-specific constants for the polynomial given by Reid et al. [41]. For a temperature given in Kelvin equation (2.40) gives the vapour pressure in bar.

Equation (2.40) performs satisfactorily down to a reduced temperature of 0.5. For iso-octane under investigation, this corresponds to a temperature of 272 K; hence iso-octane vapour pressure can be plotted in the initial temperature range of interest between 300 K and 450 K.

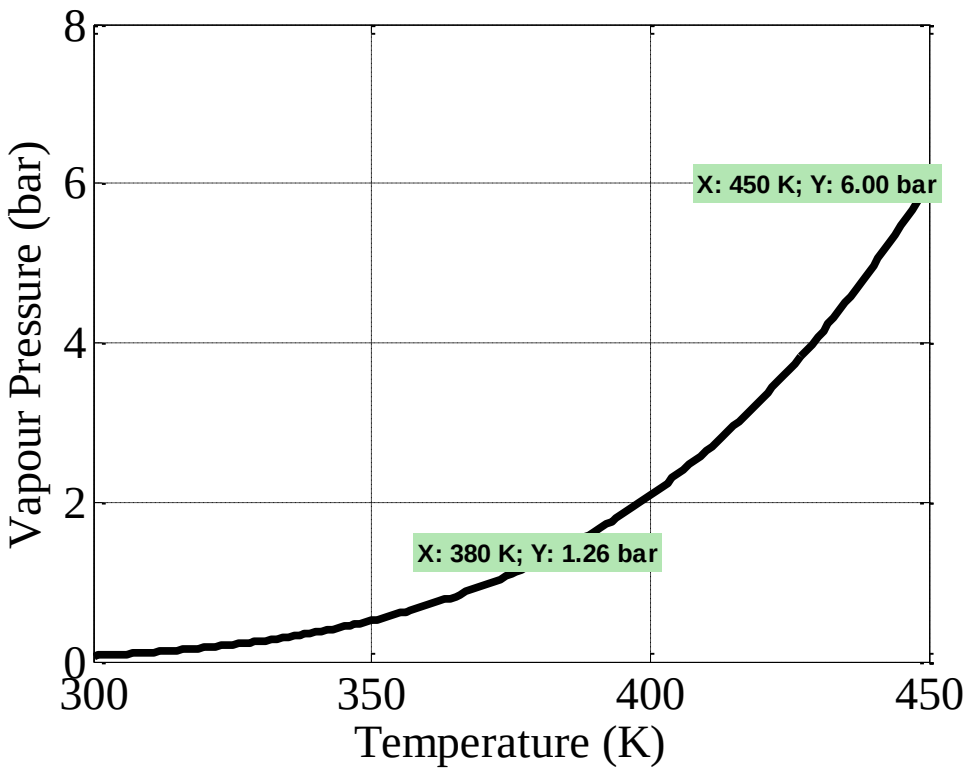


Figure 2. 10 Vapour pressure of iso-octane using the Wagner correlation equation.

As can be shown from Figure 2.10, the vapour pressure of iso-octane at 380 K is a few times the partial pressure of the fuel. Therefore an initial temperature higher than 380 K can effectively avoid any condensation of the fuel.

2.5.4 Syringe Based System

In practise, a syringe based system was proven to be a good quality precision fluid measuring device. It includes a Hamilton syringe of volume 1000 µL, a syringe actuator, and an arrangement fitted to the syringe port which allows the injection of liquid fuel into the bomb.

For the current iso-octane injection, a Hamilton C-07939-70 1.0 mL syringe was used. This gastight syringe has a precision machined TEFLON plunger tip which provides a tight seal for liquid fuels. A medical spinal needle of length of 150 mm was used with a Luer taper fitting. The KDS model 310 plus syringe actuator is an infusion / withdrawal syringe designed to hold the syringe and control the volume and flow rate of the fuel. The syringe fits securely in a mounting bracket so the fluid is delivered precisely without movement of the syringe; Figure 2.11 shows the syringe actuator. For the 1000 µL syringe, the resolution of the volume injected was 0.1 µL.



Figure 2. 11 KDS Model 310 Plus syringe actuator. From [42].

A ball valve is connecting to the syringe port, which is inside the oven. A septum is made from a disk of PTFE which is mounted onto the valve; it has a 0.83 mm hole drilled in it. A sketch of this component is illustrated in Figure 2.12.

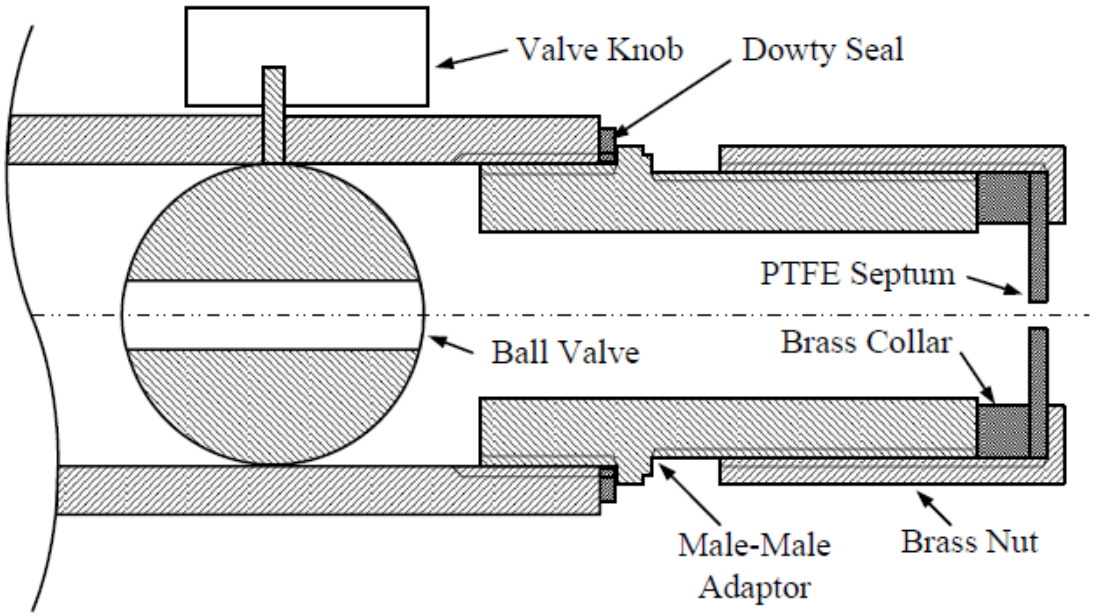


Figure 2. 12 A component fitted to the syringe port which allows the injection of liquid fuel into the bomb. From [3].

Care must be taken to ensure a good enough seal in the mixing loop. The following processes will ensure that the mixing loop is always sealed. First of all, it is necessary to make sure that there is no bubble in the syringe and no droplet on the needle. Then the needle is inserted into the PTFE septum but not as far as the ball valve. Finally, the ball valve is opened and the needle is inserted all the way in. Withdrawal is the opposite procedure.

The disadvantage of syringe based system is that the liquid fuel is injected as droplets rather than an evaporated spray; hence additional attention should be paid to make sure that the fuel is fully evaporated. For one thing, a very long needle that inserts into the inside syringe port ensures the fluid is injecting at bomb temperatures (380 K and 450K); while at high temperature, it can be effectively avoid the condensation of the fuel. For another, a

period of five minutes is required after the injection in order to create a homogeneous and fully evaporated mixture. Additionally, the LabView program will record the partial pressure of fuel and calculate for the user how much air is required to top up the mixture to ensure the correct quantities, even if the measured addition of fuel is slightly different from the intended quantity.

2.5.5 Method Validation

The current liquid fuel delivery method was validated by comparison of the air / fuel ratio from an ECM AFRecorder lambda sensor and the value reported by the LabView system. Iso-octane experiments have been carried out at T_0 = 380 and 450 K, P_0 = 1.5 and 3 bar, with various equivalence ratios, ranging from 0.7 to 1.4. The output was tested by comparison with the theoretical lambda value.

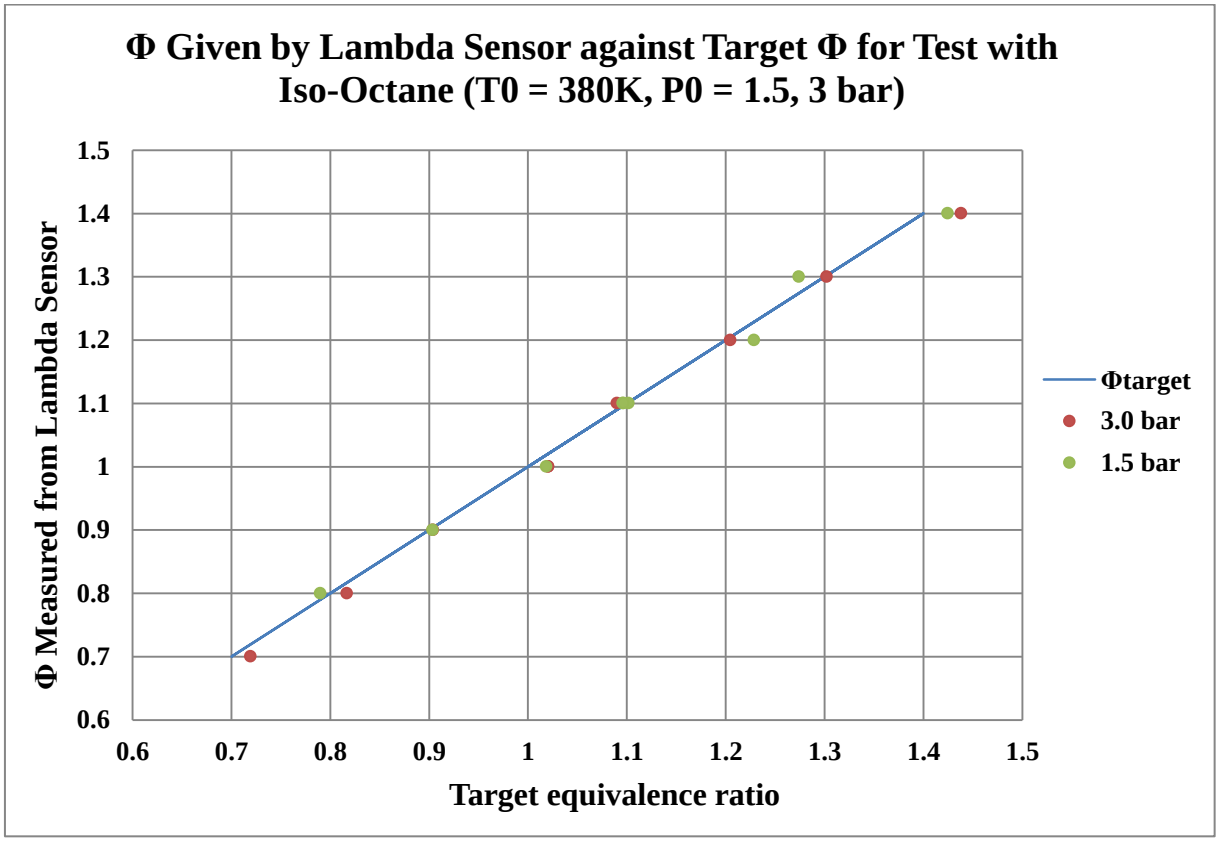


Figure 2. 13 Equivalence ratio measured by lambda sensor against target at T_0 = 380 K.

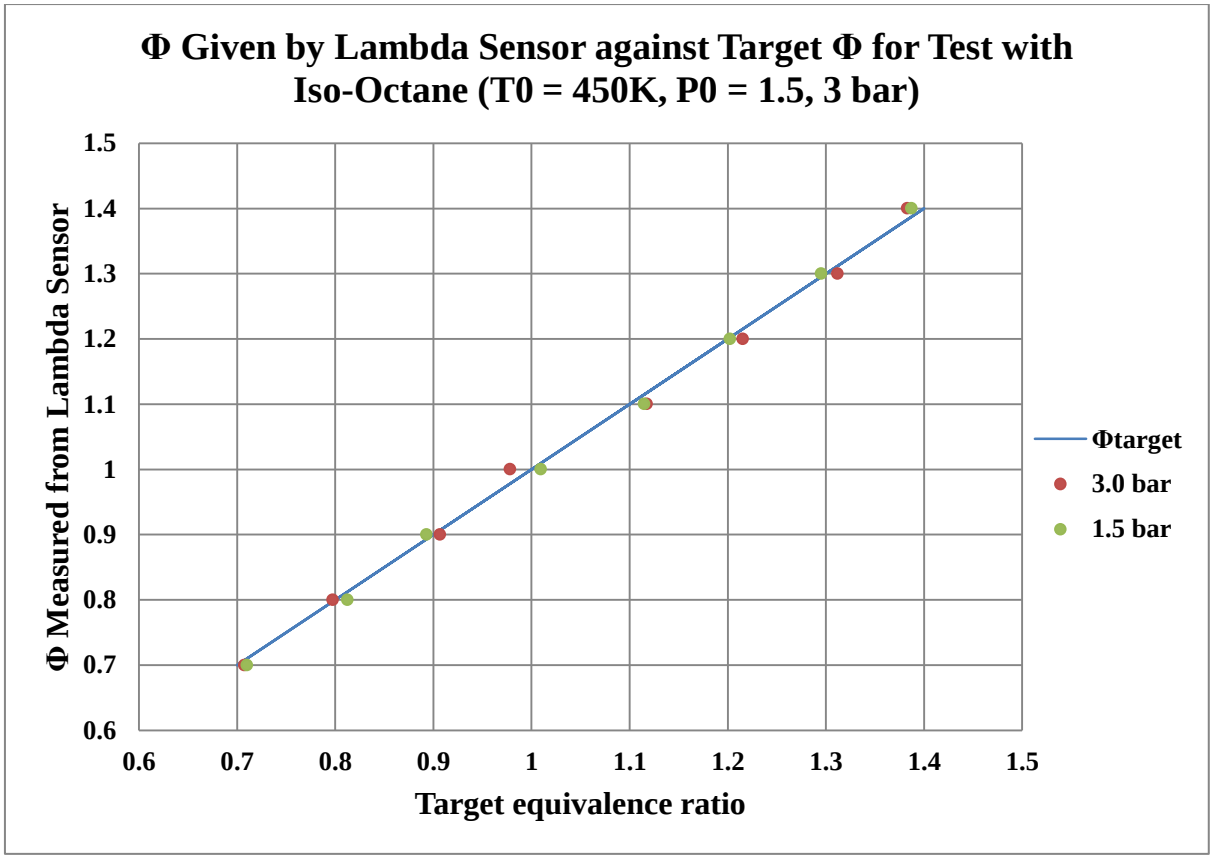


Figure 2. 14 Equivalence ratio measured by lambda sensor against target at T_0 = 450 K.

Figure 2.13 and Figure 2.14 show good agreement between the experimental measurements and theoretical values of equivalence ratio, which proves that the current liquid fuel delivery system is satisfactory.

2.6 Sensors and Data Acquisition

Air-fuel mixture preparation requires pressure transducers to measure over the range from 0 barA to the maximum mixture preparation pressure, which is currently 4.2 barA. It is worth noting that 'barA' in this chapter denotes absolute pressure, while 'barG' indicates gauge pressure with zero referenced against ambient pressure. For this requirement, three Druck PMP1400 sensors are chosen, with pressure ranges of -1 to +1.6 barG, 0-6 barA and 0-250 mbarG respectively. The measurement of dynamic pressure during a combustion process is with a Kistler 701A quartz pressure transducer. A Kistler type 5007 charge amplifier is used

to convert the charge generated by the pressure transducer to an amplified voltage, which can then be fed into the DAQ system and transferred to pressure. An exposed junction K-type thermocouple ensured that the charging process was isothermal and it also measured the initial temperature of gaseous mixture prior to ignition. It is positioned inside the bomb so that the junction just protruded into the chamber. After the completion of an experiment, the combustion products are fed past an ECM AFRecorder lambda sensor to check the equivalence ratio.

A National Instruments PCI-6024E DAQ card and break-out box were used to record the outputs of the system in conjunction with a PC, as well as for specifying and monitoring the mixture preparation process.

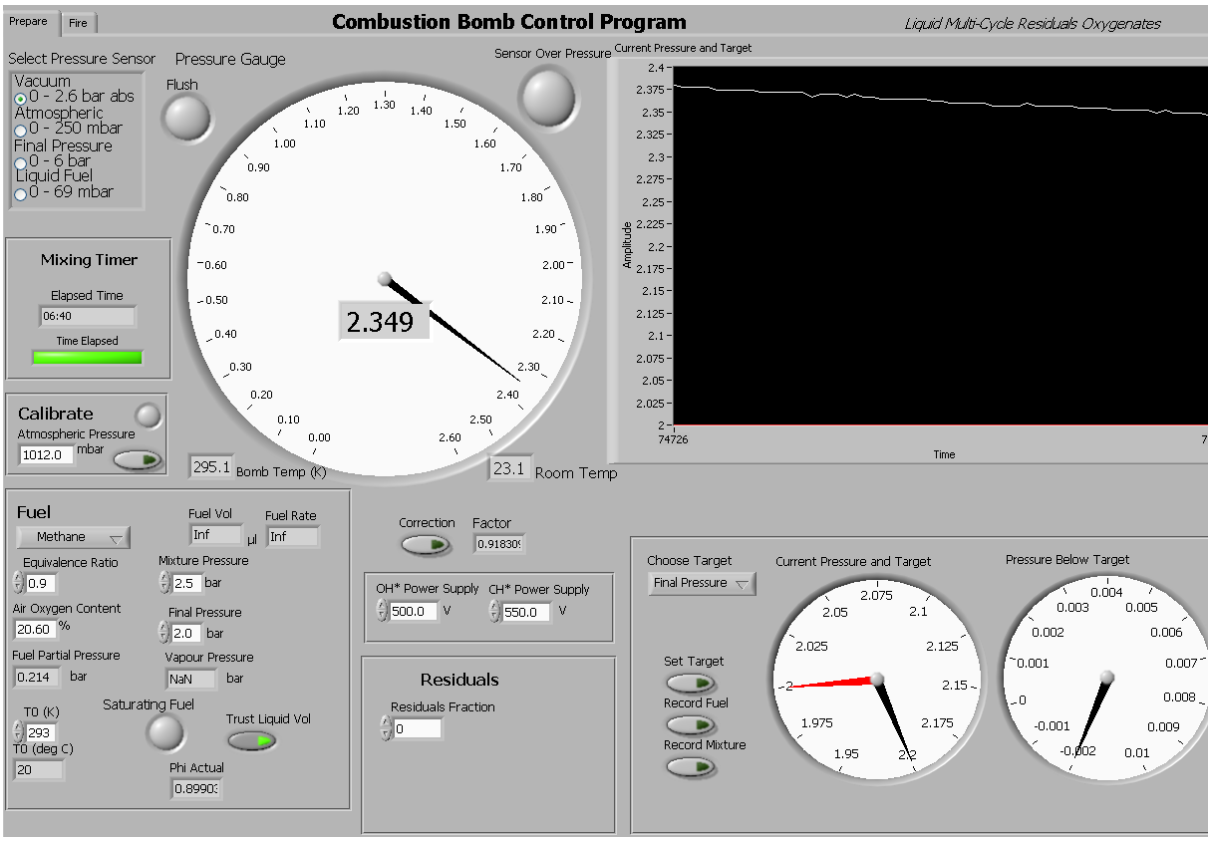


Figure 2. 15 The LABVIEW mixture preparation tab.

The measurements from the DAQ system are then fed into a National Instruments Labview program, which is written to display the data, calculate relevant parameters and

store data from the experimental pressure trace and photomultiplier tube output (voltage) traces. This program is split into two parts: the first aids mixture preparation and the second records and displays experimental combustion measurements sampled at 10 kS/s.

As shown in Figure 2.15, the first tab of the LABVIEW program records the target mixture pressure. The bomb thermocouple is used to account for any change in temperature which will affect the required partial pressure of each stage. For experiments with residuals, the saturation temperature of the water vapour is also calculated, so as to ensure that there is no condensation.

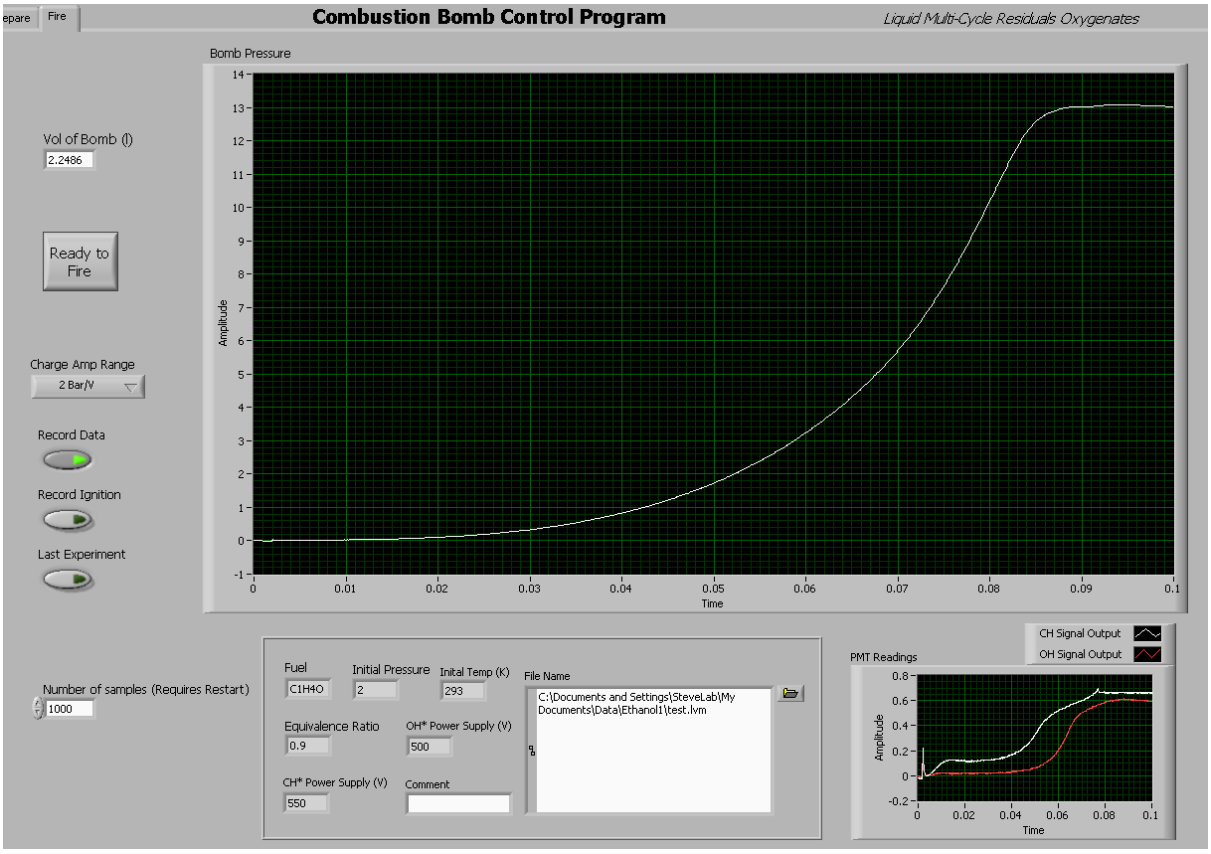


Figure 2. 16 The LABVIEW combustion tab.

The second tab, as shown in Figure 2.16, is for experiment execution. Once the user is ready to proceed with combustion, they click on ‘Ready to Fire’ which changes the mode of the program from real time data collection and display to high speed (currently 10 kS/s) data acquisition. The ignite signal triggers the DAQ system which then records data for the

specified number of samples and prompts the user to save it in an .lvm file, which can be read by either Microsoft Excel or MATLAB. The pressure record and PMT readings as well as the ignition voltage trace are then displayed to allow the user to see if a successful combustion event has occurred. The program then reverts to the mixture preparation mode in readiness for the next experiment.

Chapter 3 Optical Equipment: Modelling, Validation and Calibration

The optical system employed to detect chemiluminescence from the combustion bomb consists of a fused silica lens and a series of apertures held in a lens tube attached to the front of each Photomultiplier Tubes **(**PMT). Modelling accurately the optical setup is essential for quantitative CH* and OH* chemiluminescence measurements in the combustion bomb. Without calibration both the normalised OH* and CH* measurements will be in terms of different arbitrary units; hence an absolute calibration is an essential part of the calibration of the PMTs. This chapter reports the optical equipment's modelling, its validation and its calibration.

3.1 Overview

The optical system is applied to detect chemiluminescence from the combustion bomb. It consists of a pair of 40 mm diameter fused silica lenses (f = 40 mm), a series of apertures held in lens tubes, and photomultiplier tubes (PMT) with interference filters. For ease of alignment, the lens tube is mounted off the window retaining flange of the combustion vessel. Since the CH* and OH* light flux are expected to be very low, PMTs are used because they are extremely sensitive detectors of light; so there is a description of the photomultiplier tubes (PMTs) and their use in Section 3.2.

This optical system cannot be expected to sample the entire contents of the vessel uniformly. That is to say, some locations will be seen more clearly by the detectors than others, leading to a location dependent variation in the ability to collect the emitted photons. Indeed the field of view has been restricted to avoid collecting photons reflected off the walls of the combustion vessel. This is because photons which scatter from the inner walls of the vessel before passing out of a window and onto a detector are hard to quantify. Such photons may be absorbed instead of being reflected, and the number of bounces from the internal

surface is not easily determined. Therefore it was decided at an early stage that the system should be designed to ignore such scattered photons, and only collect so-called 'direct' photons - i.e. the detectable volume should not exceed the dimensions of the far window. Specifically, in order to understand the signals measured by the photomultiplier tubes this spatial variation of collection efficiency must be known.

In addition, as the flame burns, it will increase in radius, causing a different fraction of the total number of chemiluminescence photons to be collected. A further assumption is that the windows do not reflect any photons.

Therefore, a model of the optical system was developed, which would allow:

1. Optimisation of the optical design (i.e. position and diameter of apertures, focal length of lens, detector size and so on), in order to maximise the signal and only collect direct photons;
2. Photon collection efficiency to be quantified as a function of the flame radius.

In this chapter, Section 3.3 will describe how the optical model is developed with high accuracy, followed by a description of theoretical and experimental validation of the model, using a point light source calibration and a uniformly illuminated surface for calibration, which will be presented in Section 3.4.

This chapter finishes with the absolute CH* and OH* chemiluminescence calibration which can relate normalised CH* and OH* measurements to joules per unit mass of fuel burned.

3.2 Optical System Hardware

3.2.1 Photomultiplier

Since the incident flux of OH* and CH* photons are expected to be very low, a photomultiplier is used. This multiplies the current produced by incident light on a

photocathode by as much as 100 million times (i.e., 160 dB), in multiple dynode stages, so that individual photons can be detected. Photomultipliers are constructed from a glass envelope, which houses a photocathode, several dynodes, and an anode. Photons strike the photocathode and this releases electrons as a consequence of a photoelectric effect. Then electrons are accelerated by the electric field and strike the dynodes where more electrons are emitted at each stage by the process of secondary emission; so there is an avalanche effect. Finally, the electrons reach the anode, where the accumulation of charge indicates the arrival of a photon at the photocathode. Figure 3.1 illustrates the structure and operating principle of a photomultiplier tube.

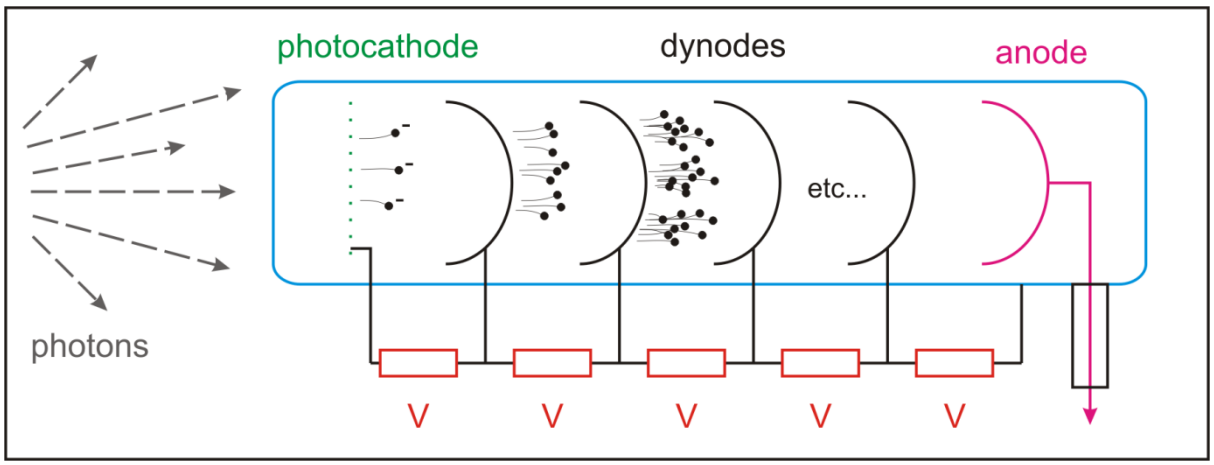


Figure 3. 1 Schematic of a photomultiplier tube.

In practice, a HAMAMATSU R955 photomultiplier and an ET Enterprises 9783B photomultiplier tube are well suited for examining OH* and CH* chemiluminescence from inside the bomb vessel. The R955 is a 9-stage side-on photomultiplier with multialkali photocathode, and a wide spectral response from ultra-violet to near-infrared. The 9783B is also a side window photomultiplier with a blue-green sensitive bialkali photocathode and 9 SbCs dynodes of circular focused design. Both of them are subject to not exceeding a maximum supply voltage between anode and photocathode of 1250V. The photocathode has a typical active area 8 × 24 mm.

The two PMTs are mounted along the optical axis of the bomb vessel at a known distance from the bomb centre, which will be determined by the optical system. Interference filters are needed for the signals of OH*, which has a wavelength of 306.4 nm, and CH*, which has a wavelength of 431.5 nm. A CVI filter was used for the OH* (310 nm and 10 nm half bandwidth, i.e. HBW), and a Comar 430-IL-25 filter was used for the CH* (430 nm CWL and 10 nm HBW). In addition, there is a tolerance of ± 2.0 nm CWL (central wavelength) and +3 / -0 nm HBW for the CVI filter; while there is ± 2.5 nm CWL and HBW tolerance for the Comar filter.

Consideration has also been made to the shifting of the central wavelength of the interference filter as a result of non-normal incidence angles. For the angular limits expected (0.0119 radians) in the present optical geometry, this effect should not be significant.

3.2.2 PMT Output Circuit

The PMT outputs for the OH* and CH* chemiluminescence need to be recorded during combustion by the LABVIEW program. The photomultiplier photocurrents had to be amplified by a high-input-impedance amplifier (in the signal path, subsequent to the photomultiplier), thus producing appreciable voltages even for nearly infinitesimally small photon fluxes. The electrical circuit for the PMT output buffering system is illustrated in Figure 3.2. It comprises the current source termination, a voltage follower and inverting amplifier.

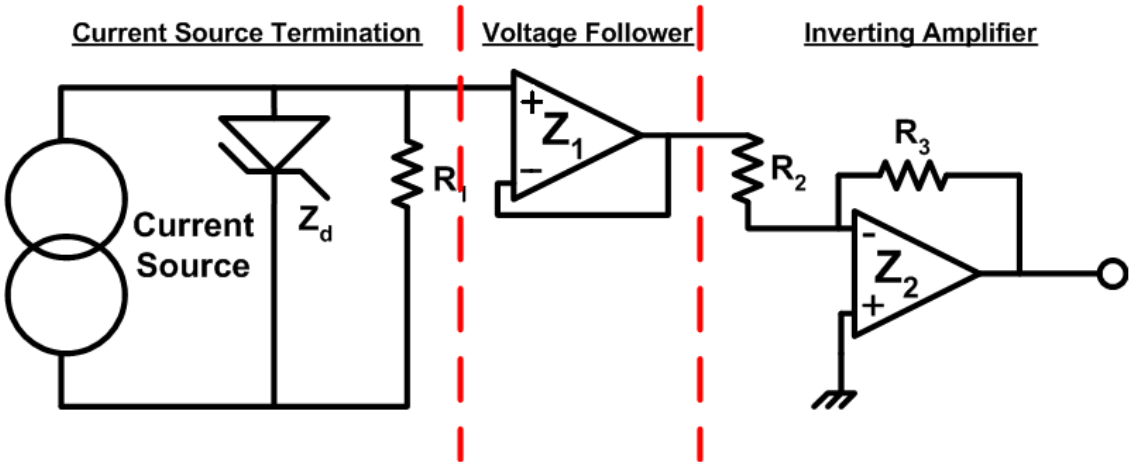


Figure 3. 2 PMT output buffering system.

As seen in Figure 3.2, the first part of the output circuit is denoted as the current source termination, which consists of the PMT, a Zener diode and a resistor. The photomultiplier acts as a nearly perfect current source owing to the high voltage utilized in extracting the tiny currents associated with weak light signals. Since the operational amplifier amplifies a differential input voltage, a resistor is acting as a current-to-voltage converter, which is in parallel with the PMT. In practice, the PMT generates a voltage across resistor $R_1 = 100\ k\Omega$ and the Zener diode. A Zener diode performs in the same manner as normal diodes when forward biased, but when reverse biased, it has a constant voltage drop across it irrespective of the current flowing through it. Thus, as long as the Zener current is above a certain level, the voltage across the Zener diode will be constant. In the test, a Zener diode with a Zener breakdown voltage of 15V is in the reverse direction, protecting the amplifier from too high a voltage input.

The voltage follower is used as a buffer amplifier to eliminate loading effects. It transfers a voltage from the first circuit with high output impedance to a subsequent circuit with low input impedance. The voltage follower is constructed by connecting the operational amplifier (op-amp) output to the inverting input, and connecting the signal source to the non-

inverting input. This is shown in Figure 3.2. The output voltage is simply equal to the input voltage:

$$V_{out} = V_{in} \tag{3.1}$$

The importance of the voltage follower does not depend on any changes in voltage, but lies on the high input impedance and low output impedance of the op-amp. The high-input-impedance ensures that the input of the op-amp does not load the signal source. The low-output-impedance ensures the voltage follower is acting as an ideal voltage source with no voltage division. Therefore it reduces the power consumption in the source and other electromagnetic interference. Another thing worth mentioning is that a trimmer potentiometer is mounted in order to balance out any DC offset effects; this is shown in Figure 3.3.

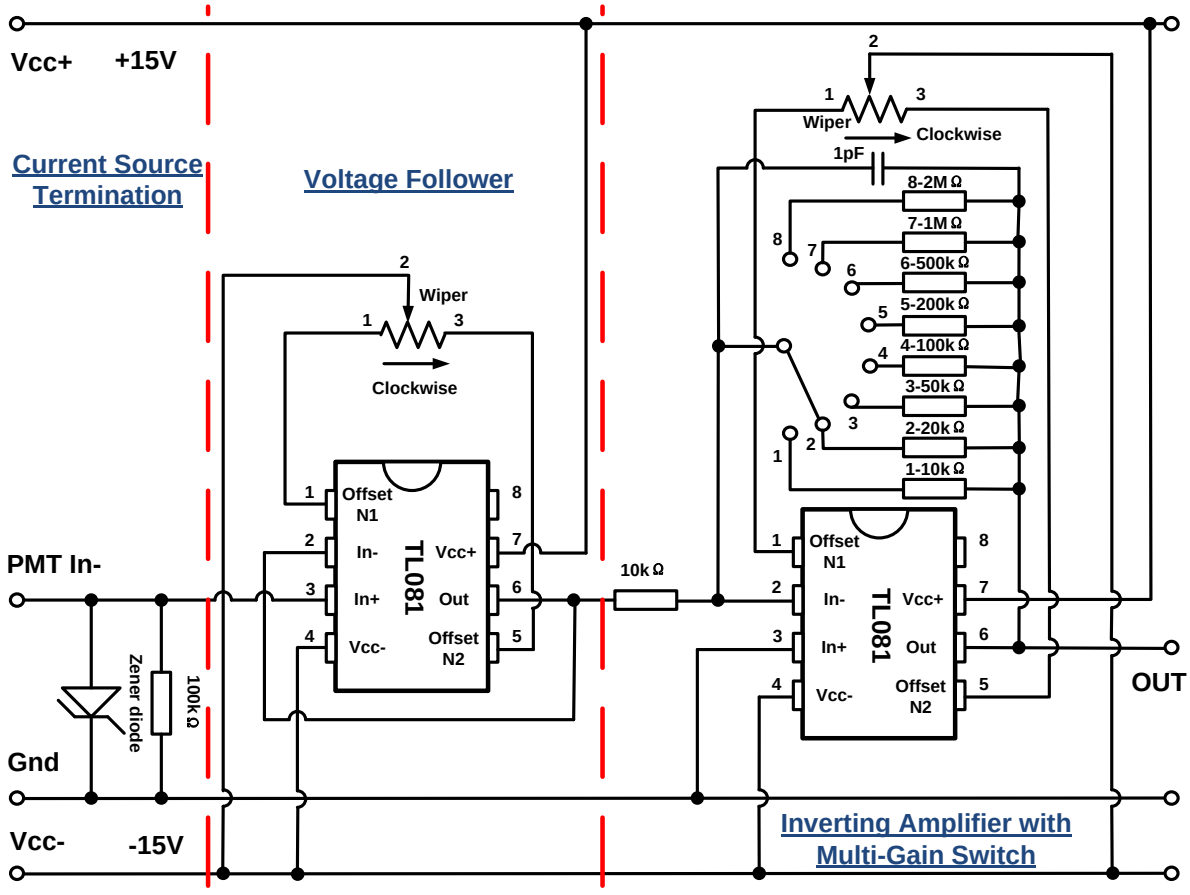


Figure 3. 3 Circuit diagram of the PMT output buffering and amplifier system.

The last part of the signal conditioning is an inverting amplifier with selectable gains in the range of 1 to 200 times, which is because the chemiluminescence intensity varies widely with mixture conditions and the PMTs were operated with fixed HT voltages applied across the dynode stages (This is because the PMT sensitivity varies non-linearly with the HT voltage). The inverting amplifier is used to invert and amplify the input voltage. The amplification is determined by two external resistors R_2 and R_3 in Figure 3.2:

$$V_{out} = -\frac{R_3}{R_2} V_{in} \tag{3.2}$$

where R_2 denotes the input resistor; R_3 represents the feedback resistor; the negative sign '-' indicates that the output is negated. In this case, $R_2 = 10\ k\Omega$, R_3 varies from 10 $k\Omega$ to 2 $M\Omega$, as shown in the complete circuit diagram of Figure 3.3. Two TL081 single channel operational amplifiers are utilised as the buffer amplifier and inverting amplifier. Similarly a trimmer potentiometer is also used to eliminate any DC offsets.

Additionally, to reduce any noise associated with the inverting amplifier, a 1 pF capacitor is in parallel with the feedback resistor, which is shown in Figure 3.3. Its capacitive reactance X_c is inversely proportional to the frequency *f*:

$$X_c = -\frac{1}{2\pi f C} \tag{3.3}$$

Both the capacitive reactance X_c and the feedback resistance R_3 are components of the impedance Z_3; accordingly the amplification is not as same as that expressed in Equation (3.2), $-\frac{R_3}{R_2}$, and the resulting output is different from the expectation. Due to the low value of the capacitor, there is large opposition to the current flow through the capacitor at low frequency, which can be regarded as open circuit. Hence the impedance Z_3 is approximately equal to the feedback resistance R_3, and the amplification of the inverting amplifier can be accordingly expressed as:

$$V_{out} = -\frac{Z_3}{R_2} V_{in} \approx -\frac{R_3}{R_2} V_{in} \tag{3.4}$$

This therefore eliminates the noise in the system. A digital oscilloscope was used to check the system performance.

3.3 The Optical Model

3.3.1 Introduction

Photons can arrive at the photo-multiplier tube (PMT) either directly ('direct photons') from the flame front, or after reflection from one of the internal surfaces ('scattered photons'). Since it is difficult to model reflected photons, and the reflective properties of the internal surfaces are unknown (and likely to change), the optical system needs to be designed with a restricted field of view, so that only 'direct photons' are collected. As the flame front will become larger than the field of view, then optical modelling is also needed to determine what fraction of the photons from the flame front will be detected as the flame radius increases. Figure 3.4 compares sensitive areas of 'wide field of view' to 'narrow field of view' scenario:

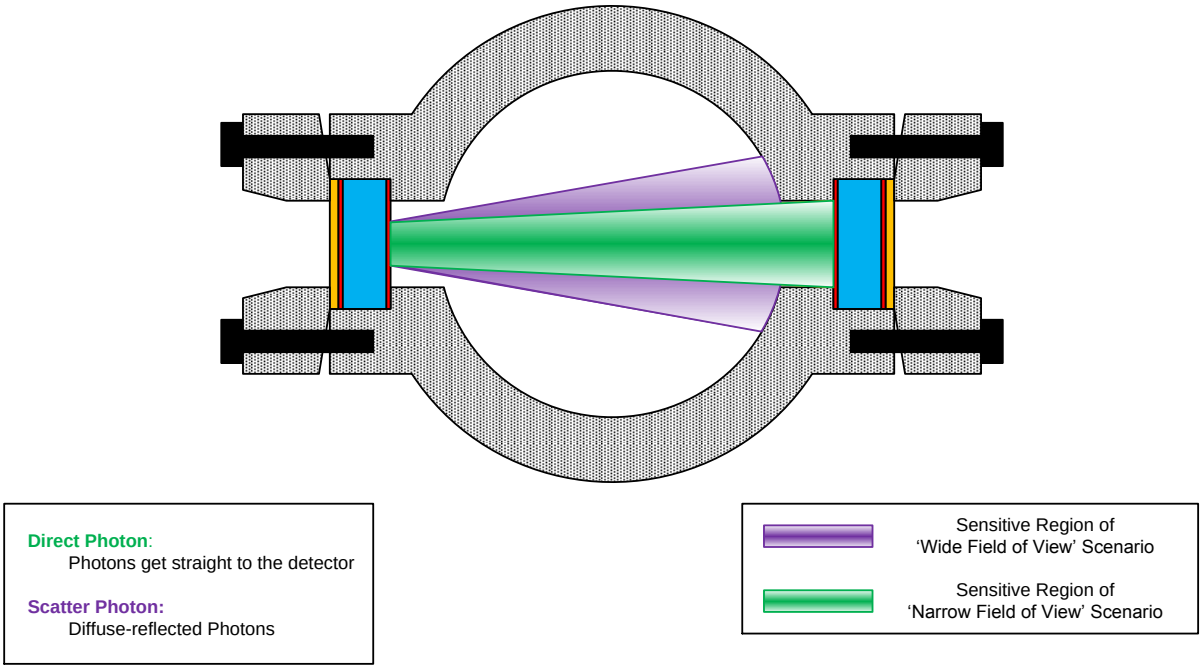


Figure 3. 4 Comparison of 'narrow field of view' sensitive area and 'wide field of view' sensitive area.

To conclude, the optical modelling work is undertaken to sort out the following two problems:

1. To determine what geometry to use in order to minimise the number of 'scattered photons' which are collected by the detector.

2. To be able to retrieve the information on photon collection efficiency from the flame front as it expands.

A suitable model has been provided, and this has led to two activities. Firstly the model has to be used to design the PMT optical system, and secondly the optical model has to be validated.

3.3.2 Assumptions, Geometry and Conventions

Ray transfer matrix analysis is at the heart of the ray tracing technique in the combustion bomb optical modelling. The developed model relies upon paraxial ray propagation and the thin lens approximation.

The paraxial approximation assumes that the rays in the system make small angles to the optical axis, so that:

$$\sin\theta = \tan\theta = \theta \tag{3.5a}$$

$$\cos\theta = 1 \tag{3.5b}$$

This assumption is justified, because for the geometries considered, the maximum ray angle from the optical axis of the system is small (approximately 0.0119 radians); meanwhile the error is always less than $7.1 \times 10^{-3}\%$ for the geometry that was finally selected, assuring that $sin(\theta) \approx \theta$.

Another fundamental simplification involved in the modelling is the thin lens approximation which assumes that the thickness of any lens involved is negligible compared to its focal length. With the known focal length (f) of the lens, 40 mm, the thin lens equation,

$$1/f = 1/u + 1/v \tag{3.6}$$

defines the relationship between the lens-to-object distance u and the lens-to-detector distance v. Despite the use of relatively short focal length lenses, validation of the model indicates that this second assumption is not a major source of error.

The combustion bomb (Figure 3.5) has an internal diameter of 160 mm, with two 40 mm diameter windows - one on either side of the vessel. The optical axis of the system is taken to go through the centres of these two windows. The detector is a photomultiplier tube (PMT), and a lens is used to focus the light from the central plane in the combustion bomb onto the photocathode in the PMT.

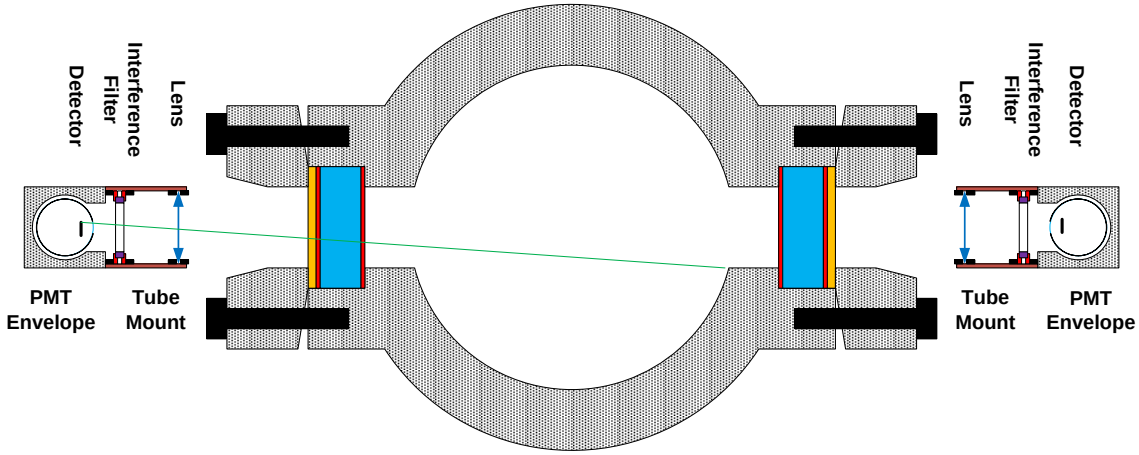


Figure 3. 5 Arrangements of the combustion bomb and photo-multiplier tube (PMT).

The photocathode in the PMT has nominal dimensions 8 × 24 mm; but as a simplification the detector is assumed to be a flat disc with a diameter of 8 mm that is normal to the optical axis. Magnification can be determined by considering the un-deviated ray that passes through the centre of the lens, subject to equation (3.6):

$$\frac{det/2}{v} = \frac{20}{D+u-D/2} \tag{3.7}$$

In equation (3.7), variable *det* is the diameter of the nominal circular detector, 20 is the half-width of a window (in mm), and *D* is the diameter of the bomb. It is worth noting that the lens-to-object distance *u* denotes the distance between the lens and the bomb centre

along the optical axis. These equations are solved, leading to: v = 51.6 mm and u = 178 mm, resulting in a magnification, $M = \frac{v}{u}$, of 0.29.

In the optical model, two field stops/apertures are introduced so that the detector area is constrained to achieve a narrow field of view. 'Aperture 2' is wrapped around the detector, and 'aperture 3' sits between the lens and the bomb. The effective diameter of the lens is taken to be 38 mm rather than 40 mm, owing to the presence of the retaining ring which holds the lens in the mounting tube.

3.3.3 2D Modelling

To investigate the spatial variation in the ability to collect emitted photons, the location dependent collection efficiency inside of the bomb vessel needs to be discussed. In this 2D modelling, the spatial collection efficiency is defined as the plane angle (in radians) subtended by a circular arc divided by the radians of one complete revolution, i.e. 2π.

The 2D collection efficiency can be obtained using the following two methods: (1) splitting the detector into a series of small elements, and then allowing the rays from those elements to propagate into the bomb; (2) visiting all locations in the bomb, for each of them determining the limits in angle for each optical element and choosing the most restrictive case, and the collection efficiency is found by taking the range of that angle in radians. Whilst the first approach showed early promise, the quantisation of the calculation caused lots of noise. Removing this noise and scaling the solution to 3D was deemed to be a losing battle, so attention was instead turned to modelling the system the other way round, and fully exploiting the cylindrical symmetry of the problem.

The approach employed by the model is to visit a matrix of points within the combustion vessel and assess what fraction of the rays (launched from each point into 2π radians) can reach the detector. This is achieved by means of ray tracing employing ray

transfer matrices. Owing to the cylindrical symmetry of the problem, only half of the volume of the chamber has to be considered, which saves computational time.

For the purposes of the model, the x axis is taken to be the optical axis, with the detector positioned at the origin, the lens sitting at *v*, the bomb centred at '$u + v$', and the interior face of the closest window at $v + u - \sqrt{(D/2)^2 - (40/2)^2}$. The y axis runs perpendicular to the x axis. The locations the other side of the optical axis have just the same values of collection efficiency, so the *r* vector contains only half of the *y* elements (and the zero value, i.e. optical axis).

Table 3. 1 Illustration of optical elements properties

Optical property	Description	Unit	Comments
D	Bomb diameter	mm	
u	Lens-to-object distance	mm	
v	Lens-to-detector distance	mm	
ld	Lens diameter	mm	
lf	Focal length of the lens	mm	
det	Detector width	mm	Assumed to be a flat disc
$a1d$	Front window diameter	mm	40mm
$a1p$	Location of front window on x axis	mm	$a1p = v + u - \sqrt{\left(\frac{D}{2}\right)^2 - \left(\frac{a1d}{2}\right)^2}$
$a2d$	Aperture 2 diameter	mm	Wrapped around the detector
$a2p$	Location of aperture 2 on x axis	mm	
$a3d$	Aperture 3 diameter	mm	Sited between the lens and the bomb
$a3p$	Location of aperture 3 on x axis	mm	
$reqres$	Requested resolution	mm	

Based on the above mentioned arrangement, the 2D optical modelling operates as follows. Firstly, the optical model visits all locations in the *r* vector, which lie between the interior face of the closest bomb window and the far window position of the *x* vector. The resolution is set by varying the '*reqres*' variable, which chooses the closest possible odd integer *p* for d*x* = d*y* = d*r* that still images the detector onto an integer number of pixels (*p*) in the object plane, i.e.

$$dy = \frac{det \times u}{v \times p} \tag{3.8}$$

where p is an odd integer in order to ensure that the number of y elements is odd. Table 3.1 explains the meaning and units for each parameter.

Secondly, the spatial collection efficiency at each *(x, r)* location is determined by considering the maximum ray angle (up and down) which would just pass each element in the optical path, and then choosing the most restrictive element as the limiting case. The underlying equation governing this comes from the series of ray transfer matrices for the system. Details about the ray transfer matrix method employed in the optical modelling can be found in Appendix B.

Finally, the collection efficiency of each *(x, r)* is then simply found by taking the range in θ and dividing by 2π.

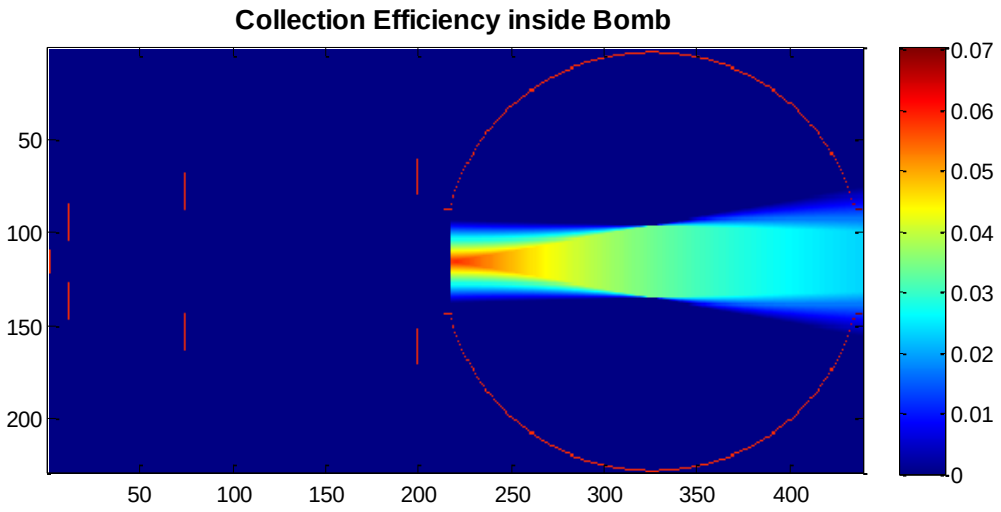


Figure 3. 6 The 2D spatial collection efficiency map. The *x* and *y* readings in the map are elemental indices rather than actual length in mm. (Conversion factor is 0.7076 mm).

Using 401 steps for the θ discretization, the 2D map of collection efficiency for *det* =8, *a2d* = 15, *a2p* = 7, *v* = 51.6, *u* = 178, *reqres* = 0.7 is shown in Figure 3.6. From left to right, the image contains four optical elements in red, indicating the detector limits, the

location and gap for aperture 2, the lens aperture, and aperture 3. The circle denotes the combustion bomb, with two gaps, which represent the front and far windows. Finally, a colour bar is included to interpret the false colouring of the image. The *x* and *y* readings in the map are elemental indices rather than actual length in mm, with the conversion factor, 0.7076 mm, from actual length to elemental indices.

It is then of interest to attempt to quantify the relative amounts of direct photon capture and scattered photon capture by the detector. An idea of the relative importance of these two contributions is ascertained by plotting a slice through the collection efficiency map at the location of the far window, as shown in Figure 3.7:

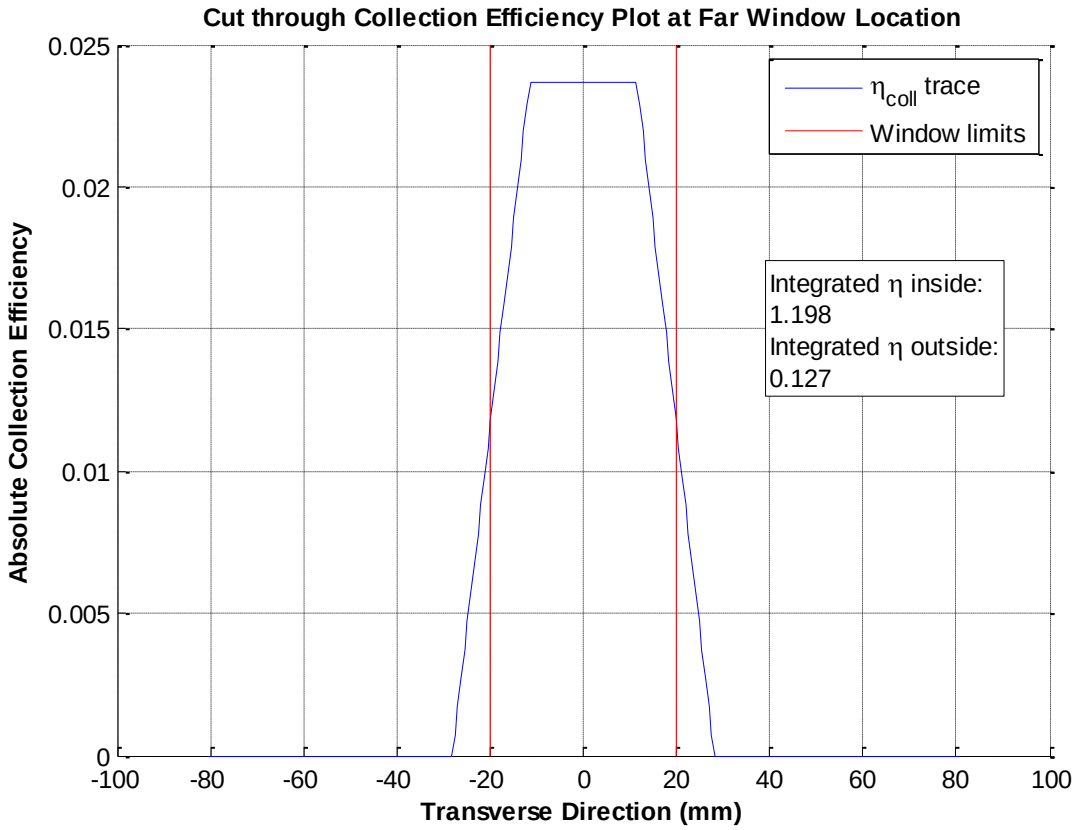


Figure 3. 7 Plot of a slice through the collection efficiency map at the far window for the 2D calculation. η_{coll} in the insert denotes the spatial collection efficiency.

In Figure 3.7 the red vertical lines indicate the extents of the window, the x axis is given in mm, and the y axis denotes the 2D absolute collection efficiency at that location. To get the relative importance of the two 'types' of photons, the collection efficiency data is

numerically integrated within the window limits and outside of them. In this case, it is seen that ‘direct’ photons far outweigh ‘indirect’ photons.

Another requirement is to determine how the signal on the PMT varies as the flame grows inside the combustion vessel. In this modelling, a circle is allowed to grow out from the centre of the bomb, and a number of sampling points are chosen around its circumference which are equally-spaced in angle. To simplify the modelling, the rate of production of chemiluminescence photons per unit length, which indicates the rate of chemiluminescence reaction, is assumed to be constant as the flame grows. By multiplying the length of each arc element, i.e. $dl = \frac{2\pi r_f}{number\ of\ samples}$, with the spatial collection efficiency for that location (interpolated from the collection efficiency map), the signal on the PMT can be derived.

By fully considering the cylindrical symmetry of the problem about the optical axis, the 2D interpretation can be quickly extended to 3D. Instead of multiplying the collection efficiency values by simple arc lengths, the arc length is multiplied by the circumference of the circle at that distance from the optical axis, giving an element of the shell area. These areas are added up to get the total signal. An example plot with same parameters of Figure 3.6 is seen in Figure 3.8. It illustrates the fraction of photons collected from the flame surface, and indicates how the fraction of photons collected from the flame surface, η, varies with flame radius r_f, where η (named as the optical system collection efficiency) is defined by:

$$\eta = \frac{\text{total number of collected photons}}{\text{total number of emitted photons}} \tag{3.9}$$

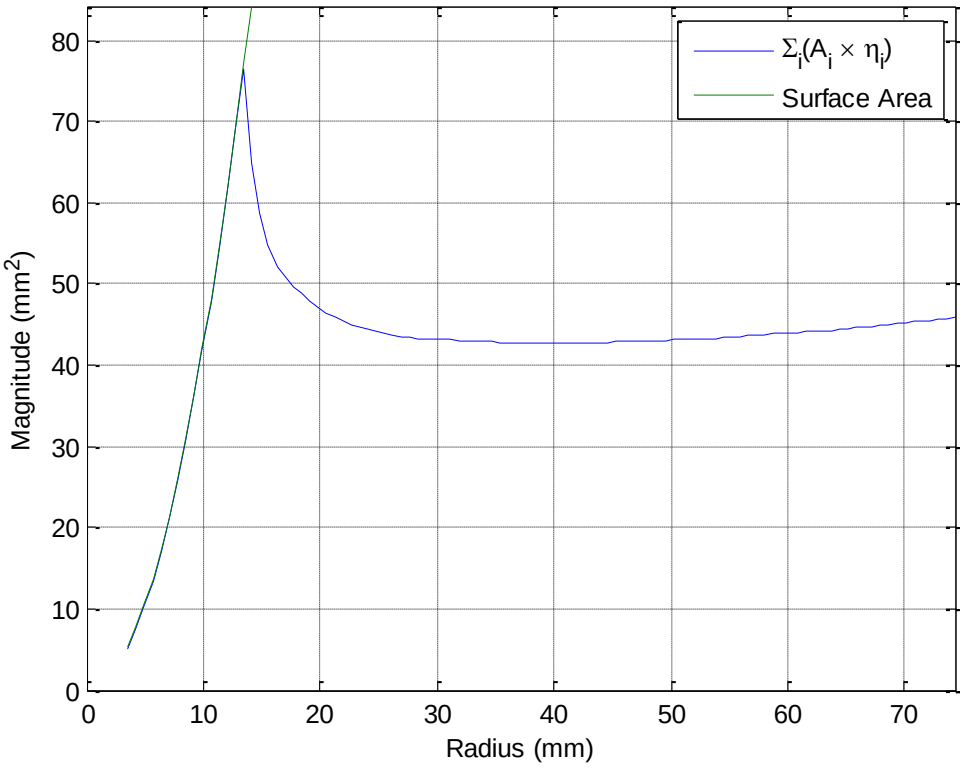


Figure 3. 8 The PMT signal for constant chemiluminescence strength as a function of flame radius r_f. Although collection efficiency map was generated in 2D, this analysis takes advantage of axial symmetry to give the 3D solution.

As shown in the plot, the PMT signal starts by following the flame surface area as is expected, given that the optical system collection efficiency is roughly flat in the region around the focus. Above a threshold radius, the shell-like flame front starts to expand outside the volume that the PMT is sensitive to, and the product of coupled surface area and collection efficiency (i.e. $A\eta$) stops following the r_f^2 curve. Instead, it remains relatively flat at larger radius, as the lower sensitivity of the far side is compensated for by the increased sensitivity of the nearer side of the flame. A final thing to bear in mind is that the model has no concept of the potential for photons to be scattered or absorbed by the medium during their travels, but the path lengths are too small for scattering and absorption to be significant.

3.3.4 3D Modelling

Similar to the method in 2D modelling, the 3D spatial collection efficiency analysis is performed initially by considering a solid angle, Ω, which is measured in steradians, $\Omega = \frac{A}{r^2}$, where A is the area of the surface that subtends solid angle at the origin of a sphere of radius r. The 3D spatial collection efficiency is defined as the area subtended at a point divided by the whole surface area of a sphere.

The 3D modelling initially calculates the 2D θ limits at each location (x, y), followed by evaluation of the maximum acceptance angle in the ϕ direction (i.e. the angle in a perpendicular plane) for each quantised θ within 2D θ limits.

Next, the area on the unit sphere that a particular stripe of $\Delta\phi$ gives for a given quantised θ is evaluated as:

$$collarea(\theta) = \left(\frac{\pi}{n}\right) \times \left(2\pi cos\theta \times \frac{\Delta\phi}{2\pi}\right) \tag{3.10}$$

where the term $2\pi cos\theta$ handles the fact that the circumference of the ring of area varies as a function of θ. The ring circumference is then multiplied by the fraction of the ring which can get to the detector, i.e. $\frac{\Delta\phi}{2\pi}$. To get to an area, the fractional length of the θ direction is then included as $\frac{\pi}{n}$, where n denotes steps of θ discretization between the 2D θ limits.

Thirdly the values of '*collarea*' are then summed to get the total area which the current location (x, y) inside the bomb vessel 'paints' onto the unit sphere. Lastly, a simple division by 4π, the surface area of the unit sphere, returns the spatial collection efficiency at that location. There is a description of the ray transfer matrix method utilised in the 3D modelling in Appendix B. Figure 3.9 is the 3D spatial collection efficiency map with the same bomb parameters as the 2D image:

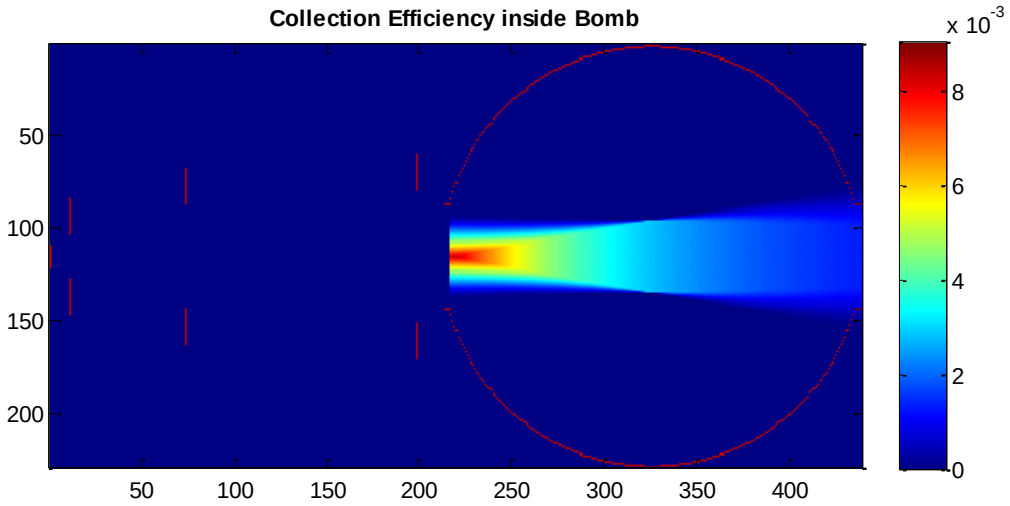
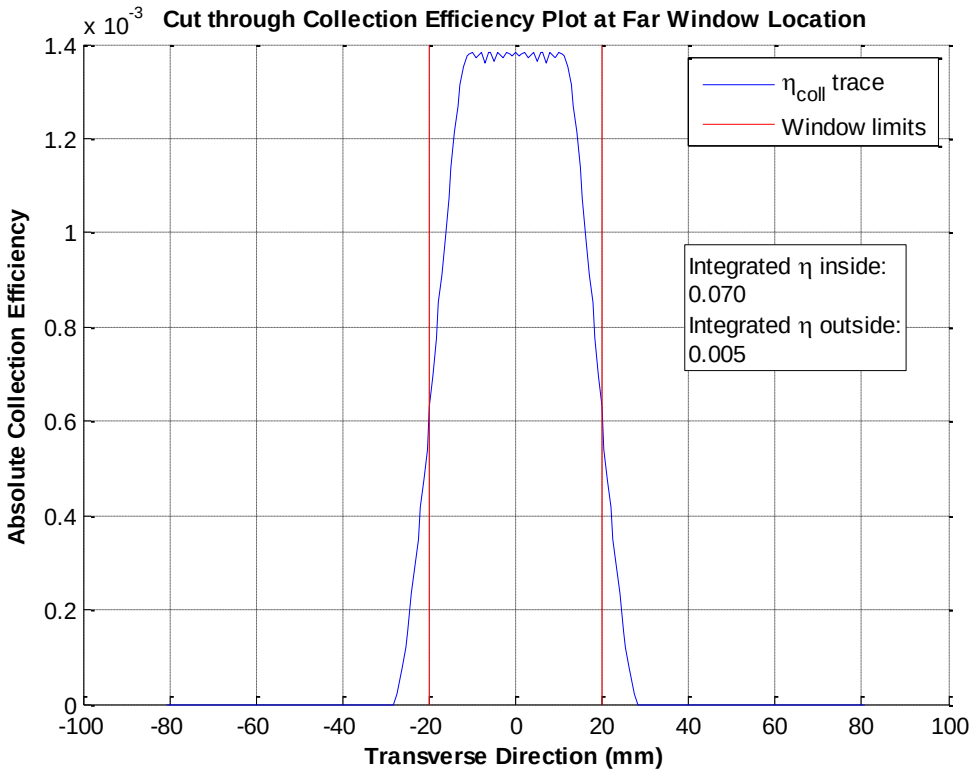


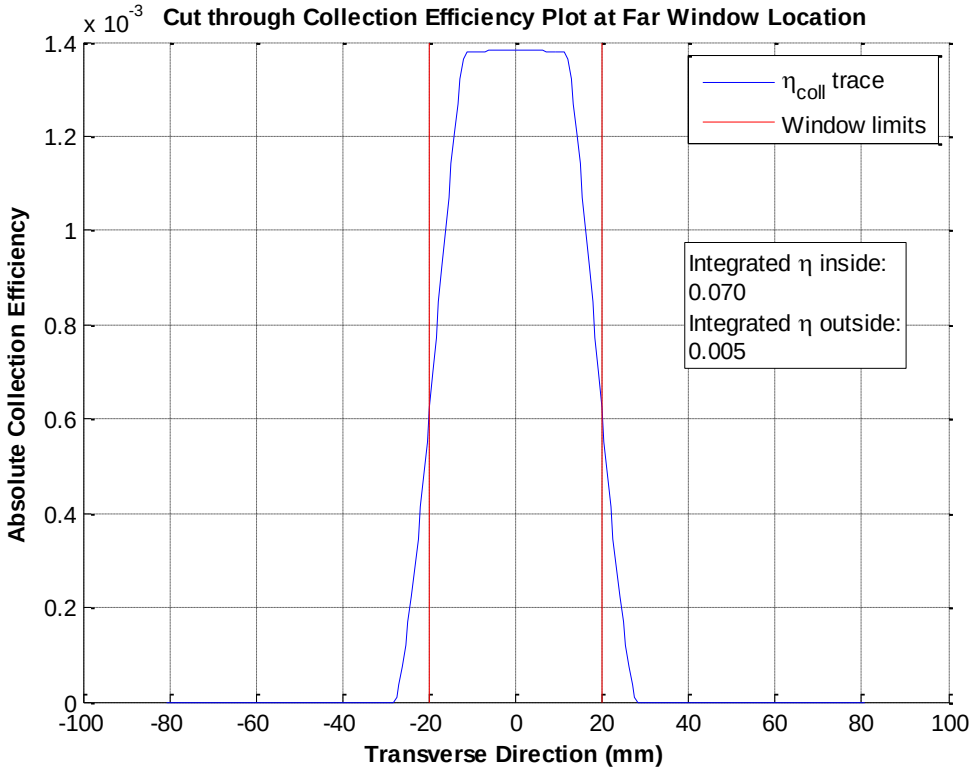
Figure 3. 9 The 3D spatial collection efficiency map. The *x* and *y* readings in the map are elemental indices rather than actual length in mm. (Conversion factor is 0.7076 mm).

The 3D cut through collection efficiency map at the far window location is seen in Figure 3.10. There is some noise on the plot. This is due to the quantisation of the θ vector, and can be reduced by using more steps. Increasing the steps from 401 in Figure 3.10a to 10001, this noise can be attenuated, which is shown in Figure 3.10b.

Figure 3.11 indicates that the fraction of photons collected from the flame surface, η, is essentially constant up to a radius of approximately 12 mm,



(a)



(b)

Figure 3. 10 Plot of a slice through the collection efficiency map at the far window for the 3D calculation (in Figure 3.10a, 401 steps in θ discretization; in Figure 3.10b, 10001 steps in θ discretization).

Above 30 mm the number of photons collected from the flame surface, $A\eta$, is essentially constant, where A is the flame surface area. The drop in η above a 12 mm radius can be attributed to the shell-like flame front propagating into regions which are less well sampled by the optical system. It will be seen later that the data selected for analysis fall within a radius range of 55-75 mm, for which $\sum A_i \cdot \eta$ is approximately constant; so the optical system collection efficiency is reducing in proportion to the radius squared.

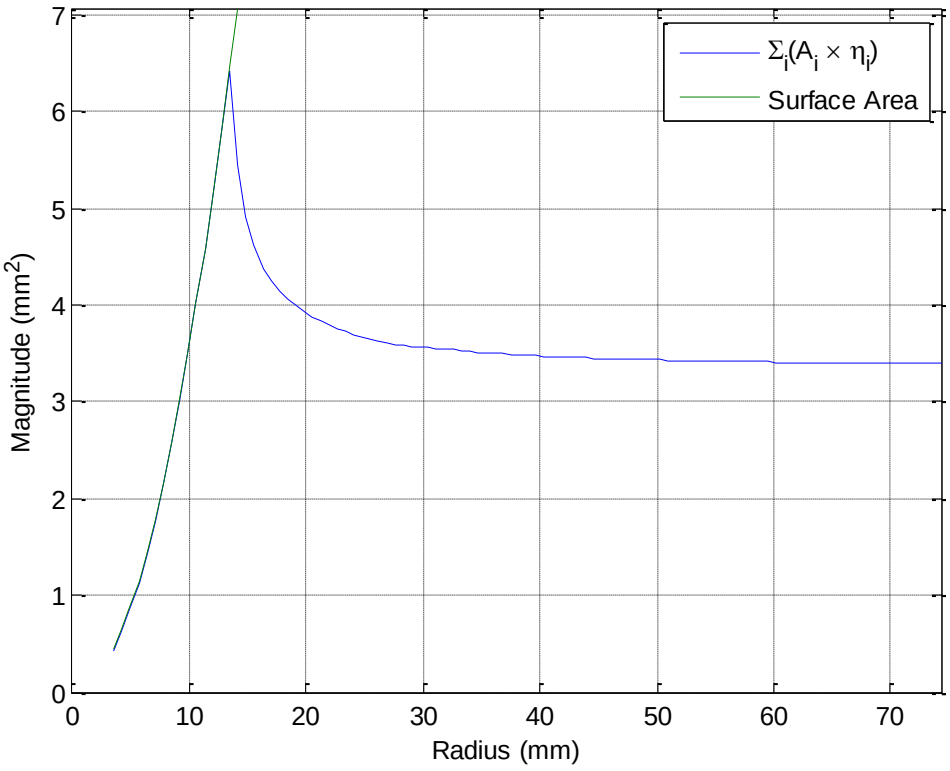


Figure 3. 11 Variation of total photon collection with radius for a spherical flame with a constant photon flux (#/(m^2·s)).

3.4 Model Validation

3.4.1 Introduction

To fully take advantage of the well-established 3D optical model for future chemiluminescence investigation, attention needs to be paid to validate the optical model in the following two aspects: for one thing, the veracity of the 3D model should be checked in a

straightforward problem which has a classical theoretical solution. For the other, validation is carried out to check the field of view (i.e. the geometry used in the optical system), and to check the overall system 'collection efficiency'. This is achieved by comparing the theoretical signal distribution with experimental measurements. Experimental validation has been conducted in two ways, firstly by traversing a point light source; this provides a direct check on the field of view, and integration of the results can be used to check the overall system 'collection efficiency'. Secondly the model was validated by using a uniformly illuminated surface that was moved along the bomb optical axis. Numerous experiments and refinements were needed to eliminate the effects of scattered light.

3.4.2 Analysis of a Pinhole Centred at the Focal Point of Lens

In order to verify the accuracy of the model, a collimated style of geometry can be used. For this geometry, aperture 2 is sitting at the focal point of the lens, and forms a relatively small pinhole. Thus the light 'beam' inside of the bomb is expected to be parallel. In the case of $a2p$ = 11.6 mm and $a2d$ = 1 mm, the spatial collection efficiency distribution of Figure 3.12 is produced.

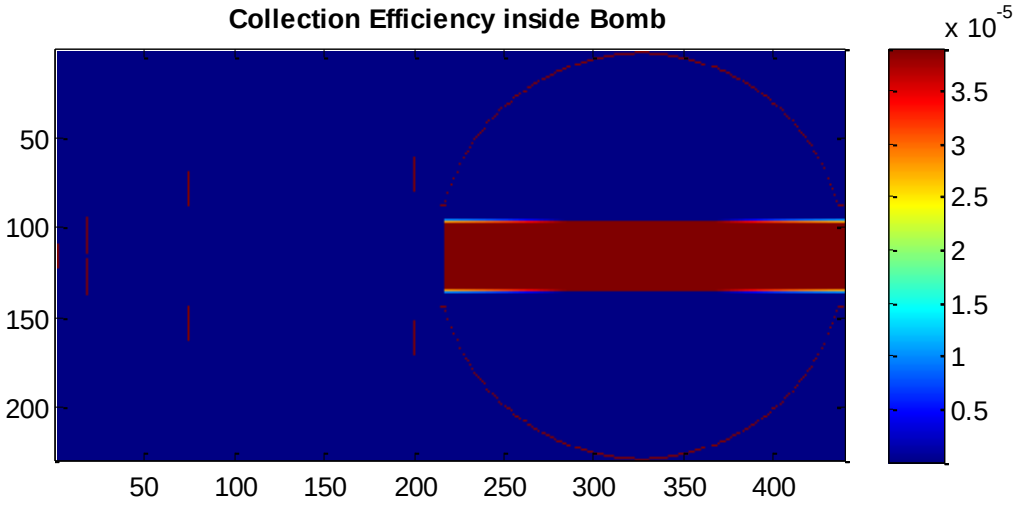


Figure 3. 12 The 3D spatial collection efficiency map in the case of a pinhole centred at the focal point of the lens.

Figure 3.12 shows that the spatial collection efficiency is uniform and consists of a fairly-well collimated ‘beam’, that is consistent with expectations. By comparison with the colour bar of Figure 3.9, it is obvious that this configuration has excellent rejection of scattered photons but too low a collection efficiency.

3.4.3 Experimental Validation with a Point Source

The accuracy of modelling has been checked by comparing the signal distribution with measurements from a point source that has been scanned across the field of view. This checked the geometry to be used in the optical system, and also the system ‘collection efficiency’. A number of experiments had to be carried out with different refinements to eliminate scattered light.

3.4.3.1 Experimental set up and LED Scan

The field of view restriction is achieved by wrapping a mask made out of black paper around the detector tube. Initial investigation was conducted by considering the detector to be an 8 mm disc. Taking the magnification of 51.6 / 178 into account, since the detector is a small distance (considered to be 7-8 mm) away from the curved envelope of the tube, the ideal size of the hole on the mask needs to be 6.91 mm diameter. Figure 3.13 illustrates the photomultiplier tube with a printed mask.



Figure 3. 13 PMT with a black paper mask wrapped around it.

A Perspex disc was mounted on the bomb with spacers, so that its far surface was at the plane of the inner surface of the far window; as shown in Figure 3.14, the centre of the disc was on the optical axis of the bomb-and-detector system, and for some experiments a mask with 3.0 mm width was attached to the Perspex disc, in order to provide a datum when the point light source (an LED) was scanned across the field of view.

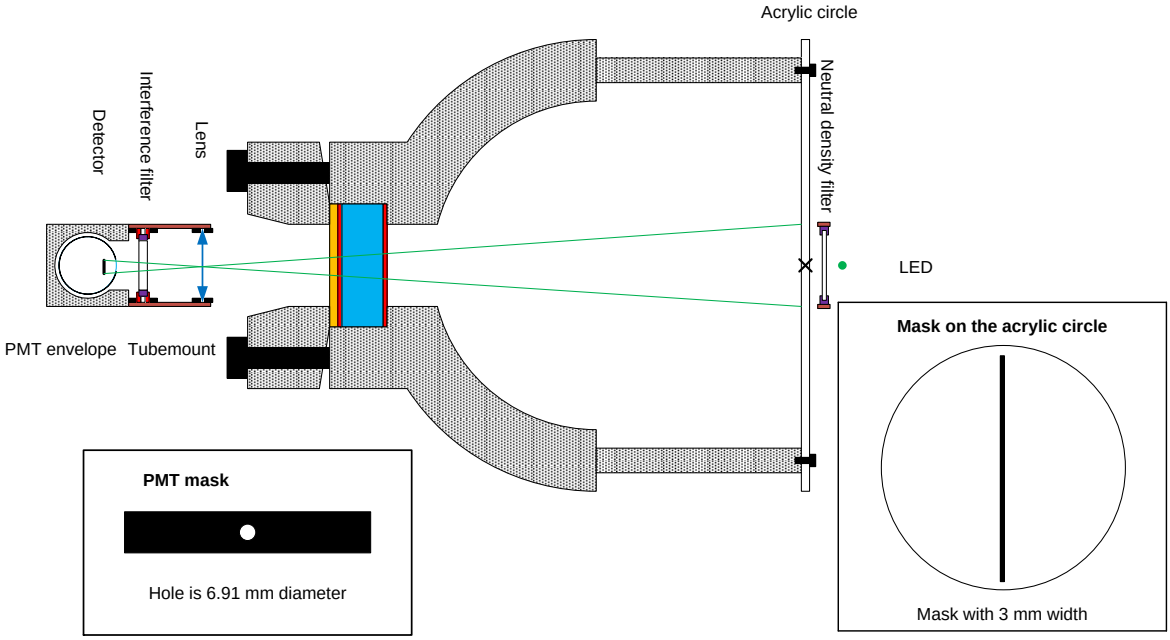


Figure 3. 14 Arrangement of the point source (LED) calibration experiment. A mask with 3 mm width was attached to the acrylic circle.

The light source was scanned in a horizontal direction (i.e. transverse direction as shown in Figure 3.7 and 3.10), and the PMT was rotated about its optical axis (so that its body was horizontal or vertical), in order to investigate the impact of the photocathode being slightly slanted. Specifically, the detector is upright in the 'vertical' case, i.e. scanning across the 8 mm wide photocathode; while the LED scans the long side of the photocathode (24 mm) when the detector is in the 'horizontal' case.

As seen in Figure 3.15, the preliminary tests showed that the results are poor in comparison to the 3D prediction. For one thing, the alignment was not spot on. For another, the edges of the scans are much less sharp than expected, which is attributed to the tilted photocathode. However, it provides confidence that the narrow field of view system rejects the majority of scattered photons.

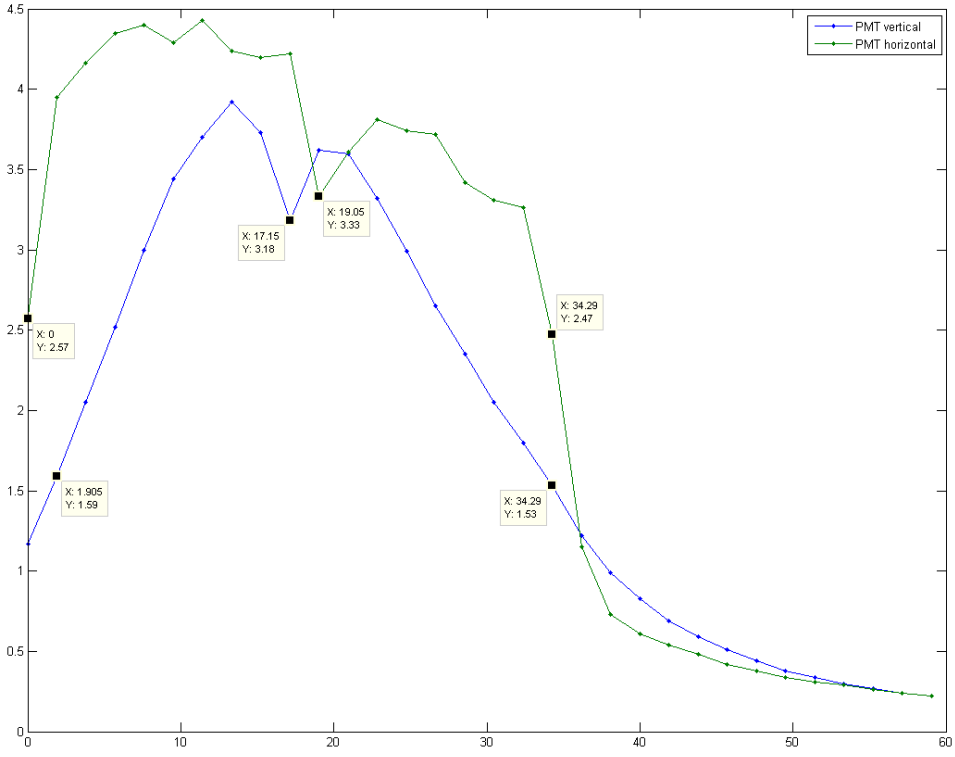


Figure 3. 15 PMT measurements using 7 mm aperture wrapped around the detector.

To deal with the misalignment, improvements were made with a two-axis translation mount for the PMT and a HeNe for the alignment, which is not discussed in detail here. To

isolate the impact of the slanted photocathode, the sensitivity limits of the detector needs to be determined. Therefore a raster-scan across the surface of the photocathode was carried out. A 7 mm aperture was still wrapped around the PMT. Figure 3.16 is a normalised contour plot, and this shows that the sensitive part of the detector, where the collection efficiency is not varying by more than about 20%, is constrained to a region (refer to the dashed blue rectangle) which is about 2-3 mm wide (horizontally) and 5 mm tall (vertically). Hence to avoid the insensitive parts of the photocathode, an effective way is to constrain the aperture of the lens, which makes the cone angle of the rays on the detector side of the pinhole smaller, so they always fall on the sensitive part of photocathode. This led to the use of smaller apertures on the PMT and the lens. Furthermore, a different, simpler lens-to-detector geometry (i.e. the lens-to-detector distance reduced to 48 mm, which means the PMT aperture sitting on the focal point of the lens) was investigated.

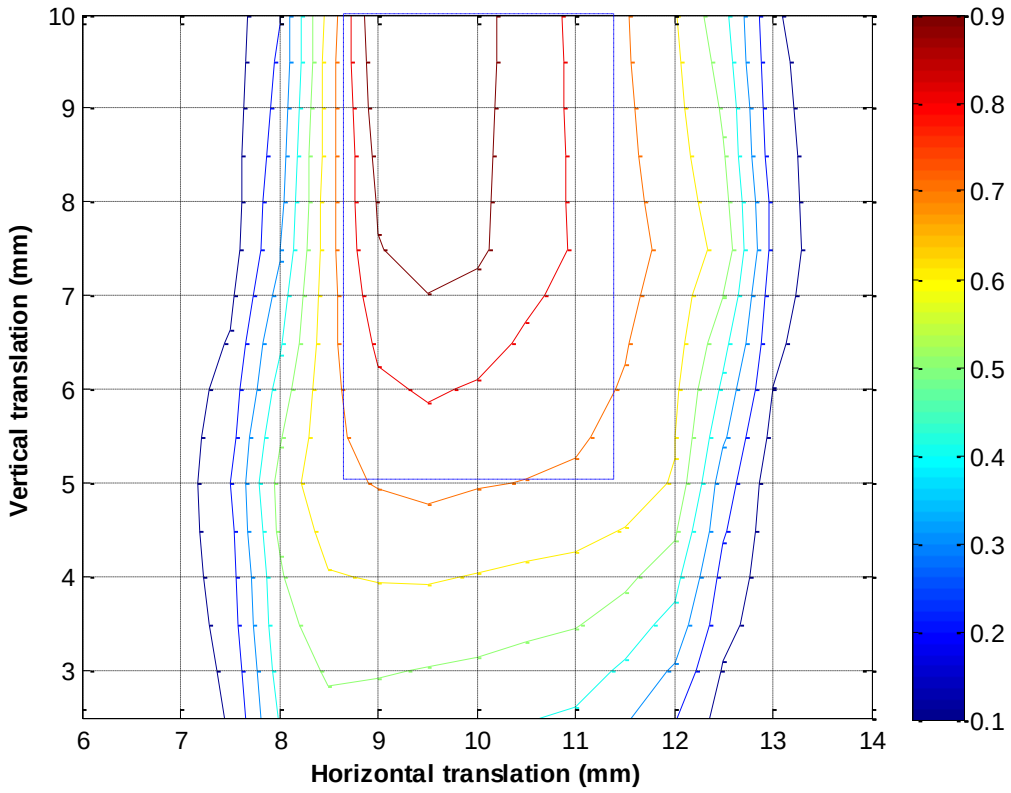


Figure 3. 16 Normalised uniformity contour plot, showing the region of high and comparatively uniform sensitivity of photocathode.

Next, is the comparison of a series of solutions with *det = 4* (effective sensitive region) to that of *det = 24* (largest detector dimension) and varying aperture size and constraining lens diameter.

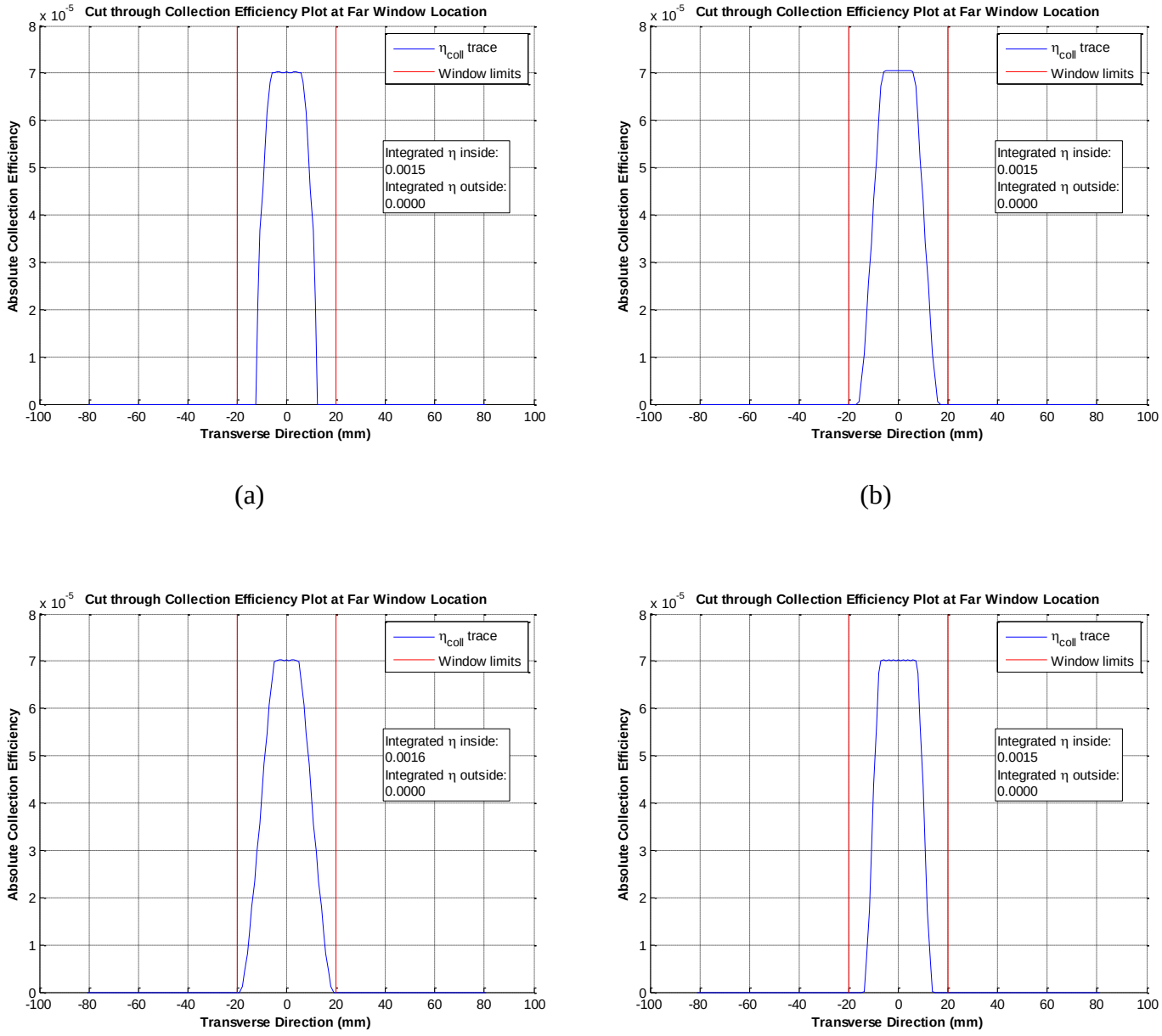


Figure 3. 17 (Figure 3.17a, b) Far-slice collection efficiency comparisons by changing detector size: (a) *det* = 4; (b) *det* = 24 (*v* = 48). (Figure 3.17c, d) Far-slice collection efficiency comparisons by modifying lens-to-detector distance: (c) *v* = 46; (b) *v* = 50 (*det* = 24).

The spatial collection efficiency in the case of a 3D model for $a2d$ = 3, $a2p$ = 8, v = 48, u = 220, ld = 10, provides a good performance in terms of the integrated collection efficiency. This is not only because the discrepancy between the collection efficiency with det = 4 and that of det = 24 is within 5%, but also the magnitude is relatively large compared with the collimated result (i.e. a small pinhole sitting at the focal length of the lens). Also investigated was the result from keeping det = 24 while the lens-to-detector distances deviated ∓ 2 mm from 48 mm, i.e. 46 mm to 50 mm respectively. This result is also pleasing, since the relative deviation of the integrated collection efficiency at the far window location is within 5%. Additionally, the output from the experiment is reassuringly in agreement with the model, which will be discussed later. Figure 3.17 illustrates the far-slice collection efficiency using the selected parameters; Table 3.2 lists the theoretical geometry of the optical system and the corresponding values used in the optical model.

Table 3. 2 Geometry of the optical system and the corresponding values

Optical property	Description	Unit	Value
D	Bomb diameter	mm	160
u	Lens-to-object distance	mm	220
v	Lens-to-detector distance	mm	48
ld	Lens diameter	mm	10
lf	Focal length of the lens	mm	40
det	Detector width	mm	4-24
$a1d$	Front window diameter	mm	40
$a1p$	Location of front window on x axis	mm	$a1p = v + u - \sqrt{\left(\frac{D}{2}\right)^2 - \left(\frac{a1d}{2}\right)^2}$
$a2d$	Aperture 2 diameter	mm	3
$a2p$	Location of aperture 2 on x axis	mm	8
$a3d$	Aperture 3 diameter	mm	50
$a3p$	Location of aperture 3 on x axis	mm	140
$reqres$	Requested resolution	mm	1

An LED scan across the field of view was then carried out using the acrylic screen with a narrow mask (3.0 mm wide) in the centre. The mask (as has been shown in Figure 3.14) is used to provide a datum to determine whether the sensitive region of the detector is

perfectly aligned (i.e. centred on the optical axis) when the LED is scanned across the field of view. Meanwhile, bearing in mind that the LED light source is a rectangular light source with a width of 2 mm, not a prefect point light source, a dip with width of 7 mm is observed in the centre. Figure 3.18 shows representative data compared with the predictions of the model at the same conditions. Two things are worth mentioning beforehand, firstly, this diagram shows LED scan traces for two PMTs, i.e. R955 and 9783B, for vertical and vertical/horizontal orientations; secondly, the LED scans are aligned so that the centre of the dip in the LED scan coincides with the centre of the plot from the model. The *x* axis then goes from -20 to +20 mm, indicating the field of view at the plane of the far window in the bomb. As the aperture wrapped around the PMT tube is made from paper, errors in manufacture are unavoidable. Actually the mask is not a perfect round, with the largest dimension being 3.46 mm and the smallest 3.196 mm. Furthermore, the edge of the circle is not smooth. Accordingly, 3.5 mm rather than 3 mm was chosen as the diameter of aperture 2 in the modelling.

In Figure 3.18 the model shows that, for the optical conditions which are currently used, then a region of about 6 mm diameter on the detector is sufficient to capture all the photons (the results for the 24 mm detector size are indistinguishable from a 6 mm diameter detector). The model also predicts that the PMT should be sensitive to a region which is 34 mm wide (vs. window apertures of 40 mm). From the experimental traces, the results show similar behaviour between the two detectors when vertically aligned. With regard to the horizontal alignment, this broadens the trace, but not too substantially. The limits of the horizontal trace in particular agree well with the model too.

However, the sensitive region is never perfectly aligned, i.e. it is always 2-3 mm out from being perfectly centred on the target. Fortunately, this still provides isolation against

scattered photons. The 9783B has a somewhat noisier trace when horizontal, which is disappointing, but not of great importance.

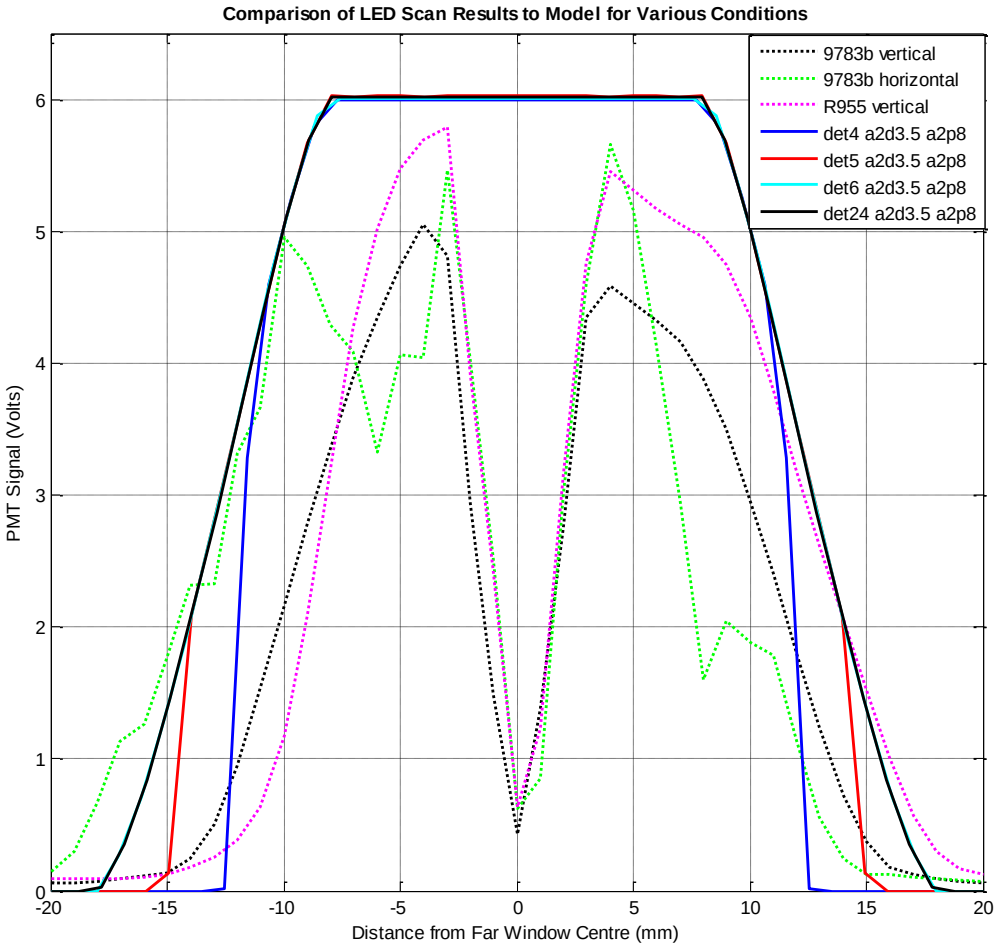


Figure 3. 18 Comparison of the LED scan results with the model results for both PMTs and orientations. The dip with width of 7 mm results from the LED being scanned across the 3 mm wide alignment mask. In the optical model, the detector diameters are varying, from 4 mm (effective sensitive region) to 24 mm (largest detector dimension). While the diameter of aperture 2 (wrapped around the PMT) is set to be 3.5 mm, the position of aperture 2 is considered to be 8 mm away from the detector.

In conclusion, these results confirm good agreement between the LED scans and the model if a 2-3 mm discrepancy between the centres of the window and the sensitive region is acceptable. In fact, validation of the model afterwards indicates that it is not a major source of error. The current field of view system is verified to isolate the scattered photons. Without

loss of any generality, further investigation will mainly focus on one of the two PMTs with vertical orientation.

3.4.3.2 LED Scans at Intermediate Distances along the Optical Axis

The model and optical system performance also need to be verified at several other axial locations. What should be expected from the model is that as the LED is brought closer to the lens / PMT, the PMT output becomes narrower and higher. This would of course require that the PMT excitation voltage was kept constant.

The set-up for this test is not very different from the previous LED scan, except that the acrylic screen was removed and the translation system was replaced with a longer one to allow measurements at 20 mm axial increments. The range of LED translation was from the far window plane (80 mm) to -40 mm from the centre of the bomb. Closer locations could not be achieved since the shell of the bomb stops the light source being traversed.

To compare the model against the experimental data, it is important to determine the fraction of photons collected from the planes at different axial locations. Considering the cylindrical symmetry of the problem about the optical axis, multiplying the spatial collection efficiency by the ring area at radius r_i (in this case, within ±20 mm) from the optical axis at each plane, i.e. $2\pi r_i \times dr_i$, it gives an element of shell area. Then summation of these elements yields the total signal. Therefore, a radius-weighted integration has been used to check the overall system performance. The gain calculation for an individual trace is as follows:

$$gain = \frac{sum(radius * experimental\ value)}{sum(radius * modelling\ value)} \tag{3.11}$$

The gain from each trace was then averaged to obtain a mean gain that was applied to all the modelling data. This provides a fair yardstick to compare the model to experiments. Equation

3.12 is used to quantify the error (which is expressed as a percentage value in the figure insets):

$$average\ fractional\ weighted\ error = \frac{gain\ of\ experimental\ measurement}{mean\ gain} - 1 \quad (3.12)$$

It is also worth mentioning that the LED used in the calibration is a rectangular light source with a width of about 2 mm, so it is not a perfect point light source. In order to eliminate the effect of the finite size light source, a moving average filter of span 5 was used in the modelling programme. The following values were chosen for the parameters defined in Table 3.1:

$$det = 5,\ a2d = 3,\ a2p = 8,\ v = 46,\ u = 221,\ ld = 11$$

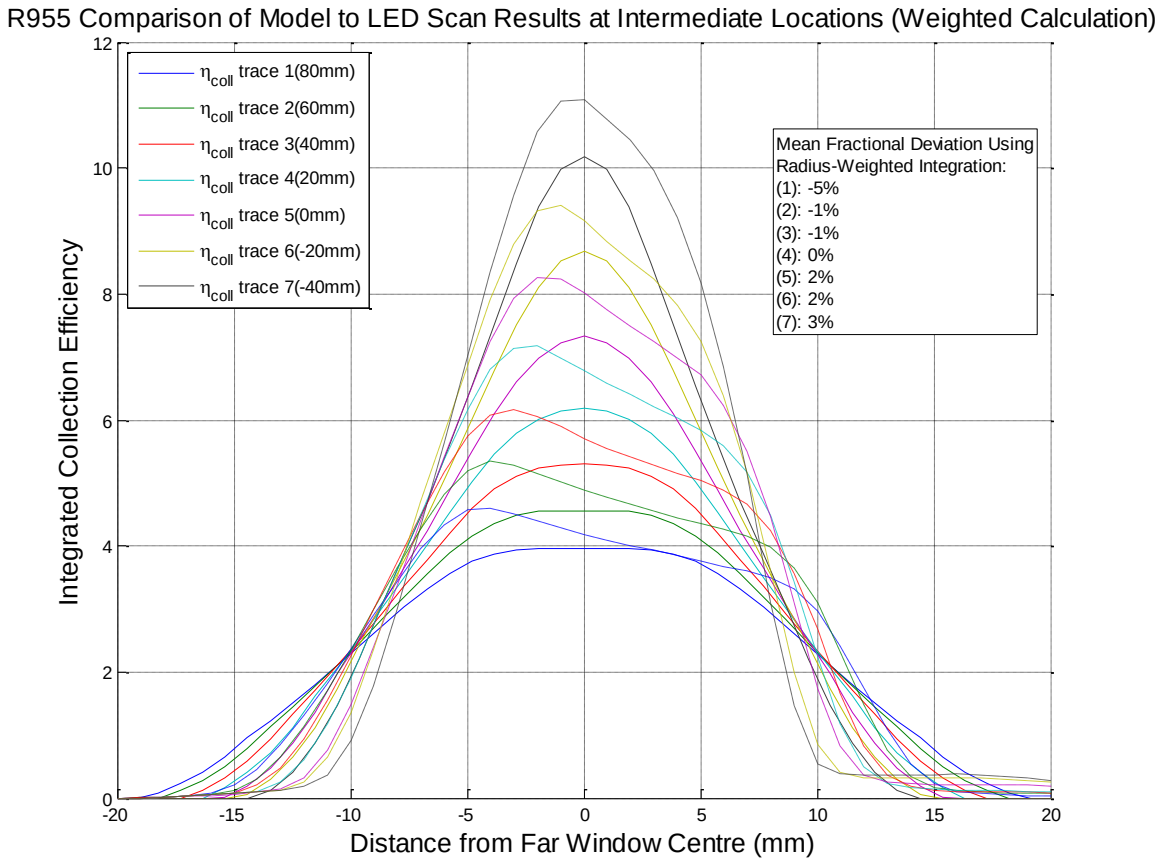


Figure 3. 19 Comparison of the model to experiments at intermediate locations using a scanned point light source.

Figure 3.19 shows a comparison of the model to experiments when a point light source is scanned transversely (i.e. along a diameter) at 7 different locations along the optical axis. The key result is that the field of view is restricted to within +/- 20 mm of the axis, so that no photons can be collected from reflections off the inner surface of the bomb (i.e. satisfying the 'direct photon' detection criterion). The asymmetry in the experimental results is due to spatial variations in the sensitivity of the photocathode within the PMT. Specifically, the PMT is vertically oriented so that the edge effect should be taken into account on each side. The system performance has been checked by using a radius-weighted integration, and the fractional deviation between the model and experiments was always within 5%. A similar comparison has been made by taking measurements with the 9783B PMT using parameters:

$$det = 8,\ a2d = 3.196,\ a2p = 7,\ v = 46,\ u = 221,\ ld = 11$$

3.4.3.3 LED Scans at Four PMT Orientations

The effective diameter of the detector varies with PMT orientation because the detector surface is not normal to the optical axis. Hence another calibration was carried out with LED scans at four different PMT orientations. The experimental set-up is basically the same as the previous LED scan. An LED is placed at the far window plane (80 mm from the centre of the bomb), and traversed across the field of view (from -20 mm to 20 mm). LED scans at various PMT orientations were undertaken for: 0°, 30°, 60° and 90°. The geometry of the optical model, as well as the PMT power supply, was the same as used in the previous section. Figure 3.20 gives a comparison of the modelling against tests for PMT R955. As before, a moving average operation of span 5 is used to provide a smooth form of the signal, removing the fluctuations due to the rectangular light source and but keeping the overall trend. In addition, the mean fractional deviation (shown in the insert to Figure 3.20) was obtained by using a radius-weighted algorithm.

The lines in yellow indicate averaged results which are the mean of the four data sets at the various orientations. Most importantly, this optical geometry retains isolation against scattered photons within ± 20 mm of the optical axis. Secondly, the horizontal alignment broadens the trace compared with other three orientations, but not too substantially. Lastly, the mean results show excellent agreement with the modelling. The same comparisons have been made for the other PMT (9783B), which also provides confidence in the optical geometry.

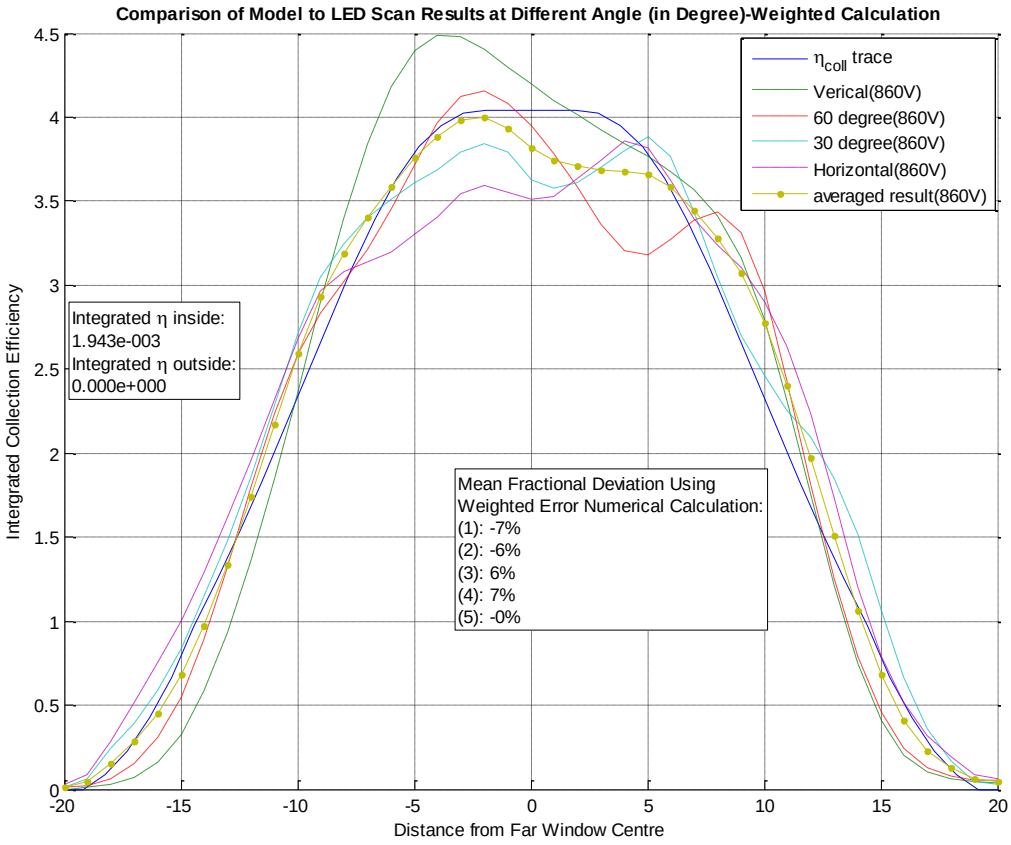


Figure 3. 20 Comparison of model to experiments with four PMT orientations.

3.4.4 Planar Uniform Light Source Calibration

To further confirm the agreement between the model and reality, it is worth using the results of the model to try to assess the impact of moving a uniform diffuse light source along the optical axis. As has been discussed in section 3.4.3.2, the planar collection efficiency is

obtained by taking the cylindrically-symmetric model data, weighting the spatial collection efficiency values by the area of a ring at the relevant distance y_i from the optical axis at each plane (with the first element being a circle on the optical axis), and summing up these shell areas with each step along the axis considered individually, i.e.

$$i = 1: shell(i) = \eta_{coll}(y_i = 0) * \left(\pi * \left(\frac{dr}{2}\right)^2\right) \quad (3.13)$$

$$i = 2,\ldots,n: shell(i) = \eta_{coll}(y_i) * (2 * \pi * y_i * dy)\ ) \quad (3.14)$$

$$planar\ efficiency = sum(\ shell(i)\ ),\ i = 1 \ldots n \quad (3.15)$$

where η_{coll} denotes spatial collection efficiency. The model predicts that the PMT signal will be constant within 0.1% as the light source is moved along the axis.

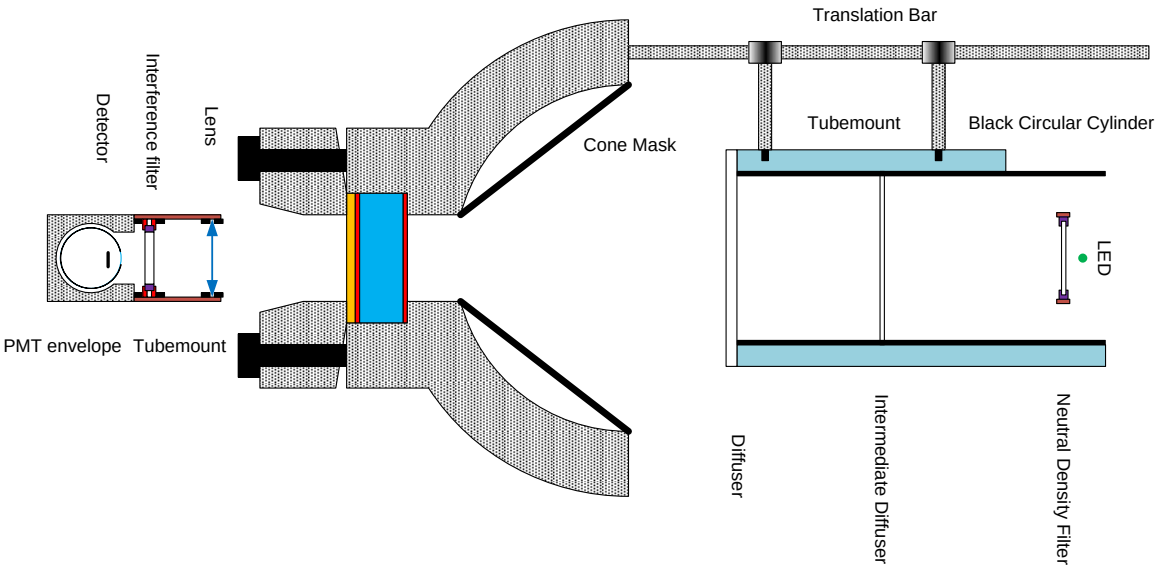


Figure 3. 21 Arrangement of planar uniform light source for calibration of the PMT optics.

A long tube (230 mm) with an internal diameter of 75 mm has been used to generate a planar uniform diffuse light source. Figure 3.21 shows that a point light source was placed at one end of the tube (with a matt black internal surface) and an opaque sheet of poly-methyl-methacrylate at the other. To ensure that the screen is illuminated entirely uniformly, an intermediate diffuser is placed part way along the mounting tube, and a circular tube made of black paper lines the interior surface of the plastic tube. The translation stage was replaced by

an axial bar so that the diffuse light source could be translated along the optical axis through 100 mm with two different PMT excitation voltages. Finally, a conical mask was placed around the interior surface of the combustion bomb, to avoid receiving light that might be back-reflected from the front surface of the diffuser.

In order to compare the model to the experiment, a scaling parameter is required to convert the model prediction value into 'volts'. To determine the scaling parameter, a simple approach is to evaluate $\frac{(exp-background\ intensity)}{(model)}$ at the mid-point along the translation. The two PMTs, (R955 and 9783B), were tested separately. Figure 3.22 shows comparison of the model to the LED scan when the uniformly illuminated screen was moved along optical axis. It is worth mentioning that the background reading is always zero so that no datum correction is required.

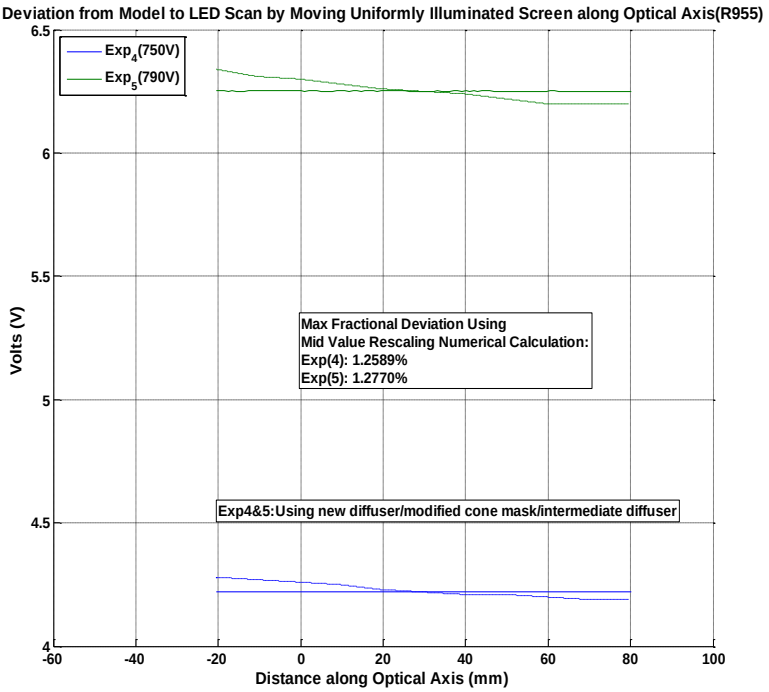


Figure 3. 22 Comparison between the model and the experiment (broken line) when moving a uniformly illuminated screen along the optical axis.

In Figure 3.22, solid lines indicate the model multiplied by a scaling parameter, while the dashed lines refer to the experiments. Calculation shows that the maximum fractional

deviations for both PMTs are within 2%, i.e. around 1.26% for R955 and nearly 1.8% for 9783B, respectively, which are within an acceptable tolerance. Furthermore, when a flame is measured the near surface will give too high a reading and the far surface will give too low a reading, so overall the errors will tend to cancel. So these results confirm the accuracy of the modelling and the satisfactory performance of the PMTs and their optics.

In conclusion, the results in Figure 3.22 show very good agreement between the model and the experiment. These results confirm the accuracy of the modelling and the satisfactory performance of the PMTs and their associated optics.

3.4.5 Conclusion

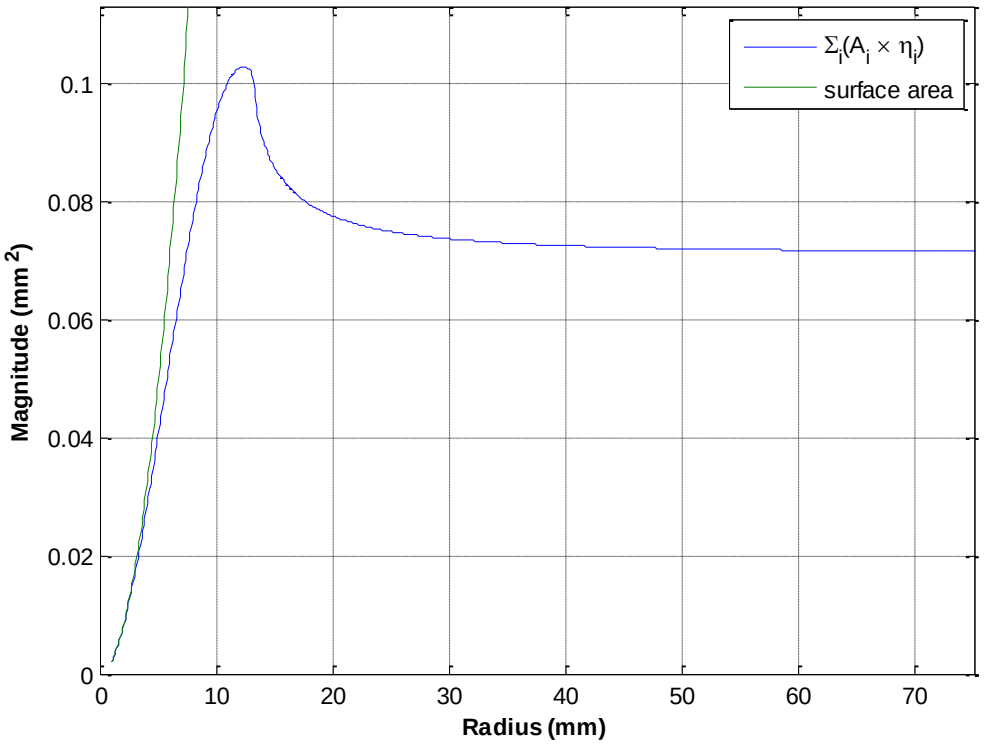


Figure 3. 23 OH* signal collected with radius with a constant photon flux (#/(m^2·s)).

The optical model was validated in two ways, firstly by traversing a point light source, and secondly by using a uniformly illuminated surface that was moved along the bomb optical

axis. Overall, these results are able to certify the accuracy of the modelling. The current optical geometry to monitor OH* (by PMT R955) and CH* (by PMT 9783B) respectively ensures that the detection volume not exceed the dimensions of the far window, hence rejecting the scattered photons. Furthermore, the optimisation of the OH* and CH* optical design with the 3D model is listed as follow:

OH*: det = 5, $a2d$ = 3, $a2p$ = 8, v = 46, u = 221, ld = 11;

CH*: det = 8, $a2d$ = 3.196, $a2p$ = 7, v = 46, u = 221, ld = 11.

Finally, Figure 3.23 plots the PMT signal that would come from an expanding spherical surface with a fixed photon flux (#/(m^2·s)).

3.5 Absolute Calibration of the PMT System for OH* and CH* Measurements

Without calibration both the normalised OH* and CH* measurements will be in terms of different arbitrary units. An Ocean Optics USB spectrometer with an absolute calibration is available, so a method is needed to transfer this calibration to the Photomultiplier Tubes **(**PMTs). Figure 3.24 shows a photograph of the general arrangement, and note how the PMTs are mounted by the lens tubes, so that the PMTs can be switched with the fibre optic of the spectrometer, without disturbing the optical alignment.

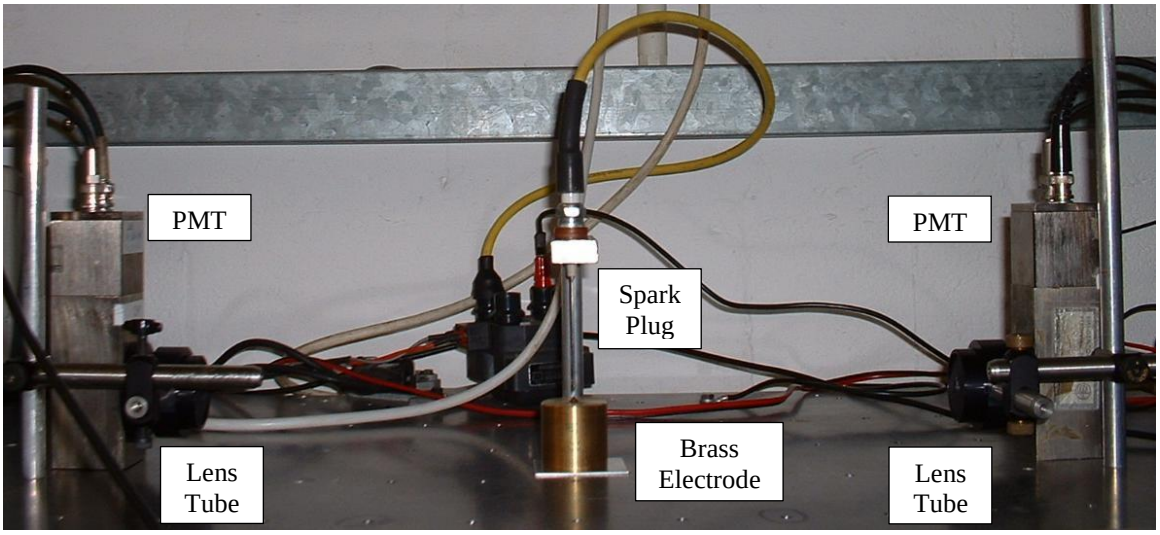
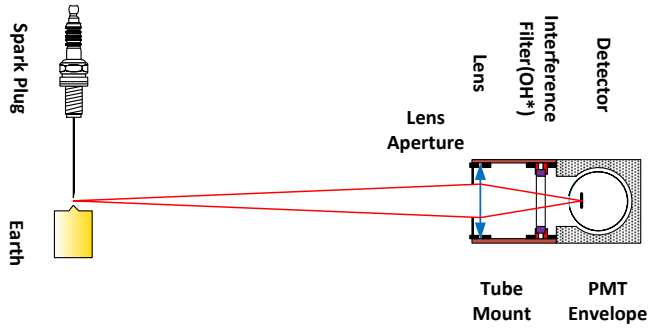
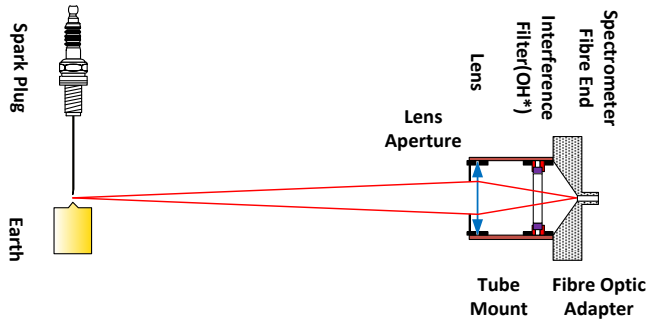


Figure 3. 24 General arrangement of the calibration system.

Figure 3.25 shows how a spark can be used as a broad-band light source (that extends into the UV).



(a)



(b)

Figure 3. 25 Use of an Ocean Optics USB spectrometer (with an absolute calibration) for calibration of PMT for OH* Chemiluminescence measurement.

The PMT is mounted the same distance apart as it is with the combustion bomb (Figure 3.25a), and the spark is arranged to be at the centre. The lens on the PMT has already been selected and mounted, along with interference filters used for the OH* and CH*. With the given lens-to-object distance u, of 221 mm, the lens-to-detector distance v of 46 mm, resulting in a magnification $M = \frac{v}{u}$, of 0:21.

Figure 3.25b shows an adapter that has been made that enables the end of the fibre optic that inputs light to the spectrometer to be mounted on the same plane as the

photocathode. The PMTs are mounted by the lens tubes, so that the PMT can be switched with the fibre optic connected to the spectrometer, without disturbing the optical alignment.

Alignment is not especially difficult for the PMTs as the photocathode is very large compared to the image size of the spark, but alignment is critical for the fibre optic of the spectrometer as it has a diameter of only 1 mm. The image size is about 1/5 of the object size, so the spark plug gap was set to be 2 mm, to give an image size of 0.4 mm.

Initial alignment was by careful measurement (digital callipers) to find the height of the optical centreline and to position the spark electrodes. A metre steel rule and square were used to position and align the bodies of the PMTs on the breadboard. A digital camera was used to check the alignment and this required several steps.

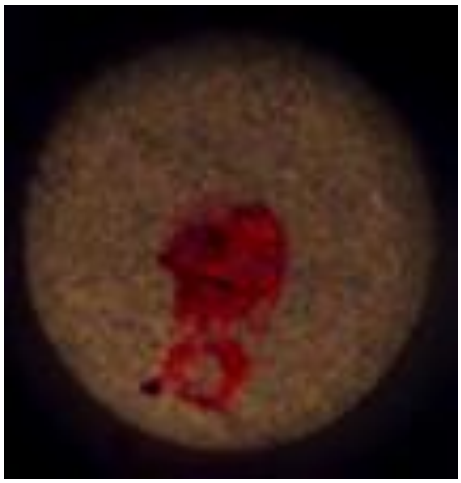


Figure 3. 26 Image of the red dot on the tracing film (the visible diameter is 3.2 mm, corresponding to a length of 188.235 pixels).

First the interference filter was removed so that sufficient light would reach the camera. Tracing film was placed at the focal plane of the adaptor that holds the fibre optic of the spectrometer; there was red dot at the centre of the tracing film. A Photron 1024 PCI camera was fitted with a 50 mm lens and a 2x macro converter set on unity magnification; the camera has a 0.017 mm pixel size. The tracing film was illuminated, and the camera position was adjusted until the image was in focus and quite close to the centre of the detector. The

outer diameter of the fibre optic cable was 3.2 mm, and the red dot was about 1 mm in diameter; an image from the camera is shown in Figure 3.26.

Once the camera was aligned and focussed the spark electrodes were illuminated so that the image of the spark plug electrodes could be seen on the tracing film (the spark was not sufficiently bright to be seen). The mounts for the PMTs were then adjusted until the spark gap image was aligned with the centre of the fibre optic mount, as can be seen in Figure 3.27.

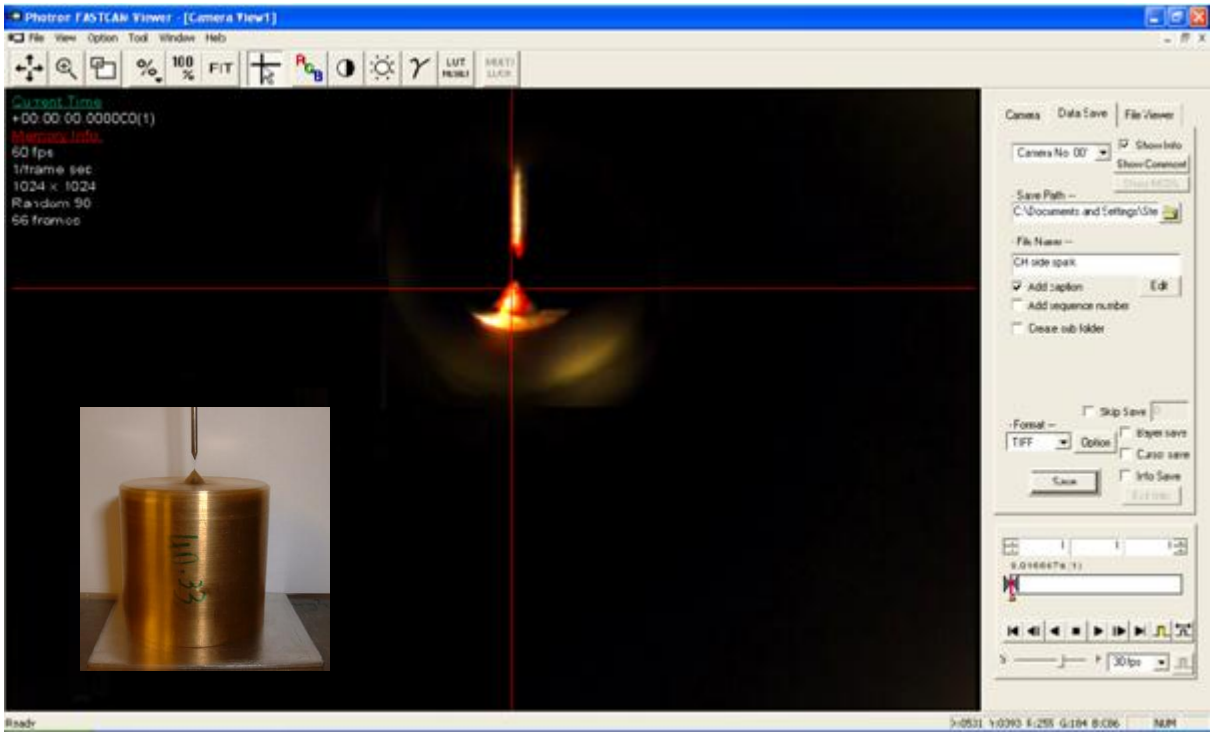


Figure 3. 27 Screenshot of the Photron FASTCAM Viewer showing the cursors that were used for checking the position on the image of the spark electrodes (the inset shows a natural light photograph of the electrodes).

Since the image of the spark plug gap is found in terms of pixels (not units of length), it is necessary to convert the pixels to a length. Each pixel is 17 μm × 17 μm, with the nominal spark plug gap (object length) of 2 mm, and the magnification factor ($M = 0.21$), the image length (in ♯ of pixels) is obtained as follow:

$$image\ length(in\ \sharp\ of\ pixels) = \frac{object\ length \times M}{pixel\ parameter} = \frac{2000 \times 0.21}{17} = 25 \qquad (3.16)$$

Counting the image length from the images such as Figure 3.27 gives 25 pixels and 27 pixels; both of which are within an acceptable tolerance.

To check the reliability of the detector system calibration using the Ocean Optics spectrometer, it is not only vital to ensure that the image size of the source on the fibre input is smaller than the diameter of the fibre core, but also important to guarantee that all light collected is transmitted by the fibre optics. Firstly, the magnification (i.e. 0.21) of the current configuration gives an image size of 0.4 mm on the fibre end, which is smaller than the diameter of the fibre end (1 mm). Secondly, the Ocean Optics optical fibre has a numerical aperture (NA) of 0.22. This means that it can collect light from a cone angle defined by:

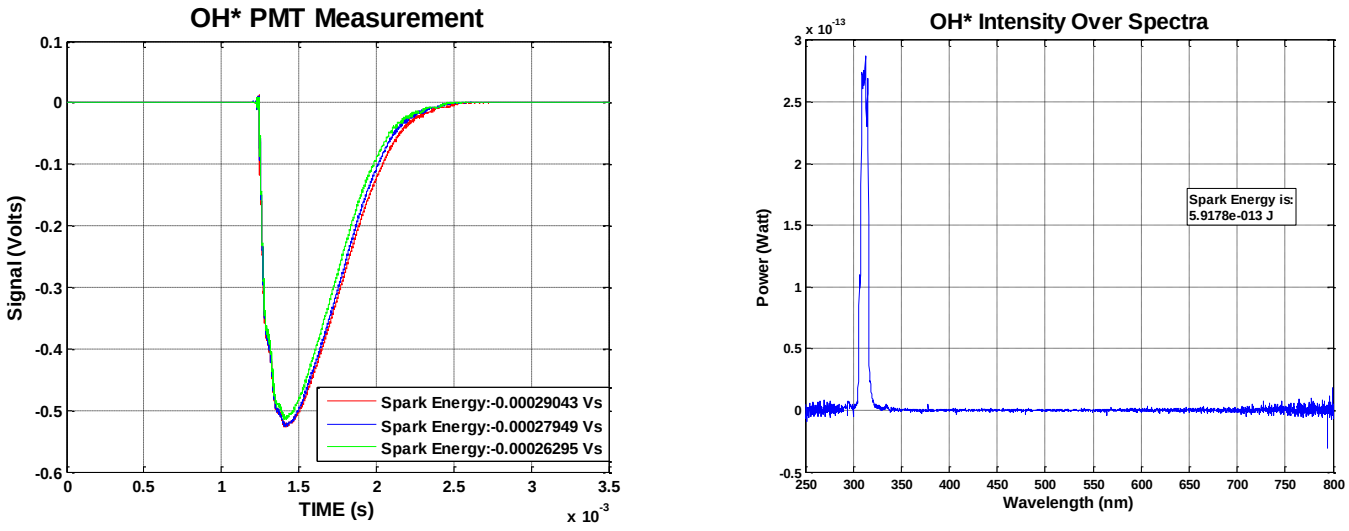
$$n \cdot sin(\theta) = NA \tag{3.17}$$

where n is the index of refraction of the medium in which the lens is working, and θ is the half-angle of the maximum cone of light from the lens into the fibre core. For air, n is approximately unity, so equation (3.17) gives the half angle θ 12.7 degrees. Turning to the lens, this was a 40 mm focal length lens, with an 11 mm aperture placed directly in front of it. The largest possible ray half-angle (α) from the lens into the fibre end can then be found from α = arctan (5.5/46), which leads to α = 6.8 degrees; and this is comfortably smaller than θ. In conclusion, the fibre was able to collect the entire incident light from the collection lens positioned 221 mm away from the spark into the optical fibre which is 46 mm on the other side of the lens.

To calibrate the PMT for the OH* measurement, the output from the PMT is logged on a Tektronix DPO2014 Digital Scope and an average is taken of 512 spark discharges. The built-in integration function is used to find the PMT output (V·s) per spark. The input to the USB spectrometer is integrated over a period of 20 s, with a spark frequency of 20 Hz.

The USB spectrometer output is in terms of counts at each pixel, and its calibration is used to calculate the energy output, and this is shown in Figure 3.28b. The data in Figure

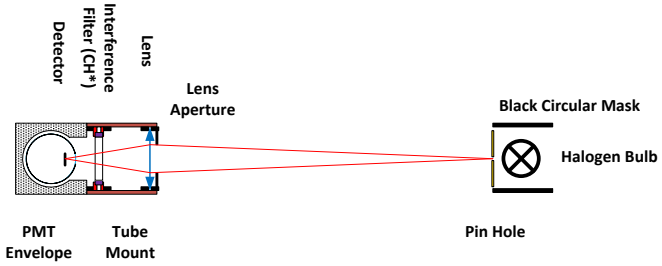
3.28b can be integrated; along with the integrated PMT output (in units of V·s), so an absolute calibration of PMT for OH* can be obtained. A series of measurements yield an average gain of 4.6×10^8 (V·s/J or V/W) with a standard deviation of 0.9%, which is within an acceptable tolerance. This then enables the absolute calibration of the PMT at the selected wavelength of 306.4 nm.



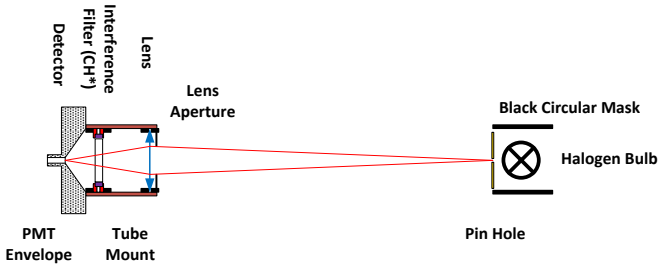
(a) (b)

Figure 3. 28 Output of the photomultiplier tube (PMT, in Figure 3.28a) and the corresponding OH* energy from the Ocean Optics USB spectrometer (in Figure 3.28b).

For the PMT calibration of the CH* measurement, the geometric arrangement is mainly the same as that for OH*. However, the light source was replaced by a halogen bulb since the spark does not have much energy at the wavelength of CH* (431.5 nm). Figure 3.29 illustrates the experimental setting-up of the photomultiplier tube calibration system for CH* measurement with a halogen bulb.



(a)



(b)

Figure 3. 29 Use of an Ocean Optics USB spectrometer (with an absolute calibration) for calibration of PMT for CH* Chemiluminescence measurement.

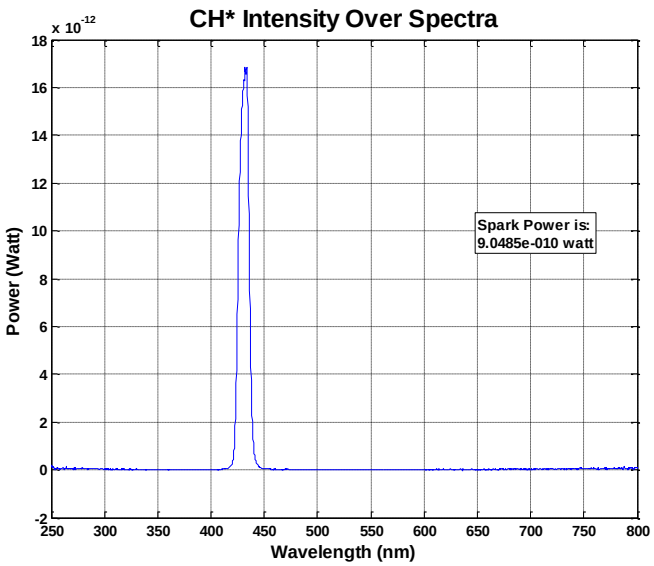


Figure 3. 30 CH* power from the USB spectrometer.

The input to the USB spectrometer is integrated over a period of 290 ms. With its own calibration, the USB spectrometer output can be converted to the power output, and this is

shown in Figure 3.30. Meanwhile, the output from the PMT was logged on a digital multi-meter rather than the oscilloscope, and this then leads an absolute calibration of 8.7×10^7 V/W with a standard deviation of 1.4%, which is acceptable, at the wavelength of 431.5 nm.

Not all of the photons at the OH* or CH* wavelengths will reach the PMT detector, so the next step is to measure the transmission efficiencies of the two interference filters using a photo-spectrometer and to include a transmission efficiency for the fused silica focussing lens and windows in the combustion bomb.

The absorbance and transmission of light through a sample can be calculated by measuring light intensity entering and exiting the sample. The Beer-Lambert Law gives the governing equations as follow:

$$A = log_{10}\left(\frac{I_0}{I}\right) \tag{3.18}$$

$$T = \frac{I}{I_0} \tag{3.19}$$

$$T = 10^{-A} \tag{3.20}$$

Where:

A: Light Absorbance;

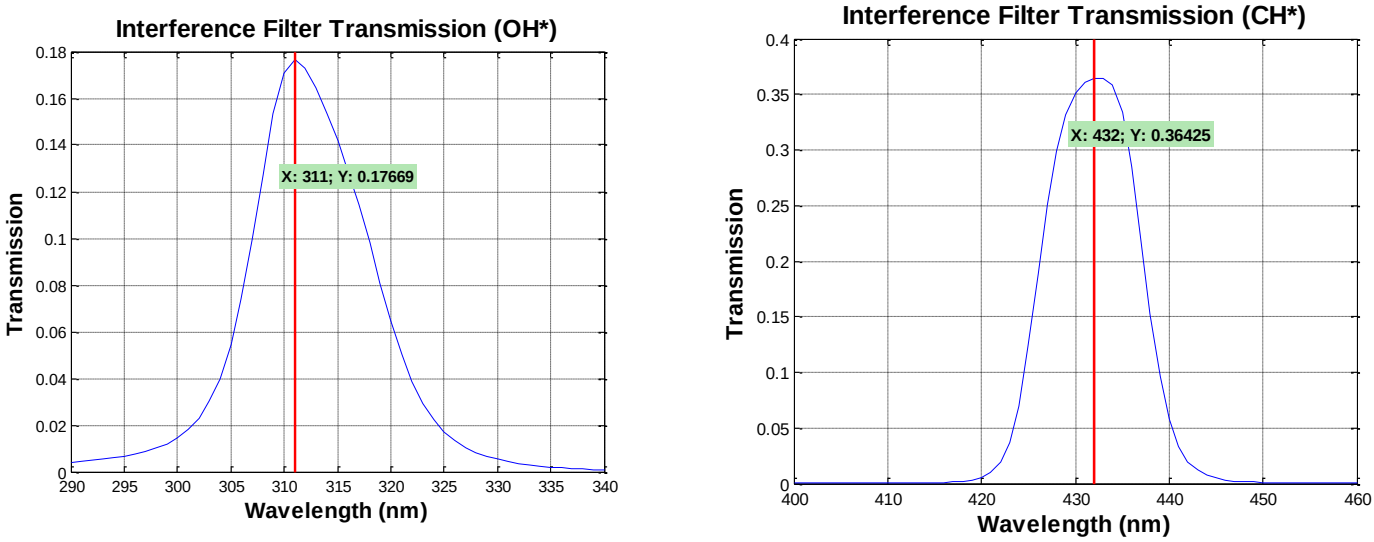
T: Light Transmission;

I_0: Light Intensity entering a sample, in this case, the interference filter;

I: Light Intensity exiting a sample, in this case, the interference filter.

Accordingly, the interference filters' transmission can be obtained using the measurement of the absorbance spectra. While Figure 3.31a illustrates the transmission for the CVI filter used for the OH^* (310 ± 2.0 nm and 10 +3 / -0 nm bandwidth), the Figure 3.31b demonstrates that for the Comar 430-IL-25 filter used for the CH^* (430 ± 2.5 nm and 10 ± 2.5 nm bandwidth).

The shapes are as expected, and this leads to the absolute calibration for the PMTs / interference filters. It is worth mentioning that, a fundamental simplification involved in the modelling is that the transmission efficiency for the fused silica focussing lens and windows in the combustion bomb approximates to unity. For the OH* chemiluminescence, it leads to an absolute calibration of 6.5×10^7 V/W with a standard deviation of 0.3%, which is acceptable. For CH* chemiluminescence, the average gain is 1.7×10^7 with a standard deviation of 2.2%, which is also within tolerance. Hence the absolute normalised OH* and CH* chemiluminescence can be related as joules per unit mass of fuel burned, which will be discussed in detail in Chapter 4.



(a) (b)

Figure 3. 31 Interference filters' transmission.

3.6 Conclusion

In conclusion, the current optical system has been proven to be well established for detecting OH* and CH* chemiluminescence inside the combustion bomb. For one thing, the optical model successfully isolated the majority of the scattered photons and optimised the optical design, which have been experimentally validated by using point light source and planar uniform light source. For the other, the optical model is able to retrieve the information of the

fraction of photons collected from the flame front as it expands. In addition, with absolute calibration, normalised OH* and CH* chemiluminescence will be in terms of joules per unit mass of fuel burned, not in terms of arbitrary units.

Chapter 4 Chemiluminescence Analysis Approach

This chapter includes an overview on the *NIICS* (Normalised Intensity Integrated Calculation System), which combines: experimental data, optical collection efficiency data, and data from the multi-zone modelling program. The chapter then reports on the theory and operation of the rigorous multi-zone computational model – *BOMB* program, the experimental summary spread sheet, and the '*nical*' code for combing the data and calculating normalised OH* and CH* intensity. In addition, important parameter during the combustion process, such as the heat release rate, will also be calculated by the *NIICS*.

4.1 Overview

A number of programs have been written to analyse the normalised CH* / OH* intensity data. Figure 4.1 gives an overview of the *NIICS* (Normalised Intensity Integrated Calculation System) that collects data from the multi-zone model, the optical modelling program, and the experimental records so as to calculate the normalised CH* / OH* intensity data. Finally, *NIICS* concatenates and saves the data, and it allows the user to find the coefficients for the curve fit for the normalised CH*/OH* ratio.

In this chapter, a novel and rigorous multi-zone computational analysis (*BOMB* program) has been used to analyse the combustion process inside the combustion vessel; this is presented in Section 4.2. The experimental summary spreadsheet is an Excel spreadsheet which gives information about the experiments in a batch. This will be discussed in Section 4.3.

The most important part of the *NIICS* is the program *nical* written in MATLAB. It reads the appropriate experimental data file (which has been identified by the conditions for each experiment in the experimental summary spreadsheet), the *zone* file (which is generated by the *BOMB* program), the photon collection efficiency of the photomultiplier tube system

as a function of flame radius (generated by the optical model), the absolute calibration data, and uses these to calculate the normalised intensities data. Additionally, *nical* also calculates the important combustion relevant parameter such as heat release rate. So there is a description of the program *nical* in Section 4.4. The final part of the *NIICS*, i.e. the fitting of a correlation expression for the normalised CH*/OH* ratio, will be discussed in detail in Chapter 5.

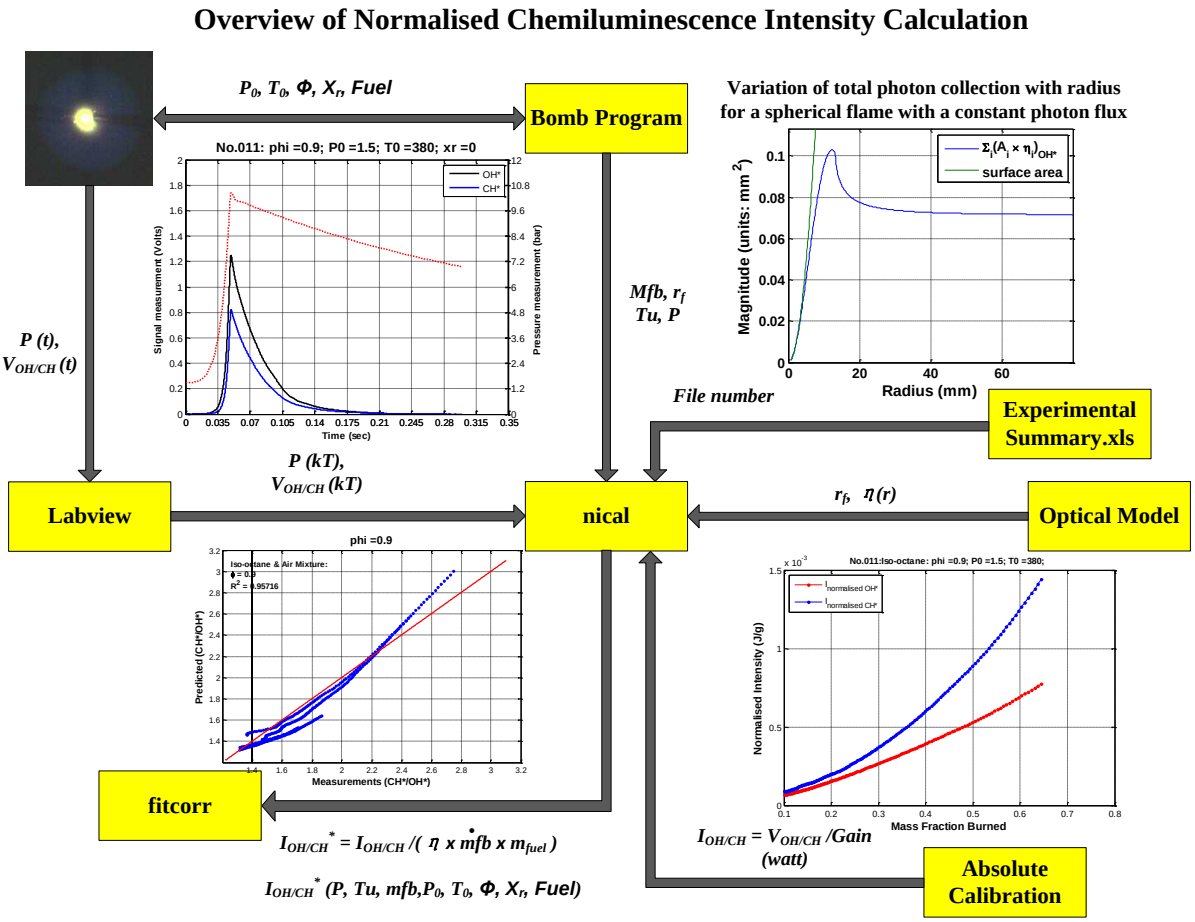


Figure 4. 1 Overview of Normalised Intensity Integrated Calculation System (*NIICS*) using data from the *BOMB* program, the optical model and experiment.

4.2 The BOMB Program

The *BOMB* program is adapted from *ISIS* (i.e. Integrated Spark Ignition Engine Simulation) for modelling Nitric Oxide emissions from a spark ignition engine, and it is an extension of

the single burned zone methodology presented by Ferguson [69]. It is a multi-zone numerical model which fetches parameters including: fuel under test, the equivalence ratio, residuals fraction, initial pressure and initial temperature; and then it solves the composition for the equilibrium of ten major combustion products for each burned-gas zone. Details about the *BOMB* program have been reported by Raine et al. [68].

The *BOMB* program solves the conservation equations for energy and mass in a constant volume vessel. It was based on the assumption of negligible flame front thickness, which along with the preheat zone separates the burned and unburned gases. In the current study, ten burned gas zones were chosen for the calculations.

To run the *BOMB* program by means of the MS-DOS prompt requires a typed data entry in response to multiple prompts, and this takes a long time. Therefore a batch file was created to run the program with an input file, which contains the input parameters. The advantage is that this allows values to be easily changed using a text editor, and the input file can be saved for later use and as a reference for the output files.

The outputs from *BOMB* program are in the format of text files. For each experiment (with specific initial conditions of initial pressure, temperature, equivalence ratio and residual molar fraction etc.), the program generates two text files - a data file and a zone file. Together the following information is provided:

1. Combustion

(a) Mass fraction burned (*mfb*);

(b) Flame radius (r_f, in mm);

(c) Pressure (p, in bar);

(d) Composition of the burned gas in terms of CO_2, H_2O, N_2, CO, H_2, H, O, OH, and NO_x;

2. State of the unburned gas

(a) Temperature (T_u, in K);

(b) Specific volume (V_u, in cm^3/g);

(c) Ratio of specific heats (γ_u);

3. State of each zone

(a) Radius of the boundaries (r_b, in mm);

(b) Temperature (T_b, in K);

(c) Specific volume of the gas (V_b, in cm^3/g).

4.3 Experimental Summary Spreadsheet

An experimental summary spreadsheet is prepared for use by the MATLAB code '*nical*' to give information about experiments in a batch. The Excel spread sheet contains the following information:

1. Experiment number. The experiment number (###) is used to define the file names within the different programs: *BOMB* program (niics###001.zon, niics###001.dat), LabView (###.lvm);
2. Equivalence ratio (Φ);
3. Initial temperature (T_0, in K);
4. Initial pressure (p_0, in bar);
5. Residual molar fraction (x_r);
6. Lambda recorded by the lambda sensor (λ);
7. A Boolean describing whether the pressure data should be included in the subsequent analysis (since some experiments can be dummy experiments for generating residuals);
8. A Boolean describing whether the photomultiplier tube measurements should be used in the analysis (since some experiments are dummy experiments).

The spreadsheet provides the conditions for each experiment. Then the user can find the corresponding experimental data file (###.lvm) and *zone* file (niics###001.zon) to do the calculations.

4.4 Nical Programme

4.4.1 Overview of Nical

The *nical* programme fetches the LabView experimental record, the relevant *zone* file from the *BOMB* program, and optical system collection efficiency (as a function of flame radius generated by the optical model) to calculate the normalised OH* / CH* chemiluminescence intensity.

Firstly, the *nical* program reads the experimental summary spreadsheet to specify the initial conditions for each experiment, and then it passes the file paths of the corresponding *zone* file and the experimental data file to a sub-program, '*normin'*, which actually does the calculation. In addition, the optical system collection efficiency (η) as a function of flame radius (r_f) is read from the optical model. While the experimental data file contains the pressure record, and the voltage from the OH* / CH* signals (V_{PMT}); the *zone* file provides the bomb pressure (*p*), the mass fraction burned (*mfb*), flame radius (r_f), the unburned gas temperature (T_u) and other parameters.

Next, the mass of fuel (m_f) used in the experiment is calculated based on the ideal gas law and the partial pressure method, which will be discussed in detail in Section 4.4.2.

Thirdly, the experimental pressure is filtered as the pressure recorded is used as the basis for interpolation between the experimental data and the *BOMB* program data. Additionally, as the bomb pressure is measured using a piezoelectric transducer, to obtain the absolute pressure the absolute initial pressure needs to be added to the change in recorded

pressure. Besides, to eliminate any experimental noise, the V_{PMT} data is filtered prior to any calculations. In this chapter, Section 4.4.3 will present the data filtering.

As the pressure record is displayed in terms of time, while the pressure and other parameters in the *zone* file are tabulated against mass fraction burned (*mfb*), then *normin* has to interpolate between these sources so as to match up the experimental pressure with the *zone* data. Similarly, another interpolation has to be carried out to generate the optical collection efficiency for each flame radius by matching up the flame radius in the optical model with that in the *zone* file. Further, the differentiation of *mfb* with respect to time (*t*) was done using the MATLAB function *gradient* in order to generate the mass fraction burned rate. This will be illustrated in Section 4.4.4.

As has been discussed in Section 3.5, the photomultiplier tube measurement (V_{PMT}, with unit of volts) can be converted to chemiluminescence intensity (I_{PMT}, with unit of watt) from the absolute calibration of the PMT system. Therefore, the chemiluminescence intensity can be normalised by division with the collection efficiency (η) and the mass burned rate ($\dot{mfb} \times m_{\mathrm{f}}$, which is proportional to the conventional rate of reaction), as follows:

$$I^{+} = \frac{I^{*}}{(\dot{mfb} \times m_{\mathrm{f}} \times \eta)} \tag{4.1}$$

where: I^{+} denotes the normalised OH* or CH* in terms of joules of light produced per unit mass of fuel burned; I^{*} means the absolute OH* or CH* chemiluminescence intensity collected by the photomultiplier tubes in unit of watt; ($\dot{mfb} \times m_{\mathrm{f}}$) represents the mass burned rate of a specific fuel; η stands for collection efficiency of photons from the burning shell at a particular radius as it expands. Hence the absolute normalised OH* and CH* chemiluminescence can be related as joules per unit mass of fuel burned.

In addition, the program also calculates the laminar burning velocity for each data point using Equation 4.2 (see Marshall [3] for details):

$$S_u = \frac{dr_i}{dt}\left(\frac{r_i}{r_b}\right)^2 \left(\frac{p_i}{p}\right)^{\frac{1}{\gamma_u}} \quad (4.2)$$

where S_u is the un-stretched laminar burning velocity (in fact, equation (4.2) calculates the stretched laminar burning velocity. However stretch effects can be neglected for a radius of curvature larger than 50 mm [83]; hence it is labelled as un-stretched laminar burning velocity instead). r_i is the radius of a mass fraction prior to combustion (t = 0), and r_b is the flame radius. p_i denotes the initial pressure, and p is the experimental pressure.

The stretch rate α is calculated using Equation 4.3 (see Marshall [3] for details):

$$\alpha = \frac{2}{r_b} S_f \quad (4.3)$$

where α is the stretch rate, r_b is the flame radius. S_f is the stretched laminar flame speed.

However the laminar burning velocity is not discussed further in this chapter. The calculation of heat release rate (which is based on the first law of thermodynamics) was implemented, and these details will be presented in Section 4.4.5.

Finally, the user needs to select which normalised chemiluminescence intensities (and normalised intensity ratios) are to be included in the correlation fitting. The data of interest is then sent back to the parent program *nical*. This process is repeated for each experiment in the batch and all the data is concatenated in a large matrix (See Section 4.4.6).

In conclusion, to carry out calculations as described above, the *nical* program is designed to implement the following tasks:

1. Calculate the mass of fuel used (m_f);
2. Filter the bomb pressure (p) and PMT measurements (V_{PMT});
3. Interpolate a value of the unburned gas temperature (T_u), the mass fraction burned (*mfb*), the ratio of specific heat (gamma, γ_u), the flame radius (r_f) for each experimental pressure; and interpolate a value of optical collection efficiency (η) for each flame radius (r_f);

4. Calculate the normalised OH* and CH* chemiluminescence intensity (I^+);
5. Calculate the laminar burning velocity (S_u) and the stretch rate (α);
6. Calculate the rate of heat release (*RoHR*);
7. Concatenate and save the data.

Task 5 is not discussed in this chapter as detailed information is found in Marshall [3].

4.4.2 Calculation of Mass of Fuel

For gaseous fuel and air mixtures, the theory of partial pressures is used to calculate the mass of fuel in the combustion bomb, based on the chosen fuel, equivalence ratio (Φ) and mixture pressure (p_{mix}). For a liquid fuel and air mixture, the molar fraction method is also based on the assumption that the liquid fuel is fully vaporised during delivery. As is shown in Equation (2.30), for a fuel burned stoichiometrically in air:

$$C_xH_yO_z + \left(x + \frac{y}{4} - \frac{z}{2}\right)\left(O_2 + \frac{79.05}{20.95}N_2\right) \rightarrow xCO_2 + \frac{y}{2}H_2O + \left(x + \frac{y}{4} - \frac{z}{2}\right)N_2 \qquad (4.4)$$

Bear in mind that the composition of the mixture contains air (n_{air}), fuel (n_f) and residuals (n_r), while $n_r = x_r \cdot n_{mix}$:

$$n_{mix} = n_{air} + n_f + n_r \qquad (4.5)$$

According to Dalton's Law of Partial Pressures, the ratio of the partial pressures of the fuel and the mixture will be equal to their molar ratio; hence Equation (2.16) will give

$$\frac{p_f}{p_{mix}} = \frac{n_f}{n_{mix}} = \frac{(1-x_r)}{1+\frac{100}{21\Phi}\left(x+\frac{y}{4}-\frac{z}{2}\right)} \qquad (4.6)$$

Assuming that the mixture pressure (p_{mix}) is equal to the required initial pressure (p_0) for combustion, the partial pressure of fuel can be calculated as:

$$p_f = \frac{n_f}{n_{mix}} \cdot p_{mix} = \frac{(1-x_r)}{1+\frac{100}{21\Phi}\left(x+\frac{y}{4}-\frac{z}{2}\right)} \cdot p_{mix} = \frac{(1-x_r)}{1+\frac{100}{21\Phi}\left(x+\frac{y}{4}-\frac{z}{2}\right)} \cdot p_0 \qquad (4.7)$$

As has been discussed in Section 2.5, throughout the liquid delivery process, care is taken to ensure that the fuel evaporates fully. In addition, the charging process is isothermal,

which indicates that the initial temperature (T_0) does not change throughout the mixture preparation process. Considering that $m_\mathrm{f} = n_\mathrm{f} \cdot M_\mathrm{f}$, Equation (2.33) leads to:

$$m_\mathrm{f} = n_\mathrm{f} \cdot M_\mathrm{f} = \frac{p_0 \cdot V_\mathrm{Bomb} \cdot (1 - x_\mathrm{r}) \cdot M_\mathrm{f}}{R_0 \cdot T_0 \cdot \left[1 + \frac{100}{21\Phi}\left(x + \frac{y}{4} - \frac{z}{2}\right)\right]} \tag{4.8}$$

As an example, for a stoichiometric mixture of methane and air without residuals at an initial pressure of 4 bar and an initial temperature at 380 K, substitution of $M_{\mathrm{CH_4}} = 16.042$ (g/mol), and $R_0 = 8.314$ ($\mathrm{m^3 \cdot Pa \cdot K^{-1} \cdot mol^{-1}}$) will yield:

$$m_\mathrm{f} = n_\mathrm{f} \cdot M_\mathrm{f} = \frac{4 \times 10^5 \times 2.249 \times 10^{-3} \times 16.042}{\left(1 + \frac{200}{21}\right) \times 380 \times 8.314} = 0.434 \text{ g} \tag{4.9}$$

4.4.3 Data Filtering

4.4.3.1 Introduction

In all experimental data there will exist a certain amount of 'noise' that is of no interest. Additionally, the differentiation required by Equation (4.2) and the interpolation will cause numerical noise. Too much noise will obscure the trends which are useful in selecting data to be used in the future fitting correlation. It is therefore necessary to filter these data to remove any unwanted noise but still keeping the overall trend.

This section describes the five steps in the calculation where smoothing or filtering is applied to:

1. The pressure trace recorded by LabView, as it is used as the basis of the interpolation of unburned gas temperature (T_u), mass fraction burned (*mfb*), the ratio of specific heats (gamma, γ_u), flame radius (r_f); and it is also featuring in the burning velocity and heat release rate calculations;
2. The OH* / CH* voltage measurements recorded by LabView; not only because any noise caused by the HT from the spark should be eliminated, but also it is vital in the calculation of normalised OH* / CH* chemiluminescence intensities;

3. The rate of mass fraction burned change ($\frac{\mathrm{d}mfb}{\mathrm{d}t}$), and the rate of pressure change ($\frac{\mathrm{d}p}{\mathrm{d}t}$), since they are differentiated, and this generates numerical noise;
4. The flame radius (r_f), because it is used as the basis for the interpolation of area collection efficiency (η) from the optical model;
5. The radius prior to combustion (r_i) can also be targeted, since this has to be differentiated.

This section will mainly focus on the previous two points. Details about other three points can be found in Marshall [3].

4.4.3.2 Filtering the Pressure Trace

As the bomb pressure is measured using a piezoelectric pressure sensor, the experimental pressure will be always the pressure above the initial pressure. Therefore to obtain the absolute pressure the initial pressure needs to be added. However, the pressure record does not normally start at zero, due to small offsets in the charge amplifier and the calibration curve of the pressure transducer. Besides, the first pressure value cannot be regarded as the datum pressure (p_datum); this is because HT interference from the spark causes noise so that the first data point is always higher than the subsequent data. Accordingly, the datum pressure is taken as the mean of the pressure values between 5 and 6 ms, when the datum pressure has settled down. After that time there will be a pressure rise due to combustion. Therefore to convert experimental pressure record to absolute pressures, the initial pressure (by subtraction from the datum pressure of the measurements) is added, i.e.

$$p_{0,\mathrm{act}} = p_0 - p_\mathrm{datum} \tag{4.10}$$

and

$$p = p + p_{0,\mathrm{act}} \tag{4.11}$$

The pressure data after the peak pressure is discarded because the flame front reaches the inner surface of the bomb so that heat transfer makes the process non-adiabatic, so the data are of no interest. Accordingly, the corresponding OH* / CH* data are also discarded.

The pressure trace is then passed through a low-pass filter. There are many MATLAB filtering techniques available; from the Butterworth type to more complex filters such as the Chebyshev and elliptic filters. A fourth-order Butterworth filter with a normalised cut-off frequency of 0.1 is sufficient to be applied to the pressure data. This means that the pass-band cut-off frequency is one tenth of the Nyquist frequency, which is defined as one-half of the sampling rate. The normalised cut-off frequency is always in the interval $0 \leq f \leq 1$. In this case, with a sampling rate of 10 kHz, the Nyquist frequency is 5 kHz and the cut-off frequency is 500 Hz. Figure 4.2 is a plot that shows the effect of applying filtering to the experimental pressure trace, and the noise of pressure trace is quantified by subtracting the filtered pressure trace from the original pressure record. This is an iso-octane experiment with an initial temperature of 380 K, initial pressure of 3 bar, equivalence ratio of 1.0 and no residuals.

As can be seen from Figure 4.2, there are two significant observations worth noting. Firstly, the experimental pressure trace from the bomb is smooth, which is as expected. Secondly, the curve of pressure difference is nice and flat after 2 ms, and it is centred at zero after 10 ms, which means that the filter employed removes the unwanted noise but keeps the overall trend of the pressure trace. In conclusion, the current numerical filter is able to eliminate the noise.

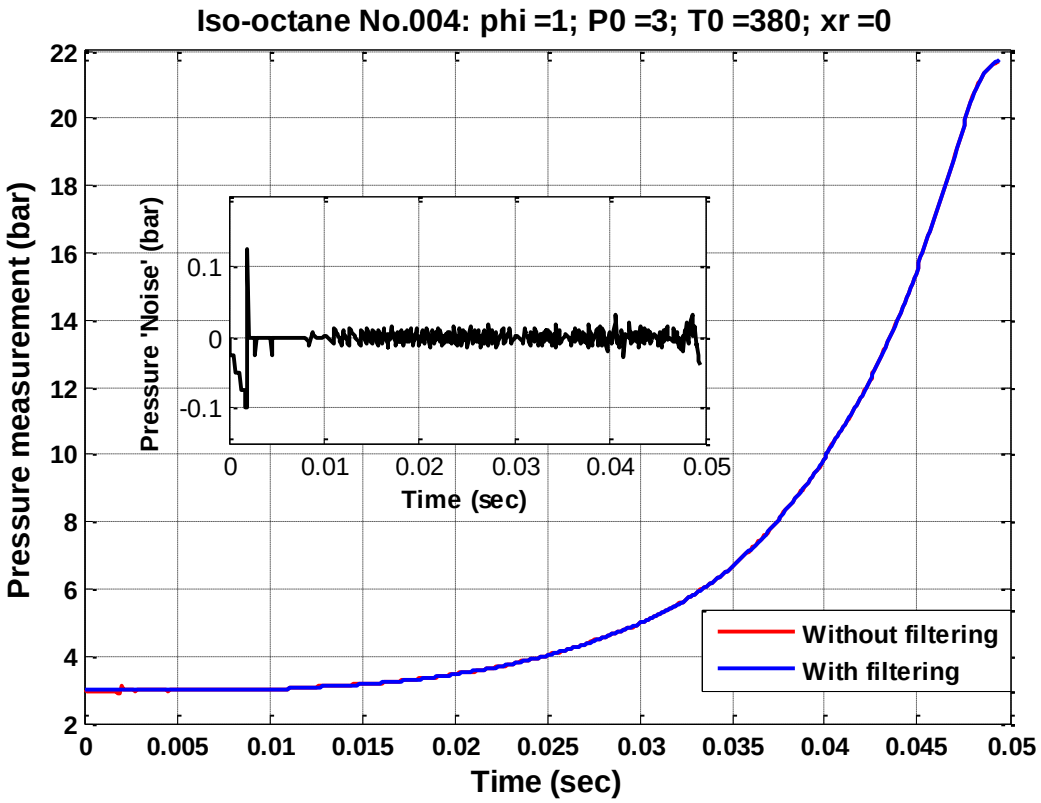


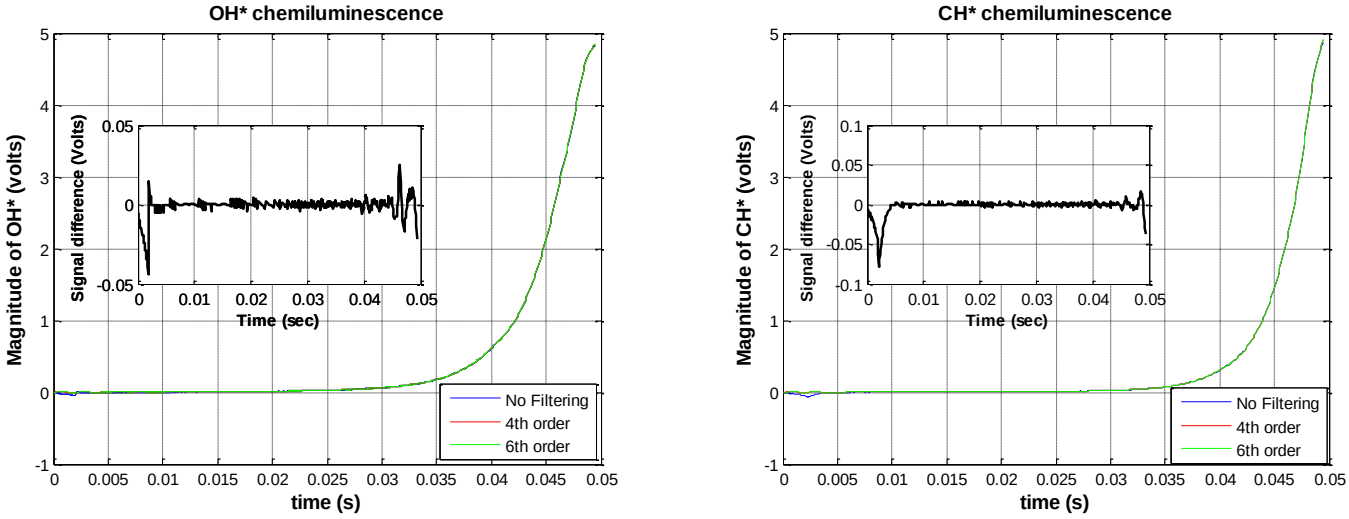
Figure 4. 2 Applying Butterworth filtering to the experimental pressure trace. Pressure 'noise' is obtained by subtracting the filtered pressure data from the original pressure record.

4.4.3.3 Filtering the OH* / CH* Measurements

Both the OH* and CH* signals have a typical 2-4 ms negative voltage spike (see Figure 4.3), which is caused by electromagnetic interference from the High Tension system. Hence the reference voltage is taken as a mean of the voltage measurement taken between 5 and 6 ms.

As can be seen from Figure 4.3 (where the iso-octane experiment has the same initial condition as has been used in Figure 4.2), the filter performs well and a fourth-order Butterworth filter is sufficient to eliminate most of the noise (the results for the sixth-order Butterworth filter are indistinguishable from a fourth-order's results). It can be further verified by looking at the signal differences, which are basically centred at zero. Although the OH* voltage difference after 45 ms is tending to increase, the relative error (relative to the

signal magnitude) is about 0.5 %, which is not a huge source of error. Therefore, a fourth-order Butterworth filter with a normalised cut-off frequency of 0.1 is used on the OH* and CH* chemiluminescence measurements, and another fourth-order MATLAB *butter* function with a 0.07 normalised cut-off frequency is employed on the rate of change of mass fraction burned ($\frac{\mathrm{d}mfb}{\mathrm{d}t}$), the rate of pressure change ($\frac{\mathrm{d}p}{\mathrm{d}t}$), the flame radius ($r_\mathrm{f}$), and the radius prior to combustion (r_i).



(a) (b)

Figure 4. 3 Original OH* / CH* traces versus that filtered using the MATLAB *butter* function for a fourth order Butterworth filter. 'Noise' associated with the chemiluminescence is obtained by subtracting the filtered data from the original measurements.

4.4.4 Interpolation

The *normin* program matches up the experimental pressure data with that in the *zone* file, where pressure and other parameters are tabulated against mass fraction burned. This is then used to interpolate a value of unburned gas temperature (T_u), mass fraction burned (*mfb*), the specific heat ratio (γ_u), and flame radius (r_f) for each experimental pressure data. The *interp1* MATLAB command is provided to implement the linear interpolation. The interpolated mass fraction burned is then differentiated to generate the rate of mass fraction burned change

($\frac{\mathrm{d}mfb}{\mathrm{d}t}$). The program used the MATLAB script *gradient*, which returns the one-dimensional numerical gradient of *mfb* ($\frac{\mathrm{d}mfb}{\mathrm{d}x}$), i.e.

$$\frac{\mathrm{d}mfb}{\mathrm{d}t} = \frac{\mathrm{d}mfb}{\mathrm{d}x} \cdot \frac{\mathrm{d}x}{\mathrm{d}t} = sampling\ rate \cdot gradient(mfb) \tag{4.12}$$

Any artefacts associated with mass fraction burned rate $\frac{\mathrm{d}mfb}{\mathrm{d}t}$, either by means of interpolation or by means of numerical differentiation, were eliminated by the above mentioned filtering technique.

Similarly, the MATLAB code compares the flame radius (r_f) data with those in the optical model; then another interpolation is used to generate the area collection efficiency for each flame radius.

4.4.5 Calculation of Rate of Heat Release

The rate of heat release is used in other studies of chemiluminescence, so for completeness it is also computed here. By definition it is a less rigorous calculation than the calculation of the mass fraction burned. The rate of heat release (*RoHR*) is calculated on the basis of the first law of thermodynamics for a quasi-static system, i.e. with uniform pressure and mean temperature at any instant in time. According to the first law of thermodynamics,

$$\mathrm{d}U = \mathrm{d}Q - \mathrm{d}W \tag{4.13}$$

where dU represents change in internal energy, dQ stands for heat added to the system, and dW means the work done by the system. When a system expands in a quasi-static process, the work done by the system on the environment is pdV.

Next, bear in mind that vessel is constant volume, hence

$$W_{1-2} = \int_1^2 p\mathrm{d}V = 0 \tag{4.14}$$

$$\mathrm{d}U = \mathrm{d}Q \tag{4.15}$$

By assuming a single zone at a uniform temperature, then according to the ideal gas law,

$$p \cdot V = m \cdot \frac{R}{M} \cdot T = m \cdot R_{\text{specific}} \cdot T \tag{4.16}$$

The specific gas constant R_{specific} is related to the specific heats of the gas by:

$$R_{\text{specific}} = c_{\text{p}} - c_{\text{v}} \tag{4.17}$$

where c_{p} denotes specific heat at constant pressure, c_{v} represents specific heat at constant volume, and $\gamma = c_{\text{p}}/c_{\text{v}}$ is the specific heat ratio. Taking the derivative on both sides of equation (4.16), for a constant volume reaction, it will yield:

$$m \cdot \mathrm{d}T = \frac{1}{R_{\text{specific}}} \cdot (p\mathrm{d}V + V\mathrm{d}p) = \frac{1}{R_{\text{specific}}} \cdot V\mathrm{d}p \tag{4.18}$$

The internal energy change dU at constant volume is determined by:

$$\mathrm{d}U = \mathrm{d}Q = c_{\text{v}} \cdot m \cdot \mathrm{d}T \tag{4.19}$$

Combing equations (4.18) and (4.19) will lead to

$$\mathrm{d}Q = \frac{1}{\gamma - 1} \cdot V \cdot \mathrm{d}p \tag{4.20}$$

and finally:

$$RoHR = \frac{\mathrm{d}Q}{\mathrm{d}t} = \frac{1}{\gamma - 1} \cdot V \cdot \frac{\mathrm{d}p}{\mathrm{d}t} \tag{4.21}$$

As with the calculation of rate of change of mass fraction burned ($\frac{\mathrm{d}mfb}{\mathrm{d}x}$), the MATLAB script *gradient* returns the one-dimensional numerical gradient of *p*, i.e.

$$\frac{\mathrm{d}p}{\mathrm{d}t} = \frac{\mathrm{d}p}{\mathrm{d}x} \cdot \frac{\mathrm{d}x}{\mathrm{d}t} = sampling\ rate \cdot gradient(p) \tag{4.22}$$

4.4.6 Concatenating and Saving the Data

For each experimental file, three graphs are generated, i.e. a plot of normalised OH* / CH* chemiluminescence against mass fraction burned (*mfb*), a graph of laminar burning velocity versus pressure, and a truncated plot of the OH* / CH* signals as a function of mass fraction

burned (*mfb*). The program *normin* allows the user to select which data are of particular interest and to be used in the subsequent fitting correlation. This is achieved by choosing the region from the laminar burning velocity plot.

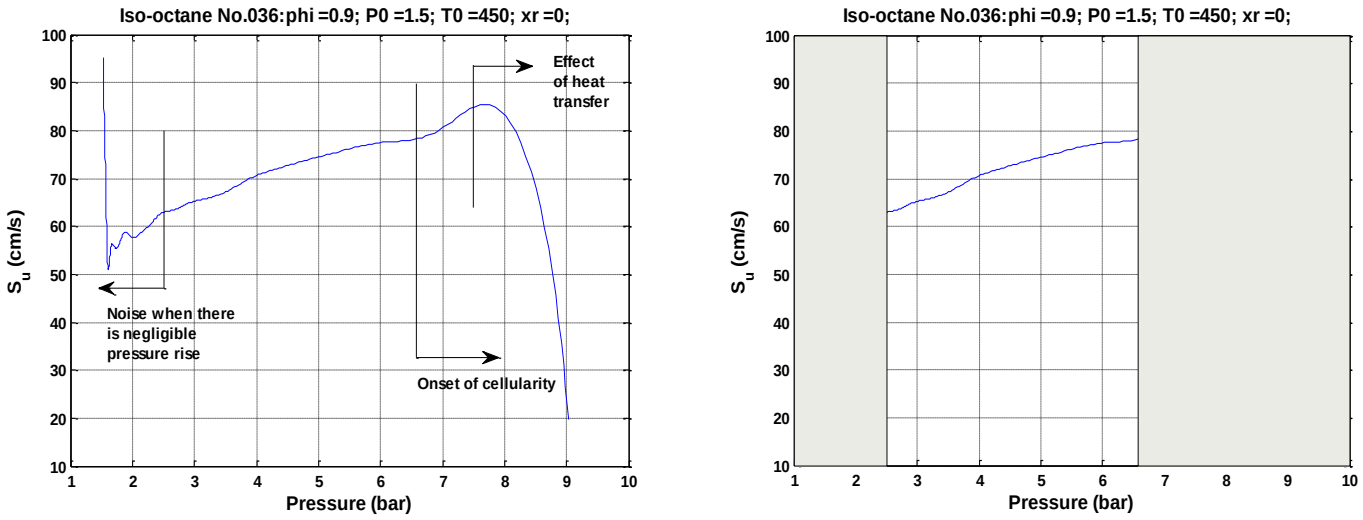
As has been considered previously, one of the objectives of this project is to determine the feasibility of using normalised OH* and CH* chemiluminescence as active-control parameters for premixed flames. For this purpose, chemiluminescence is to be normalised against the mass of fuel burned rate. Based on the assumption that the mixture is fully evaporated and created homogeneously, the mass of fuel burned rate ($\frac{\mathrm{d}m_\mathrm{f}}{\mathrm{d}t}$) is proportional to the mass burned rate in the bomb ($\frac{\mathrm{d}m}{\mathrm{d}t}$) for any known initial condition (i.e. specified p_0, T_0, Φ, and x_r); and the burned rate of the mass of gas in the bomb ($\frac{\mathrm{d}m}{\mathrm{d}t}$) is related to the laminar burning velocity:

$$S_\mathrm{u} = \frac{m}{A_\mathrm{f}\rho_\mathrm{u}} \cdot \frac{\mathrm{d}mfb}{\mathrm{d}t} = \frac{1}{A_\mathrm{f}\rho_\mathrm{u}} \cdot \frac{\mathrm{d}m}{\mathrm{d}t} \tag{4.23}$$

where m represents the mass of gas in the bomb, ρ_u is the (unburned) gas density, and A_f is the area of the flame front. Therefore study of the laminar burning velocity is closely related to the normalised chemiluminescence. It is not necessary to pay attention to the chemiluminescence data where the corresponding laminar burning velocity is not valid and of no interest.

The user then needs to select the data of particular interest by removing the start data points (whose data is noisy at low pressures) and the end data points (which are affected by heat transfer to the bomb). Meanwhile it is also not recommended to select data after the onset of cellularity when the burning velocity data is not valid. Marshall [3], who also had schlieren data, noted that 'the calculated burning velocity rapidly rises, corresponding to the onset of cellularity', and this allowed the onset of cellularity to be identified.

Using the iso-octane experiment with an initial temperature of 450 K, initial pressure of 1.5 bar, equivalence ratio of 0.9 and no residuals as a typical example, the laminar burning velocity plot is shown in Figure 4.4a. Once the lower and higher limits are chosen, the areas to the left hand side and to the right hand side become grey; this is shown in Figure 4.4b.



(a) (b)

Figure 4. 4 Example of a graph of laminar burning velocity. The lower limit and higher limit have been chosen by the user; hence the regions outside of these are grey in Figure 4.4b.

Correspondingly, the normalised CH* / OH* data of interest is plotted as a function of mass fraction burned (*mfb*), which is shown in Figure 4.5.

Next, all the truncated data is concatenated in a large *output_matrix*, containing:

1. Laminar burning velocity (S_u, in cm/s);
2. Pressure (p, in bar);
3. Unburned gas temperature (T_u, in K);
4. Mass fraction burned (*mfb*);
5. Rate of change of mass fraction burned ($\frac{\mathrm{d}mfb}{\mathrm{d}t}$, in s^{-1});
6. Flame radius (r_f, in cm);
7. Voltage of OH* (V_{OH^*}, in volts);
8. Voltage of CH* (V_{CH^*}, in volts);

9. Normalised OH* chemiluminescence intensity ($I^{+}_{OH^*}$, in J/g);

10. Normalised CH* chemiluminescence intensity ($I^{+}_{CH^*}$, in J/g);

11. OH* collection efficiency (η_{OH^*});

12. CH* collection efficiency (η_{CH^*});

13. Equivalence ratio (Φ);

14. Initial pressure (p_0, in bar);

15. Initial temperature (T_u, in K);

16. Residuals molar fraction (x_r);

17. Time (t, in s);

18. Stretch rate (α, in s^{-1});

19. Rate of Heat Release ($RoHR$, in kW)

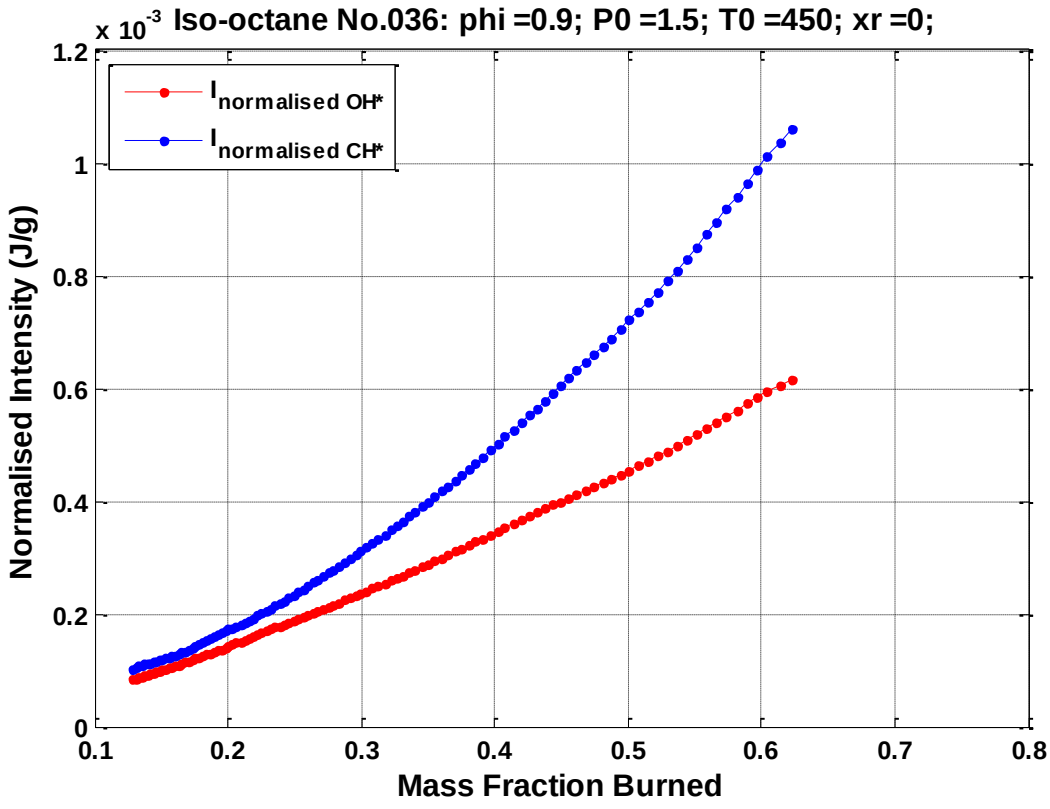


Figure 4. 5 Normalised OH* and CH* chemiluminescence (unit: J/g) of interest as a function of mass fraction burned for the data selected in Figure 4.4b.

The *output_matrix* is saved by the *normin* program both in the format of an Excel file and in the format of the MATLAB MAT-file. Then the data is sent back to the parent program *nical*. This process is repeated for each experiment in the experimental summary spreadsheet.

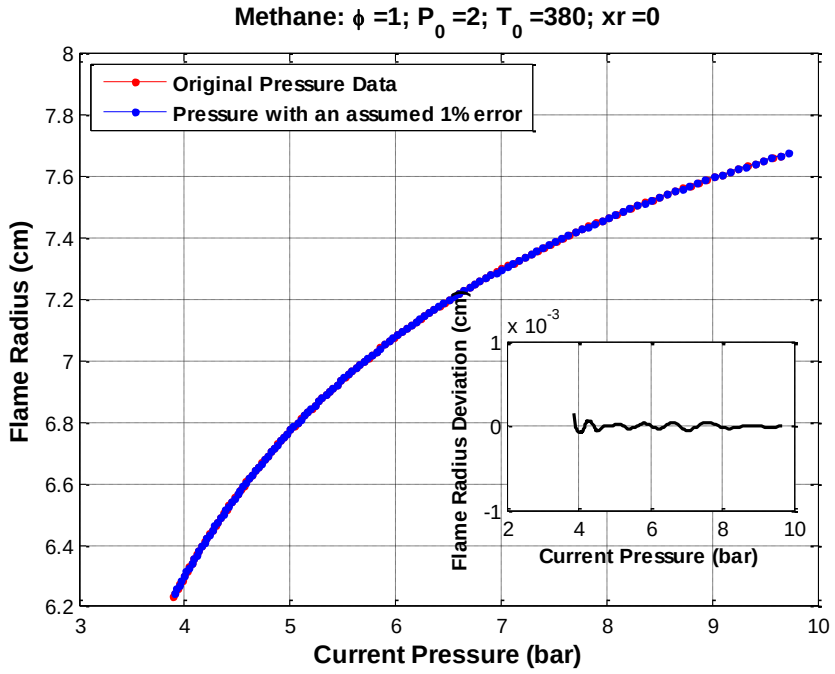
4.5 Discussion of Errors

In this section, the uncertainties in the measured quantities, especially the normalized OH* and CH*chemiluminescence, are outlined. There are three significant possible errors in the measurements: the measurement and calibration of the PMTs, the measurement of the equivalence ratio and the measurement of pressure during combustion. The excitation voltage on the PMTs was kept constant, but the amplifier gain was changed. The calibration of the photomultiplier tubes has been discussed in Section 3.5.

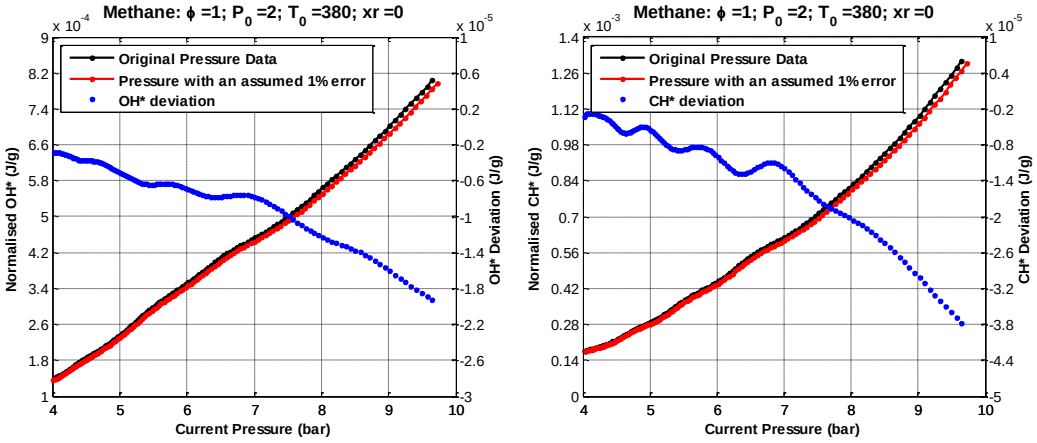
For the lambda sensor, the manufacturer claims a worst case performance of ± 0.014 for the equivalence ratio. Tests were conducted with two calibration gases, 6.29 ±0.13% O_2 (balance nitrogen) for which the lambda sensor reported 6.09% O_2, and an 'MOT' mix that represented the rich products of combustion – 14.02% CO_2, 3.52% CO, 0.1965% C_3H_8 (balance nitrogen). A computation of the corresponding equivalence ratio (see Appendix A) yields an equivalence ratio of 1.125 while the measured value was 1.08. The compositional tolerance for the MOT mix is 2% and this could account for a major part of the discrepancy, though there is some evidence that the accuracy is lower than claimed by the manufacturer for rich mixtures; there is a fuller discussion in Appendix A. The uncertainty in the measured equivalence ratio is probably less than ± 0.02.

Errors in the pressure measurement lead to errors in the computation of the flame radius, mass fraction burned and the normalised chemiluminescence intensities. The pressure transducer had been calibrated as a pair with its charge amplifier and the accuracy is better

than 1%. As an indicator of the systematic error, a typical stoichiometric methane / air mixture with an initial condition of 2 bar and 380 K was checked; the results of a sensitivity study with an assumed 1% error are used here to illustrate the effect of errors in the pressure measurement on the computed flame radius (Figure 4.6a) and the normalised chemiluminescence intensities (Figure 4.6b, c).



(a)



(b) (c)

Figure 4. 6 Sensitivity study with an assumed 1% error to illustrate the effect of errors in the pressure measurement from stoichiometric methane / air flames with p_0 = 2 bar and T_0 = 380 K on the computed flame radius (Figure 4.6a) and the normalised chemiluminescence intensities (Figure 4.6b, c).

As can be seen in Figure 4.6, the computed flame radius from the pressure measurements is indistinguishable from that derived from the pressure with an assumed 1% error. Meanwhile the variation of normalised OH* intensity is within 3%, (as was the CH* normalised intensity); therefore, the systematic errors arising from the pressure measurement are assumed to be small.

Repeatability tests were undertaken on a number of occasions, and some typical results are presented later in Figure 6.1 and in Figure 7.20 in the context of the final spectroscopic measurements. The nature of the regression analysis makes it difficult to quantify the effect of errors. Random errors will tend to be averaged out but systematic errors (such as those discussed above) will be propagated.

4.6 Conclusion

In summary, the above sections have outlined a number of programs written to analyse the normalised CH* / OH* chemiluminescence intensity data. *NIICS* (Normalised Intensity Integrated Calculation System) covers a series of calculations as follow:

- Firstly, it allows the analysis code to read the experimental summary spreadsheet, and fetch the corresponding experimental file and *zone* file.
- Secondly, the optical data are only dependent on the experiment geometry so they do not vary with different experiments.
- Next, the *normin* program can be run to get the normalised OH* / CH* intensity.
- Finally, the rate of heat release rate can be calculated and *normin* program allows users to concatenate and save the data.

Chapter 5 Correlation of the CH*/OH* Chemiluminescence Ratio

The CH*/OH* chemiluminescence ratio has been found to be useful for combustion sensing and diagnostic applications in various flames. This chapter presents a mathematical formulation for CH*/OH* chemiluminescence ratio as a function of unburned gas temperature, operating pressure, and equivalence ratio. It then probes the feasibility of using the CH*/OH* chemiluminescence ratio as an active control for laminar premixed combustion. Two fuels, i.e. methane and iso-octane, are investigated in this chapter since they are highly engine relevant.

5.1 Overview

Many researchers have shown that the chemiluminescence of flame species such as CH*, OH*, C_2*, and CO_2 can be used as a qualitative and/or quantitative combustion diagnostic tool [13, 16, 17, 19, 47, 48, 49]. Their purpose is to obtain experimental data and to investigate experimentally and/or numerically the possibility of developing an active-control system for the flame. Active control can be realized if the following criteria are met: (1) there is a direct correlation between chemiluminescence, equivalence ratio [48, 49] and heat release [13, 16, 21, 22, 48]; (2) a relationship between these variables can be developed that includes mass flow rate, operating pressure [47].

The CH*/OH* chemiluminescence ratio has been found to be useful for sensing the equivalence ratio in various flames [17, 48, 51, 52], but only at certain pressure and reactant temperature conditions. Although Muruganandam et al. [52] proposed a 'universal relationship between CH*/OH* and Φ' for various conditions, they only presented their results graphically with no accurate mathematical formulation. Thus this chapter parametrically examines the usefulness of the CH*/OH* chemiluminescence ratio as a diagnostic tool for combustion processes over a wide range of combustion conditions:

equivalence ratio in the range 0.8 to 1.1, pressure in the range 0.5 to 20 bar, and unburned gas temperature in the range 450 to 600 K. Two fuels, i.e. methane and iso-octane, are of particular interest since they have been widely used in many combustion systems, for example, stationary gas turbines and spark ignition engines.

This functional relationship is deduced by two separate but closely interrelated processes: curve fitting and correlation. The curve fitting analysis is to fit experimental data to a mathematical equation that describes the behaviour; this is also called regression analysis. Correlation analysis is a procedure for determining the extent to which the variables are related. The aim of the curve fitting and correlation analysis is to find a suitable regression line, parameter estimates (regression analysis) and to measure the goodness of fit (correlation analysis).

In this section, a sequential correlation and regression analysis is employed to identify the relationship between the dependent variable (i.e. the normalised CH*/OH* ratio) and three independent variables (i.e. unburned gas temperature, operating pressure, and equivalence ratio). During this process, the correlation coefficients between two variables are examined to measure the degree of dependence. This successive regression analysis gives a multi-variate functional curve fitting form and preliminary values for the correlation coefficients (in Equation (5.8)). The details of the curve fitting and correlation will be illustrated in Section 5.2.

As the above-mentioned multi-variate functional curve fitting form is initially posed as a hypothesis concerning the relationship among the dependent and independent variables, a minimization method is used for developing estimates of the multi-variate regression model parameters. Hence there is a description of the minimisation method in Section 5.3.

Finally, Section 5.4 gives the current functional forms to fit the measurements for methane and iso-octane respectively, followed by an investigation of the CH*/OH* chemiluminescence ratio as an indicator of the equivalence ratio in Section 5.5.

5.2 Curve Fitting and Correlation

5.2.1 Introduction

Many pioneer works have studied the CH* and OH* chemiluminescence emitted during combustion, and have assessed the potential of the CH*/OH* chemiluminescence ratio as an active–control feedback parameter. Higgins et al. [17] conducted experiments and reported the effect of pressure and strain rate on the CH* chemiluminescence of premixed fuel-lean methane / air flames in a Bunsen burner. They found a relation between the ratio of the OH*/CH* chemiluminescence, the pressure and the equivalence ratio, but without a temperature effect. Nori et al. [70] analysed the chemiluminescence in methane and Jet-A fuel combustion. They reported that the CH*/OH* ratio monotonically increases with equivalence ratio from 0.7 to at least 1.3 and is only a weak function of preheating for methane flames; for Jet-A fuel, the ratio is shown to be non-monotonic. However they did not study the pressure effect. A subsequent work developed by Nori et al. [7] graphically studied the effects of pressure, preheat and strain on the chemiluminescence sensing in methane / air combustion, but they did not provide a mathematical formulation. Most recently, Tinaut et al. [48] focused on the measurements of OH* and CH* chemiluminescence in premixed flames in a constant volume combustion bomb and they verified the relationship between the OH*/CH* chemiluminescence ratio and the equivalence ratio, but without considering other affecting factors, such as temperature and pressure. In sum, many researchers investigated CH*/OH* ratio graphically under limited conditions; hence there is a need to study CH*/OH* ratio mathematically over a wide range of combustion conditions from the

premixed combustion of methane and iso-octane with air in a well-controlled combustion bomb.

Factors affecting chemiluminescence have been reduced to: pressure, equivalence ratio, temperature, stretch rate and the consumption of fuel [17]. Strain rate is shown to have no significant effect on chemiluminescence [17] (and Chapter 6 reveals that the stretch rate in the current tests is very low). Furthermore, the CH* / OH* chemiluminescence data are normalised in the current work against mass of fuel burned rate (see Equation (4.1)). Based on what has been considered previously, this section extends the correlation of CH*/OH* ratio as a function of unburned gas temperature, operating pressure and equivalence ratio, but using absolute measurements that have been normalised for the mass of fuel burned rate. In addition, it should be pointed out that this section will develop the mathematical curve fitting model using methane data. The procedures with iso-octane for curve fitting and correlation are the same, so these will not be discussed in detail in this section.

5.2.2 Choice of Functional Fit

Measurements of the normalised CH*/OH* chemiluminescence ratio for methane / air mixtures are shown in Figure 5.1 as a function of unburned gas temperature T_u for the equivalence ratio Φ = 0.9, 1.0, and 1.1 at the specified initial temperature T_0 = 380 K. At each equivalence ratio, there are three sets of points along the unburned gas isentropes starting at the initial pressures p_0 = 1.0, 2.0, and 4.0 bar respectively. Because the unburned gas temperature T_u and operating pressure p_u are correlated along an unburned gas isentrope, the effects of pressure and temperature then can be decoupled by varying the initial pressure and/or initial temperature. In addition, it is worth noting that each isentrope includes overlapping points from two runs, the first starting at the specified initial temperature T_0 = 380 K and the second one at T_0 = 450 K which is not shown in the figure. For example,

at stoichiometric, 1 bar/380 K and 2 bar / 450 K the isentrope curves are close to overlapping. Another thing worth mentioning is that only one in every ten data points from the experimental data sets are plotted in Figure 5.1.

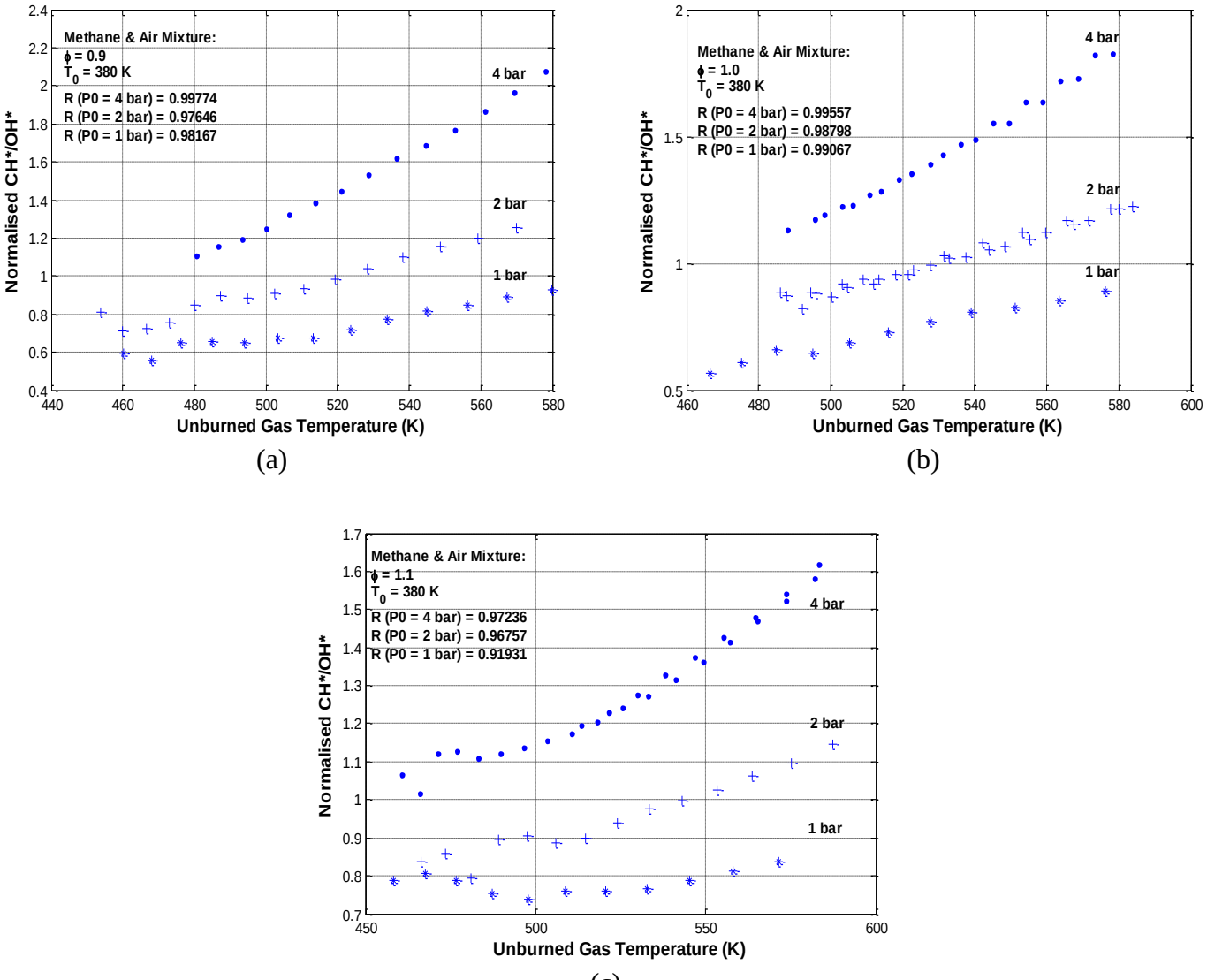


Figure 5. 1 Normalised CH*/OH* ratio of methane-air mixtures for equivalence ratios Φ = 0.9, 1.0, and 1.1, along unburned gas isentropes at T_0 = 380 K and p_0 = 1.0, 2.0, and 4.0 bar. R is Pearson's correlation coefficient to assess how closely different variables are interdependent.

As has been seen in Figure 5.1, for any fixed equivalence ratio and fixed initial pressure, the CH*/OH* ratio is almost linearly proportional to unburned gas temperature. To assess how much of a linear relationship exists between the CH*/OH* ratio and the unburned

gas temperature, the correlation coefficient is introduced. In MATLAB, a function *corr2* computes Pearson's correlation coefficients (assuming a linear relationship) using:

$$R = \frac{\sum_{i=1}^{n}(x_i-\bar{x})\cdot(y_i-\bar{y})}{\sqrt{\sum_{i=1}^{n}(x_i-\bar{x})^2}\cdot\sqrt{\sum_{i=1}^{n}(y_i-\bar{y})^2}} \tag{5.1}$$

where R is the correlation coefficient. x and y are two quantitative, continuous variables, and $\bar{x}$ and $\bar{y}$ are the mean values. The correlation coefficients between the normalised CH*/OH* ratio and unburned gas temperature are shown in the key at the top left of Figure 5.1, which reflects the high degree of linear association between them. Although the R value of 0.919 at p_0 = 1.0, Φ = 1.1 indicates a not perfect linear correlation between these two variables, further investigation shows that the assumption of a linear dependence on the unburned gas temperature is not a major source of error. Hence the measured CH*/OH* ratio in Figure 5.1 has been fitted by the following functional form:

$$\frac{\mathrm{CH^*}}{\mathrm{OH^*}} = f(P,\phi)\cdot(\alpha T+\beta) \tag{5.2}$$

where:

$$T = \frac{T_u}{298},\ P = \frac{p_u}{1.0} \tag{5.3}$$

T_0 = 298 K and p_0 = 1.0 bar are the reference temperature and pressure; and f (P, Φ) will be expressed in Equation (5.4). This multiple regression determines the parameters of the linear relationship between CH*/OH* ratio and the unburned gas temperature. Additionally, as has been mentioned before, T_u and p are correlated along an unburned gas isentrope, therefore the parameters α and β depend on the multiple regression expressed in Equation (5.2) to fit the measurements instead of the term $(\alpha T+\beta)$.

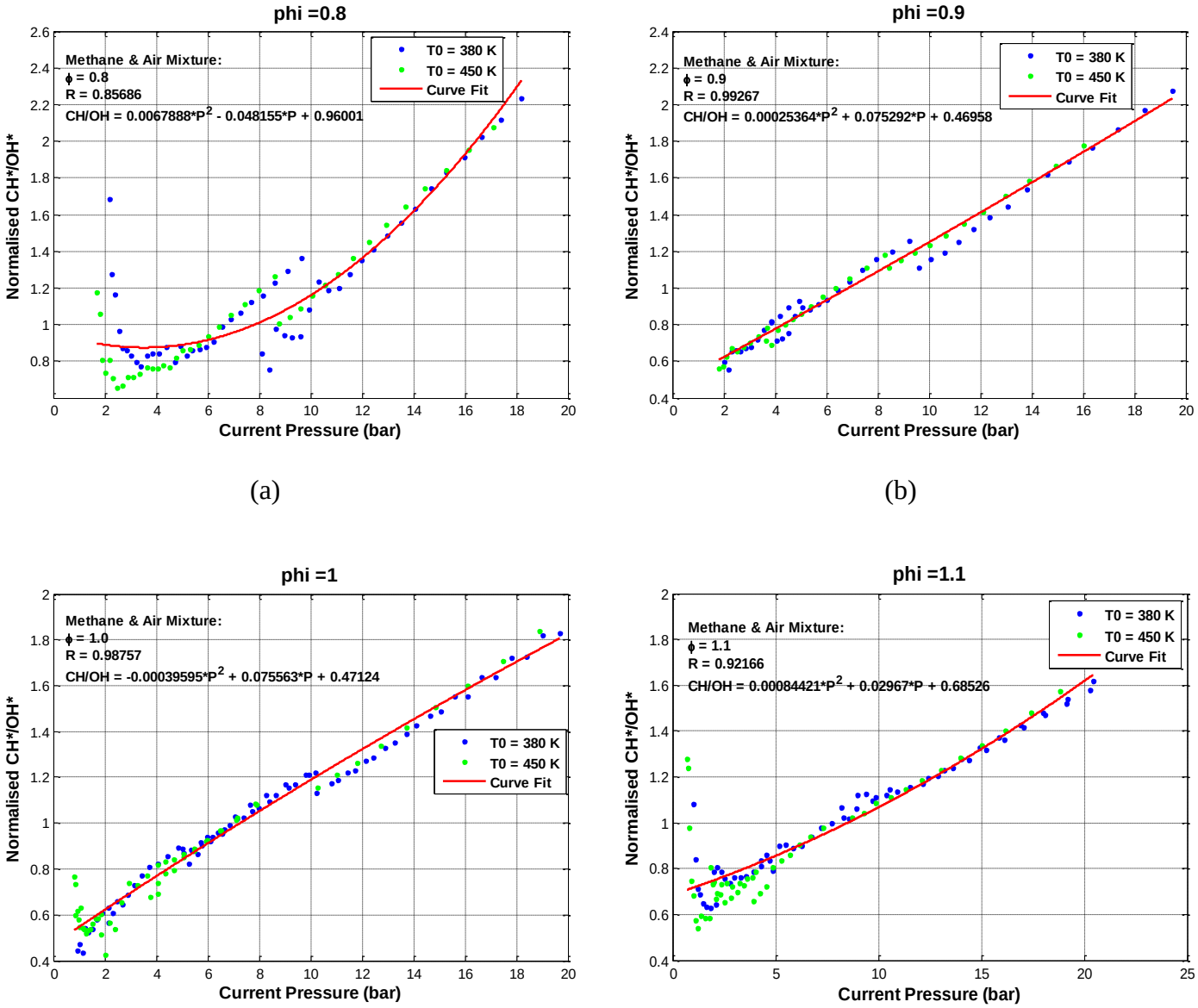


Figure 5. 2 Dependence of the normalised CH*/OH* ratio for mixtures of methane with air on the operating pressure for equivalence ratios Φ = 0.8, 0.9, 1.0, and 1.1, along unburned gas isentropes starting at values of T_0 = 380 K or 450 K and p_0 = 1.0, 2.0, and 4.0 bar. The curves show the least square fit of Equation (5.4) to the points. R is a measure of the degree of linear relationship between CH*/OH* ratio and the pressure.

The effect of pressure on the ratio of CH*/OH* chemiluminescence can be seen by plotting the data from Figure 5.1 (as well as data at T_0 = 450 K) versus pressure for equivalence ratios Φ = 0.9, 1.0, and 1.1 at the specified initial temperatures of T_0 = 380 K and 450 K, which is shown in Figure 5.2. There are several observations to be made from Figure

5.2. Firstly, for any fixed equivalence ratio, the CH*/OH* ratio increases with increasing operating pressures. Secondly, data at T_0 = 380 K and T_0 = 450 K are highly overlapped (the points in blue are close to being indistinguishable from those in green), which means the CH*/OH* ratio is a weak function of the initial temperature. In fact, the effect of unburned gas temperature is also less pronounced, which can be further verified by Table 5.1. Accordingly it is regarded as a constant factor in this chemiluminescence-pressure dependence analysis. Thirdly, it can be seen that the Pearson correlation coefficients at Φ = 0.9, 1.0, and 1.1 are pretty close to unity, (0.993, 0.988, and 0.922 respectively), which indicates a strong positive linear correlation between the ratio of CH*/OH* and operating pressure. However, when extending the data set to include Φ = 0.8, the correlation coefficient is 0.857, which is not as linear as expected. Hence the points for methane at a fixed equivalence ratio have been fitted by a second-order polynomial of the form:

$$\frac{\mathrm{CH^*/OH^*}}{f(T)} = a \cdot P^2 + b \cdot P + c \tag{5.4}$$

A MATLAB script *polyfit* finds the coefficients of a polynomial that fits the data using a least squares method; while *polyval* returns the value of the polynomial fit.

The polynomial fits are shown by the solid red curves in Figure 5.2. It can be seen that the overall fit is quite good, although there appear to be some small deviations of points from the curves particularly at operating pressures less than 3 bar. It is also worth noting that the coefficients *a*, *b*, *c* are functions of equivalence ratio, which will be discussed next.

Figure 5.3 shows that the coefficients *a*, *b*, *c* from Equation (5.4) are dependent on the equivalence ratio and can be represented by a set of second-order polynomials:

$$a = x_1 \cdot \phi^2 + x_2 \cdot \phi + x_3 \tag{5.5}$$

$$b = x_4 \cdot \phi^2 + x_5 \cdot \phi + x_6 \tag{5.6}$$

$$c = x_7 \cdot \phi^2 + x_8 \cdot \phi + x_9 \tag{5.7}$$

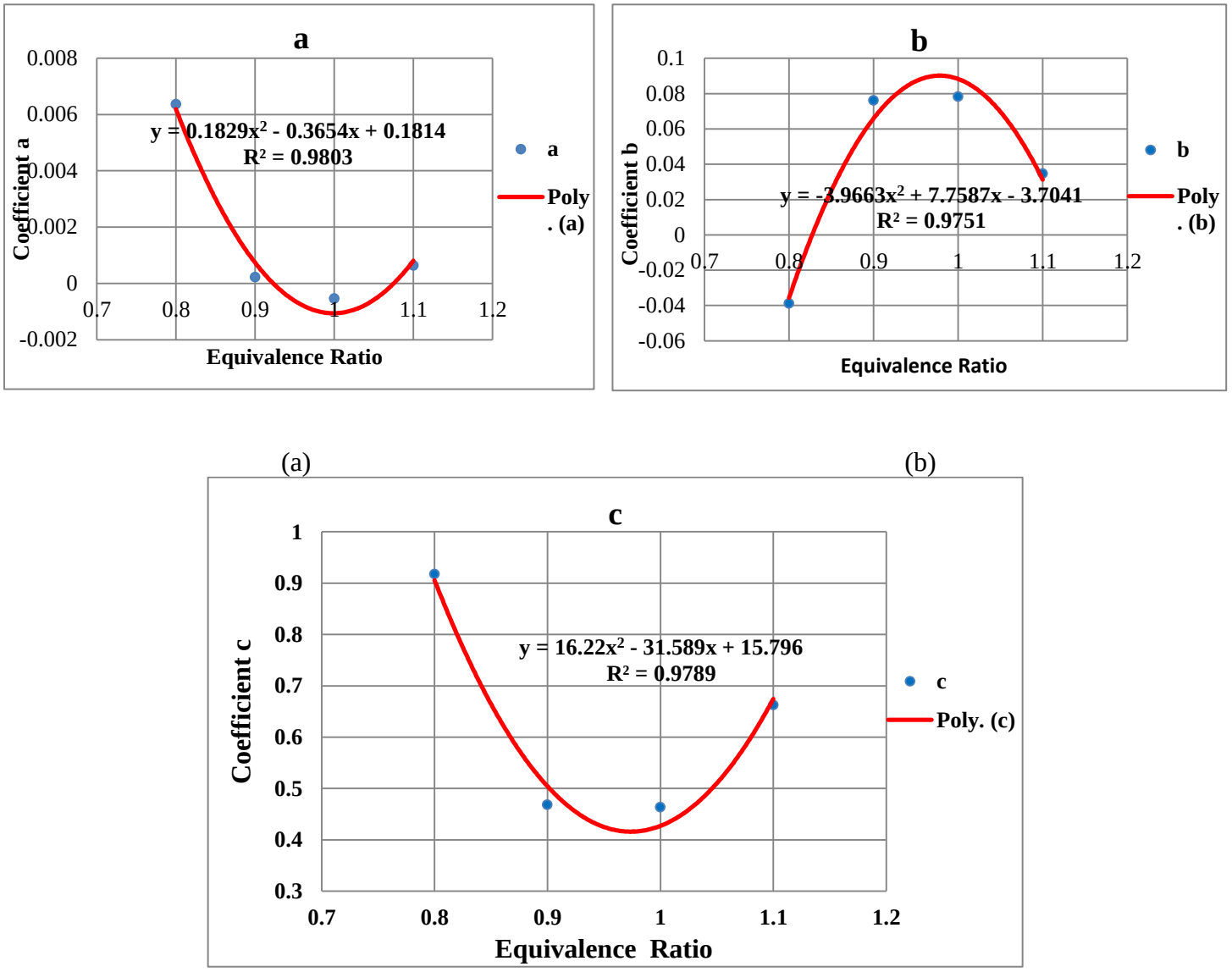


Figure 5. 3 Parameters *a*, *b*, and *c* for methane obtained from least squares fits of Equations (5.5) to (5.7) to data in Figure 5.2.

To find out how good the regression line fits the observations, R-squared (sometimes known as the coefficient of determination) is used as measure of the quality of the regression. For example, if all the observations were on the regression line, then $R^2 = 1$ would indicate a perfect fit. In this case, all three values of R-squared are good, even allowing for the fact that there are only four data points, which indicates that 2nd order polynomial fits well to the data.

In summary, the dependence of the unburned gas temperature, operating pressure and equivalence ratio on the ratio of CH*/OH* for the methane / air mixture can be found with the form of:

$$\frac{\mathrm{CH}^*}{\mathrm{OH}^*} = \{[x_1 \cdot \phi^2 + x_2 \cdot \phi + x_3] \cdot P^2 + [x_4 \cdot \phi^2 + x_5 \cdot \phi + x_6] \cdot P + [x_7 \cdot \phi^2 + x_8 \cdot \phi + x_9]\} \cdot (x_{10} \cdot T + x_{11}) \quad (5.8)$$

Where:

$$T = \frac{T_\mathrm{u}}{298}, P = \frac{p_\mathrm{u}}{1.0} \quad (5.9)$$

5.3 Multi-Variate Minimisation Method

The initial curve fitting has used a successive approach, and this was useful in identifying a suitable functional form. However, to obtain a more rigorous result it is better to fit a combined function for the effect of pressure, temperature and equivalence ratio in a single operation - this is a multi-variate fitting method. The curve fitting and correlation process fits equations to the experimental data. The best-fitting curve, with a minimal deviation from all data points, can be obtained by the method of least squares. The program *CH_OH_fitcorr* fits the eleven-term expression of Equation (5.8) and (5.9) to the data set generated by the *nical* program.

The method of least squares assumes that the best-fit curve of a given type is the curve that has the minimal sum of the deviations squared (least square error) from a given set of data. Unfortunately, the current functional curve fitting in the form of Equation (5.8) is nonlinear in the parameters with more than one control factor (i.e. unburned gas temperature, pressure and equivalence ratio). Therefore this nonlinear function can only be linearized by taking logarithms. To do this, an objective function *CH_OH_error* was created to calculate the sum of the squares of the differences between the natural logarithms of the normalised

CH*/OH* intensity ratio calculated for each experiment (i.e. experimental measurement) and that given by the correlation, given values of the coefficients ($x_1, \ldots, x_{11}$):

$$f = \sum \left(\log \frac{\mathrm{CH^*}}{\mathrm{OH^*}_{\mathrm{corr}}} - \log \frac{\mathrm{CH^*}}{\mathrm{OH^*}_{\mathrm{exp}}} \right)^2 \tag{5.10}$$

The logarithm terms are included to make the equation closer to being linear and it also has the advantage that the square of the percentage errors are minimised. The MATLAB function *fminunc* was then used to perform an unconstrained nonlinear minimisation on this problem, given initial values for the parameters ($x_1, \ldots, x_{11}$) listed in Equation (5.8). Hence it seeks to minimise the error, i.e. fit the correlation to the experimental data. It produces updated values for the parameters as its output. Note that ($x_1, \ldots, x_{11}$) are unknown coefficients; to obtain the least square error, the unknown coefficients must yield zero first derivatives. Hence it is provided with the gradient vector, which is a vector of partial differentials, of the objective function. Without the gradient vector, the *fminunc* function will estimate gradients using finite differences. So for a simple function of three variables:

$$f = f(x, y, z) \tag{5.11}$$

$$g = \begin{bmatrix} \frac{\partial f}{\partial x} \\ \frac{\partial f}{\partial y} \\ \frac{\partial f}{\partial z} \end{bmatrix} \tag{5.12}$$

Fitting an eleven dimensional surface to a huge data set is computationally difficult. To aid the speed of convergence, the minimisation is performed in three stages, with the coefficients produced by each being used as the initial values for the next stage. The three stages are:

1. Only the stoichiometric data is used. The initial values of the coefficients are set to values found from the successive regression analysis (Section 5.2). While ($x_1, \ldots, x_9$) are found from Figure 5.3, (x_{10}, x_{11}) are initialised to be (0, 1). For the methane / air experiments

under study, the initial values of the coefficients are chosen to be (0.1829, -0.3654, 0.1814, -3.9663, 7.7587, -3.7041, 16.22, -31.589, 15.796, 0, 1);

2. One in every ten data points from the data set of experiments is used and the initial values of coefficients are set to values found from previous runs.

3. The eleven coefficient minimisation is performed on the full data set of experiments, using the initial conditions from (2).

To help convergence, for each function to be minimised, the Hessian matrix of the objective function is provided. The Hessian for an unconstrained problem is the matrix of second derivatives of the objective function *f*:

$$H_{\mathrm{ij}} = \frac{\partial^2 f}{\partial x_{\mathrm{i}}\, \partial x_{\mathrm{j}}} \tag{5.13}$$

Once the eleven coefficients have been found, *CH_OH_fitcorr* shows the user a plot of normalised CH*/OH* intensity ratio against pressure or unburned gas temperature. This contains the experimental data as well as the predicted CH*/OH* ratio calculated from the correlation; this is shown in Figure 5.4. *CH_OH_fitcorr* also generate a plot showing the predicted CH*/OH* values versus measurements, and this clearly shows the user how well the correlation has fitted the experimental data; this is shown in Figure 5.5.

5.4 Current Fits for the Fuels of Methane and Iso-octane Mixtures with Air

Fitting the data for the methane / air mixture from Figure 5.2 in the functional form of Equation (5.8) gives values of the eleven coefficients in Table 5.1.

Once the eleven best parameters are estimated, program *CH_OH_fitcorr* allows users to generate a plot of normalised CH*/OH* ratio (both measurements and predicted values) against combustion conditions such as pressure, temperature, and equivalence ratio. For example, Figure 5.4 gives the normalised CH*/OH* ratio as a function of unburned gas temperature for methane / air mixtures. While the measurements are shown in blue (as

already seen in Figure 5.1), the curve fitting of Equation (5.8) to the measurements are shown as red curves.

Table 5. 1 Values of Curve Fitting Coefficients for the Methane / Air Mixture

Coefficients	Values
x_1	0.1140
x_2	-0.2273
x_3	0.1127
x_4	-2.4066
x_5	4.7016
x_6	-2.2421
x_7	9.3166
x_8	-18.1386
x_9	9.0901
x_{10}	-0.0119
x_{11}	1.6500

The quality of this correlation can be visualised in Figure 5.5 by plotting the measured data versus the corresponding values predicted by the curve fit of Equation (5.8). The line with unity slope represents ideal agreement between the curve fit and experimental data. The quality of the correlation fit is indicated by the R-squared values; all of which are relatively good. That is to say, the current curve fit for methane / air mixtures is able to predict CH*/OH* ratio with known unburned gas temperature, pressure and equivalence ratio. Table 5.2 gives the values of R-squared for the current methane / air combustion curve fit.

Table 5. 2 Values of R-squared for the Methane / Air Mixture Curve Fitting

R-squared	$\Phi = 0.8$	$\Phi = 0.9$	$\Phi = 1.0$	$\Phi = 1.1$
R^2	0.94623	0.98265	0.98068	0.97114

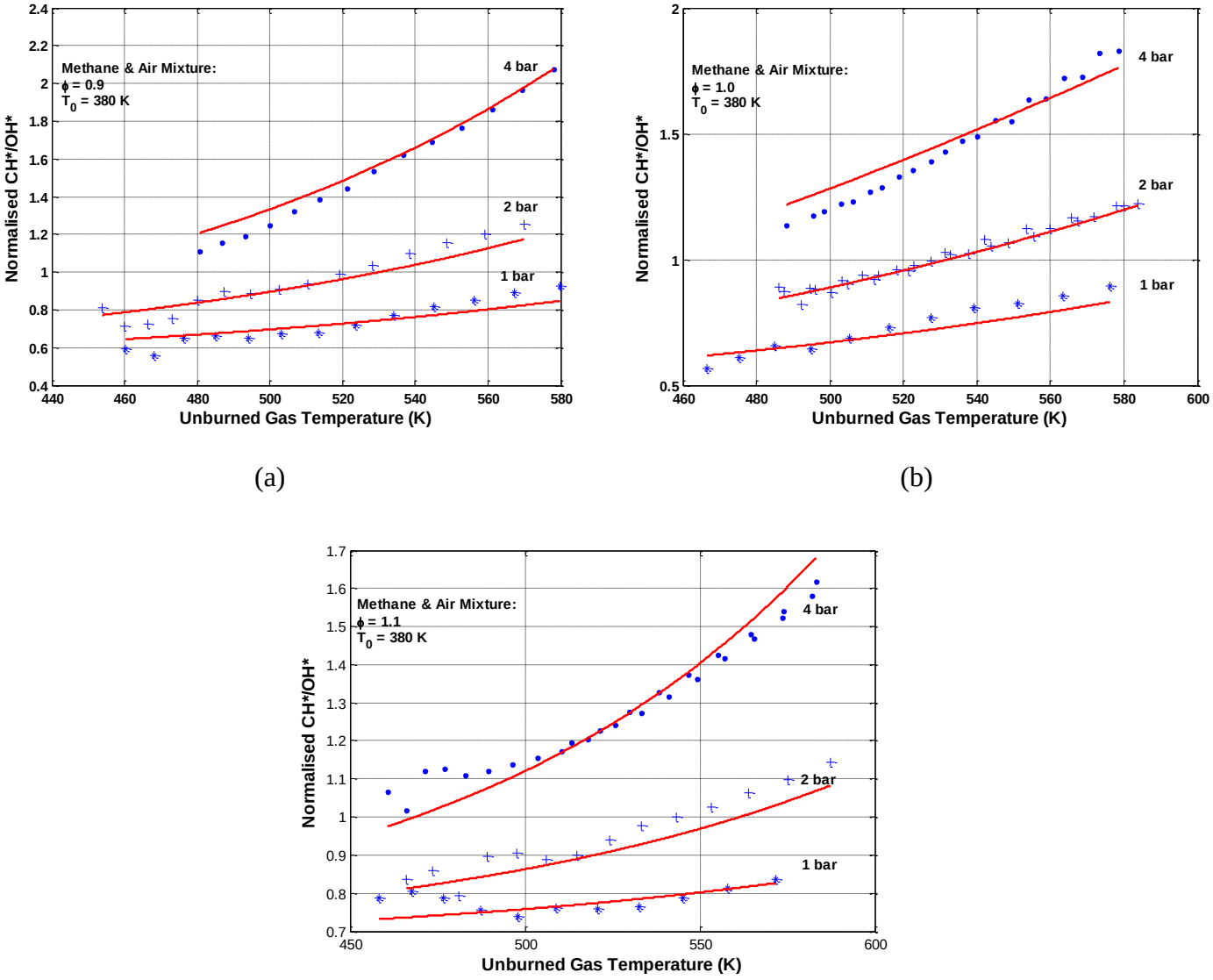


Figure 5. 4 Normalised CH*/OH* ratio of methane-air mixtures for equivalence ratios Φ = 0.9, 1.0, and 1.1, along unburned gas isentropes at T_0 = 380 K and p_0 = 1.0, 2.0, and 4.0 bar. The red curves indicate the curve fitting of Equation (5.8) to the measurements.

Based on the same multi-variate correlation and regression algorithm, the CH*/OH* ratio can be determined by the functional form expressed in Equation (5.8) for the iso-octane / air mixtures as a function of equivalence ratio, local temperature and pressure. The values of the eleven parameters are shown in Table 5.3.

Table 5. 3 Values of the Equation (5.8) Coefficients for the Iso-octane / Air Mixture

Coefficients	Values
x_1	0.1110
x_2	-0.2743
x_3	0.1648
x_4	-1.3479
x_5	3.3198
x_6	-1.9186
x_7	3.3302
x_8	-8.4208
x_9	6.0497
x_{10}	0.0658
x_{11}	0.9897

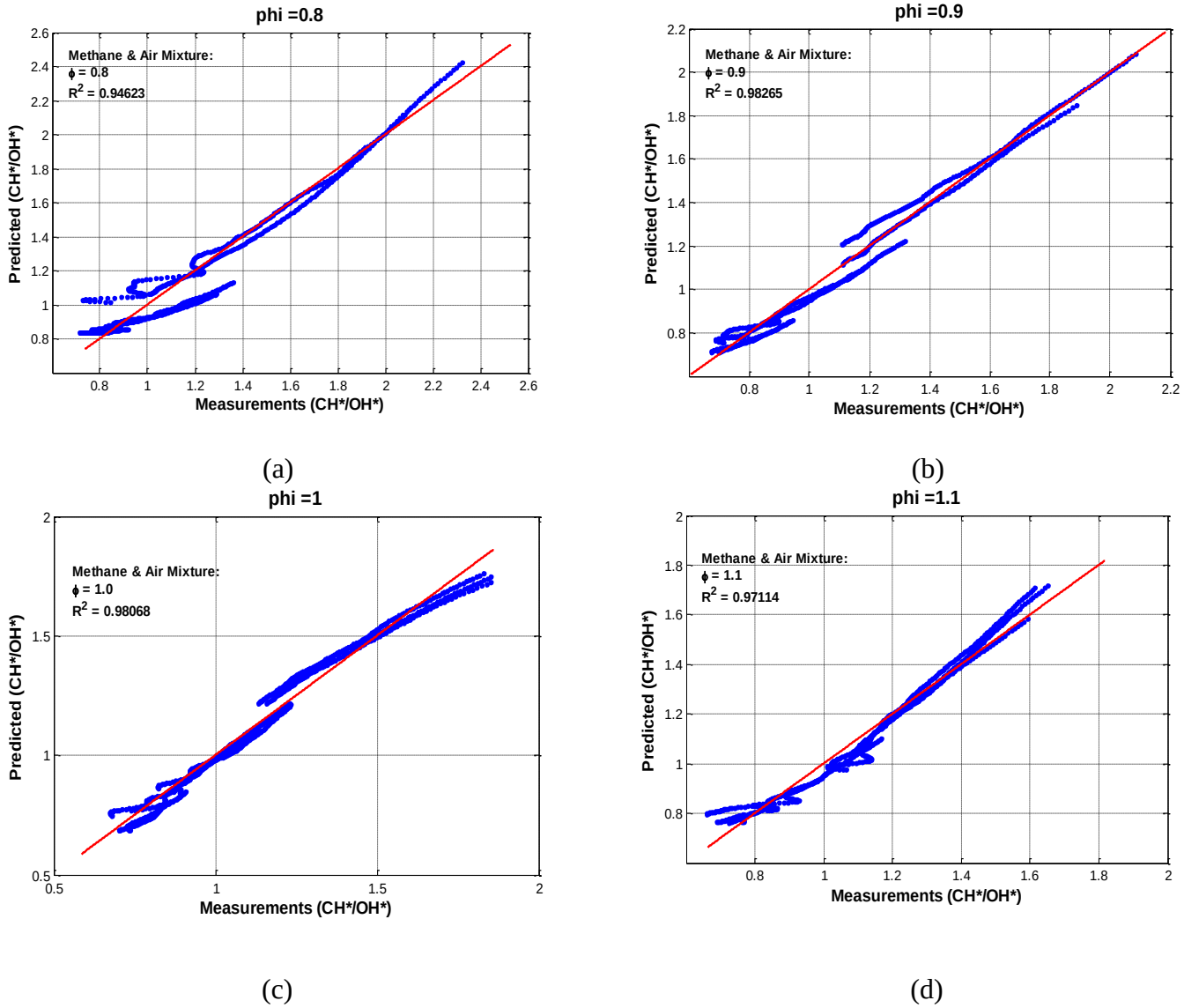


Figure 5. 5 Individual methane / air experimental data points from Figure 5.2 plotted against their corresponding values predicted by Equation (5.8) using the coefficients in Table 5.1.

As an indication of the accuracy of the best fit, Figure 5.6 plots the predicted CH*/OH* ratio, versus the actual measurement CH*/OH* chemiluminescence, where the line with unity slope represents ideal agreement between the curve fit and experimental data.

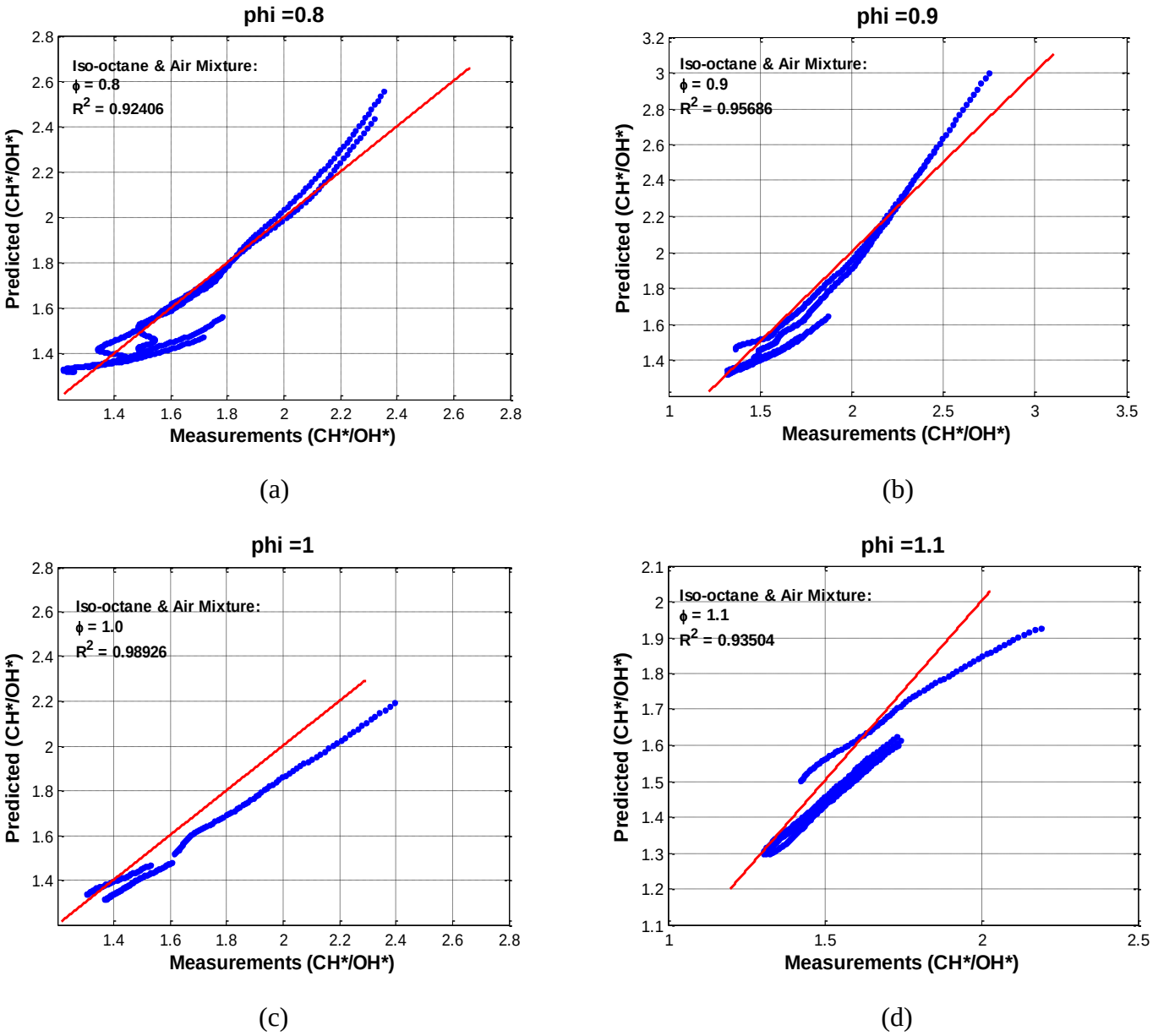


Figure 5. 6 Individual iso-octane / air experimental data points plotted against their corresponding values predicted by Equation (5.8) using the coefficients in Table 5.3.

The quality of the curve fitting and the correlation (represented by R^2) is generally good, although a bit poorer compared with the methane data, indicating that the current

prediction mechanism is able to assess CH*/OH* ratio with known local pressure, unburned gas temperature and equivalence ratio.

5.5 CH*/OH* Ratio for Sensing Equivalence Ratio

To examine the use of CH*/OH* ratio for equivalence ratio sensing, Figure 5.7 shows the predicted (Equation (5.8)) signals' dependence on equivalence ratio and pressure in methane / air flames. The unburned gas temperature effect on the CH*/OH* ratio is generally less pronounced, which can be verified by the curve-fitting coefficients listed in Table 5.1; hence it is not discussed in this figure.

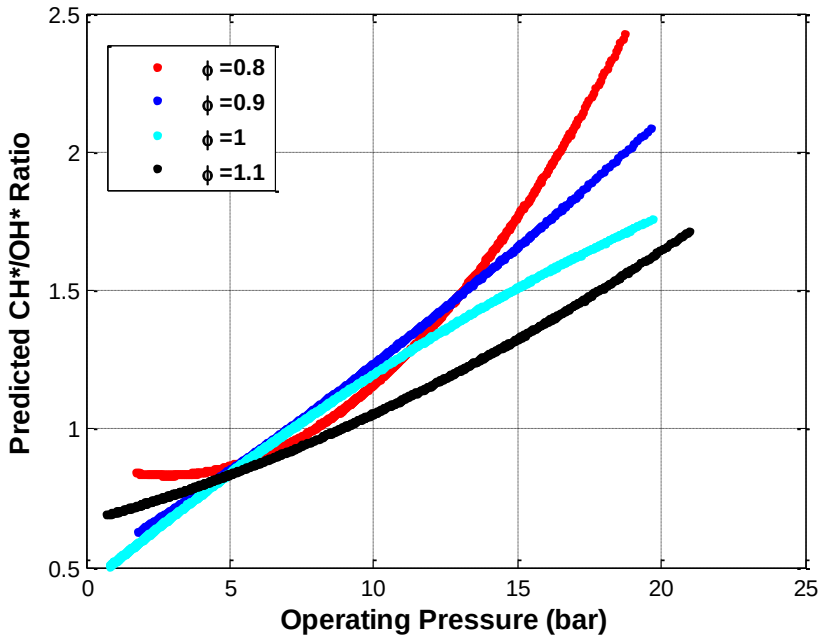


Figure 5. 7 Predicted CH*/OH* ratio (Equation (5.8) using parameters listed in Table 5.1) for varying pressure and equivalence ratios in methane / air flames.

As can be seen in Figure 5.7, for local pressure between 5 bar and 20 bar, the normalised CH*/OH* ratio increases as the mixture is made weaker for a given local pressure, which means the CH* intensity reduced less than the OH* intensity for a lean mixture; and this trend is more pronounced for the near-stoichiometric range ($0.9 \leq \Phi \leq 1.1$). This argument is consistent with Nori's [7] observation. Meanwhile the absolute value of the CH*/OH* ratio

increases monotonically with pressure in the range of 5 – 20 bar for any specific equivalence ratio. For even leaner equivalence ratios (such as Φ = 0.8), although there is sensitivity of the chemiluminescence ratio to variations in operating pressure, the low signal level might introduce error if measurement precision cannot be maintained at these lower light levels. However, only at pressures above 15 bar does it seem possible to use the normalised CH*/OH* ratio to deduce the equivalence ratio.

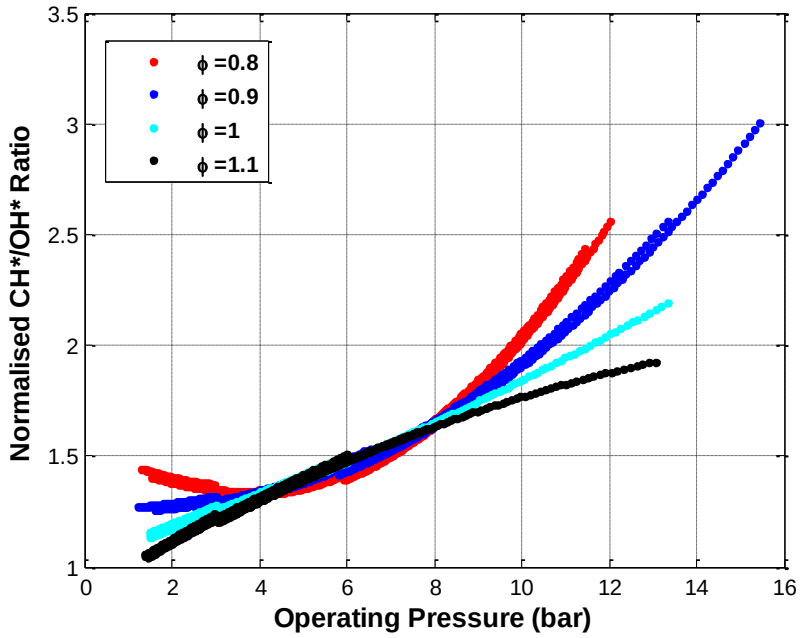


Figure 5. 8 Predicted CH*/OH* ratio (Equation (5.8) using parameters listed in Table 5.3) for varying pressure and equivalence ratios in iso-octane / air flames.

As with the methane / air chemiluminescence study, Figure 5.8 shows the feasibility of using CH*/OH* ratio for sensing the equivalence ratio in iso-octane / air flames. Across the low local pressure range (0.5 bar<p_u<3 bar) and high operating pressures (p_u>10 bar), the CH*/OH* ratio has a monotonic dependence on equivalence ratio, i.e. the ratio increases monotonically as Φ decreases towards lean for a known local pressure in iso-octane flames, which is strikingly opposite to Hardalupas's finding [14]. By contrast, the CH*/OH* ratio at high pressures shows better sensitivity, and it appears to be a possible method for determining the equivalence ratio.

In summary, the CH*/OH* chemiluminescence ratio has potential to predict the local equivalence ratio in near stoichiometric methane / air systems; the CH*/OH* ratio is shown to indicate the local equivalence ratio at high local pressures for iso-octane / air combustion with equivalence ratio ranging from 0.8 to 1.1. It should also be noted that the relationship between CH*/OH* ratio and Φ is a strong function of local pressure and less dependent on local temperature.

5.6 Conclusions

Based on the measurements of CH* / OH* chemiluminescence from premixed methane/air and iso-octane/air flames, which cover the range of equivalence ratios Φ = 0.8 - 1.1, operating pressures p_u = 0.5 - 20 bar, and unburned gas temperatures T_u = 450 - 600 K, a functional relationship has been presented that monotonically increases with increasing unburned gas temperature and increasing pressure. It can be seen that the CH*/OH* ratio calculated from the fitting correlation is reassuringly in broad agreement with the measurements.

From this multi-variate regression analysis, for a given system, one can deduce the equivalence ratio if the PMT output (CH*/OH* intensity), the unburned gas temperature, and the pressure are known. The relationship between the CH*/OH* ratio, equivalence ratio, pressure and unburned gas temperature has been quantified, providing a basis for the use of the CH*/OH* chemiluminescence ratio as an active control parameter.

Chapter 6 Absolute CH* and OH* Chemiluminescence Data Analysis

This chapter studies CH* and OH* chemiluminescence curves obtained in the constant volume combustion bomb to examine the influence of the equivalence ratio, unburned gas temperature, and operating pressure on the absolute chemiluminescence emissions. Then it analyses the relationship between the absolute CH* and OH* chemiluminescence and the heat release rate. Finally, there are two issues to be reported: (1) when combustion is started at different points along an isentrope, then the chemiluminescence emissions are not just dependent on the unburned gas temperature, pressure and equivalence ratio, and, (2) chemiluminescence after the end of combustion. Two fuels are again of particular interest: methane and iso-octane.

6.1 Overview

The goal of this work is to study the feasibility of using measurements of chemiluminescence as an active control for premixed combustion systems. Engine manufacturers are under increasing pressure to produce intelligent products offering improved flexibility and reliability for both gas turbines and internal combustion engines. Monitoring combustor performance and combustor health requires reliable and versatile sensors. Equivalence ratio sensing is important in combustion diagnostics, especially in the region where combustion occurs. Additionally, it is also desired to allow engines to be actively controlled to operate with reduced combustion instability and permissible NO_x levels. Chemiluminescence measurement is one of the most common and most promising ways of implementing optical diagnostics in combustion monitoring applications, owing to its simplicity and non-intrusive nature.

Among the four common chemiluminescent species in hydrocarbon-air flames, i.e. CH*, OH*, CO_2* and C_2* [50], CH* and OH* have been widely investigated in combustion

diagnostics as a measure of heat release rate [7, 13, 16, 20, 22, 48] and for sensing equivalence ratio [47, 48, 49, 51, 52]. Therefore this chapter will start with a brief description of OH* and CH* chemiluminescence mechanisms.

A series of experiments has been reported that examines CH* and/or OH* chemiluminescence in premixed methane / air flames [7, 16, 17, 47, 48, 49, 53]. Although some investigations studied flames with varying conditions, such as pressure [17, 47, 53] and stretch [16, 17]; most of these researchers gathered data under limited conditions, for example measurements at atmospheric pressure. In practice, combustors often operate at a range of pressures above atmospheric pressure; hence any changes in pressure might affect the reaction mechanism, and influence the chemiluminescence emission. Additionally, most interpretation of CH* and OH* chemiluminescence rely either on heuristic arguments or empirical data obtained under restricted conditions. Therefore more rigorous analysis is required to understand the effects of combustion conditions such as operating pressure, unburned gas temperature, and equivalence ratio.

Heat release rate is an important parameter for combustion diagnostics [15, 65]. However, there is still no agreement whether CH* and/or OH* chemiluminescence can be regarded as reliable indicators for the rate of heat release. Thus this chapter examines the usefulness of CH*/OH* chemiluminescence ratio as a diagnostic tool for combustion processes over a wide range of combustion conditions: equivalence ratio in the range 0.8 to 1.1, pressure in the range 0.5 to 20 bar, and unburned gas temperature in the range 450 to 600 K.

Moreover, this chapter will discuss two unexpected results. Firstly, the OH* and CH* chemiluminescence (as mJ/g) does not just depend solely on the equivalence ratio, local pressure and unburned gas temperature, but also time (or some other parameter). The second puzzling result is that chemiluminescence continues after the ‘end of combustion’.

Background CO_2* chemiluminescence is likely to be the largest source of systematic error in the current measurements.

In addition, it is worth noting that methane and iso-octane were chosen for this evaluation, because they are highly relevant to many combustion systems. For example natural gas, in which methane is the major component, is considered to be a favourable fuel in engines, and the utilization of natural gas has been realized in the spark-ignition engines. Meanwhile liquid fuels are also of considerable practical significance in many combustors such as internal combustion engines and aero-engines.

6.2 OH* and CH* Kinetic Mechanisms

Hydroxyl radical chemiluminescence results from the spontaneous emission of light from the excited state hydroxyl radical (OH*). Summarising from Gaydon [5], Carl et al. [29], Lichtin et al. [30], and Smith et al. [31, 58], in hydrocarbon-air flames, the primary OH* formation reaction is:

$$CH + O_2 \rightarrow OH^* + CO \tag{6.1a}$$

While in hydrogen-oxygen flames, OH* is also produced through the following chemical-kinetic mechanisms [33, 34, and 58]:

$$H + O + M \rightarrow OH^* + M \tag{6.1b}$$

$$H + OH + OH \rightarrow OH^* + H_2O \tag{6.1c}$$

where M represents a third collisional partner.

In all of these reactions, OH* is produced in the first electronically excited state. Then the de-excitation of excited state OH* will occur through several reactions, (1) spontaneous emission of a photon which peaks at 306.4 nm [5], i.e.

$$OH^* \rightarrow OH + hv \tag{6.2a}$$

and, (2) non-radiative ‘quenching’ via collisional relaxation of OH* to OH [47]:

$$OH^* + M \rightarrow OH + M \quad (6.2b)$$

Hydroxyl radicals exist either in the flame front or in post-combustion gases [49], but the most likely hydroxyl formation mechanisms result in the electronically ground state radical (OH) [49].

The strongest CH* chemiluminescent emission appears around 430 nm. The formation of CH* has been identified with the following reactions in the literature [5, 6, 7, 8, 9, 10, and 11]:

$$C_2 + OH \rightarrow CH^* + CO \quad (6.3a)$$

$$C_2H + O \rightarrow CH^* + CO \quad (6.3b)$$

$$C_2H + O_2 \rightarrow CH^* + CO_2 \quad (6.3c)$$

The depletion of CH* occurs by ways of spontaneous chemiluminescence or by quenching (i.e. collisions):

$$CH^* \rightarrow CH + hv \quad (6.4a)$$

$$CH^* + M \rightarrow CH + M \quad (6.4b)$$

In methane / air flames, M represents a range of possible colliders such as N_2, H_2O, H_2, O_2, CO, CO_2 and CH_4.

The CH* chemiluminescence is produced 'in the high-temperature reactions, which takes place in the flame front of the combustion' [48]. As with OH*, the electronically excited CH* in general have low concentrations due to the low production rate and due to their rapid removal by the above mentioned collisional quenching.

6.3 Methane Results

6.3.1 Introduction

The objectives of this section are as follow. Firstly, the shape of the OH* and CH* chemiluminescence curves and the relationships with parameters of interest during the

combustion process (i.e. pressure, unburned gas temperature, and equivalence ratio) are studied. Secondly, while the technique required to detect chemiluminescence is relatively mature, there is a need to develop data interpretation strategies that can relate optical flame emission data to meaningful combustion state information such as the heat release rate.

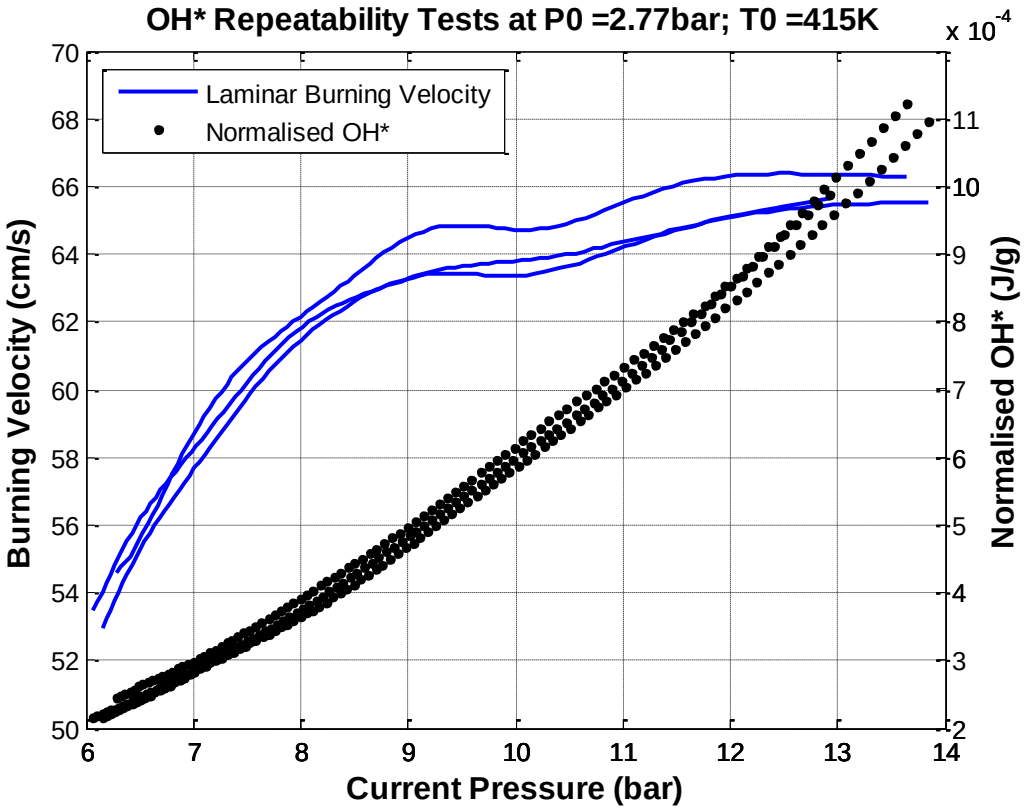


Figure 6. 1 Repeatability of laminar burning velocities and normalised OH* as a function of pressure (p) with initial conditions of p_0 = 2.77 bar, T_0 = 415 K.

To reach these objectives, a sequence of methane / air tests was conducted covering a wide range of mixtures at equivalence ratios Φ, unburned gas temperatures T_u, and operating pressures p ranging from 0.8 to 1.1, 450 to 600 K, and 0.5 to 20 bar, using a constant volume combustion bomb. As has been mentioned in Section 4.4, care was taken to remove the electrical and numerical noise. Thus experimental errors primarily came from signal variation. As an indicator of the experimental variation, the repeatability of 3 separate tests for a stoichiometric methane / air mixture with an initial condition of 2.77 bar and 415 K was checked; this is shown in Figure 6.1. The burning velocity is repeatable within 1 cm/s and the

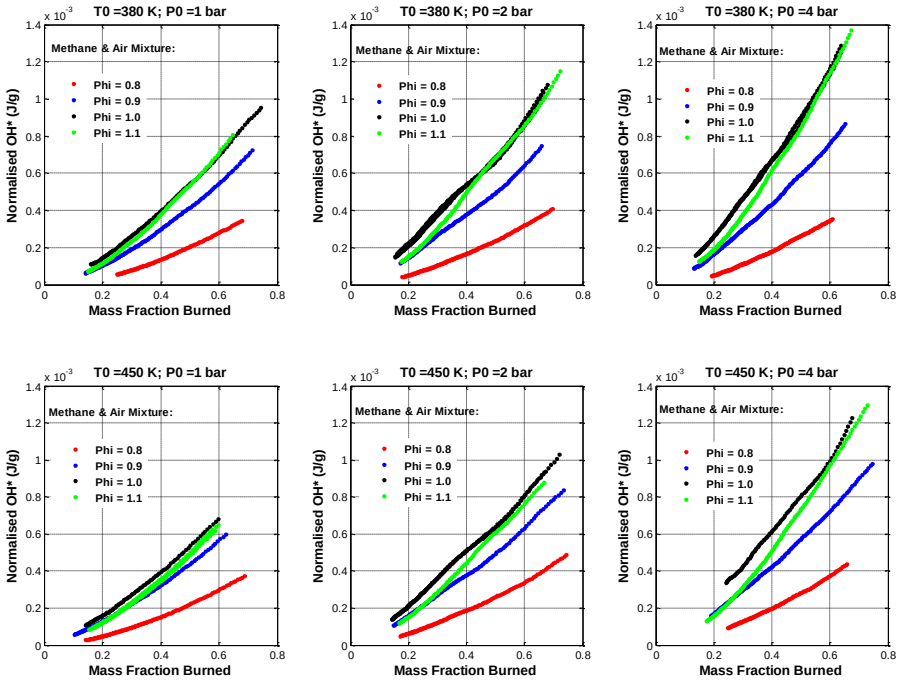
variation of normalised OH* intensity is within 5%, (as was the CH* normalised intensity); therefore, the systematic errors due to experimental variability are assumed to be small.

6.3.2 Influence of the Equivalence Ratio, Temperature, Pressure and Stretch on the Chemiluminescence Curve Development

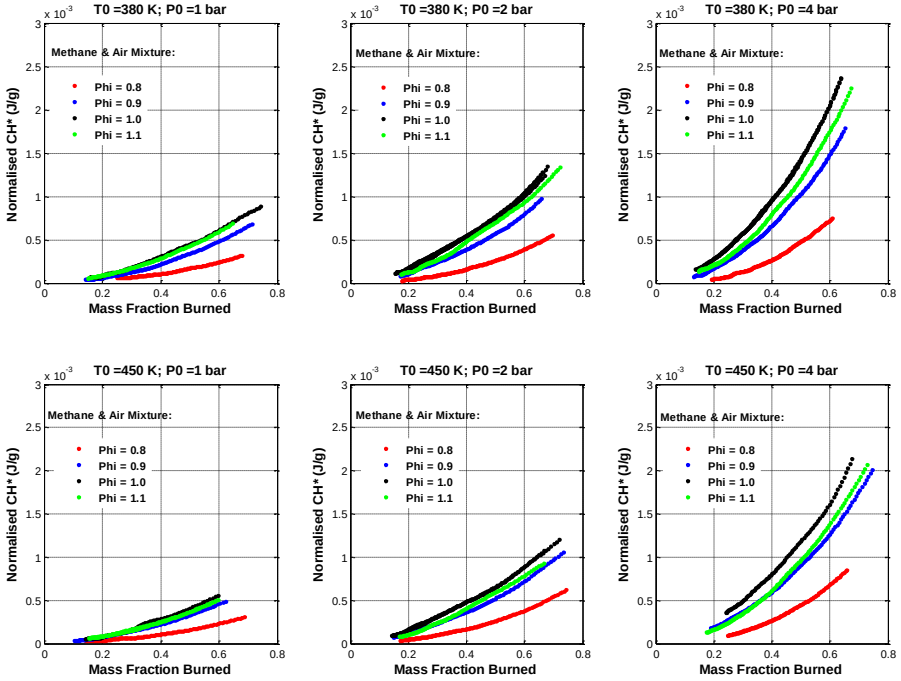
In a constant volume combustion bomb, a single ignition event provides access to chemiluminescence emissions arising from a range of pressures and temperatures. Hence to investigate the effect of the equivalence ratio, temperature, and pressure, the isentropic link between temperature and pressure during a single ignition event needs to be de-coupled by varying the initial pressure and/or temperature. In addition, the chemiluminescence intensities OH* and CH* are normalised by the mass of fuel burned rate for each condition. In this way, the influence of equivalence ratio, temperature, and pressure on chemiluminescence intensity can be evaluated independently of the fuel burned rate.

6.3.2.1 Effect of Equivalence Ratio, Φ

In Figure 6.2, the normalised OH* (in Figure 6.2a) and CH* (in Figure 6.2b) are displayed in terms of mass fraction burned for different equivalence ratios, i.e. 0.8 to 1.1, for three given initial pressures, 1.0, 2.0, and 4.0 bar, and two given initial temperatures, i.e. 380 and 450 K, respectively.



(a)

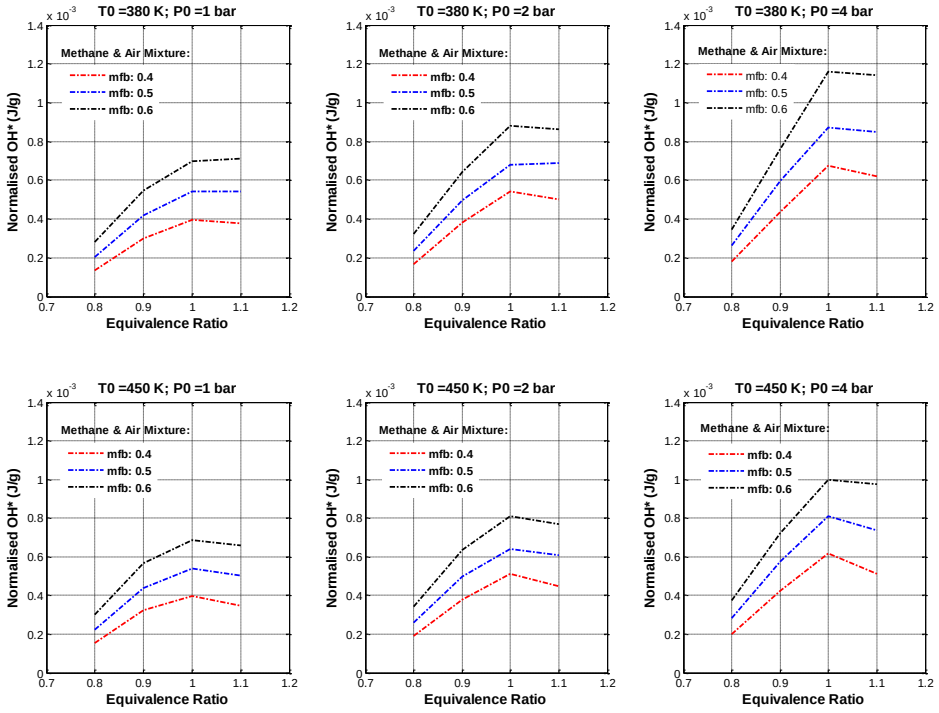


(b)

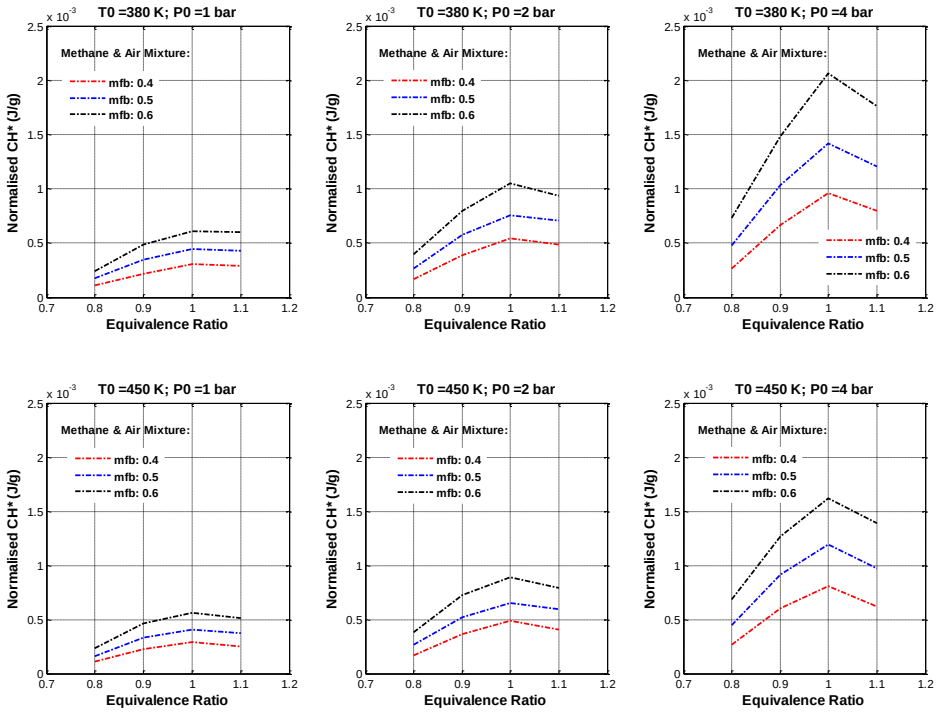
Figure 6. 2 Normalised OH* (in Figure 6.2a) and CH* (in Figure 6.2b) chemiluminescence as a function of mass fraction burned in premixed methane / air combustion for different equivalence ratios ranging from 0.8 to 1.1, for two known initial temperatures, i.e. 380 K and 450 K, and for three given initial pressures, i.e. 1, 2, and 4 bar. In each subplot, four different curves indicate normalised chemiluminescence with various equivalence ratios at the same initial temperature and pressure.

As can be seen from Figure 6.2, for any fixed initial pressure and initial temperature, the normalised OH* and CH* increase monotonically with equivalence ratio under lean burn conditions ($0.8<\Phi<1.0$), which is in excellent agreement with Higgins' [17] and David's [48] assertion; the decrease in chemiluminescence on the rich side is somewhat less steep than on the lean side (sometimes the normalised OH* and CH* chemiluminescence at $\Phi = 1.1$ are close to overlapping with the stoichiometric results). This trend can be further investigated by plotting a slice through each subplot at locations of specific mass fraction burned, as shown in Figure 6.3. The reason for this characteristic can be found by investigating the formation of the chemiluminescence radicals.

OH* has been suggested [25, 26, 27, 28, 29, 30, 31, 58] to be the product of a reaction between CH and molecular oxygen. The values of normalised OH* intensity are relatively small for lean mixtures because there are other faster reactions that consume most of the CH that is produced. For richer mixtures, there is less O_2 present for reaction with CH, and the reaction $CH + O_2 = CO + OH^*$ must compete with other oxidation reaction. This interpretation is consistent with Bowman's report [54] that there exists a direct and strong dependence of OH* production on O_2 concentration which indicates that OH* increases as Φ increases towards stoichiometric; while the reciprocal dependence of OH* intensity on CH_4 concentration indicates a competition for oxygen between CH_4 fragments (eg. CH, H) and CH species which is leading directly to OH* as the ratio of CH_4/O_2 increases.



(a)



(b)

Figure 6. 3 Normalised OH* (in Figure 6.3a) and CH* (in Figure 6.3b) chemiluminescence as a function of equivalence ratio at three selected mass fraction burned values for two known initial temperatures, i.e. 380 K and 450 K, and for three given initial pressures, i.e. 1, 2, and 4 bar.

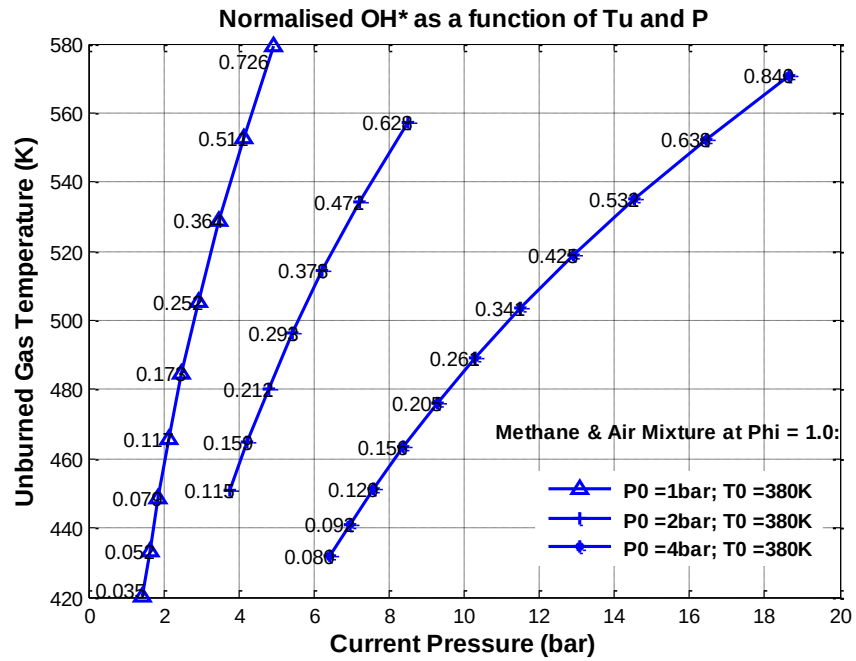
With regard to CH*, there is still debate on the importance of the three proposed production mechanisms (Equations 6.3a, b, and c) responsible for CH*. Devriendt and Peters [10] suggested that CH* is predominately formed by C_2H and atomic oxygen; Petersen et al. [76] provided the rate coefficients, which have a positive dependence on temperature. Elsamra et al. [11] studied the temperature dependence of the rate constant for the formation reaction (6.3c) over the temperature range 316 – 837 K. They presented a positive temperature dependence of rate constant for the reaction with C_2H and molecular oxygen, and concluded that the C_2H - O_2 regime has a much greater contribution to CH* under fuel lean conditions, whilst the C_2H – O reaction dominates under fuel rich condition. Full details of the rate coefficients for OH* and CH* formation have been summarised by Panoutsos et al. [14]. Higgins [17] attributes the observed increase in CH* chemiluminescence intensity as Φ increases towards stoichiometric to an increased flame temperature as the equivalence ratio moves towards stoichiometric. For an over-oxidized system, the excess air must be heated to the product temperature; thus the temperature drops from the stoichiometric value. For a fuel rich system, there is not enough oxygen to burn all the carbon and hydrogen to their most oxidized state, so the specific energy release is less and eventually the temperature drops as well. The temperature increase just rich of stoichiometric enhances the reaction of the ethynyl radical (C_2H) with atomic oxygen and molecular oxygen to contribute to CH*. Thus the maximum chemiluminescence intensities of OH* and CH* are for equivalence ratios close to stoichiometric, and the evidence discussed above suggests that these radical intensities are useful for sensing equivalence ratio.

6.3.2.2 Effect of Temperature and Pressure

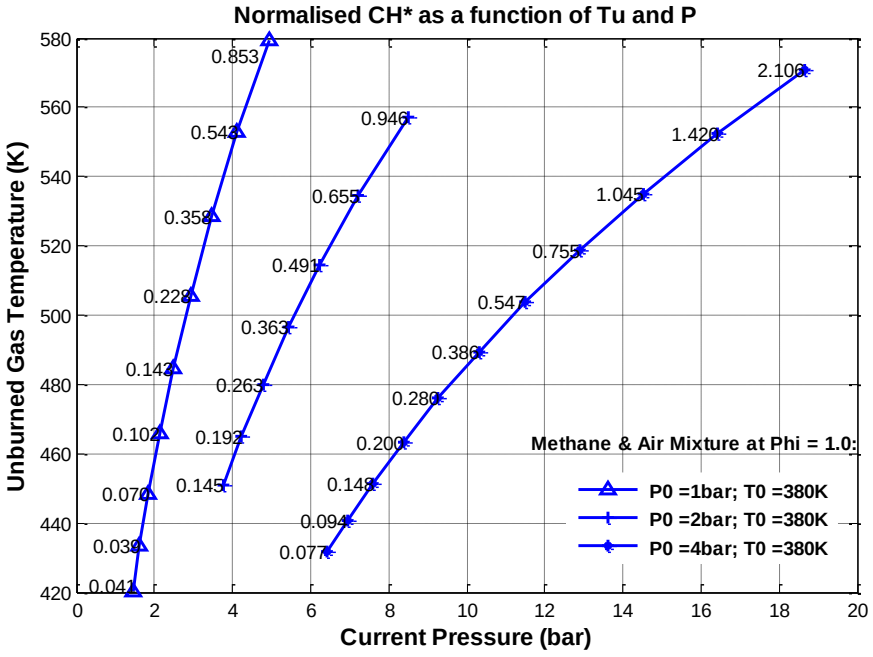
The effect of unburned gas temperature and operating pressure is best illustrated by the results for stoichiometric mixtures of methane and air, which are plotted in Figure 6.4.

Figure 6.4 shows the isentropes followed by the compression of the unburned gas, and the 'spot values' are the normalised OH* and CH* intensity (in terms of millijoules of light produced per unit mass of fuel burned, i.e. mJ/g). Data points are for normalised OH* and CH* measurements at initial pressures p_0 = 1.0, 2.0, and 4.0 bar for stoichiometric methane / air flames at an initial temperature T_0 = 380 K (only one in every ten data points from the experimental data sets are plotted in Figure 6.4 to avoid clutter). It is worth noting that the isentropic link between unburned gas temperature and current pressure is decoupled by varying the initial pressure for a given initial temperature. Additionally, the characteristic of the isentropes at an initial temperature T_0 = 450 K is similar to that in Figure 6.4.

There are several notable trends observed in the chemiluminescence curve shapes for a given equivalence ratio (in this case, stoichiometric). The first observation is, that for any given operating pressure, the normalised intensity is higher for the mixtures that were ignited at a lower initial pressure. This can be attributed to the effect of unburned gas temperature, i.e. OH* and CH* chemiluminescence intensities increase with increasing unburned gas temperature at any specific pressure. This is consistent with David's [49] and Higgins' [17] arguments. To explore the effect of unburned gas temperature on normalised OH* and CH* intensities, chemical-kinetic mechanisms for the OH* and CH* formation need to be investigated.



(a)



(b)

Figure 6. 4 Effect of current pressure (p_u) and unburned gas temperature (T_u) on normalised OH* (in Figure 6.4a) and CH* (in Figure 6.4b) for stoichiometric methane / air mixtures. Normalised intensities (mJ/g) are shown as 'spot values'.

Although the rate constant for OH* formation (i.e. reaction 6.1a) reported by Walsh [55] is different from the ones derived by Porter [56] and by Smith [57], there is an agreement that the rate constant is independent of temperature. The temperature dependence

of the OH* is closely related to the CH radical (i.e. the precursor of OH* radical) producing reactions. Referring to Dandy [49], the dominant formation reaction for the CH radicals in the flame is:

$$CH_2 + OH \rightarrow CH + H_2O \tag{6.5}$$

Turns [1] proposed that this reaction displays a direct dependence on temperature-squared (T^2); hence increasing temperature will drive the reaction in the forward direction and accordingly generate more excited OH* radicals. Additionally, OH* is shown to be sensitive to the reaction [49]:

$$O + OH \rightarrow H + O_2 \tag{6.6}$$

which is verified to be inversely dependent on temperature. Thus the consumption of OH decreases with increasing temperature, which further drives reaction (6.5) in the forward direction.

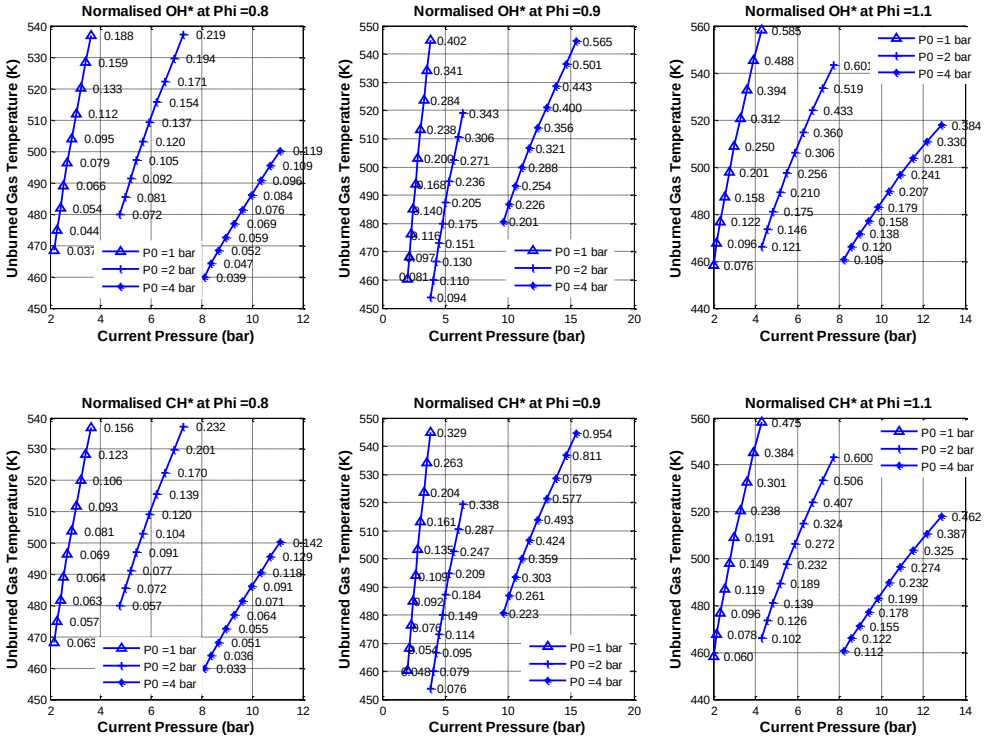


Figure 6. 5 Effect of current pressure (p_u) and unburned gas temperature (T_u) on normalised OH* and CH* at initial temperature T_0 = 380 K, and at equivalence ratios 0.8, 0.9, and 1.1 respectively for methane / air mixtures. Normalised intensities (mJ/g) are shown as 'spot values'.

As noted previously, CH* intensity is positively correlated with flame temperature since the rate constant of reaction 6.3b is directly dependent on temperature [11, 76]. Besides, Smith [58] studied the rate constant for CH* formation of C_2H with molecular oxygen (Equation 6.3c) and reported that the rate constant has also a positive temperature dependence. In conclusion, the kinetic mechanism for the production of chemiluminescent species, i.e. OH* and CH*, is consistent with experimental observations that for a fixed equivalence ratio the chemiluminescence intensities increase with increasing temperature.

The second observation, that for any given unburned gas temperature the normalised intensity is slightly higher for the mixtures that were ignited at a high initial pressure (which is consistent with Tinaut's [48] argument), can be attributed to the effect of pressure, i.e. OH* and CH* chemiluminescence intensities increase slightly with increasing pressure at any specific unburned gas temperature. This observation is closely related to the chemical mechanisms for the production of OH* and CH*, and can be explained by considering Le Chatelier's Principle. Le Chatelier's Principle states that if a system in equilibrium is subjected to changes in temperature, pressure or concentration, then the equilibrium shifts in such a way to reduce the effect of the changed condition. For hydrocarbon combustion, apart from NO_x and CO_2 formation reactions, all other hydrocarbon oxidation reactions are very fast. Hence at any instant in time, it can be seen as a system in equilibrium; accordingly Le Chatelier's Principle can be used. For the excited hydroxyl radical OH*, there is no effect of pressure on the predominant producing-reaction (Equation 6.1a) as there are the same number of moles of reactants and products. However OH* is also produced through two other pathways:

$$H + O + M \rightarrow OH^* + M \qquad (6.1b)$$

$$H + OH + OH \rightarrow OH^* + H_2O \qquad (6.1c)$$

Thus increase in pressure favours a decrease in the number of moles that occurs with the forward direction and OH* intensity is enhanced.

For CH* chemiluminescence, apart from the three mechanisms proposed already (Equation 6.3a, b, and c), Hall et al. [59] presented another CH* formation reaction:

$$\mathrm{C} + \mathrm{H} + \mathrm{M} \rightarrow \mathrm{CH}^{*} + \mathrm{M} \tag{6.7}$$

As with the OH* reactions, at high pressures the equilibrium will shift in the forward direction that favours the reduction in the number of moles. Neither equation (6.1b, c) nor Equation (6.7) is the dominant formation reaction; hence the pressure effect is not as pronounced as the temperature effect.

In summary, the normalised OH* and CH* chemiluminescence increases with increasing unburned gas temperature for stoichiometric methane / air flames. Meanwhile it is suggested that increased pressure has an effect on increasing the normalized OH* and CH* signals. This argument is also valid for non-stoichiometric methane / air mixtures as shown in Figure 6.5.

6.3.2.3 Effect of Stretch Rate

Flame stretch is a local, time-varying property of a flame. It is defined as rate of change per unit area of an element of flame surface, i.e.

$$\alpha = \frac{1}{A} \cdot \frac{dA}{dt} \tag{6.8}$$

where α is the stretch, A is the element of flame area defined by points on the flame surface moving at the local tangential gas velocity and t is the time. For spherically outwardly propagating flames, the spherical symmetry means that the stretch is the same everywhere and the total flame area ($4\pi r_b^2$) can be used in the expression. Therefore the stretch is calculated by:

$$\alpha = \frac{1}{A} \cdot \frac{dA}{dt} = \frac{1}{4\pi r_b^{\,2}} \cdot \frac{d\left(4\pi r_b^{\,2}\right)}{dt} = \frac{2}{r_b} \cdot \frac{dr_b}{dt} = \frac{2}{r_b} \cdot S_f \tag{6.9}$$

where r_b denotes flame radius, and S_f represents stretched flame speed.

A propagating flame can be stretched for two reasons: (a) due to curvature; (b) due to an imbalance between mass and heat transport. Stretch affects the propagation rate by changing the diffusive flux of reactants upstream into the reaction zone and of heat downstream out of it. Since the balance of these fluxes has an influence on the flame temperature, and since the reaction rate (including OH* and CH* formation reactions) varies strongly with temperature, flame stretch can affect the reaction rate and therefore the OH* and CH* chemiluminescence intensities. However the analysis here has been normalised for the mass of fuel burned rate.

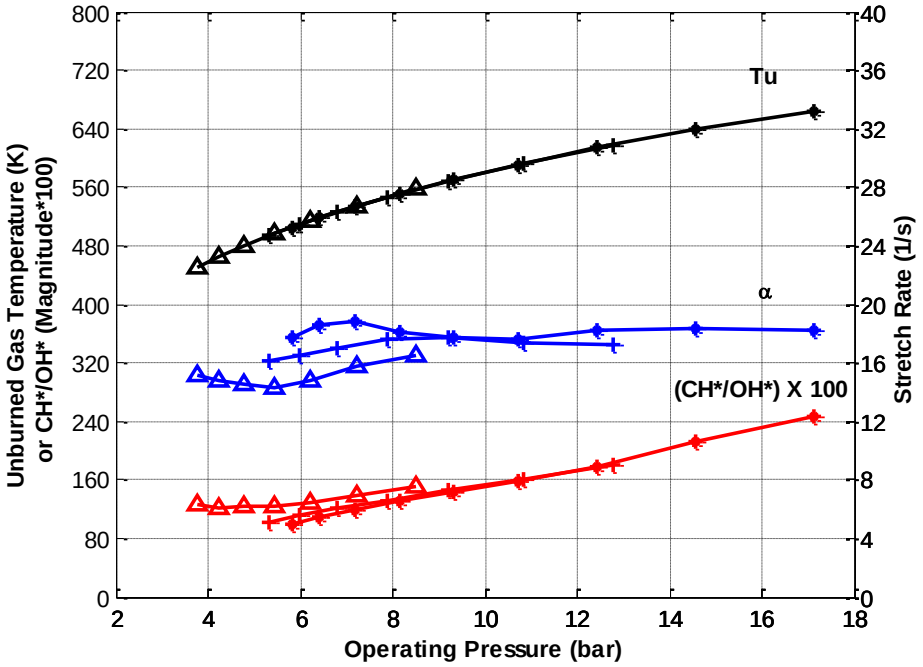


Figure 6. 6 Effect of stretch rate (α, in units of s^{-1}) on the normalized CH*/OH* ratio for stoichiometric methane / air mixtures. The results are for a single isentrope, but with different initial pressures and temperatures of p_0 / T_0 = 2.0 bar/380 K (Δ), 2.77 bar/415 K (+), and 3.75 bar/450 K (*).

To investigate the effect of stretch, stoichiometric tests have been conducted at different initial unburned gas temperatures and pressures. These were chosen to follow a single isentrope (therefore to isolate the effect of unburned gas temperature and pressure on chemiluminescence); hence the single unburned gas temperature line in Figure 6.6. For this

particular isentrope the results of the CH*/OH* ratio also collapse to become an almost linear function of pressure.

There are two notable observations from Figure 6.6: firstly, for the laminar premixed methane / air flames under study, the stretch rate is restricted to a low level and does not change much across the stoichiometric range (typically below 20 s-1); and this is a value that has a negligible effect on the laminar burning velocity. This is because the Lewis number (Le) does not deviate too much from unity (according to Law et al. [60]) for methane / air mixtures; the stretch due to aerodynamic strain (imbalance between mass and heat diffusion) is therefore limited. The non-dimensional Lewis number is defined as the ratio of thermal diffusivity to mass diffusivity, i.e.

$$Le = \frac{\alpha}{D} \tag{6.9}$$

where α is thermal diffusivity, and D is mass diffusivity.

Secondly, compared with the CH*/OH* ratio, there is a much greater variation and scatter in the stretch rate. Thus, it can be assumed that a stretch of below 20 s^{-1} will not have a significant effect on the chemiluminescence. This stretch independence conclusion is in general consistent with other researchers' investigations [7, 14, 16, and 17]. Specifically, Higgins et al. [7] and Nori et al. [17] insisted that no systematic CH* dependence was observed on aerodynamic stretch. Hardalupas et al. [16] studied chemiluminescence in natural-gas-fuelled, premixed, counter-flow flames and concluded that the OH*/CH* chemiluminescence ratio is independent of the stretch. A subsequent work by Panoutsos et al. [14] measured chemiluminescence in premixed and non-premixed methane / air flames and reported that there is no effect of stretch on the OH*/CH* intensity ratio; in contrast, the stretch has an effect on both OH* and CH* intensities. Hence, when parametrically examining the normalised CH*/OH* ratio with respect to combustion parameters, stretch rate has not been taken into consideration in the current work.

Overall, it is found that for the low level of stretch in these experiments the stretch effect on OH* and CH*chemiluminescence is less pronounced than the signal's dependence on equivalence ratio, temperature and pressure for a laminar premixed methane / air flame at stoichiometric. This conclusion is also supported by the non-stoichiometric methane / air measurements.

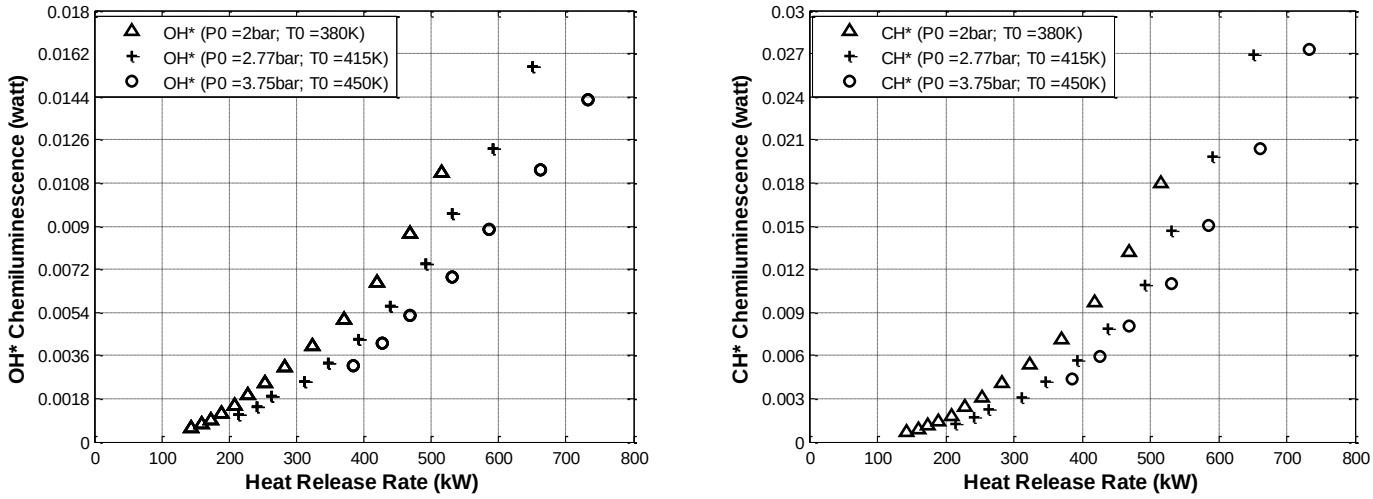
6.3.3 CH* and OH* as an Indicator of Heat Release Rate

In combustion dynamics research, heat release rate is a fundamental property for the understanding and prediction of unstable combustion behaviour such as combustion noise and combustion instabilities [15, 65]. Early researchers, Prince and co-workers [66], related the oscillating heat release to oscillations in the strength of the chemiluminescence signal from the reaction zone. From then on, many works have investigated the applicability of chemiluminescence as an indirect measure for heat release rate numerically and experimentally. While Aleiferis et al. [19] predicted that chemiluminescence from OH*, CH*, and C_2* are good indicators of heat release and reaction rate in premixed flames; Najm [13] insisted that CH* and OH* are poor indicators of heat release rate in areas of high flame strain and curvature. Therefore there is a need to assess the potential usefulness of CH* and OH* as an indicator of heat release rate.

Figure 6.7 presents the absolute CH* and OH* intensities plotted against heat release rate for three stoichiometric methane / air mixtures with three different initial conditions that were chosen to follow an isentrope: p_0 / T_0 = 2.0 bar/380 K, 2.77 bar/415 K, and 3.75 bar/450 K (these experiments are discussed in more detail in Section 6.5.1 where Figure 6.10 shows the overlapping isentropes).

There are two observations from Figure 6.7: firstly, for any single experiment, the OH* and CH* chemiluminescence increases monotonically with heat release rate. However,

the chemiluminescence is not proportional to heat release rate which contrasts with what Prince [66] found in 1968.



(a) (b)

Figure 6. 7 Absolute OH* (Figure 6.7a) and CH* (Figure 6.7b) chemiluminescence as a function of heat release rate (*RoHR*) for stoichiometric methane / air mixtures with different initial conditions that were chosen to follow an isentrope.

Secondly, the absolute values of the OH* and CH* chemiluminescence intensity do not just depend on the heat release rate, as the chemiluminescence obtained from different starting points along an isentrope depends on the starting point (and not solely on the heat release rate). This trend can also be seen in non-stoichiometric methane / air flames, which means that, the absolute OH* or CH* chemiluminescence cannot be regarded as a measure for the rate of heat release in laminar premixed methane / air flames in a constant volume combustion bomb. This is discussed further in Section 6.5.1.

6.4 Iso-octane Results

6.4.1 Introduction

For many practical uses, the combustor is partially premixed; hence the local equivalence ratio Φ is difficult to determine. The previous investigation studied chemiluminescence in methane flames, and the objective of this section is to extend the experimental and numerical

investigation to iso-octane, and to assess the feasibility of sensing the local equivalence ratio using the chemiluminescence from iso-octane / air flames.

A series of experiments has been carried out, which cover a wide range of equivalence ratios, i.e. 0.8 to 1.1, for three given initial pressures, 0.75, 1.5, and 3.0 bar, and two given initial temperatures, i.e. 380 and 450 K, respectively. It is worth noting that the highest initial pressure is tied to the volume of the Hamilton syringe used for dispensing the fuel. Substitution of equation (2.38) into equation (2.31), bearing in mind that the ratio of the partial pressures of the fuel and the air will be equal to their molar ratio, yields:

$$V_f = \frac{p_{mix} \cdot (1 - x_r) \cdot V_{bomb}}{R_0 \cdot T \cdot Y_f \cdot \left(1 + \frac{100}{21\Phi}\left(x + \frac{y}{4} - \frac{z}{2}\right)\right)} \tag{6.10}$$

The syringe volume of 1000 µL limits the initial pressure to 3 bar.

6.4.2 CH* and OH* Chemiluminescence for Equivalence Ratio Sensing

Chemiluminescence emissions from OH* and CH* have not been investigated as extensively for iso-octane compared with methane. Figure 6.8 shows the normalised OH* and CH* from iso-octane / air flames burning at a various equivalence ratios, i.e. Φ = 0.8 – 1.1, at three given initial pressures, i.e. p_0 = 0.75, 1.5, and 3 bar, and at known initial temperature, i.e. T_0 = 450 K (iso-octane / air mixtures at T_0 = 380 K have a similar trend).

The overall emissions of OH* and CH*, in general, increase monotonically with equivalence ratio for lean mixtures ($0.8 < \Phi < 1.0$). However, this trend on the rich side was deemed less obvious. These results suggest that OH* and CH* chemiluminescence might be used as an indicator of equivalence ratio in premixed iso-octane / air combustion within a small Φ range ($0.8<\Phi<1.0$).

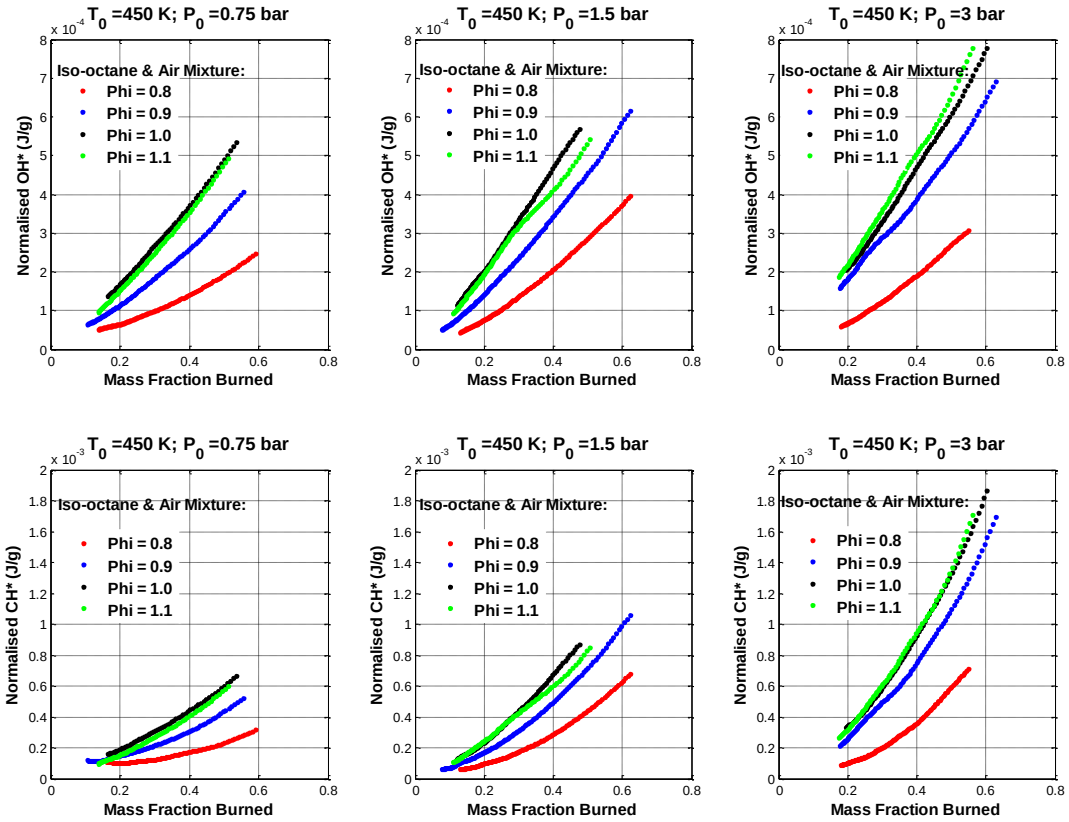
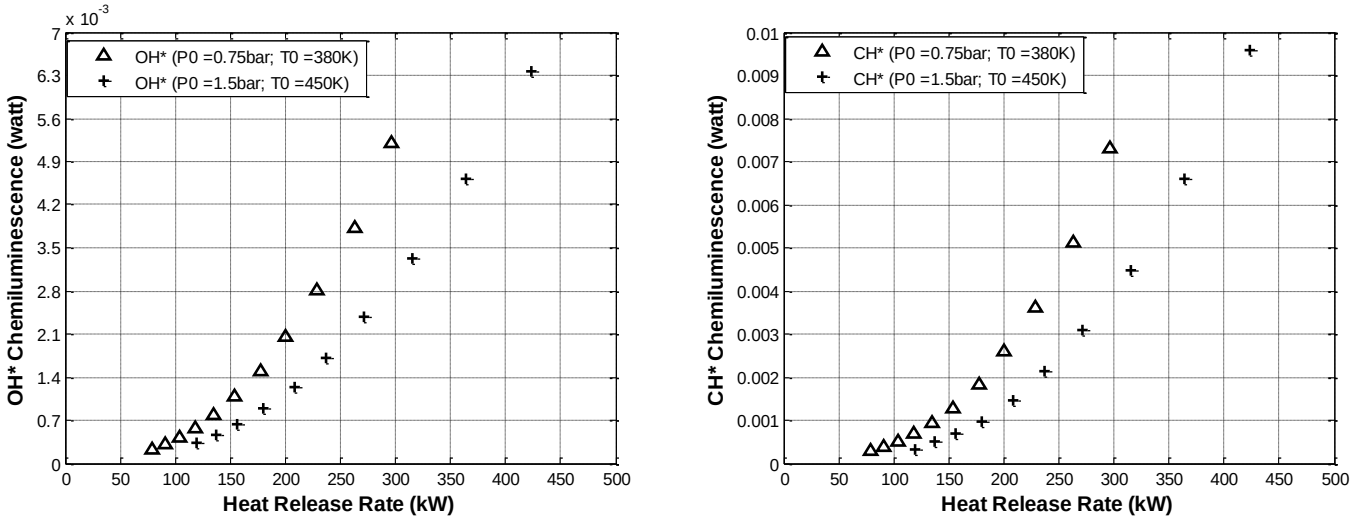


Figure 6. 8 Normalised OH* and CH* chemiluminescence as a function of mass fraction burned in premixed iso-octane / air combustion for different equivalence ratios ranging from 0.8 to 1.1, for a known initial temperature (450 K), and for three given initial pressures, i.e. 0.75, 1.5, and 3 bar. In each subplot, four different curves indicate normalised chemiluminescence with various equivalence ratios at the same initial temperature and pressure.

The influence of local pressure and local temperature on the absolute values of OH* and CH* (as can be seen in Figure 6.12b) is similar to that in methane flames. The stretch rate is restricted to a level below 26 s^{-1}, which has a limited effect on the laminar burning velocity and chemiluminescence. Finally, as with methane /air combustion, the absolute OH* and CH* chemiluminescence values are also not indicative values of heat release rate for laminar premixed iso-octane / air combustion in a constant volume combustion bomb, and this can be seen in Figure 6.9.



(a) (b)

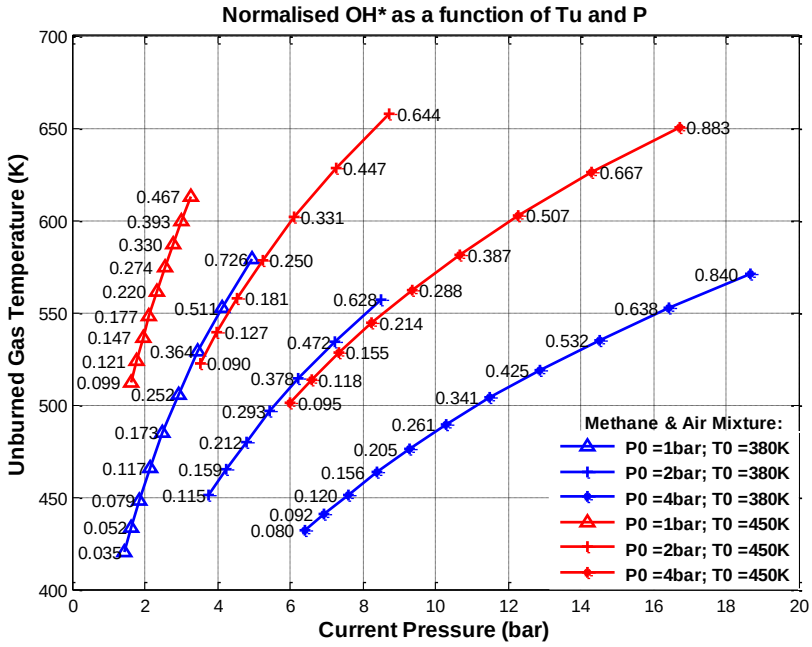
Figure 6. 9 Absolute OH* (Figure 6.9a) and CH* (Figure 6.9b) chemiluminescence as a function of heat release rate (*RoHR*) for stoichiometric iso-octane / air mixtures with different initial conditions, under which the isentropes are close to overlapping.

6.5 Issues to be Discussed

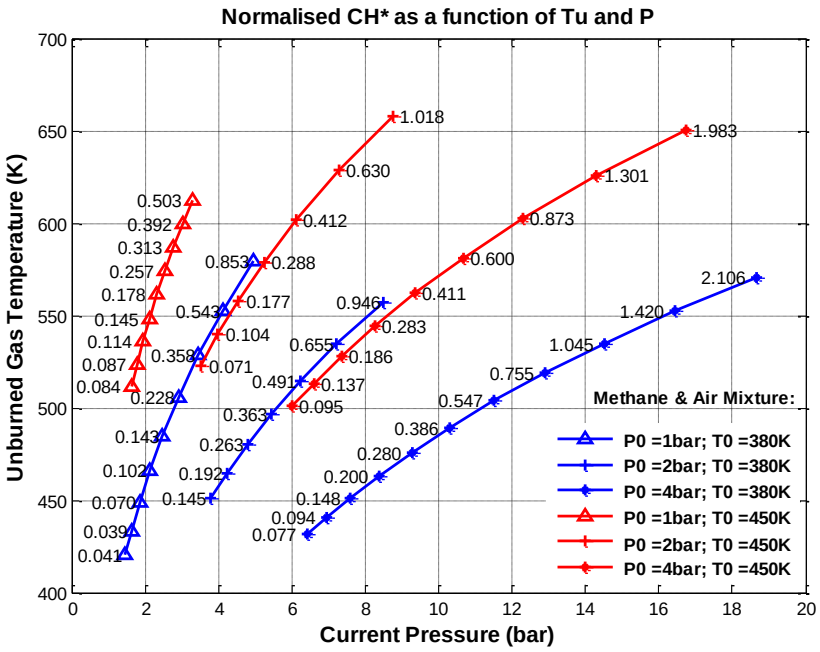
This work is an experimental study of OH* and CH* chemiluminescence emitted during combustion of different fuels (methane and iso-octane) at various initial conditions of pressure, temperature, and equivalence ratio. After ignition in the combustion bomb the pressure will rise (thereby increasing the temperature) so that a single experiment generates a sequence of data along an isentrope (as the unburned gas is in an adiabatic core). Therefore, by using a spherically propagating premixed laminar flame with careful control of the initial temperature and pressure, it is possible to start at different points along an isentrope. This leads to the first of two unexpected results, i.e. the OH* and CH* chemiluminescence (in terms of mJ/g) does not solely depend on the local pressure and temperature, but also on the time (or some other parameters). The second puzzling result is that chemiluminescence continues after the end of combustion, which cannot be explained by the combustion mechanism. Details about these two issues will be discussed next.

6.5.1 Chemiluminescence Discontinuity along Isentropes

The OH* and CH* chemiluminescence discontinuity can be best illustrated by the results for stoichiometric mixtures of methane and air which cover a wide range of local pressures and temperatures; and these are plotted in Figure 6.10. Figure 6.10 shows the isentropes followed by the compression of the unburned gas, and the 'spot values' are the normalised OH* and CH* intensities (mJ/g). Two of the isentropes are close to overlapping, and it is immediately apparent that in the overlap regions the normalised intensity is higher for the mixtures that were ignited at the lower initial pressure. These totally unexpected results led to the decision to choose the initial temperature and pressure such that there would be exact overlapping of the isentropes, with initial conditions of p_0 / T_0 = 2.0 bar/380 K, 2.77 bar/415 K, and 3.75 bar/450 K.

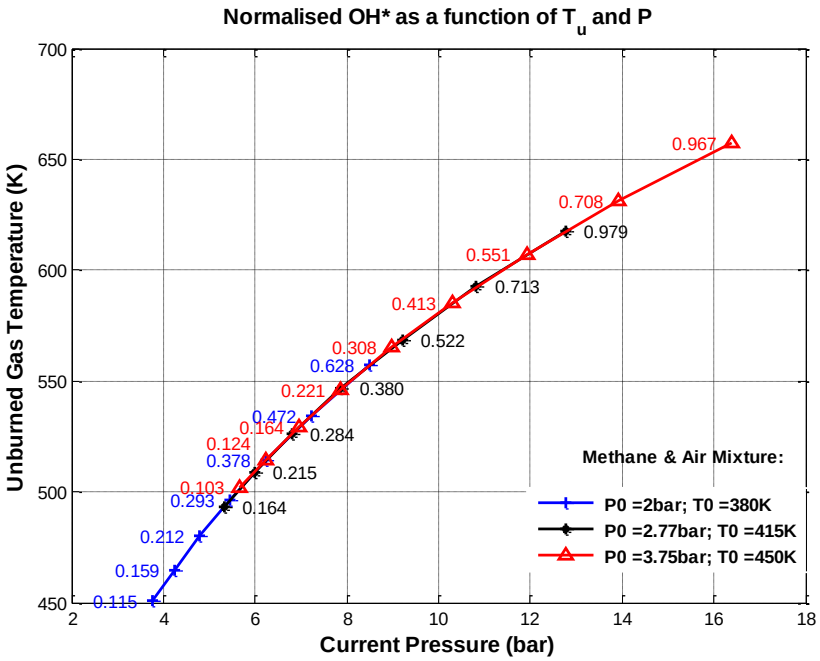


(a)

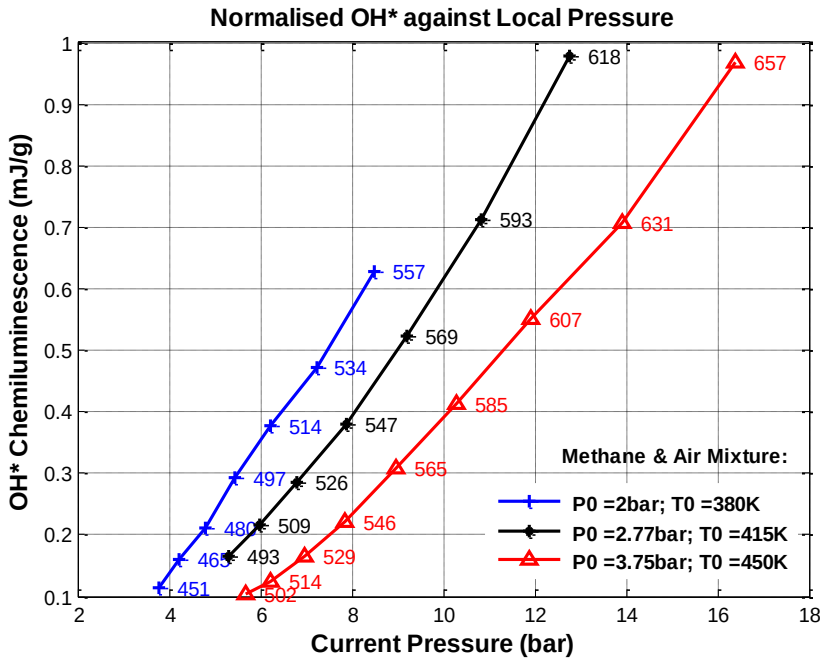


(b)

Figure 6. 10 Chemiluminescence from OH* (in Figure 6.10a) and CH* (in Figure 6.10b) with discontinuities along the isentropes for stoichiometric methane / air mixtures. Normalised chemiluminescence intensities (mJ/g) are shown as 'spot values'.

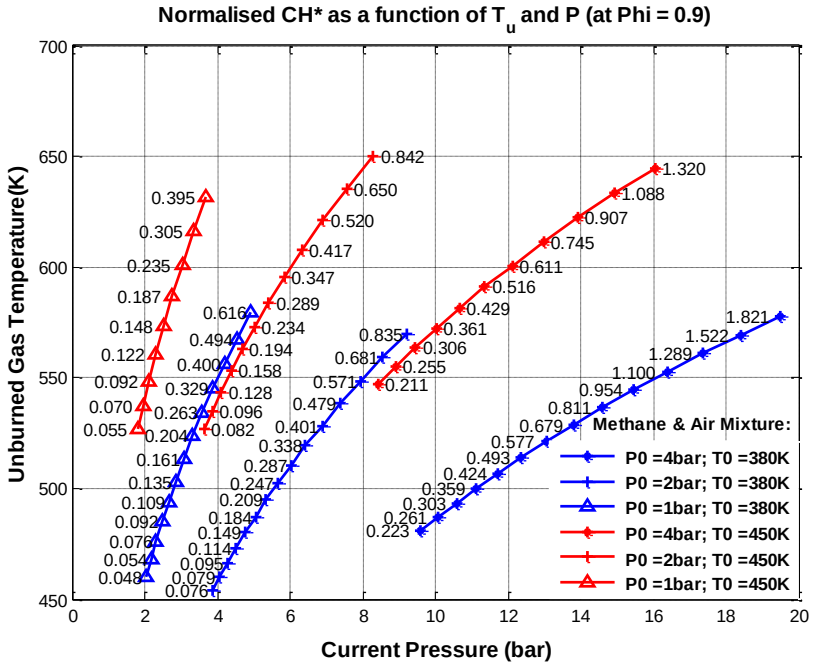


(a)

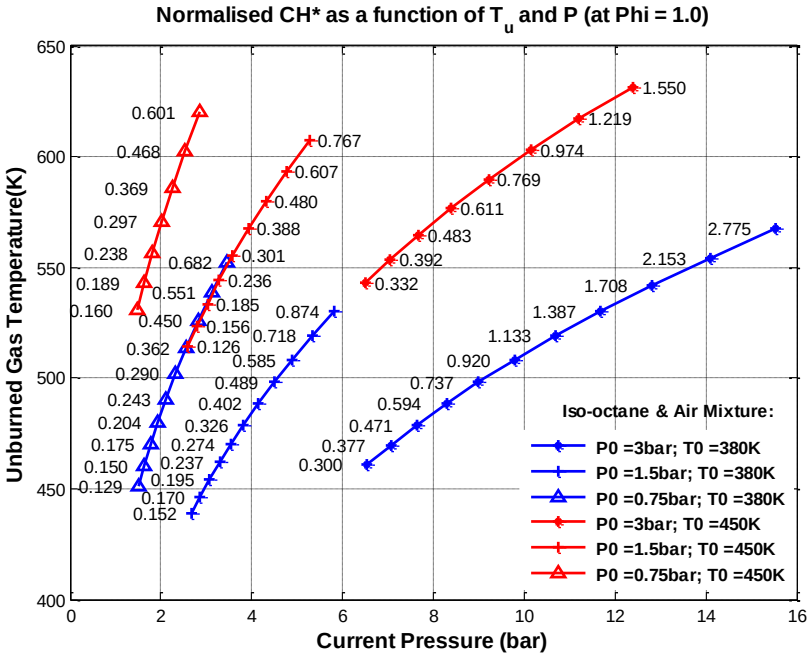


(b)

Figure 6. 11 (a) Three stoichiometric methane / air mixtures with different initial conditions of p_0 / T_0 = 2.0 bar/380 K, 2.77 bar/415 K, and 3.75 bar/450 K, chosen to follow an isentrope. Normalised OH* (mJ/g) are shown as 'spot values'. (b) The same data as Figure 6.11a, plotted to show the different normalised OH* chemiluminescence (mJ/g) at the same pressures (as the unburned gas is compressed isentropically, then the same pressure means the same unburned gas temperature); the unburned gas temperatures (K) are shown as 'spot values'.



(a)



(b)

Figure 6. 12 Chemiluminescence from CH* with discontinuities along isentropes for weak methane / air mixtures (Φ = 0.9, in Figure 6.12a) and stoichiometric iso-octane / air mixtures (in Figure 6.12b). Normalised intensities (mJ/g) are shown as 'spot values'.

Figure 6.11a shows the normalised OH* chemiluminescence intensity measurements (the normalised CH* intensity showed very similar results) for stoichiometric methane / air mixtures as 'spot values' for the three overlapping isentropes. It is quite clear that the chemiluminescence intensity does not just depend on the stoichiometry, operating pressure and combustion temperature, but that the mixtures which have been compressed over a longer period of time result in higher levels of chemiluminescence. These data are also plotted in Figure 6.11b, in which the normalised OH* chemiluminescence intensity has been plotted against pressure (the temperature, now shown as 'a spot value', is of course rising as well), and this makes the effect of history even more apparent. In addition, this unexpected result is not only seen in the stoichiometric methane / air flames, but can also be observed in non-stoichiometric methane / air and iso-octane / air flames as shown in Figure 6.12.

A possible explanation is that pre-flame reactions are occurring in the unburned gas, and that slight changes in the concentration of products of 'thermal decomposition' can have

a profound effect on the chemiluminescence intensity, perhaps because the combustion precursors have an influence on the relative importance of different the pathways for methane oxidation (Figure 1.2). As the pathways for OH* and CH* chemiluminescence are not the dominant ones, then small changes to the dominant pathway will have a larger effect on the OH* and CH* chemiluminescence pathways. One approach might be to simulate the build-up of radicals in the unburned gas using a Chemical Kinetics simulation code. For example, any reduction of OH concentration will drive reaction (6.5) in the reverse direction reducing the CH concentration which then leads to a reduction of the OH* concentration.

Results from a detailed chemical-kinetic mechanism were obtained with the assistance of Dr Trevor Davies of Shell from Professor Bernd Rogg of Rotexo GmbH. Professor Rogg modelled the adiabatic, spherically expanding methane / air flame in a combustion bomb with multi-species transport using *Cosilab*. As can be seen in Figure 6.13, at the time of the screenshot the flame has travelled about 5 cm; and the bomb radius has been taken as 30 cm (which is different from Oxford bomb radius of 8 cm).

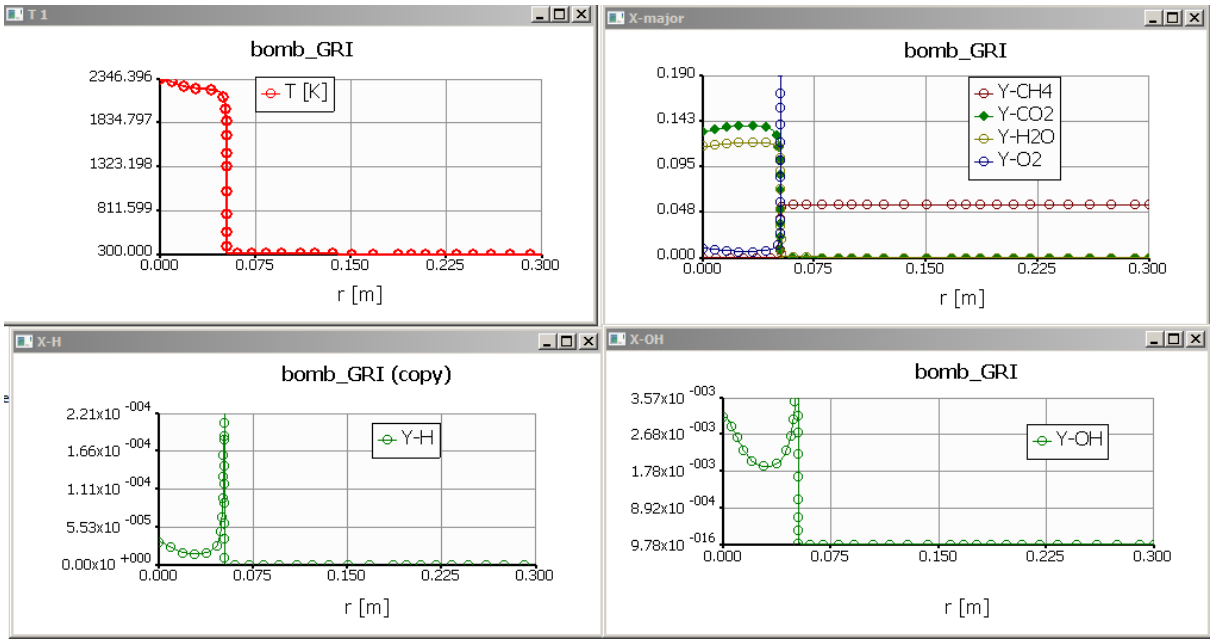


Figure 6. 13 (a) the top-left picture shows the instantaneous temperature profile, (b) the top-right picture shows the mass fractions of the stable species CH_4, CO_2, H_2O and O_2, (c & d) and the two bottom pictures show the mass fraction profiles of H and OH. (Modelled by Professor Bernd Rogg)

Dr Davies performed a simulation of the radical pool in the unburned gas for the methane / air experiments (starting at two different conditions on the same p_u - T_u isentrope). The simulations suggested there was no noticeable difference between the OH and H radical concentrations for the two isentropes. However, this bomb modelling is based on the assumption that the flame front is infinitely thin; and in addition, the effects of flame stretch are negligible. As mentioned in Section 6.3.2.3, the stretch effect is negligible so that does not need to be taken into consideration; while the flame front thickness, which is closely related to the preheat zone and reaction zone, might have some influence on the CH* and OH* chemiluminescence since it is supposed that chemiluminescence related reactions can occur in these regions.

The flame thickness, Δx, is defined [61] by the steepest tangent to the temperature profile between the unburned gas temperature (T_u) and burned gas temperature (T_b). For a steady laminar flame, the heat flux is given by [62]:

$$\dot{Q} = -\lambda \frac{T_b - T_u}{\Delta x} \tag{6.11}$$

where Δx is the flame thickness, λ is thermal conductivity calculated at the average temperature of T_u and T_b.

This heat flux diffuses from the reaction zone to the preheat zone and heats the downstream gas. Therefore its enthalpy rises to the ignition point due to this heat transfer. Assuming the unburned mixture is initially at rest, and that the kinetic energy is negligible:

$$\dot{m} c_p (T^0 - T_u) = -\dot{Q} \tag{6.12}$$

where $\dot{m}$ is the mass flux; c_p is specific heat at constant pressure and is the average of T_u and T_b. T^0 is the temperature at point of maximum rate of fuel depletion. Combining equations (6.11) and (6.12) yields:

$$\lambda \frac{T_b - T_u}{\Delta x} = \dot{m} c_p (T^0 - T_u) \tag{6.13}$$

Based on this, Heravi [63] presented an empirical equation used to estimate the flame thickness for the stated conditions of local temperatures and pressures for laminar methane / air mixtures at stoichiometric:

$$\Delta x = 0.2643 \left(\frac{T_\mathrm{u}}{300}\right)^{-0.85} (p_\mathrm{u})^{-0.58} \tag{6.14}$$

$$300\ \mathrm{K} \leq T_\mathrm{u} \leq 700\ \mathrm{K} \tag{6.15}$$

$$0.5\ \mathrm{bar} \leq p_\mathrm{u} \leq 30\ \mathrm{bar} \tag{6.16}$$

However, for methane / air mixtures starting at different conditions on the same p_u - T_u isentrope, the flame thickness are identical, so this cannot explain the differences in the chemiluminescence. Further investigation into the OH* and CH* reaction mechanisms was deemed as unprofitable, so attention was instead turned to other radicals coexisting with CH* and OH*, such as CO_2*.

Apart from the narrow-band chemiluminescence radicals CH* and OH*, the broad-band emission from the CO_2* reaction happens at a slower pace than the others [71]:

$$\mathrm{CO} + \mathrm{O} \rightarrow \mathrm{CO_2}^* \tag{6.17}$$

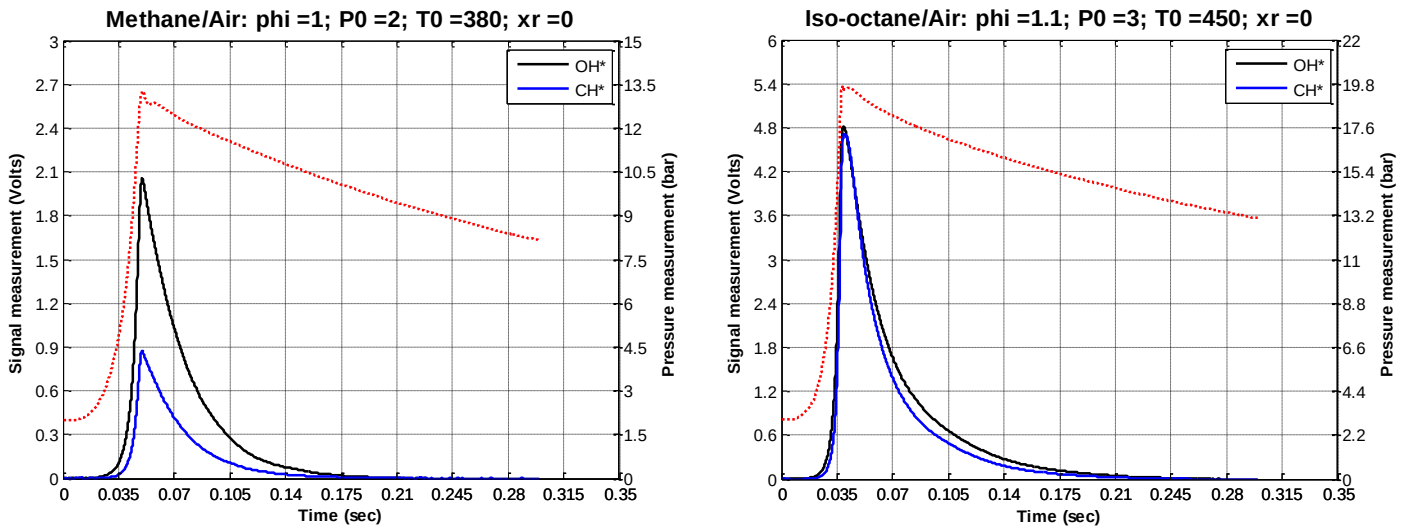
Rather than collecting light from a thin flame front, it might pick up a glowing volume of CO_2* from behind the flame front, that grows as time passes. This conjecture led to the spectral measurements, which will be discussed in detail in Chapter 7.

6.5.2 Chemiluminescence after the End of Combustion

The second puzzling result is that OH* and CH* chemiluminescence both continue after the end of combustion. Figure 6.14a shows results from methane / air mixtures; and iso-octane / air flame results can be observed in Figure 6.14b.

The work reported by Tinaut et al [48] is in some ways similar to the current work, as they too recorded the CH* and OH* chemiluminescence from a spherically propagating flame inside a combustion bomb using interference filters and PMTs. However, their optical

collection efficiency is undefined, but they did use a heat release type analysis to infer the rate of reaction. Tinaut et al also show CH* and OH* chemiluminescence signals persisting after the end of combustion, but they did not undertake any spectroscopic studies that would enable them to attribute these signals to species such as OH* or CO_2*. Comparing the measured peak pressure with an adiabatic model value (from the *BOMB* program), then it is always in the range of 95 – 100%. The experimental pressure is lower because the vessel is not adiabatic and the flame does not grow spherically, especially if combustion is slow and buoyancy has an effect. The chemiluminescence after the maximum pressure cannot be explained by the same combustion mechanism nor is it likely that there is post flame oxidation and chemiluminescence in the thermal boundary layer.



(a) (b)

Figure 6. 14 OH* and CH* chemiluminescence continue after the maximum pressure for methane / air (in Figure 6.14a) and iso-octane / air (in Figure 6.14b) flames.

The life time of excited state chemiluminescent radicals is very short ($<10^{-5}$ s) compared to the experiments (in the order of milliseconds), so this cannot account for the light emission after the 'end' of combustion. In addition, since there is an RC circuit in the PMT output circuit (in the inverting amplifier, details can be found in Chapter 3), the capacitor will discharge its stored energy through the resistor and this voltage across the

capacitor is time dependent. Hence it is necessary to examine the time delay in the RC circuit. Substitution of the largest feedback resistance R = 2 MΩ and the 1 pF capacitance into the time constant formula ($\tau = R \cdot C$) yields:

$$\tau = R \cdot C = 2 \times 10^{6} \times 1 \times 10^{-12} = 2 \times 10^{-6}\ \text{s} \qquad (6.18)$$

Compared with the experiments, this cannot be regarded as a possible explanation. Besides, the time response of the PMT is in the order of a nanosecond, which does not need to be taken into consideration.

Another possibility is that when the flame is being quenched that different kinetic mechanisms become more important, and this leads to more chemiluminescence. Although this would explain the chemiluminescence after the end of combustion, it would not explain why data from the same isentrope (but with different initial conditions) gives different levels of chemiluminescence.

As has been mentioned before, the hydroxyl radicals will be in equilibrium behind the flame front. Broida [64] found that the OH concentration in methane flames was about 2.5 times higher in the reaction zone than in the burnt-gas region. However, the most likely hydroxyl formation mechanisms result in electronically ground state radical (OH). Beside, even if this is able to explain OH* after the end of combustion, it is not possible to explain the CH* 'tail' since CH can only exist in the flame front. In conclusion, neither consideration of the hardware time response nor insight into CH* and OH* mechanisms are enough to explain the CH* and OH* chemiluminescence after the end of combustion.

In this case, broadband CO_2* mechanism could be the explanation. After the end of combustion as the pressure falls, the temperature in the adiabatic core also falls and the equilibrium will shift, so there will be more conversion of CO to CO_2*. Therefore it is vital to use a spectrometer with an ICCD on the output to record the broadband radiation from CO_2*; Chapter 7 will investigate and report on some spectroscopic measurements.

6.6 Conclusion

Chemiluminescence data were obtained from two engine-relevant fuels, i.e. methane and iso-octane, at different initial conditions of pressure, temperature, and equivalence ratio. For both fuels, the main CH* and OH* dependence found is upon equivalence ratio, local temperature and pressure. As the differences in stretch are so small, no conclusions can be made. However absolute values of OH* and CH* chemiluminescence investigated in a combustion bomb do not provide a practical way to monitor the heat release rate.

However, there are two striking results encountered, i.e. the discontinuity of the absolute OH* and CH* measurements along single isentropes, and chemiluminescence after the end of combustion, for which broadband CO_2* is suspected to be responsible. Chapter 7 will investigate spectroscopic measurements from the combustion bomb.

Chapter 7 Spectroscopic Results

The spectral analysis of laminar premixed flames in a constant volume combustion bomb provides valuable information on the chemiluminescence mechanisms. In this chapter, the experimental setup and the optical detection systems are briefly described. Then the spectrally resolved OH* and CH* chemiluminescence is studied analytically. This chapter also develops a spectra integration technique and quantifies the absolute OH* chemiluminescence. In addition to methane, butane was also investigated for sensing the CH* emission.

7.1 Overview

The local equivalence ratio [17, 47, 48, 49, 73] and heat release rate [48, 73] in flames have been indirectly measured by the band-pass filtered chemiluminescence in the wavelength range of the peak OH* and CH* transitions. However, these measurements are problematic because the measured OH* and CH* chemiluminescence is a superposition of the absolute OH* and CH* emissions on the contributions of broadband CO_2*. The spectroscopic measurements and analysis should help in a better understanding of the chemiluminescence mechanisms. It should also be useful in determining whether the absolute chemiluminescence and their ratio are useful in developing combustion diagnostics and sensors.

The flame radiation is sensitive to many factors such as the air/fuel ratio, the gas purity, the burner type, and the temperature. There is a scarcity of spectroscopic data from flame emissions in a constant volume combustion bomb. Hence experimental data are needed for analysis. Two optical detectors were chosen for this study, an Ocean Optics USB4000 spectrometer and a Princeton ICCD Kinetics spectrometer from the EPSRC Equipment Loan Pool. The description of the two spectrometers and their optics is in Section 7.2. The Ocean

Optics spectrometer has an absolute calibration while the ICCD kinetics spectrometer has a faster response.

The flame spectra are examined, so as to quantify the background intensity emission from CO_2*. The consistency between the Ocean Optics spectrometer output and the PMT results are also investigated in Section 7.3.

Two types of fuel, methane and butane, were studied. The ability of absolute OH* chemiluminescence to be used for sensing important combustion parameters, along with other future work, will be discussed in Chapter 8.

7.2 Optical Equipment

7.2.1 Ocean Optics USB4000 Fiber Optic Spectrometer

A spectrometer is a device that measures the radiation intensity as a function of wavelength. It basically consists of a diffraction grating, a slit, and some kind of photo-detector (such as a CCD), all automated and controlled by a computer.

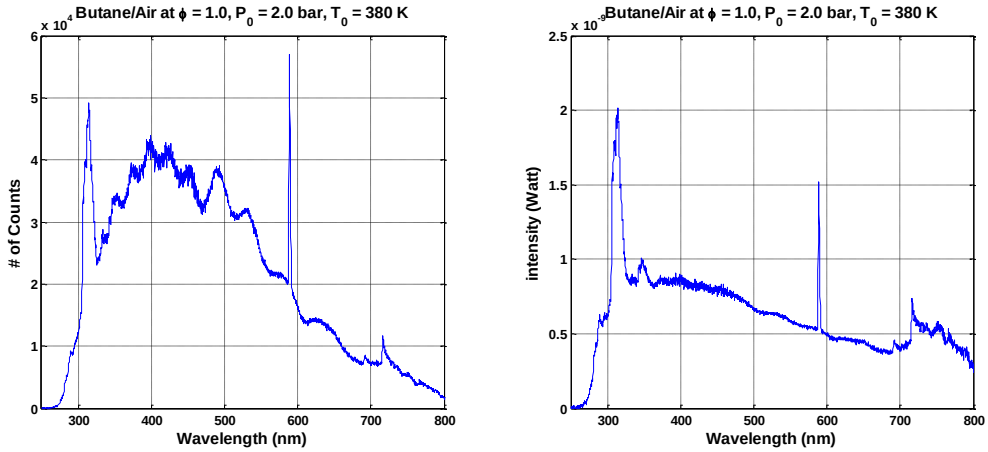


Figure 7. 1 Example of a spectroscopic measurement using the Ocean Optics USB4000 spectrometer. The left plot shows radiation (in terms of # of counts per pixel) as a function of wavelength, the right one converts the data to spectral intensity (in units of watts) as a function of wavelength using its calibration data.

The Ocean Optics USB4000 spectrometer has an optical bench, where light from an optical fibre enters, reflects from an internal mirror, as a collimated beam towards the grating,

and is separated according to its wavelength by the diffraction grating. The grating is permanently fixed in place to eliminate mechanical shifts or drift. The diffraction grating in this study has 600 lines/mm blazed at 400 nm, allowing the observation of a 650 nm spectral range in the UV–visible region. For the USB4000, the 3648-element Toshiba TCD1304AP linear (i.e. 1D) CCD array detector is installed. Each pixel responds to the wavelength of light that strikes it. Electronics bring the complete spectrum to the software. The USB4000 has a 16-bit A/D, with a 300:1 (at full signal) signal-to-noise ratio, and an electronic shutter for spectrometer integration times as fast as 3.8 milliseconds (which corresponds to a maximum repetition rate of 101 Hz for either an external hardware trigger or normal mode data acquisition). The USB4000 spectrometer output is displayed in terms of counts at each pixel, and its calibration is available to convert the data to a spectral intensity plot (see Figure 7.1).

7.2.2 Princeton ICCD Kinetic Spectrometer

The Princeton ICCD kinetic spectrometer is suitable for spectroscopy of low-intensity UV and visible sources. It has a 1024×256 pixel sensor array, which is an unremarkable specification. It is however recommended to use an ROI (region of interest) that runs from column 1 to 1008 since the last few pixels on the sensor give spurious results.

In the Princeton ICCD, light is fibre-optic-coupled into a grating spectrograph, in which the radiation is spectrally dispersed by a choice of gratings (i.e. 150 lines/mm, 600lines/mm, and 2400 lines/mm) onto the intensified CCD camera fitted to the exit port of the spectrograph. Experimental parameters such as the spectral window (wavelength range), exposure time, intensifier gain and triggering mode are set in the software and accompanying controller unit or on the camera. Two readout rates are available: 430 kHz (16 bit digitisation) and 1 MHz (14 bit digitisation). The faster digitiser comes at a cost to precision as a result of increased readout noise. The built in thermoelectric cooler for the ICCD was used to reduce

dark noise, so the camera system was supplied with cooling water and a gas purge of dry nitrogen.

The distinguishing feature of the Princeton ICCD is that the sensor has a 'kinetics' design. This means that a metal mask has been applied to cover the entire face of the chip, exposing only row number 252. At the end of each exposure period, the accumulated charge can be shifted from the exposed row to the neighbouring row in as little as 15 µs, shielding the charge from any further accumulation and preparing for the next exposure. The charge continues to be shifted down the sensor as further exposures occur. This approach allows a burst of spectral measurements to be made at a high repetition rate.

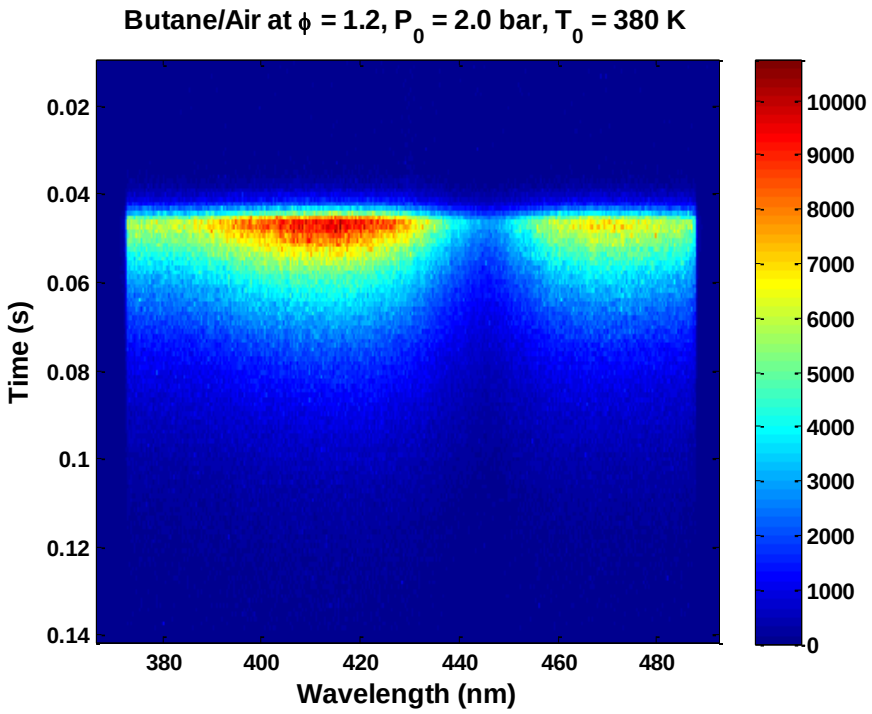


Figure 7. 2 Example of an image from the Princeton ICCD kinetics spectrometer (with 600 lines/mm diffraction grating with centre wavelength at 430 nm).

A 'free run' image in kinetics mode will initially fill the sensor and then read it out. Note that filling the sensor with data will take a duration of $N \times (\tau + 15\ \mu s)$, where N is the number of rows (i.e. 255) in the image and τ is the exposure duration set in the software; so a 10 ms exposure takes longer to appear (about 2.6 s) than would at first be expected. The

resulting image from the Princeton ICCD kinetics spectrometer system will essentially encode wavelength in one dimension (columns) and time in the other (rows). A sample image is shown in Figure 7.2.

The kinetics system can be instructed to move the charge more than one row at a time by varying the 'Window Size' parameter in the 'hardware setup'. A window size of 1 moves charge by one row at a time, whereas a window size of 5 will move the charge by 5 rows.

Whatever kinetics mode options is chosen, the camera will not read out the sensor until the CCD is full. In a kinetics experiment, it is likely that only one exposure is to be read out. If M exposures are to be collected, the window size needs to be adjusted to ensure $255/\text{window size} \geq M$.

In 'experiment setup' there is also a choice when running in kinetics mode between 'single trigger' and 'multiple trigger'.

Single trigger waits for a negative-going TTL pulse (i.e. external sync pulse) at the external sync input. Figures 7.3 – 7.6 show timing diagrams for this configuration. In essence, the camera will open the shutter upon receiving the external sync pulse, and then move the charge (with the accompanying dip in norm3) after each exposure duration (τ, in this case, 3.8 ms) passes. The camera does not wait between exposures; it simply gets them done as quickly as possible. The camera shutter is open during charge transfer, which could be a drawback of using this mode. Exposures will be collected at a rate given by the inverse of the exposure duration (so long as the charge transfer duration is much smaller than exposure duration).

The multiple trigger mode is shown in Figure 7.7 and Figure 7.8. It is shown that a separate exposure is made for each external sync pulse. Once each exposure is complete, the camera moves the charge the distance required (set by the window size) and waits for the next sync pulse to arrive. This means that this triggering mode is the most flexible. In the

example of Figures 7.5 and 7.6, the time between external sync pulses was set to 20 ms. Window size was set to 5, corresponding to 80 µs (5 × 16 µs, though the theoretical charge transfer time is 15 µs as mentioned before) charge transfer time at the end of each exposure.

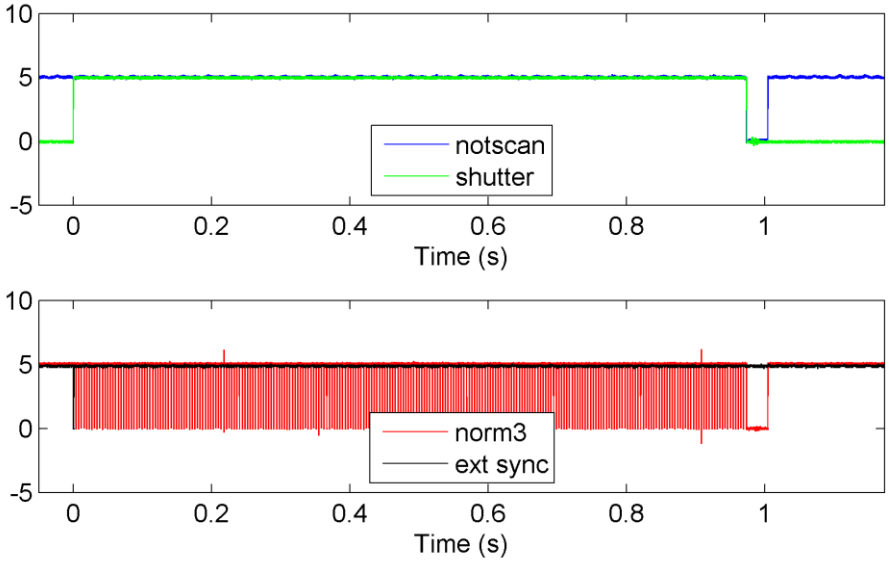


Figure 7. 3 Single trigger kinetics mode (window shift size is set to be 1). The exposure duration (τ) is set to be 3.8 ms. A surprisingly short readout time is shown (by the notscan pulse being low) at the end. The shutter is open for entire exposure, and the shutter open duration is 255 × 3.8 ms = 969 ms.

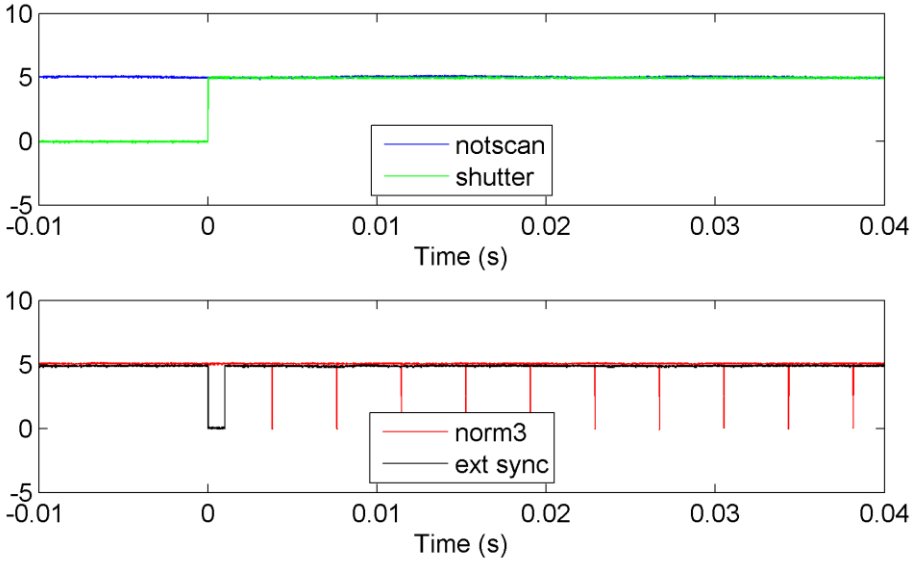


Figure 7. 4 Zoomed in version of Figure 7.3. Time between norm3 pulses is 3.8 ms. Negative pulses on norm3 are 16 µs wide, indicating the time taken to move the charge one row. The negative-going sync pulse (i.e. external sync pulse) is 1 ms wide, which was set by a function generator.

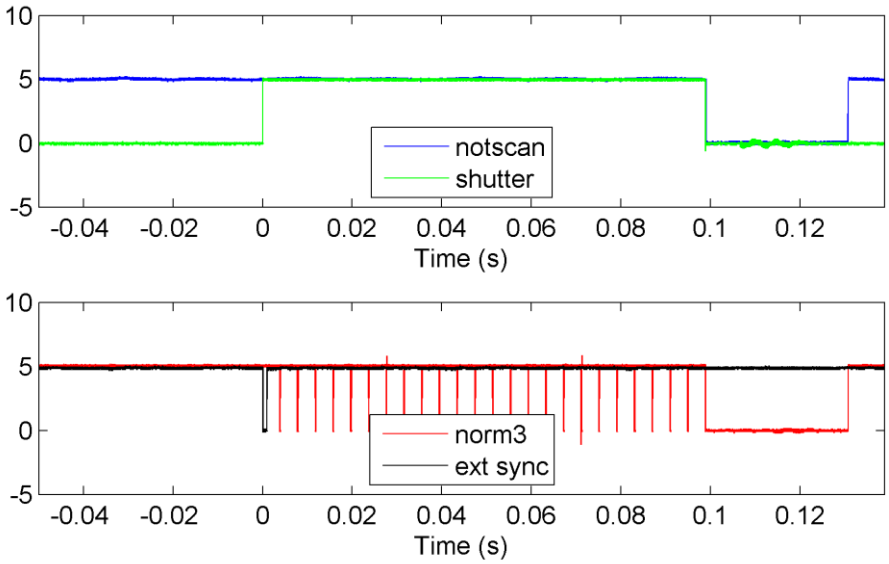


Figure 7. 5 Single trigger kinetics mode (window shift size is set to be 10). The exposure duration (τ) is set to be 3.8 ms. The shutter is open for entire exposure, and the shutter duration is for (255/10) × 3.8 ms = 95 ms.

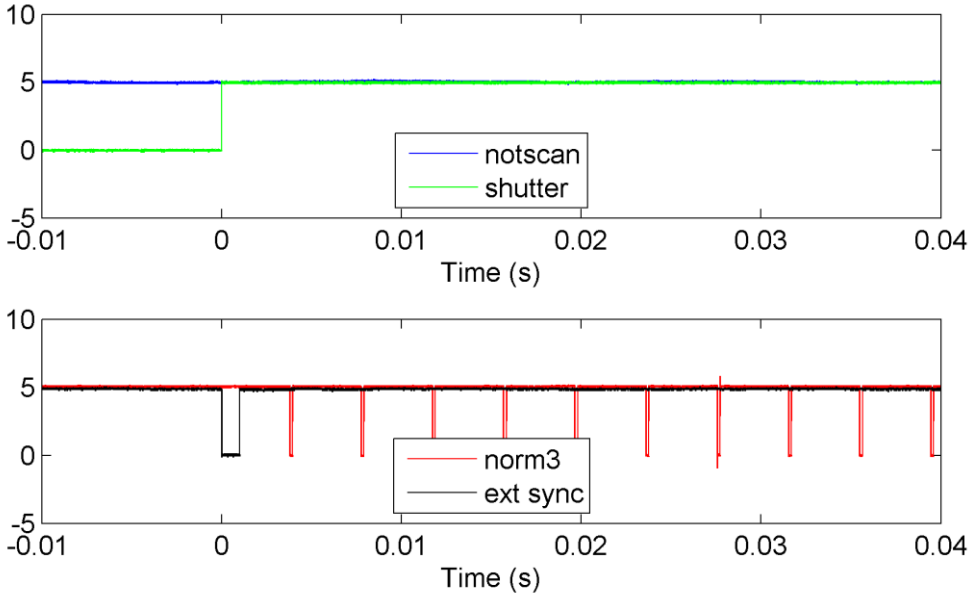


Figure 7. 6 Zoomed in version of Figure 7.5. Negative pulses on norm3 are 160 µs wide, indicating time taken to move charge ten rows. The time between the norm3 pulses is 3.8 ms.

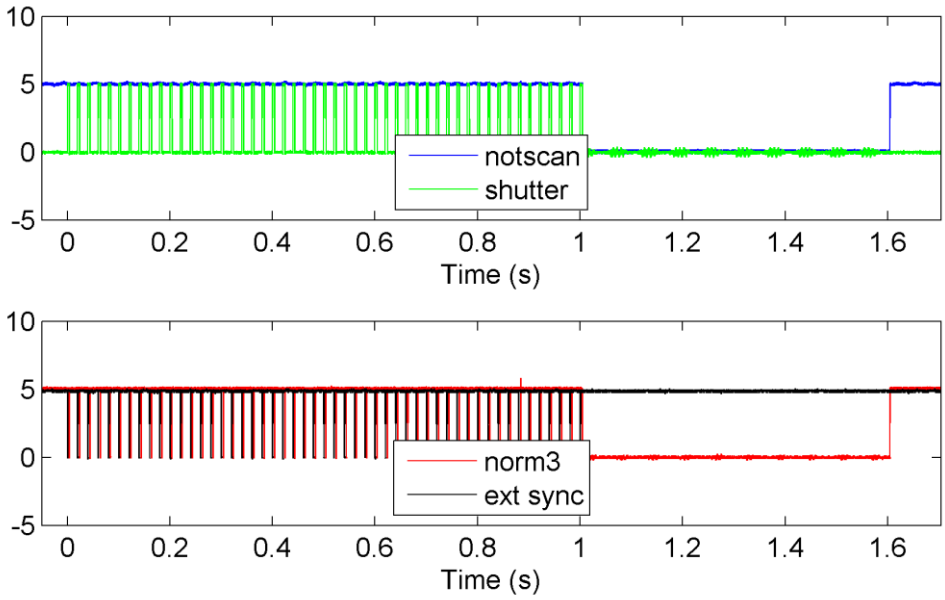


Figure 7. 7 Multiple trigger kinetics mode (window shift size is set to be 5). The exposure duration (τ) is set to 3.8 ms. External sync pulses arrive every 20ms. 51 (i.e. 255/5) exposures mean that the total experiment time is just over 1 s (i.e. 51 × 20 ms = 1020 ms). The readout duration is 600 ms as can be seen from the notscan pulse.

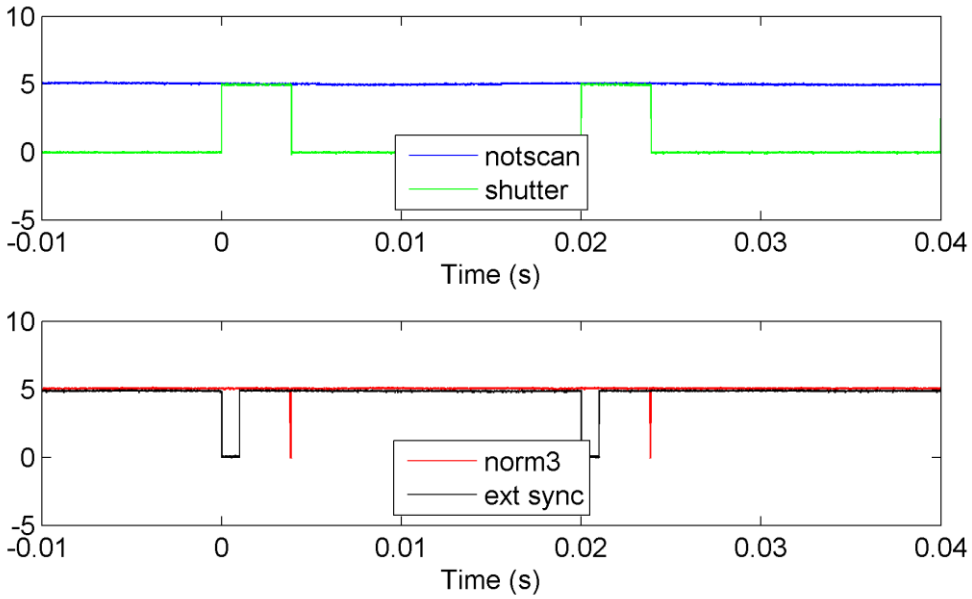


Figure 7. 8 Zoomed in version of Figure 7.7. The negative pulses on norm3 are 80 µs wide, indicating the time taken to move the charge five rows. Each external sync pulse is followed by a 3.8 ms shutter exposure.

In the following spectral measurements, the single trigger mode was used.

7.2.3 Narrow field of View Optical System

The optical system for the Princeton ICCD consists of an optics cage holding a 25 mm diameter fused silica lens (f = 40 mm) and the fibre optic link to the detector.

Figure 7.9 shows that a narrow field of view system is being used with the Princeton optical system (as with the PMT system) so as to avoid collecting scattered photons from the inner walls of the vessel. That is, the detectable volume should not exceed the dimensions of the far window. This is because the scattered photons may be absorbed instead of being reflected and would be hard to quantify. However, the diameter of the detector and lens has been changed, which means the well-established PMT optical system geometry will not be suitable for the current optical systems. Hence a new narrow field of view optical system needs to be developed. In this section, the Princeton optical system will be presented in detail; the optical system for the Ocean Optics was developed in the same way.

The narrow field of view system is based on two simplifications: (a) paraxial ray propagation; and (b) the thin lens approximation.

The combustion bomb has an internal diameter of 160 mm, with two 40 mm diameter windows - one on either side of the vessel. The optical axis of the system is designed to go through the centres of these two windows. A 25 mm diameter lens is used to focus the light from the central plane in the combustion bomb onto the fibre end of the Princeton spectrometer. The effective diameter of the lens is taken to be 22.5 mm rather than 25 mm, owing to the presence of the retaining ring which must holds the lens in the mounting tube. The fibre end is sitting at the focal length (40 mm) of the lens. The fibre end of the spectrometer has a diameter of 1 mm (Figure 7.9 is shown out of scale). The most restricting case (i.e. farthest lens-to-object distance u) can be determined by considering a beam of parallel light rays, among which the outer ray from the edge of the far window just passes the

edge of the lens and the un-deviated ray that passes through the centre of the lens arrives the edge of the fibre end:

$$\frac{det/2}{v} = \frac{(40-22.5)/2}{u} \tag{7.1}$$

In Equation (7.1), variable *det* is the diameter of the spectrometer fibre end, i.e. 1 mm, (40-22.5)/2 represents the radius-difference between the bomb window and the lens (in mm), *D* is the diameter of the bomb, and *v* is lens-to-detector distance, i.e. 40 mm. Solving this equation will lead to *u* = 700 mm. So, for any location smaller than 700 mm, the detector will collect photons within the far window limits (i.e. a narrow field of view).

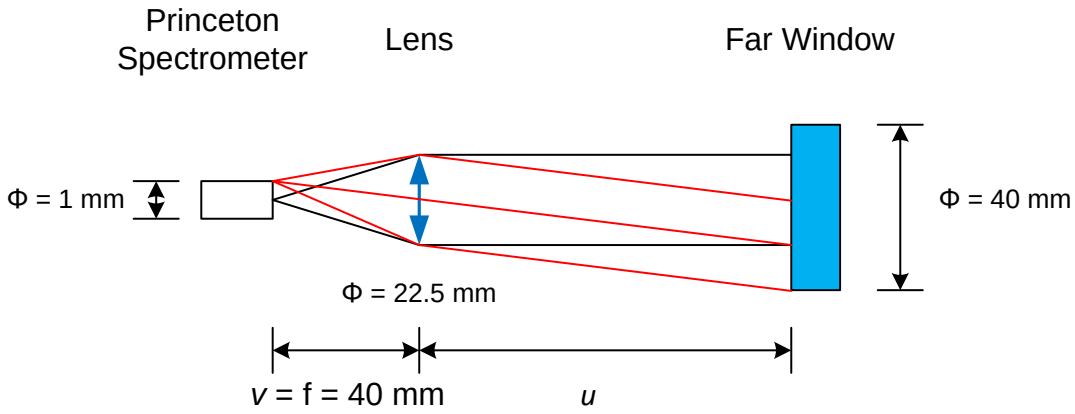


Figure 7. 9 Geometric arrangement for the Princeton optical system.

7.3 Results

7.3.1 Introduction

Spectral analysis investigates electromagnetic radiation as a function of its wavelength. Spontaneous emissions of flames, in the part of ultraviolet and visible part of spectrum, are of particular interest since the chemiluminescent radiation mainly falls into this domain.

There is a general agreement that the following chemiluminescent radicals are emitted naturally with hydrocarbon flames, i.e. OH*, CH*, C_2* and CO_2*. The hydroxyl radical OH* gives a strong spectrum which peaks at 306.4 nm; three band spectra ascribed to the CH* radical are emitted in the reaction zone of the flame, the strongest of which lies at 431.5 nm. Another narrow-band hydrocarbon radical C_2* gives the characteristic blue-green colour. C_2*

is not considered because it can only be seen in rich to slightly lean flames; while CH* and OH* are the primary narrow-band sources of chemiluminescence across a wide range of air / fuel ratio. Besides, the three mentioned radicals are superimposed on another fairly strong broadband spectra from excited CO_2*, which extends from below 300 nm to 600 nm. Additionally, CO_2* is stronger compared with other possible broadband emissions in the UV and visible regions of the spectrum, hence CO_2* chemiluminescence is used as a label for the background emissions. Other weak emissions, such as HCO*, CO*, and CH_2O* are of secondary importance.

It is worth noting that the flame radiation is 'not only sensitive to temperature, varying with wavelength and the kind of gas mixture, but also depends on many other factors which include the gas / air or gas / oxygen mixture ratio, the gas purity, the burner type, the gas flow (laminar or turbulent) [67]'. Chemiluminescence measurements were conducted under particular experimental conditions; therefore spectra obtained in the current test rig may not be always relevant to other flames. The published literature does not contain information on chemiluminescence spectra from a constant volume combustion vessel. As this combustion system covers a wide range of local pressures and temperatures, there is a need to investigate the chemiluminescence spectra from a combustion bomb.

The remainder of this section has been divided into three parts. The first part examines a typical flame spectrum. In the second part, interleaved measurements have been carried out with the USB4000 spectrometer so as to build-up a composite spectra history. This enables a comparison to be made of the consistency between the temporal evolution of the integrated chemiluminescence spectra and the photomultiplier tube measurements. The last part quantifies the absolute OH* chemiluminescence after subtraction of the background intensity emissions from the CO_2*. Additionally, butane/air combustion was studied since the CH* signals are stronger than in methane/air combustion.

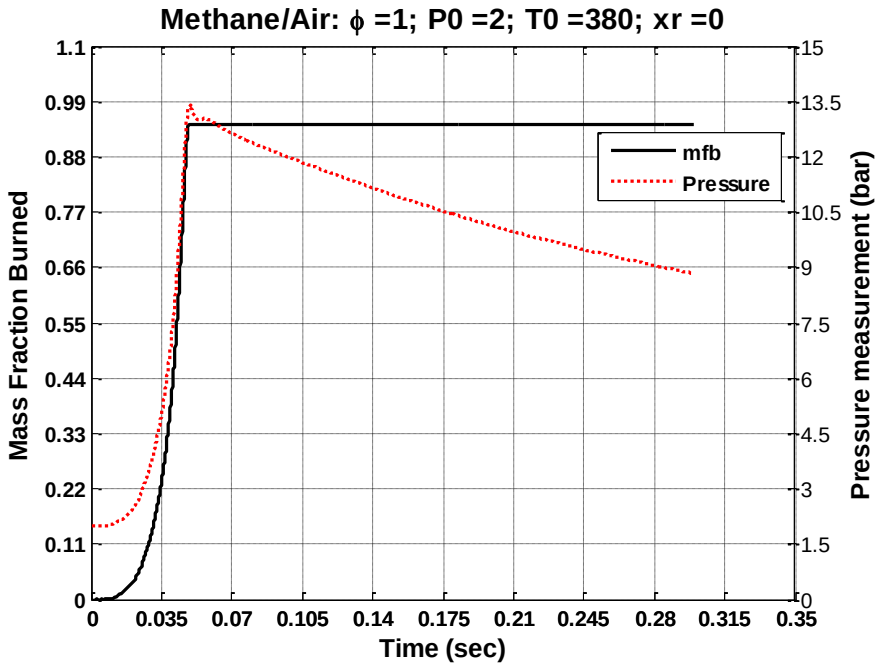
7.3.2 Chemiluminescence Spectra

7.3.2.1 Methane / Air Flame Spectra

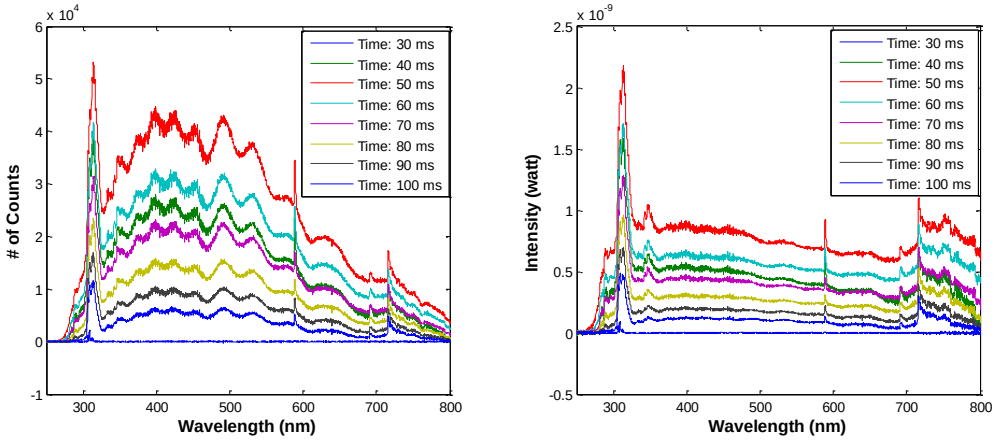
Preliminary stoichiometric methane/air combustion tests were conducted at initial conditions p_0, T_0 of 2 bar and 380 K. Chemiluminescence measurements were performed using the ICCD spectrometer with 150 lines/mm diffraction grating and a USB4000 fibre-optic spectrometer with an integration duration of 3.805 ms. Both of them were simultaneously triggered by a TTL pulse that generated the ignition spark.

Figure 7.10b shows the spatially and spectrally resolved chemiluminescence in terms of counts at each pixel from the USB4000 spectrometer; its calibration is used to calculate the energy output, which is shown in Figure 7.10c. This time-normalised (against integration time) energy is given in terms of watt, and it is a wavelength dependent output. When the USB4000 spectrometer is externally triggered it allows a burst of measurements to be made at the highest repetition rate of 100 Hz; the curves in Figure 7.8 represent eight sequential emission spectra obtained at this repetition rate. The wavelength resolution of the detector is 0.2 - 0.22 nm at 510 nm and 0.17 – 0.19 nm at 890 nm.

As can be seen in Figure 7.10c, there are several distinct spectral bands superimposed on a broadband background emission CO_2*, which is caused by the recombination of CO with atomic oxygen. The excited hydroxyl OH* has a strong narrowband spectra in the UV region (it peaks at 306.4 nm). It should be pointed out that it is the only observable OH* band spectra in methane / air flame; the other two OH* band systems in the UV at 224.8 to 260.0 nm ‘have never been identified in flames’ [67]. There is a sodium band spectrum with a peak at 589.6 nm, which may come from contamination. There are also strong bands ascribed to water vapour in the infrared region. Another thing worth mentioning is that the background radiation has been removed by subtracting a measurement taken by the spectrometer before the start of combustion.



(a)



(b) (c)

Figure 7. 10 (a) Pressure and mass fraction burned as a function of time, and (b, c) chemiluminescent emission spectra from combustion bomb for stoichiometric methane / air flames with p_0 = 2 bar and T_0 = 380 K measured by the Ocean Optics USB4000 spectrometer. Figure 7.10b shows the detected signal in terms of counts, and Figure 7.10c illustrates the wavelength-dependent emission intensity.

Figure 7.10c shows that in the ultraviolet, the OH* and broadband CO_2* radiation from the reaction zone are increasing as the spherical flame expands towards the bomb wall, and the radiation continues after the peak pressure (achieved at around 50 ms) and then decays with time. The previous PMT results (as can be seen in Figure 6.13) show that the

maximum radiation occurs coincident with the peak pressure, but OH* and CO_2* chemiluminescence continue after the end of combustion. In high pressure methane flames, Nori [71] explained that 'the post flame product gases are a source of both OH* and CO_2* chemiluminescence, due to the formation of OH* via (H+O+M) and CO_2* via CO+O'. Furthermore, as the pressure decreases there will be a shift towards more conversion to excited OH* and CO_2*. The time evolution of various spectral species is shown in Figure 7.11.

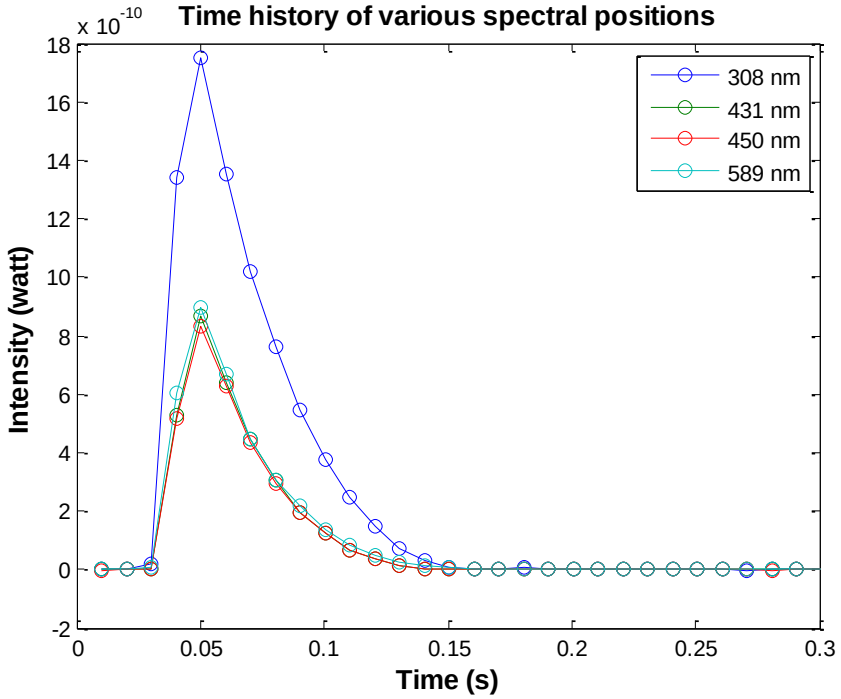


Figure 7. 11 Time history of the spectral intensities at 308, 431, 450, and 589 nm. Emission spectra were measured from stoichiometric methane / air flames with p_0 = 2 bar and T_0 = 380 K.

The most striking observation is that there is no obvious evidence of CH* can be found in the flame spectra. Figure 7.11 compares the maximum CH* intensity (located at 431 nm) with a line spectrum at (450 nm) which gives a characteristic value for the CO_2*chemiluminescence, and the two spectra are close to be overlapping. It is worth noting that 450 nm wavelength is chosen because CO_2* is the only spectral source in this range. Since the flame spectra indicates little variation in the background intensity of CO_2* (as is

seen in Figure 7.10c) over the range of wavelength of the CH* feature spectra, a further data processing procedure is to separate the CH* radical and CO_2* chemiluminescence by comparison of the CH* band-pass filtered emission (centred at 430 nm with a half bandwidth of 5 nm) with emissions from the spatially adjacent region (i.e. between 415 nm and 425 nm). Therefore the mean values for the CH* feature spectra are calculated as the arithmetic average of the intensities at 425 and 435 nm, and the mean CO_2* intensity takes the average of the intensities at 415 and 425 nm, i.e.

$$I_{\mathrm{CH}^*} = \frac{1}{2}(I_{425} + I_{435}) \tag{7.2}$$

$$I_{\mathrm{CO_2}^*} = \frac{1}{2}(I_{415} + I_{425}) \tag{7.3}$$

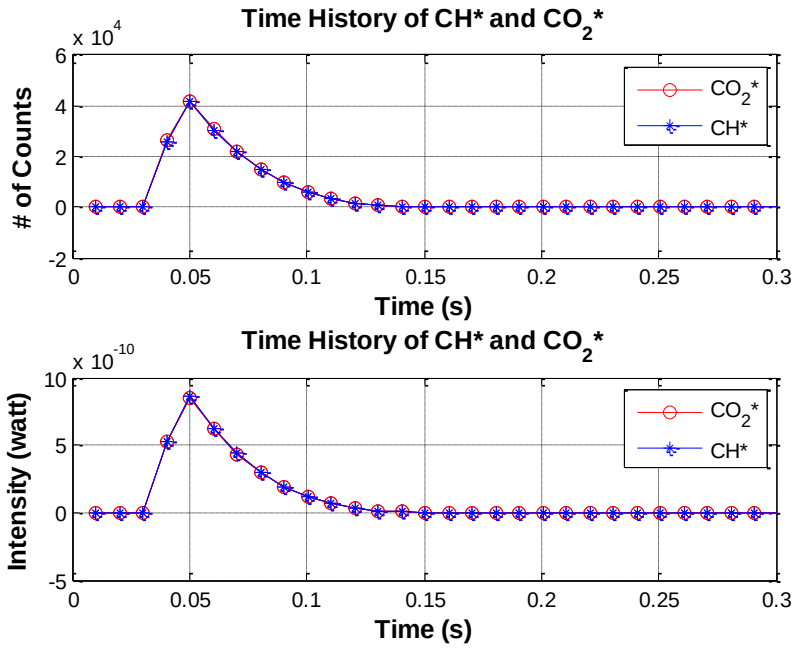
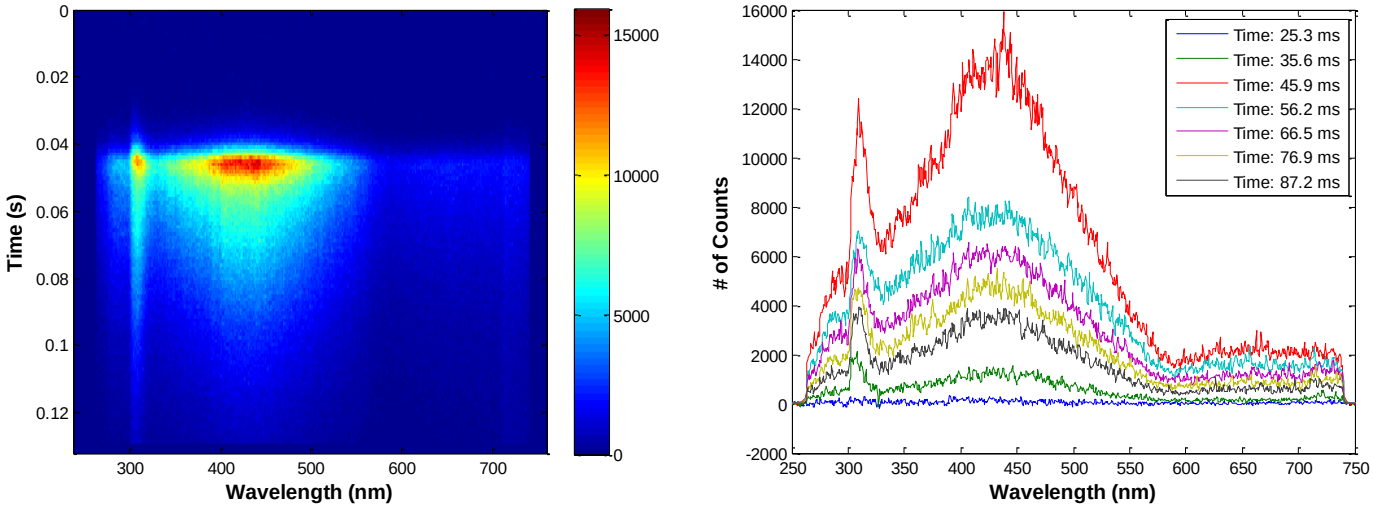


Figure 7. 12 Time history of CH* and background CO_2* 'line spectrum' from the stoichiometric methane/air flame with p_0 = 2 bar and T_0 = 380 K detected by USB4000 spectrometer. In this plot, either the CH* or CO_2* 'line spectrum' is obtained by averaging values at the upper (i.e. 435 nm and 425 nm) and lower (i.e. 425 nm and 415 nm) boundaries.

It can be seen that temporal trajectories of both the CH* and CO_2* are fully overlapped, which means that the integrated chemiluminescence detected by the photomultiplier tube with the interference filter (430±5 nm) is almost entirely from CO_2*.

The high repetition-rate Princeton ICCD was also used to check the spectral features of the flame chemiluminescence. In Figure 7.13, the chemiluminescence emissions in the methane / air flame during combustion process are visualised by the Princeton ICCD spectrometer. Figure 7.13a gives temporal and spatial information on an image plot, and the colour bar interprets the scale (i.e. chemiluminescence measurements in terms of # of counts). The *x* and *y* axes in the map represent wavelength in nm and time in seconds respectively. Figure 7.13b measures the spatially and spectrally resolved chemiluminescence in terms of counts at each pixel from the Princeton ICCD spectrometer. The grating dispersion allowed simultaneous capture of the ultraviolet and visible optical emission spectrum in the range of around 238 – 767 nm. The data were collected at a repetition rate of 1 kHz (exposure time: 1 ms). As with Figure 7.10, the background noise (in terms of # of counts) has been removed.



(a) (b)

Figure 7. 13 The same methane / air combustion event as in Figure 7.10 (Φ = 1, p_0 = 2 bar, and T_0 = 380 K), recorded by the Princeton ICCD spectrometer. The colour bar included in Figure 7.13a is to interpret the false colouring scale (i.e. chemiluminescence spectra in terms of # of counts) of the image.

Figure 7.13 gives the temporal evolution of the spatially and spectrally resolved chemiluminescence emissions during the combustion process. Compared with the Ocean Optics USB4000 spectrometer it is clear that the Princeton ICCD spectrometer has a much

higher noise level. The consistency between ICCD spectrometer and USB4000 spectrometer is investigated by comparing the spectra of various chemiluminescence radicals. As with the records from the USB4000 spectrometer (in Figure 7.10b), the spectral features of the OH* and CO_2* radicals can be recognized in the Princeton ICCD measurements. Furthermore, both OH* and CO_2* extend farther into the post-combustion region. The spectral lines of CH*, again, cannot be detected. However, some spectral resolution was lost (such as the sodium lines). The disappearance of the sodium spectra can be attributed to the relatively poor red-sensitivity in the ICCD spectrometer (with 150 lines/mm diffraction grating with centre wavelength at 500 nm), since there is an order of magnitude reduction in red sensitivity compared with blue sensitivity; but this alone cannot explain CH* disappearance. Another explanation is that the intensifier has compromised the spectral resolution by 'leakage' between pixels. Although there is background signal variation in the CH* wavelength region, a similar process (as with Figure 7.12) has been implemented to compare the CH* band-pass filtered emission and the adjacent emission (regarded as background CO_2*), which is shown in Figure 7.14.

There are three significant observations to be seen in Figure 7.14. Firstly, the temporal traces of CH* and CO_2* are indistinguishable, and this might be because CH* chemiluminescence intensity is too faint to be detected in laminar premixed stoichiometric methane / air flames. Secondly, the CO_2* chemiluminescence rises steeply followed by a long tail after the end of combustion, which suggests that the CO_2* chemiluminescence extends throughout the burnt-gas zone due to the formation of CO_2* via recombination of CO and O atoms in the hot products. Thirdly, the peak chemiluminescence occurs 4 ms earlier than that measured by USB4000 spectrometer, but this can be attributed to the lower repetition rate of the USB4000 spectrometer.

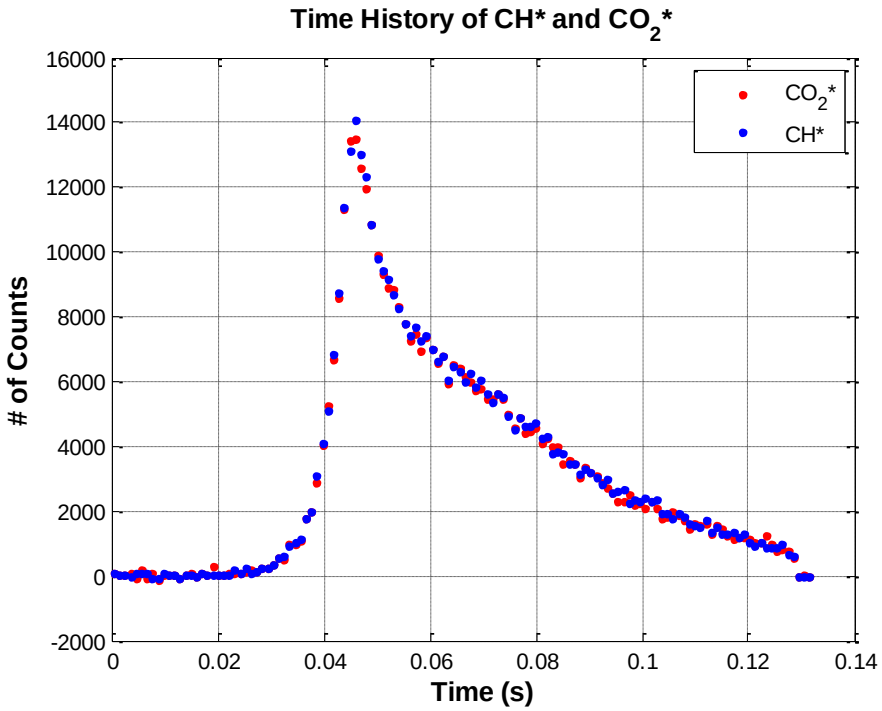
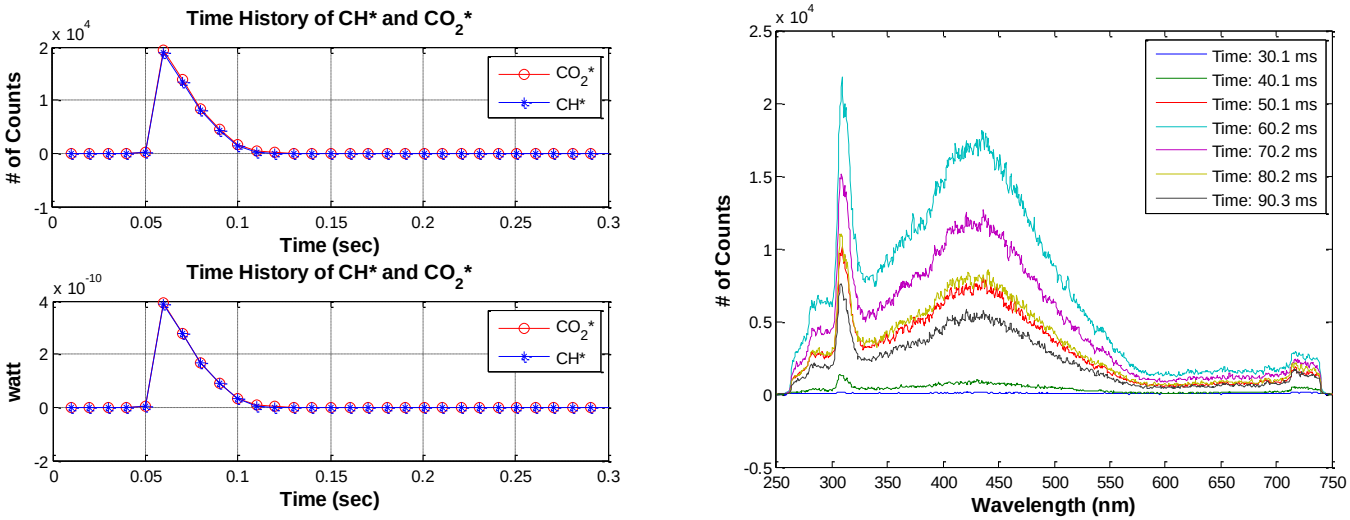


Figure 7. 14 Time history of CH* and background CO_2* 'line spectrum' from stoichiometric methane / air flame (p_0 = 2 bar, T_0 = 380 K) detected by the Princeton ICCD spectrometer. In this plot, either CH* or CO_2* 'line spectrum' (in terms of # of counts) is obtained by averaging values at the upper (i.e. 435 nm and 425 nm) and lower (i.e. 425 nm and 415 nm) boundaries.

It is also worth pointing out that there is no ICCD calibration data available to convert the measurements (in terms of # of counts) to energy output. The USB4000 spectrometer has an absolute calibration, so it is possible to transfer this calibration to the Princeton ICCD by comparing their relative sensitivities. However, the poor signal-to-noise ratio and wavelength resolution of the Princeton ICCD spectrometer would limit the quality of the data. Instead, it was decided to use interleaved measurements taken with the Ocean Optics spectrometer, and this is discussed in Section 7.3.3.

For rich mixtures there is an abundance of CH_4 for producing CH, therefore it is expected that more CH* radicals might be in equilibrium behind the flame front. Accordingly, optical detection has been carried out for rich methane / air (Φ=1.2) combustion. In this test, to facilitate comparison between CH* temporal evolutions from the two detectors, the Princeton ICCD system was operated with a 100 Hz repetition rate (i.e. 10 ms exposure time);

while the external synchronization trigger mode (a multiple trigger mode) was selected for the USB4000 spectrometer, which was triggered by negative pulses on norm3 (16 μs wide). As the CH* signal was very small compared to the background CO_2* signal, and there is noise in the Princeton ICCD spectrometer measurements, hence there is no need to further investigate the 'CH*' temporal evolution.



(a) (b)

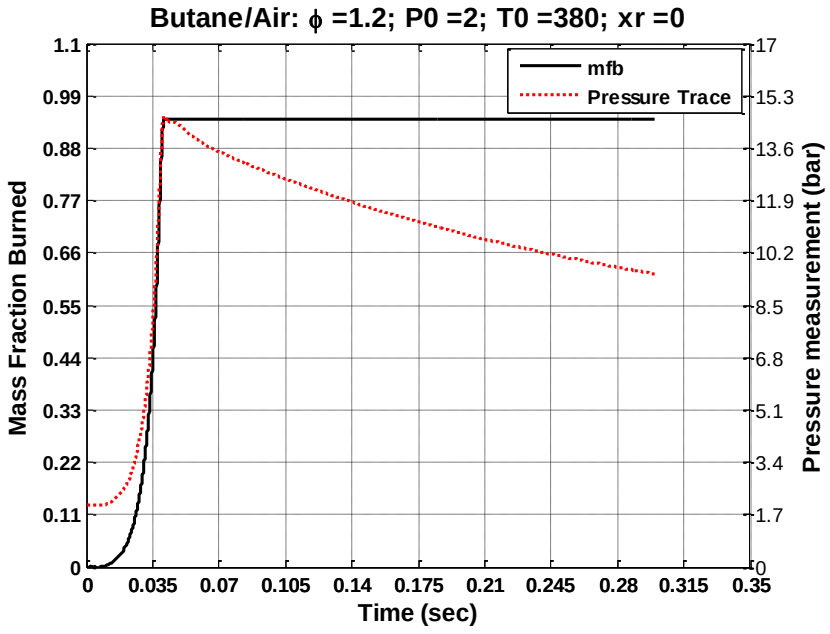
Figure 7. 15 (a) Time history of CH* and background CO_2* 'line spectrum' from the rich methane/air (Φ=1.2, p_0 = 2 bar, and T_0 = 380 K) flame detected by the USB4000 spectrometer; (b) Spatially and spectrally resolved flame spectra measured by the Princeton ICCD spectrometer.

No CH* feature can be observed from either the USB4000 spectrometer or the Princeton ICCD spectrometer. That is to say, the major constitution of 'CH*' signal measured by the photomultiplier tube is the background CO_2* rather than the narrow-band CH*; similar data is in the paper by Tinaut et al [48]. Even if CH* is deemed to be produced in the flame front (too tiny to be detected) from rich methane/air flames, it is orders of magnitude lower in comparison with the OH* intensity. According to Zizak [67], OH* and CH* chemiluminescence are of similar orders of magnitude from rich butane / air flames. Therefore butane/air combustion tests were performed for further sensing CH* chemiluminescence.

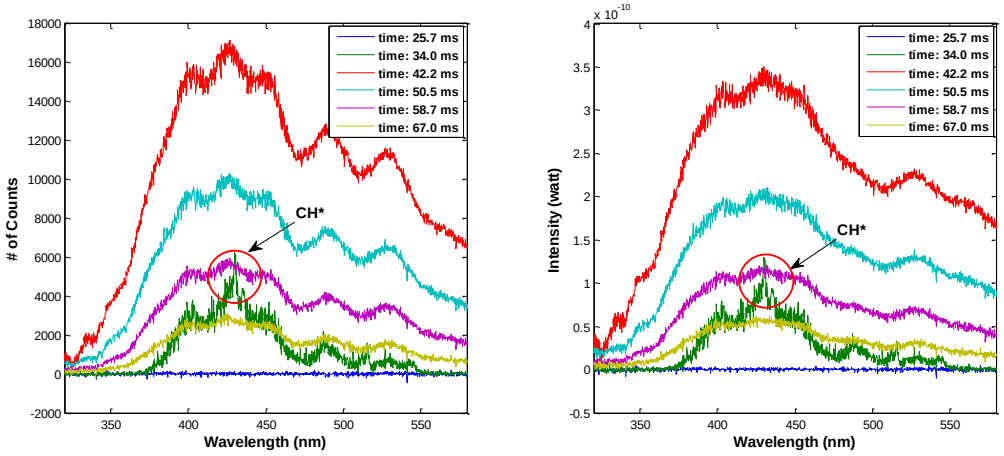
In conclusion, the comparison between USB4000 spectrometer and Princeton ICCD spectrometer results from stoichiometric methane / air flame demonstrate satisfactory agreement in prediction of the spectra features of OH* and CO_2*. Secondly, results from both detection optics reveal that OH* and CO_2* are formed in the burnt-gas region. Thirdly, neither instrument is able to detect CH* chemiluminescence either from rich or from stoichiometric methane / air flames, and this leads to the study of flame radiation from butane / air combustion.

7.3.2.2 Butane / Air Flame Spectra

In a rich butane / air flame, chemiluminescence from a number of electronic transitions is observed from reactive intermediate species. A neutral density filter was used with the USB4000 spectrometer in order to avoid it being saturated, but this sacrificed the detection of any OH* signals in UV region (as the filter was only neutral density in the visible spectrum). This compromise is acceptable for sensing the CH* spectra. Figure 7.16b and Figure 7.16c demonstrate flame spectra from rich butane/air combustion (Φ=1.2) at initial conditions p_0, T_0 of 2 bar, 380 K.



(a)



(b) (c)

Figure 7. 16 (a) Pressure and mass fraction burned as a function of time, and (b, c) CH* chemiluminescence emission from a rich butane/air flame (Φ=1.2, p_0 = 2 bar, and T_0 = 380 K) measured by the Ocean Optics USB4000 spectrometer.

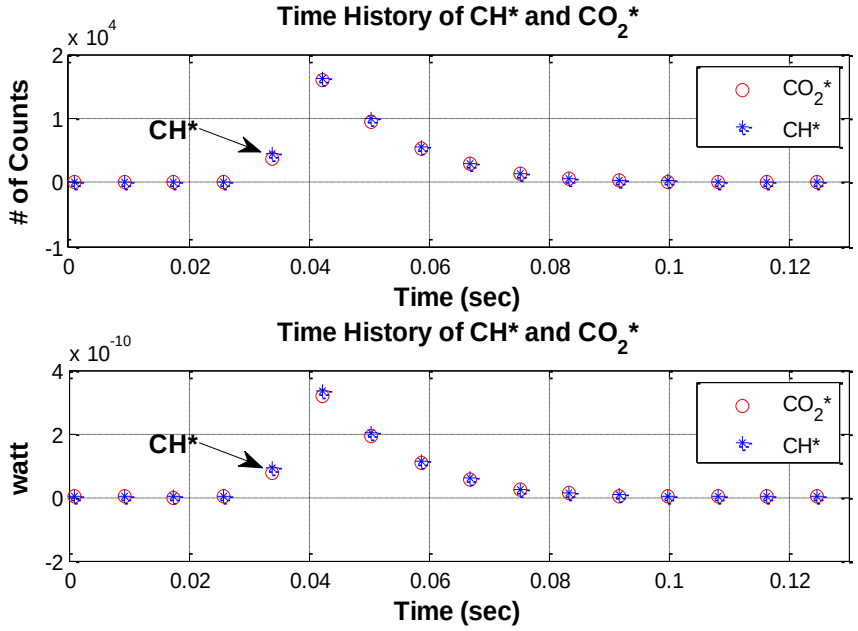


Figure 7. 17 Time history of CH* and background CO_2* 'line spectra' from rich butane/air (Φ=1.2, p_0 = 2 bar, and T_0 = 380 K) flame detected by the USB4000 spectrometer. In Figure 7.17, the CH* chemiluminescence has been characterised by averaging the spectral values at 435 nm and 425 nm, and the CO_2* chemiluminescence has been characterised as the mean of the intensities at 425 nm and 415 nm.

The CH* chemiluminescence (with bandwidth of 4 nm) is only emitted from the primary combustion zone of the butane flame, and the temporal response shows that the CH*

is only distinguishable from the CO_2* at 34 ms. The drawback of the USB4000 spectrometer is that, as the increase in chemiluminescence from the reaction zone is very steep, the relative low repetition-rate of the spectrometer limits the details about the temporal evolution of the CH* emission. The Princeton ICCD spectrometer, in this case, takes the advantage of an outstanding repetition rate with multiple exposures. In Figure 7.18, the data were collected at a repetition rate of 1 kHz (1 ms duration exposure). Furthermore, the diffraction grating has been changed to 600 lines/mm with a centre wavelength at 430 nm, and an intensifier gain of 6.5, so as to focus on the wavelength region of interest for the CH* band spectra. However there is no apparent CH* in the ICCD signals (in Figure 7.18) nor did using a diffraction grating with 2400 lines/mm make any difference.

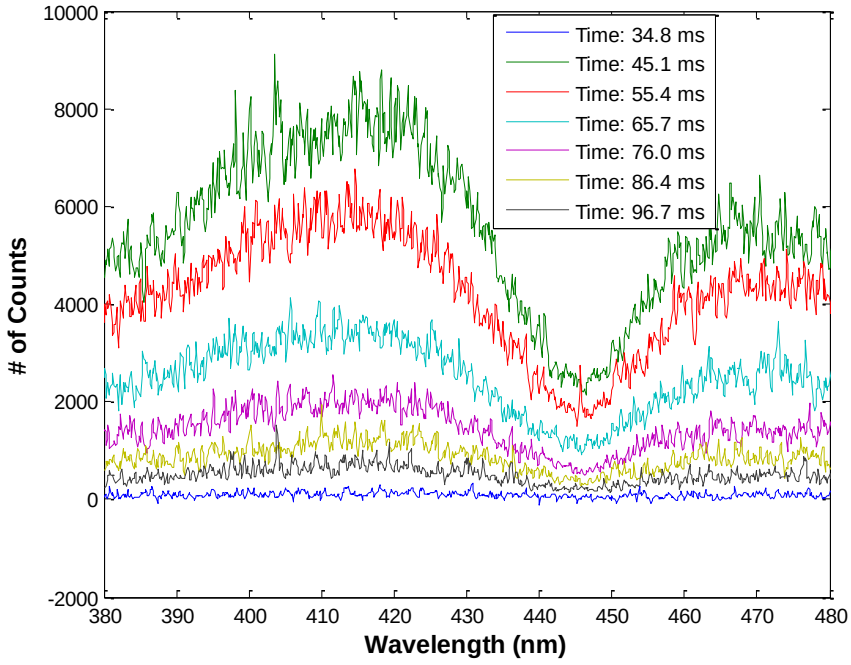


Figure 7. 18 Spatially and spectrally resolved rich butane/air flame spectra (Φ=1.2, p_0 = 2 bar, and T_0 = 380 K) measured by the Princeton ICCD spectrometer (with 600 lines/mm diffraction grating with centre wavelength at 430 nm).

The wavelength accuracy of the calibration at each pixel was suspected of being responsible, since a wavelength shift by just a single pixel (i.e., the limit of resolution) in a narrow CH* band spectral might render the strongest CH* line spectrum (431.5 nm)

unrecognizable. The calibration was checked by illuminating the entrance slit with a mercury lamp source and recording the line spectra. Although the spectra recorded were in agreement with mercury wavelength emission line, it was immediately found that the spectra were broadened, with the 600 lines/mm diffraction grating having a typical 2-3 nm bandwidth, and this smearing will introduce instrumental artefacts in the measurement of the narrow-band CH* transition at 431.5 nm.

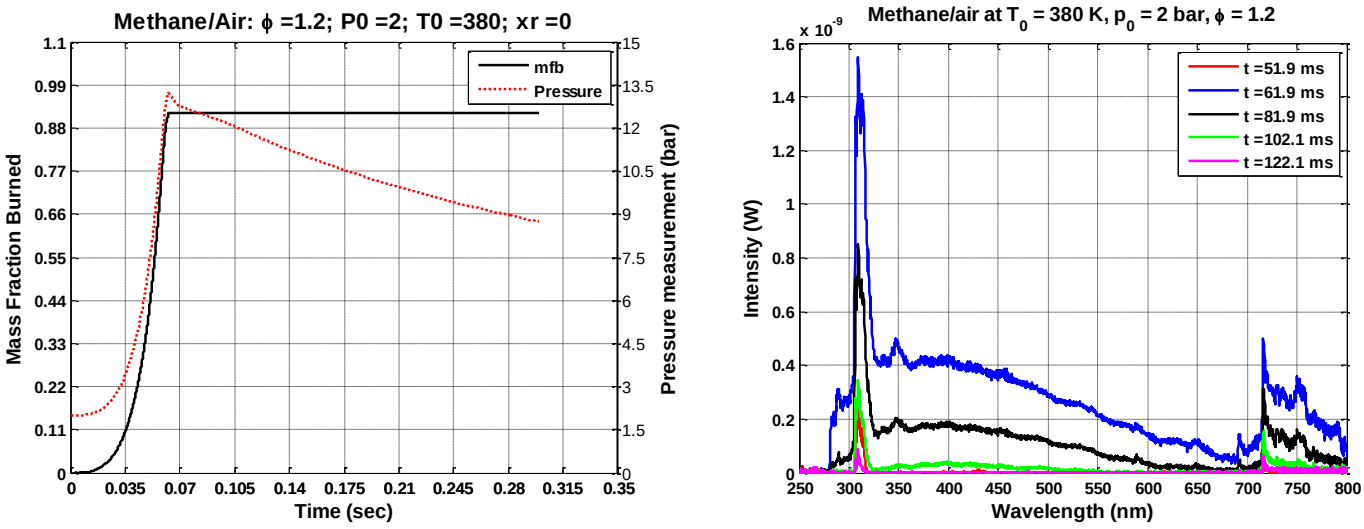
In sum, the strongest CH* chemiluminescent emission that emerges from electronic transition around 431.5 nm can be detected in the flame front by the USB4000 spectrometer, but the spectra is much weaker than the background CO_2*. Although the Princeton ICCD is capable of a high repetition-rate, the smearing of the dispersive spectra hinder detection of the CH* transition, especially when the radiation intensity is low; hence it is not able to detect narrow-band CH* chemiluminescence. The USB4000, on the other hand, cannot provide details about temporal evolution during combustion. However, interleaved measurements using the USB4000 spectrometer could provide a comprehensive temporal history of the chemiluminescence spectra, and this will be discussed next.

7.3.3 Interleaved Measurements

Flame spectra analysis has been used to provide information on the temporally and spectrally resolved chemiluminescence, which occurs when intermediate radicals, such as OH*, CH*, and CO_2*, formed within the flame front, relax to a low energy state by emitting light. The spatially resolved chemiluminescence can be integrated to validate the global flame chemiluminescence data obtained by the photomultiplier-tubes. Meanwhile, the real-time flame spectra can be related to the combustion relevant parameters such as local pressure, unburned gas temperature and equivalence ratio, and this can be further used to examine the robustness of the chemiluminescence mechanisms. For example, as can be seen in

Figure 7.19, both the maximum pressure and maximum OH* intensity occurred at approximately the same time; and the integral intensity of the OH* transition at each time would correspond to the current pressure. Therefore the study of the real-time integral spectra from the flame front are needed (especially CH*, since no robust measurements of absolute CH* in a constant volume combustion bomb has been reported).

Due to the repetition-rate restriction, limited spectra images during combustion are collected by the USB4000 spectrometer from a single experiment. To overcome this limitation, interleaved experiments were conducted using the USB4000 spectrometer. Specifically, to provide a time base for the recorded data, the USB4000 was initially triggered at the same time as the spark and the DAQ, and then the subsequent USB4000 measurements were started 2, 4, and 6 ms later than the spark and the DAQ. This allows a sequence of data to be acquired along the rising edge of the temporal chemiluminescence profile. Secondly, as the PMT signal is effectively continuous, it can be 'sampled' after collection by the DAQ in a way that imitates the sampling by the USB4000 spectrometer, for comparison with the USB4000 data. Experiments were performed in laminar butane/air flames with an equivalence ratio of 1.2, and initial temperatures of 380 and 450 K, with an initial pressure of 2 bar. The detection optics consists of a USB4000 spectrometer and a PMT coupled to a CH* band-pass filter.



(a) (b)

Figure 7. 19 The same data as Figure 7.15. Pressure and mass fraction burned traces (Figure 7.19a) and spatially and spectrally resolved flame spectra (Figure 7.19b) measured by the Ocean Optics USB4000 spectrometer. It can be seen that both maxima are achieved approximately at the same time (~65 ms).

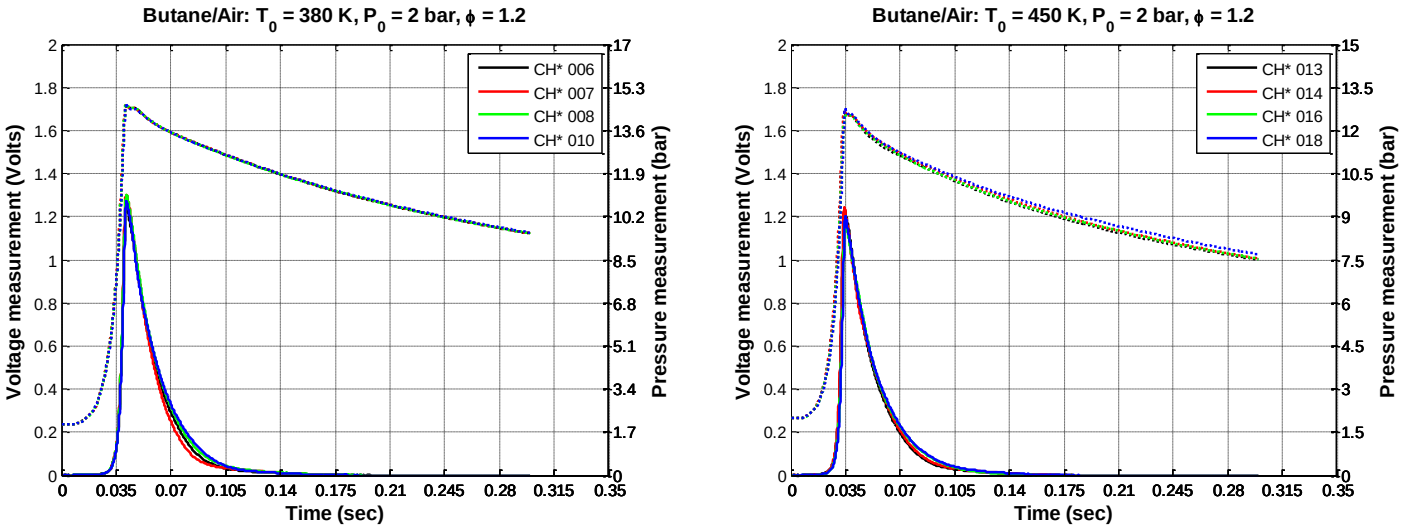
In order to compare the USB4000 data to the sampled results from a PMT, firstly the spatially integrated chemiluminescence was calculated. The chemiluminescence of the CH* transition with superimposed CO_2* background was measured with an interference filter centred at 430 nm with 10 ± 2.5 nm half-bandwidth. The measured transmission of the interference filter gave characteristic values of the wavelength-dependent intensities over the band-pass region. The integral intensity of the CH* radical (without background correction) can be calculated by integrating the line spectrum over the wavelength range, i.e.

$$I_{CH^*}{}' = \int_0^{\infty} (I_{CH^*}{}'(\lambda) \cdot T_{CH^*}(\lambda))\, d\lambda \qquad (7.4)$$

Where $I_{CH^*}{}'$ stands for the integral of band-pass filtered chemiluminescence in the wavelength range of CH* (without broadband CO_2* removal). $I_{CH^*}{}'(\lambda)$ and $T_{CH^*}(\lambda)$ denote the wavelength dependent band-pass filtered chemiluminescence and transmission of the CH* interference filter; λ represents the wavelength.

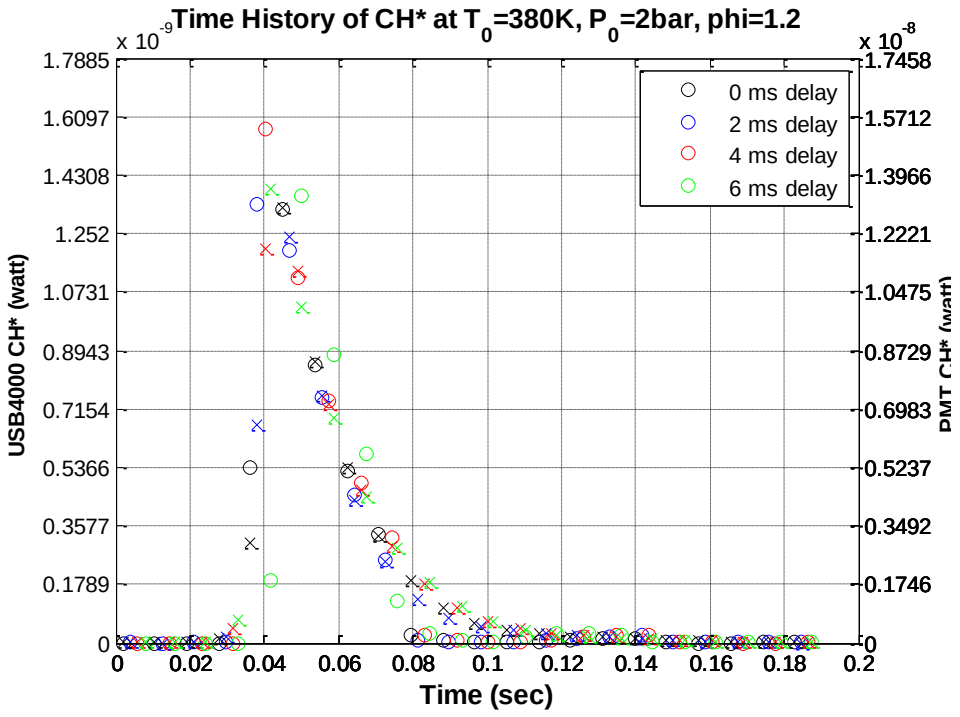
As before, the PMT data were 'sampled' after collection in such a way as to replicate the sampling by the USB4000 spectrometer. Figure 7.20 shows that the pressure is repeatable

within 3% at initial temperature of either 380 K or 450 K, (as was the CH* measurements, in unit of volts); therefore, the systematic errors due to experimental variability are assumed to be small. It should be pointed out that different scales in Figure 7.21 can be attributed to the different collection efficiencies of the two optical systems.

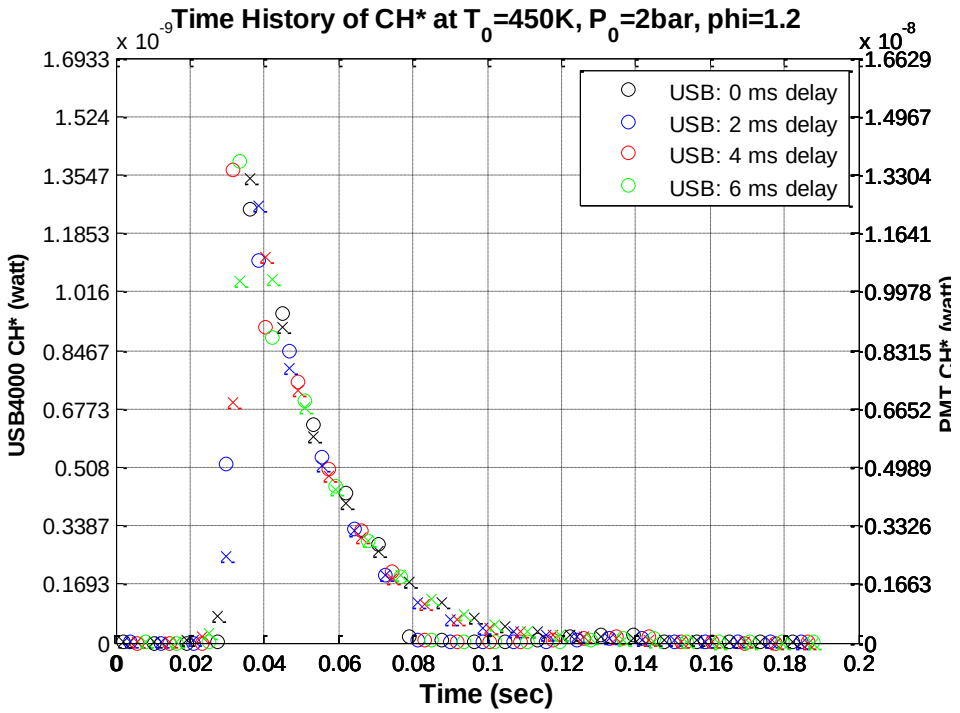


(a) (b)

Figure 7. 20 Repeatability of the PMT measurements from PMT measurements of rich butane/air combustions with equivalence ratio of 1.2, initial temperatures of 380 K (Figure 7.20a) and 450 K (Figure 7.20b), initial pressure of 2 bar. The solid curves represent V_{CH^*} (in unit of volts), and the dashed curves denote the pressure traces.



(a)



(b)

Figure 7. 21 Comparison of integral CH* chemiluminescence (without background correction) and global chemiluminescence profiles from the interleaved measurements of rich butane/air combustion with equivalence ratio of 1.2, initial temperatures of 380 K (Figure 7.21a) and 450 K (Figure 7.21b), initial pressure of 2 bar. The circle markers represent data collected by the Ocean Optics USB4000 spectrometer; the cross markers denote sampled PMT signals. The marker colour denotes measurements from a particular experiment.

There are several significant observations that can be seen from Figure 7.21. Firstly, it is found that the variation of CH* chemiluminescence measured by either USB4000 or the PMT is very small; although there are singular points away from the overall profile (mainly from the test with 6 ms delay) in Figure 7.21a, these occur after the end of combustion, which is of no interest. Secondly, the overall Ocean Optics profile is well in line with the PMT profile, which verifies the reliability of the global chemiluminescence emission measured by the PMT. Thirdly, there is less good overlap between the integral CH* values and the sampled PMT data along the rising edge of the profile. This is because along the rising edge, the gradient of the chemiluminescence increase is very steep; hence any small time-offset in the trigger pulse and the pulse train might result in a large discrepancy in their readings. This

means it is difficult to separate the real-time CH* emission accurately from the CO_2* emission within the flame front from a constant volume combustion bomb.

In conclusion, the 'continuum' CO_2* is responsible for the discontinuity along the isentropes and 'CH* emissions' after the end of combustion that have been reported in Section 6.5, and further investigation of the CH* chemiluminescence is deemed to be unprofitable. This is for one reason because the absolute CH* emission is very small to be distinguished from the background CO_2*, for the other, the real-time integral CH* chemiluminescence is hard to be detected accurately. More effort, in turn, has been made to study the absolute OH* chemiluminescence emission, which is discussed next.

7.3.4 Absolute OH* Chemiluminescence

In spectrally and temporally resolved chemiluminescence measurements the broadband emission CO_2* can be evaluated and the absolute OH* chemiluminescence can be isolated. This is impossible in the band-pass filtered PMT measurements. In this section, rich methane/air data (the same measurement as Figure 7.15) are used to analyse the absolute OH* chemiluminescence.

To separate the OH* radical and CO_2* contribution in the band-pass filtered measurements, integral OH* and CO_2* measurements need to be obtained. As can be seen in Figure 7.22, the broadband CO_2* emission can be approximated by a fifth-order polynomial with high accuracy, which is consistent with the curve fitting used by Lauer et al. [15]. It has been found that the polynomial fit is self-similar for flame spectra collected at different times during combustion. Accordingly, the broadband CO_2* in the wavelength range of OH* chemiluminescence can be integrated as the product of the polynomial fit and the transmission of OH* band-pass filter over the wavelength range, i.e.

$$I_{CO_2^*} = \int_0^\infty \left(P_{CO_2^*}(\lambda) \cdot T_{OH^*}(\lambda)\right) d\lambda \tag{7.5}$$

where $I_{CO_2^*}$ stands for the integral of band-pass filtered CO_2* chemiluminescence in the wavelength range of OH*. $P_{CO_2^*}(\lambda)$ and $T_{OH^*}(\lambda)$ denote the wavelength dependent CO_2* approximation and transmission of the OH* interference filter; λ represents the wavelength.

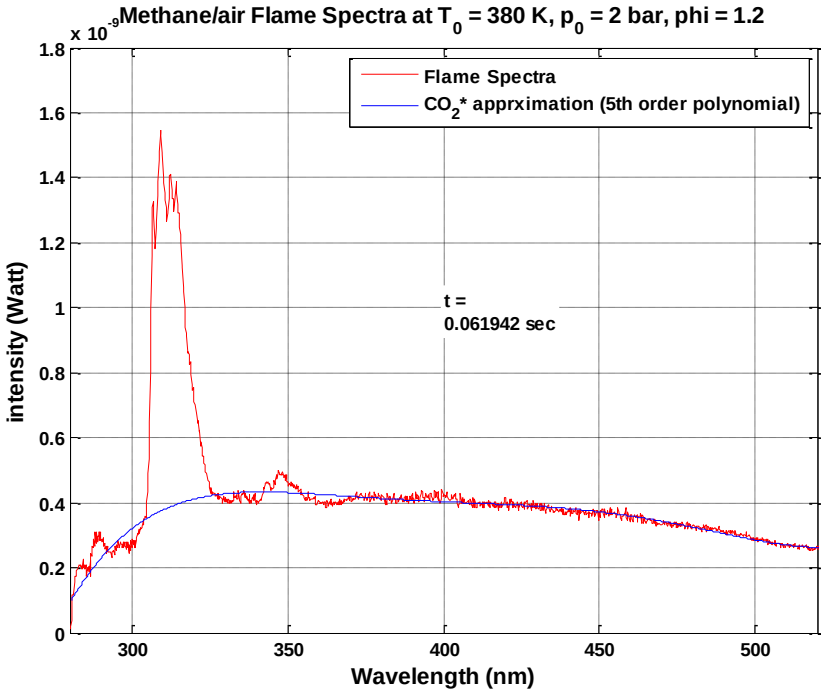


Figure 7. 22 A fifth-order polynomial fit for the estimation of the broadband CO_2* emission.

The integral intensity of the band-pass filtered chemiluminescence in the wavelength range of OH* is evaluated in the same way as the integral intensity of the band-pass filtered CH* chemiluminescence, i.e.

$$I_{OH^*}{}' = \int_0^{\infty} (I_{OH^*}{}'(\lambda) \cdot T_{OH^*}(\lambda))\, d\lambda \tag{7.6}$$

Where $I_{OH^*}{}'$ stands for the integral of band-pass filtered chemiluminescence in the wavelength range of OH* (without broadband CO_2* removal). Hence the absolute integral intensity of OH* (denoted as I_{OH^*}) can be calculated as follow:

$$I_{OH^*} = I_{OH^*}{}' - I_{CO_2^*} \tag{7.7}$$

The CO_2* contribution corrected OH* chemiluminescence profile is illustrated in Figure 7.23. These absolute OH* and CO_2* chemiluminescence measurements could be used in the future

for the further study of chemiluminescence mechanisms, and to probe the feasibility of chemiluminescence as an indirect measure of equivalence ratio and heat release rate.

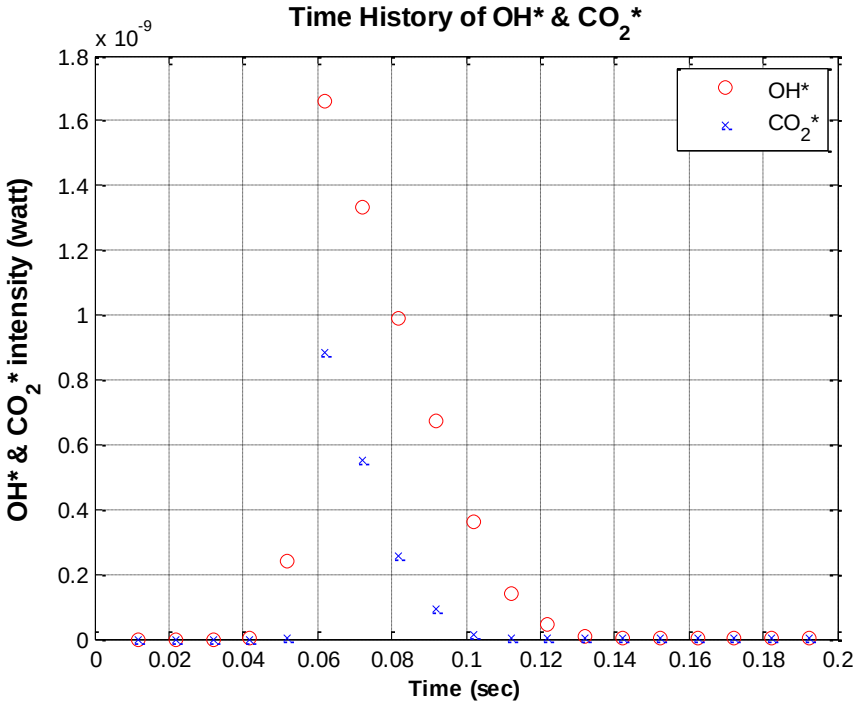


Figure 7. 23 Global (band-pass filtered) chemiluminescence profiles for the absolute OH* and broadband CO_2* from measurements of rich methane/air combustions with equivalence ratio of 1.2, initial temperatures of 380 K, and initial pressure of 2 bar.

7.4 Conclusion

Precise and detailed measurements of spectrally resolved flame emission has been conducted to study the chemiluminescence characteristics in a constant volume combustion vessel. This has verified the hypothesis (see for example Figure 7.10) that the broadband CO_2* is responsible for the discontinuity in the CH* and OH* emission along the isentropes that have been reported in Section 6.5. Besides, the OH* and CO_2* chemiluminescence signal comes either from the reaction zone or from the burned gas region, which explains why the chemiluminescence continues after the end of combustion.

With regard to the CH* chemiluminescence, it has been found that it is very faint in laminar premixed methane and butane flames within the combustion bomb. The band-pass

filtered chemiluminescence in the wavelength range of the CH* transition is shown to be almost entirely from CO_2*.

Finally, absolute OH* chemiluminescence has been separated from the background CO_2* contribution, which was fitted by a 5^{th} order polynomial. This can be used to examine the usefulness of chemiluminescence for combustion sensing and diagnostic applications under various conditions.

Chapter 8 Conclusions and Future work

8.1 Conclusions

Optical diagnostics are attractive in monitoring combustion processes because the measurements are non-intrusive and the optical sensors generally have the advantage of a fast time response. Chemiluminescence measurement is one of the most frequently-used optical diagnostics in combustion monitoring applications owing to its simplicity and non-intrusive nature. The primary objective of this thesis is to identify the feasibility of using chemiluminescence as an active control algorithm in combustion research.

Chemiluminescence is affected by many parameters such as equivalence ratio, temperature, pressure, stretch rate and mass burned rate. However, chemiluminescence data from OH* and CH* have frequently been gathered under limited conditions, such as atmospheric pressure. The constant volume vessel is versatile, allowing the OH* and CH* chemiluminescence to be measured over a wide range of pressures and temperatures, from 0.5 to 20 bar, and 450 to 600 K, due to the isentropic compression of the unburned gas (Chapter 2). Methane and iso-octane were chosen because they are of practical significance in many combustors. Furthermore, the OH* and CH* emissions have not been investigated as extensively for iso-octane compared with methane. For iso-octane, a syringe based system was proven to be a good quality precision fluid measuring device, enabling the iso-octane data to be gathered for a range of operating conditions, including variation in the initial pressure, initial temperature, and equivalence ratio (Section 2.5).

To develop a general, quantitative correlation between the chemiluminescence and other physical quantities, quantitative OH* and CH* chemiluminescence measurements are needed. An optical system, which consists of a pair of lenses, a series of apertures, and photomultiplier-tubes with interference filters in the wavelength range of OH* (306.4 nm)

and CH* (431.5 nm), has been established to detect OH* and CH* chemiluminescence accurately (Chapter 3). The optical design was optimised by an optical model, which successfully avoids collecting scattered photons from the inside surface of the combustion bomb. This model also provides information on the optical system collection efficiency as a function of flame radius. With an absolute calibration, the OH* and CH* chemiluminescence are quantified in terms of watt.

The absolute OH* and CH* measurements (in terms of watt) and global chemiluminescence intensity ratio (CH*/OH*) have been normalised with mass of fuel burned rate by an analysis code, i.e. the *NIICS* (Normalised Intensity Integrated Calculation System). The chemiluminescence can then be expressed as J/g. *NIICS* also allows the user to calculate an important flame parameter, the heat release rate (Chapter 4).

Finally, measurements of the spectrally resolved flame emissions, including CH*, OH*, and CO_2* have been reported in Chapter 7.

The majority findings from the global chemiluminescence signals and spectral tests, which have been described in Chapter 5, 6, and 7, can be divided into the following three categories. Firstly, this experimental study has parametrically examined the CH*/OH* ratio as a function of local pressure, local unburned gas temperature and equivalence ratio. Secondly, it studied the dependence of absolute CH* and OH* chemiluminescence on combustion conditions (such as pressure, temperature and equivalence ratio), and the link with other flame parameters (such as the equivalence ratio and heat release rate). Thirdly, the spectral analysis provides valuable information on the chemiluminescence emissions. These are summarized as follow.

8.1.1 Quantitative Modelling of CH*/OH* chemiluminescence ratio (Chapter 5)

Measuring the CH*/OH* chemiluminescence ratio as a function of equivalence ratio (0.8 – 1.1), unburned gas temperature (450 – 600 K), and pressure (0.5 – 20 bar), a mathematical formulation for use in predicting the CH*/OH* ratio has been developed that monotonically increases with increasing unburned gas temperature and increasing pressure, and is given by the following:

$$\frac{\mathrm{CH}^*}{\mathrm{OH}^*} = \{[x_1 \cdot \phi^2 + x_2 \cdot \phi + x_3] \cdot P^2 + [x_4 \cdot \phi^2 + x_5 \cdot \phi + x_6] \cdot P + [x_7 \cdot \phi^2 + x_8 \cdot \phi + x_9]\} \cdot (x_{10} \cdot T + x_{11}) \tag{5.8}$$

Where:

$$T = \frac{T_\mathrm{u}}{298}, P = \frac{p_\mathrm{u}}{1.0} \tag{5.9}$$

This mathematical representation was derived from a multi-variate fitting and correlation analysis. It produced broad agreement with the experimental data for methane and iso-octane flames.

Table 8. 1 Values of Curve Fitting Coefficients for the Methane / Air and Iso-octane / Air Mixtures

Coefficients	Methane Values	Iso-octane Values
x_1	0.1140	0.1110
x_2	-0.2273	-0.2743
x_3	0.1127	0.1648
x_4	-2.4066	-1.3479
x_5	4.7016	3.3198
x_6	-2.2421	-1.9186
x_7	9.3166	3.3302
x_8	-18.1386	-8.4208
x_9	9.0901	6.0497
x_{10}	-0.0119	0.0658
x_{11}	1.6500	0.9897

With the help of this functional relationship, the equivalence ratio was able to be deduced at pressures above 15 bar in near stoichiometric methane / air systems; the CH*/OH* ratio was also able to indicate the local equivalence ratio across high operating

pressures (p_u > 10 bar) in iso-octane / air flames. It should be pointed out that the curve fit is not a strong function of the unburned gas temperature.

8.1.2 Dependence of the Absolute CH* and OH* Chemiluminescence on Combustion Conditions (Chapter 6)

Chapter 6 analysed the fundamental behaviour of the absolute CH* and OH* chemiluminescence in combustion systems, and examined the usefulness of the experimental results to evaluate chemiluminescence for sensing the equivalence ratio and heat release rate. The influences of pressure, unburned gas temperature, and equivalence ratio were studied for both methane and iso-octane, and can be summarised as follows:

- The normalised OH* and CH* increase monotonically with equivalence ratio under lean burn conditions ($0.8 \leq \Phi \leq 1.0$), but the trend for rich conditions was deemed to be less obvious. This experimental evidence does not contradict the proposed OH* and CH* formation mechanisms;
- The absolute OH* and CH* chemiluminescence increase monotonically with increasing pressure and unburned gas temperature, and the temperature effect is more pronounced than the pressure effect;
- As the differences in stretch are so small, no conclusions about stretch can be made.

With regard to the relationship between the absolute OH* and CH* and other flame parameters such as the equivalence ratio and heat release rate, these can be summarised as follows:

- It is suggested that the absolute OH* and CH* chemiluminescence measurements are useful for sensing the equivalence ratio;
- The absolute OH* and CH* chemiluminescence are not able to predict the heat release rate.

However, there are two disconcerting results from the global flame chemiluminescence, firstly, the discontinuity of the absolute OH* and CH* measurements along single isentropes, and secondly, chemiluminescence after the end of combustion. The broadband CO_2* emission was thought to be responsible, and this led to the spectroscopic study in Chapter 7.

8.1.3 Spectroscopic Measurements (Chapter 7)

The spectrally resolved chemiluminescence was measured by two optical detectors, i.e. an Ocean Optics spectrometer and a Princeton ICCD spectrometer. The flame spectra show that the broadband CO_2* is 'continuous' and strong, which explains the discontinuity in the CH* and OH* emission along the isentropes. Furthermore, the OH* and CO_2* chemiluminescence 'originates' either in the region of reaction zone or in the burned gas area, and this can account for the chemiluminescence after the 'end' of combustion.

Secondly, the CH* chemiluminescence is found to be very small hence the band-pass filtered CH* is mainly from CO_2*. This suggests that the absolute CH* chemiluminescence is not a reliable indicator for combustion relevant parameters, and that in the past measurements assigned to CH* chemiluminescence might have come from CO_2* chemiluminescence.

Thirdly, the absolute OH* has been separated from the background CO_2*, which has been approximated by a 5^{th} order polynomial fit. This could be used for the future application of OH* chemiluminescence in the measurement of equivalence ratio and heat release rate.

The Princeton Kinetics Spectrometer from the EPSRC Loan Pool had a fast sampling rate, but insufficient wavelength resolution and a high noise level. In contrast the Ocean Optics spectrometer had a limited sampling rate, but interleaved measurements enabled a sequence of spectra to be assembled that replicated a faster sampling system.

8.2 Future Work

8.2.1 Absolute Measurements of OH* Chemiluminescence

For absolute OH* chemiluminescence to be used for sensing combustion parameters over a wide range of combustion conditions (such as pressure, temperature, equivalence ratio and residual molar fraction), it is necessary for the chemiluminescence measurements to be accurate and robust. Ideally, a spectrometer is needed with a fast response and good signal to noise ratio. Another option might be to use two PMTs with interference filters in the wavelength region for OH* chemiluminescence, and there would seem to be two options. Firstly, if one had a wider bandwidth centred on the OH* than the other, then this would enable an assessment to be made of the background CO_2* emission, so that the OH* chemiluminescence could then be isolated from the background CO_2* emission. This would require either the OH* band to be considered to be narrow, or the CO_2* emission to be flat. Secondly, a narrow bandwidth filter could be selected for a wavelength range adjacent to the OH* band (but not including any emission bands). In both cases, the measured spectra could be modelled with the filter transmission efficiencies to decide on the best measurement system. A similar strategy could be applied to CH* chemiluminescence measurements.

8.2.2 Analysis of Absolute OH* Chemiluminescence

Another important step would be to normalise the absolute OH* chemiluminescence accurately. To deal with this, firstly, the optical collection efficiency (as a function of flame radius) of the Ocean Optics spectrometer will need to be quantified on the basis of a ray tracing analysis. Then the absolute OH* chemiluminescence (in unit of J/g) can be separated from the background CO_2* emission (by fitting a 5^{th} order polynomial), followed by the normalisation of the OH* chemiluminescence using Equation (4.1).

Next, the dependence of OH* on combustion conditions such as pressure, temperature, and equivalence ratio could be investigated, and use to validate the existing OH* chemiluminescence mechanisms.

The existing 'CH*' chemiluminescence data is in reality from CO_2*, so correlations for the OH*/CO_2* ratio, although reported here as an OH*/CH* ratio, would still have potential uses. To exploit the chemiluminescence measurements from realistic combustors, it is necessary to obtain correlations for the OH* (or OH*/CO_2* ratio) derived from a multi-variate fitting and correlation analysis.

8.2.3 Fuel Variability

To make sure that the OH* is a viable indicator in industrial combustion, many other fuels (for example ethanol, toluene, biogas, and syngas) should be studied, because different fuels may have significant differences in their chemiluminescence, and also in the heat release rate sensitivity. Moreover, the variability of the mixture composition also needs to be considered for its effect on chemiluminescence; so various molar residual fractions will need to be studied in addition to differences in the equivalence ratio.

References

[1] Turns S. R., *An Introduction to Combustion: concepts and applications*. International Editions, McGraw-Hill, Singapore, 1996.

[2] Fristrom R. M., *Flame Structure and Processes*. OUP, New York, 1995.

[3] Marshall S., *Measuring Laminar Burning Velocities*. DPhil Thesis, University of Oxford, 2010.

[4] Balachandran R., Ayoola B.O., Kaminski C.F., Dowling A.P., Mastorakos E., *Experimental investigation of the nonlinear response of turbulent premixed flames to imposed inlet velocity oscillations*. Combustion and Flame 143 (2005) 37–55.

[5] Gaydon A., *the Spectroscopy of Flames*. Chapman and Hall, 2nd Edition, London, 1974.

[6] Glass G., Kistiakowsky G., Michael J., Niki H., *The oxidation reactions of acetylene and methane*. Proc. Combust. Inst. 10 (1965) 513-522.

[7] Nori V. N., Seitzman J. M., *CH* Chemiluminescence Modelling for Combustion Diagnostics*. Proc. Combust. Inst. 32 (1) (2009) 895-903.

[8] Grebe J., Homann K., *Blue-Green Chemiluminescence in the System C_2H_2/O/H Formation of the Emitters CH ($A^2\Delta$), C_2 ($d^3\Pi_g$) and C_2H**. Ber Bunsen Phys Chem 86 (7) (1982) 587-597.

[9] Renlund A., Shokoohi F., Reisler H., Wittig C., *Reaction of C_2H with O_2 - Chemiluminescent Products*. J Phys Chem-Us 86 (21) (1982) 4165-4170.

[10] Devriendt K., Peters J., *Direct Identification of the C_2H ($X^2\Sigma^+$) + O (^3P) → CH ($A^2\Delta$) + CO Reaction as the Source of the CH ($A^2\Delta \rightarrow X^2\Pi$) Chemiluminescence in C_2H_2/O/H Atomic Flames*. J. Phys. Chem. A (1997), 101(14), 2546-2551.

[11] Elsamra R., Vranckx S., Carl S., *CH ($A^2\Delta$) Formation in Hydrocarbon Combustion: The Temperature Dependence of the Rate Constant of the Reaction $C_2H + O_2 \rightarrow CH\ (A^2\Delta) + CO_2$*. J. Phys. Chem. A 109 (45) (2005) 10287-10293.

[12] Hall J. M., Petersen E. L., *an Optimized Kinetics Model for OH Chemiluminescence at High Temperatures and Atmospheric Pressures.* International Journal of Chemical Kinetics, 38 (12) (2006) 714–724.

[13] Najm H., Paul P., Mueller C., Wyckoff P., *On the Adequacy of Certain Experimental Observables as Measurements of Flame Burning Rate*. Combustion and Flame 113 (3) (1998) 312-332.

[14] Panoutsos C. S., Hardalupas Y., Skevis G., Taylor A. M. K. P., *Numerical Evaluation of Equivalence Ratio Measurement Using OH* and CH* Chemiluminescence in Premixed and Non-Premixed Methane-Air Flames*. Combustion and Flame 156 (2) (2009) 273-291.

[15] Lauer M., Sattelmayer T., *On the Adequacy of Chemiluminescence as a Measure for Heat Release in Turbulent Flames with Mixture Gradients.* Journal of Engineering for Gas Turbines and Power, Vol. 132 / 061502-1, June 2010.

[16] Hardalupas Y., Orain M., *Local Measurements of the Time-Dependent Heat Release Rate and Equivalence Ratio Using Chemiluminescent Emission from a Flame*. Combustion and Flame 139 (3) (2004) 188-207.

[17] Higgins B., McQuay M., Lacas F., Candel S., *An Experimental Study on the Effect of Pressure and Strain Rate on CH* Chemiluminescence of Premixed Fuel-Lean Methane/Air Flames*. Fuel 80 (11) (2001) 1583-1591.

[18] Taupin B., Cabot G., Martins G., Vauchelles D., Boukhalfa A., *Experimental Study of Stability, Structure and CH* Chemiluminescence in a Pressurized Lean Premixed Methane Turbulent Flame*. Combust. Sci. Technol. 179 (1-2) (2007) 117-136.

[19] Aleiferis P., Hardalupas Y., Taylor A., Ishii K., Urata Y., *Flame Chemiluminescence Studies of Cyclic Combustion Variations and Air-to-Fuel Ratio of the Reacting Mixture in a Lean-Burn Stratified-Charge Spark-Ignition Engine*. Combustion and Flame 136 (1-2) (2004) 72-90.

[20] Hultqvist A., Christensen M., Johansson B., Franke A., Richter M., Alden M., *A Study on the Homogeneous Charge Compression Ignition Combustion Process by Chemiluminescence Imaging*. SAE Technical Paper 1999-01-3680.

[21] Hultqvist A., Christensen M., Johansson B., Richter M., Nygren J., Hult J., Alden M., *the HCCI Combustion Process in a Single Cycle | Speed Fuel Tracer LIF and Chemiluminescence Imaging*. SAE Technical Paper 2002-01-0424.

[22] Thirouard B., Cherel J., Knop V., *Investigation of Mixture Quality Effect on CAI Combustion*. SAE Technical Paper 2005-01-0141.

[23] Ömer L. Gülder, *Burning Velocities of Ethanol-Isooctane Blends*, Combustion and Flame 56: 261-268 (1984).

[24] Ikeda Y., Nishihara H., Nakajima T., *Measurement of Flame Front Structure and its Thickness by Planar and Local Chemiluminescence of OH*, CH*, and C_2**. SAE Technical Paper 2001-01-0920 (2001) 1-10.

[25] Belles F. E., Lauver M. R., *Origin of OH Chemiluminescence during the Induction Period of the $H_2 – O_2$ Reaction behind Shock Waves*. The Journal of Chemical Physics (1964), 40, 415–422.

[26] Gutman D., Lutz R. W., Jacobs N. F., Hardwidge E. A., Schott G. L., *Shock-Tube Study of OH Chemiluminescence in the Hydrogen-Oxygen Reaction.* The Journal of Chemical Physics (1968), 48, 5689–5694.

[27] Gardiner W. C., Morinaga K., Ripley D. L., Takeyama T., *Shock–Tube Study of OH ($^2\Sigma$ - $^2\Pi$) Luminescence*. The Physics of Fluids Supplement I 1969, 1, 120–124.

[28] Hldaka Y., Takaharhl S., Kawano H., Suga M., and Gardiner W. C., *Shock-Tube Measurement of the Rate Constant for Excited OH ($A^2\Sigma^+$) Formation in the Hydrogen-Oxygen Reaction.* The Journal of Chemical Physics (1982), 86, 1429–1433.

[29] Carl S. A., Van Poppel M., Peeters J., *Identification of the CH + O_2 → OH (A) + CO Reaction as the Source of OH (A - X) Chemiluminescence in C_2H_2/O/H/O_2 Atomic Flames and Determination of Its Absolute Rate Constant over the Range T=296 to 511 K.* The Journal of Chemical Physics A (2003), 107, 11001–11007.

[30] Lichtin D. A., Berman M. R., Lin M. C., *NH ($A^3\Pi \rightarrow X^3\Sigma^-$) Chemiluminescence from the CH ($X^2\Pi$) + NO Reaction*. Chemical Physics Letters (1984), 108, 18–24.

[31] Smith G. P., Luque J., Park C., Jeffries J. B., Crossley D. R., *Low Pressure Flame Determinations of Rate Constants for OH(A) and CH(A) Chemiluminescence.* Combustion and Flame (2002), 131, 59–69.

[32] Baulch D. L., Drysdale D. D., Duxbury J., Grant S. J., *Evaluated Kinetic Data for High Temperature Reactions*. Vol. 3, Butterworths, London, 1976.

[33] Kaskan W. E., *Abnormal Excitation of OH in $H_2/O_2/N_2$ Flames*. The Journal of Chemical Physics (1959), 31, 944–956.

[34] Zeegers P. J. Th., Alkemade C. Th. J., *Radical Recombinations & Acetylene-Air Flames*. Proc Combust Inst (1965), 10, 33–40.

[35] Saeed K., *Laminar Burning Velocity Measurements*. DPhil Thesis, University of Oxford, 2002.

[36] Stone R., Clarke A., Beckwith P., *Correlations for the Laminar-Burning Velocity of ethane/Diluent/Air Mixtures Obtained in Free-Fall Experiments.* Combustion and Flame (1998), 114, 546-555l.

[37] Mass Flow Controller (MFCs) Principles – A Basic Course. http://www.qualiflow.com/support/mfc-principles.pdf.

[38] Ir. H.J. Boer, *Precision Mass Flow Metering for CVD Applications*, http://www.bronkhorst.com/files/published_articles/precision-mass-flow-metering.pdf.

[39] Hayward A. T. J., *Flowmeters – a Basic Guide and Source – Book for Users*. First edition, Macmillan Publishers Ltd, 1979.

[40] Daubert T. E., Danner R. P., *Physical and Thermodynamic Properties of Pure Chemical.* Taylor & Francis (1997).

[41] Reid, R. C., Prausnitz, J. M., Poling, B. C., *the Properties of Gases and Liquids*. Mc-Graw Hill Book Company, 4th edition (1987).

[42]http://www.kdscientific.com/downloads/KDS%20Literature/Brochures_Datasheets/KDS%20310%20Plus%20Datasheet.pdf

[43] http://www.comaroptics.com/pdfs/Comar_filters_and_diffusers.pdf

[44] Maly R. R. (1984). 'Spark ignition: its physics and effect on the internal combustion engine', in Hillard J. C. and Springer C. S. (eds), *Fuel Economy: in Road Vehicles Powered by Spark Ignition Engines*. Plenum, New York.

[45] Ekic O., *Computational Study of Arc Discharges: Spark Plug and Railplug Ignitors*. DPhil Thesis, the University of Texas at Austin, 2007.

[46] Metghalchi M. and Keck J. C., *Burning Velocities of Mixtures of Air with Methanol, Iso-octane and Indolene at High Pressures and Temperatures*. Combustion and Flame, 48:211-217 (1982).

[47] Higgins B., McQuay M., Lacas F., Rolon J. C., Darabiha N., Candel S., *Systematic Measurements of OH Chemiluminescence for Fuel-Lean, High-Pressure, Premixed, Laminar Flames*. Fuel 80 (1) (2001) 67-74.

[48] Tinaut F. V., Reyes M., Gimenez B., Pastor J. V., *Measurements of OH* and CH* Chemiluminescence in Premixed Flames in a Constant Volume Combustion Bomb under Auto-Ignition Conditions*. Energy Fuels 2011, 25, 119-129.

[49] Dandy D. S., Vosen S. R., *Numerical and Experimental Studies of Hydroxyl Radical Chemiluminescence in Methane-Air Flames*. Combustion Science and Technology. 82 (1), 131-150, 1992.

[50] Gaydon A. G., Wolfhard H. G., *Flames: Their Structure, Radiation, and Temperature*. Fourth edition, Chapman and Hall, 1978.

[51] Kojima J., Ikeda Y., Nakajima T., *Spatially Resolved Measurement of OH*, CH*, and C_2* Chemiluminescence in the Reaction Zone of Laminar Methane/Air Premixed Flames*. Proceedings of the Combustion Institute, Volume 28, 2000/pp. 1757–1764.

[52] Muruganandam T. M., Kim B. H., Morrell M. R., Nori V., Patel M., Romig B.W., Seitzman J.M., *Optical Equivalence Ratio Sensors for Gas Turbine Combustors*. Proceedings of the Combustion Institute 30 (2005), 1601 – 1609.

[53] Docquier N., Belhafaoui S., Lacas F., Darabiha N., Rolon C., *Experimental and Numerical Study of Chemiluminescence in Methane / Air High-Pressure Flames for Active Control Application*. Proceedings of the Combustion Institute, Volume 28, 2000/pp. 1765–1774.

[54] Bowman C. T., Seery D. J., *Chemiluminescence in the High-Temperature Oxidation of Methane*. Combustion and Flame, Volume 12, Issue 6, December 1968, Pages 611–614.

[55] Walsh K. T., Long M. B., Tanoff M. A., Smooke M. D., *Experimental and Computational Study of CH, CH*, and OH* in an Axisymmetric Laminar Diffusion Flame*. Proc. Combust. Inst. 27 (1998) 615-623.

[56] Porter R. P., Clark A. H., Kaskan W. E., Browne W. E., *A Study of Hydrocarbon Flames*. Proc. Combust. Inst. 11 (1967) 907-917.

[57] Smith G. P., Luquea J., Parka C., Jeffriesa J. B., and Crosleya D. R., *Low Pressure Flame Determinations of Rate Constants for OH (A) and CH (A) Chemiluminescence*. Combustion and Flame, Volume 131, Issues 1–2, October 2002, Pages 59–69.

[58] Smith G. P., Park C., Luque J., *A Note on Chemiluminescence in Low-Pressure Hydrogen and Methane–Nitrous Oxide Flames*. Combustion and Flame 140 (2005) 385–389.

[59] Hall J. M., Rickard M. J. A., Petersen E. L., *Comparison of Characteristic Time Diagnostic for Ignition and Oxidation of Fuel/Oxidizer Mixtures behind Reflected Shock Waves*. Combustion Science and Technology, Volume 177, Issue 3, 2005.

[60] Law C.K., Zhu D.L., Yu G., *Propagation and Extinction of Stretched Premixed Flames*. Symposium (International) on Combustion, Volume 21, Issue 1, 1988, Pages 1419–1426.

[61] Gottgens J., Mauss F., Prters N., *Analytic Approximations of Burning Velocities and Flame Thicknesses of Lean Hydrogen, Methane, Ethylene, Ethane, Acetylene, and Propane Flames*. Twenty-Fourth Symposium (International) on Combustion, the Combustion Institute, 1992/pp. 129-135.

[62] Incropera F. P., Dewitt D. D., *Introduction to Heat Transfer*. John Wiley and Sons Inc., New York, 2008.

[63] Heravi H. M., Azarinfar A., Kwon S. I., Bowen P. J., Syred N., *Determination of Laminar Flame Thickness and Burning Velocity of Methane – Air Mixture*. Third European Combustion Meeting ECM 2007.

[64] Broida H., *Rotational Temperatures of OH in Methane – Air Flames*. The Journal of Chemical Physics, volume 19, number 22, November, 1951.

[65] Ayoola B.O., Balachandran R., Frank J.H., Mastorakos E., Kaminski C.F., *Spatially Resolved Heat Release Rate Measurements in Turbulent Premixed Flames.* Combustion and Flame 144 (2006) 1–16.

[66] Price R., Hurle I., Sugden T., *Optical Studies of the Generation of Noise in Turbulent Flames*. Twelfth Symposium (International) on Combustion, pages 1093-1102 (1968).

[67] Zizak G., *Flame Emission Spectroscopy: Fundamentals and Applications*. Lecture given at the ICS Training Course on Laser Diagnostics of Combustion Processes, NILES, University of Cairo, Egypt, 18 – 22 Nov. 2000.

[68] Raine R R., Stone C. R., Gould J., *Modelling of Nitric Oxide Formation in Spark Ignition Engines with a Multi-Zone Burned Gas*. Combustion and Flame (1995), 102: 241-255.

[69] Ferguson C. R., *Internal Combustion Engines*. John Wiley & Sons, 1986.

[70] Nori V. N., Seitzman J. M., *Chemiluminescence Measurements and Modelling in Syngas, Methane and Jet-A Fuelled Combustor*. 45th AIAA Aerospace Sciences Meeting and Exhibit, Reno, Nevada, 8 – 11 Jan 2007.

[71] Nori V. N., *Modelling and Analysis of Chemiluminescence Sensing for Syngas, Methane and Jet-A Combustion*. DPhil Thesis, Georgia Institute of Technology, 2008.

[72] Boster E., Behm T., *CCD Camera Operation and Theory – a Basic Introduction*. http://www.google.co.uk/url?q=http://instrumentation.tamu.edu/files/ccds.pdf&sa=U&ei=8rOjUdW9IfLZ0QWru4HwCQ&sqi=2&ved=0CD8QFjAH&usg=AFQjCNE0tGQBTU-abvCT0vhv1K2Nr2kenA, 2010.

[73] Tinaut F. V., Melgar A., Gimenez B., Reyes M., *Characterization of the Combustion of Biomass Producer Gas in a Constant Volume Combustion Bomb*. Fuel, Volume 89, Issue 3, March 2010, Pages 724–731.

[74] Haber L. C., *an Investigation into the Origin, Measurement and Application of Chemiluminescent Light Emissions from Premixed Flames*. MSc thesis, Faculty of the Virginia Polytechnic Institute and State University, 2000.

[75] Devriendt K., Van Look H., Ceursters B., Peeters J., *Kinetics of formation of chemiluminescent CH($A^2\Delta$) by the elementary reactions of C_2H ($X^2\Sigma^+$) with O (^3P) and O_2 ($X^3\Sigma_g^-$): a pulse laser photolysis study*. Chemical Physics Letters 261 (1996) 450-456.

[76] Hall J. M., De Vries J., Amadio A.R., Petersen E. L., *Towards a Kinetics Model of CH Chemiluminescence*. AIAA Paper 2005-1318, 43rd AIAA Aerospace Sciences Meeting and Exhibit, Reno, Nevada, 2005.

[78] Hidaka, Y., Takahashi, S., Kawano, H., Suga, M., Gardiner, W. C. Jr., *Shock-tube Measurement of the Rate Constant for Excited OH ($A^2\Sigma^+$) Formation in the Hydrogen-Oxygen Reaction*. J. Phys. Chem. 1982, 86, 1429-1433.

[79] Slack M., Grillo A., *High-temperature rate coefficient measurements of CO + O chemiluminescence*. Combustion and Flame, vol. 59 (2), pp. 189-196, 1985.

[80] Hu M., Williams B., Stone R., Davy M., *CH* and OH* Chemiluminescence Measurements from Controlled Pre-Mixed Combustion*. Proceedings of the European Combustion Meeting 2011.

[81] Lambda Sensor – 20 questions and answers. http://ngkntk.co.uk/wp-content/uploads/2011/03/Lambda-Sensor-20-QAs.pdf

[82] Zhao H., Ladommatos N., *Engine Combustion Instrumentation and Diagnostics*. Society of Automotive Engineers, Inc (2001).

[83] Andrews G. E., Bradley D., *Determination of Burning Velocities: A Critical Review*. Combustion and Flame, 18(1): 133-153, 1972.

Appendix A Lambda Sensor Calibration

It was necessary to ensure that the air-fuel mixture was of the correct equivalence ratio. An ECM AFRecorder lambda sensor is used to display the actual air-fuel ratio by measuring the proportion of oxygen (O_2) in the exhaust gas. This chapter starts with a description of the basics of lambda sensor operation. Then it discusses lambda sensor calibration by comparing the measured $\%O_2$ with the theoretical value. This chapter ends by lambda sensor calibration with lab air, nitrogen and two calibration gases.

A.1 Overview of Lambda Sensor

A Lambda sensor, also known as an exhaust gas oxygen sensor, is a device to monitor the concentration of residual oxygen within the exhaust gases. The term 'Lambda' refers to the ratio of actual AFR to the stoichiometric AFR for a given mixture. The most common application is to measure the exhaust gas concentration of oxygen for internal combustion engines in automobiles, in order to ensure that the fuel – air mixture was of the correct equivalence ratio.

There are three sensor strategies for automotive application. The first is the zirconia sensor. This sensor generates a small voltage that varies in relation to the oxygen concentration. The second type is the titania sensor; this does not generate a voltage but it has the ability to modulate an applied voltage in relation to the oxygen concentration. Its output signal has a similar characteristic to the zirconia type. The third type is the wide band or air / fuel sensor. This sensor is considerably more sophisticated and accurate than the other two types. This sensor can also be termed a current generating sensor.

A.1.1 Working Principle of the Zirconia Sensor

Stoichiometric operation can be determined from a Zirconia or a Titania type lambda sensor, while to measure the air-fuel ratio the wide band sensor is needed. The wide band sensor is in effect a par of lambda sensors; and the operating principles complex but similar to the zirconia sensor. Hence there is a need to illustrate the working principle of Zirconia sensor. Figure A.1 illustrates the structure of Zirconia type Lambda sensor.

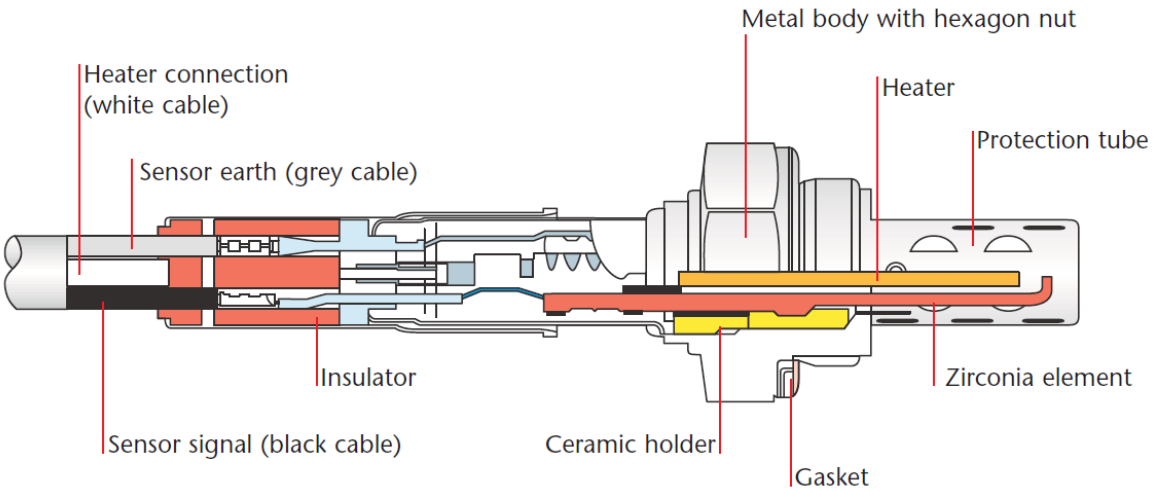


Figure A. 1 A schematic cutaway view of a Zirconia sensor. From NTK online resource [81].

At temperature in excess of 300 ℃ the Zirconia element possesses a property that causes a transfer of oxygen ions. This movement creates a voltage. The greater the difference of oxygen concentration between the exhaust gas and the ambient reference air in the centre of sensor thimble, the higher the voltage produced. The voltage produced in the fuel lean position should be approximately 0.1 volts and in the fuel rich position approximately 0.9 volt. The very useful part of this function is that at around the stoichiometric point there is a large easily readable change in voltage. Hence the sensor is most sensitive near the stoichiometric point. The basic working principle has can be seen in Figure A.2.

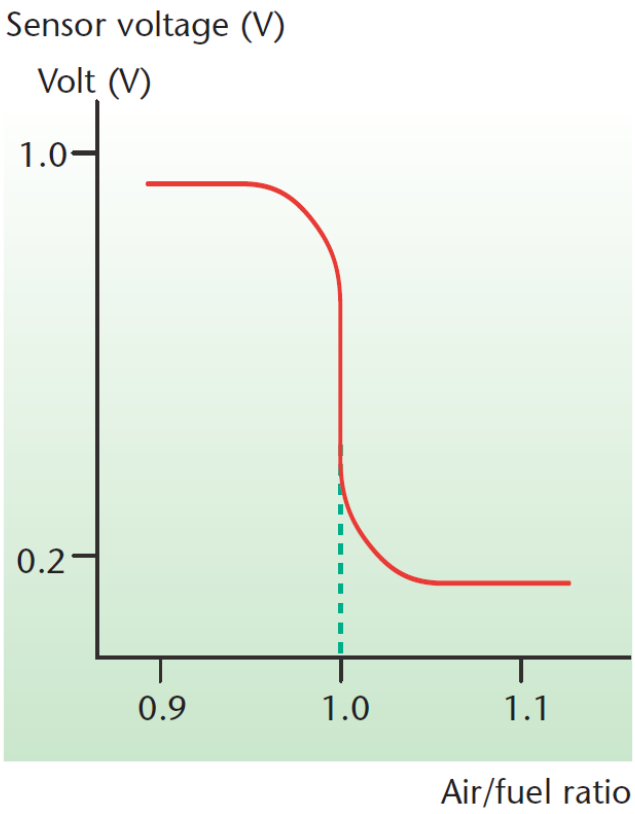


Figure A. 2 Zirconia sensor output signal. From NTK online resource [81].

The wide band sensor is constructed from three layers of zirconia, all of which are heated; but only the top two layers have platinum electrodes and electrical connections. The whole assembly is heated to maintain a constant temperature, since the voltage, i.e. oxygen partial pressure response, is temperature dependent. The sensing cell measures the oxygen partial pressure, and the current imposed on the pumping cell seeks to maintain a constant oxygen partial pressure in the measurement cavity between the sensing cell and the pumping cell.

As has been shown in Figure A.3, when there is a weak mixture, the concentration gradient between the exhaust gas and the measurement cavity will cause oxygen to diffuse through the porous gas intake, and the electrical current in the pumping cell (that is removing oxygen) will be proportional to the oxygen concentration in the exhaust gas. With rich mixtures, the partial products of combustion (CO, H_2 and hydrocarbons) that have diffused

into the measurement cavity will be oxidised, thus causing more to diffuse through the porous gas intake. The richer the mixture, then the greater the flow rate of reactants diffusing into the measuring cavity, and the greater the current flow in the pumping cell that is adding oxygen (to maintain the constant oxygen level), so the current will be proportional to the richness exhaust gas. Another thing worth mentioning is that, in the test facility, a highly integrated air-fuel ratio analyser that displays figures of AFR (air – fuel ratio), λ (lambda), and $\%O_2$.

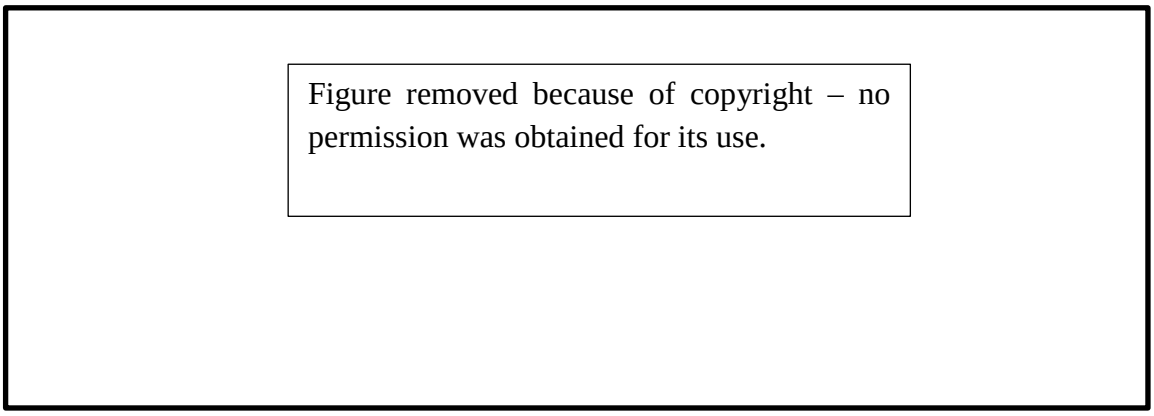


Figure A. 3 The wide band sensor structure (a) and operation (b). From Zhao and Ladommatos [82, Fig. 1.17].

A.2 Lambda Sensor Calibration

To ensure accurate measurement of the air – fuel ratio, careful calibration needs to be carried out. The system can be initially calibrated by comparing the $\%O_2$ measurement in still air with the theoretical $\%O_2$. The oxygen concentration in dry air (zero humidity) is 20.95% and decreases with increasing humidity. The $\%O_2$ in air can be calculated from the barometric pressure (P_b), the relative humidity (R_h), and the saturated water vapour (P_{ws}) by using Equation A.1:

$$\%O_2 = 20.95\% \times \frac{\left(P_b - P_{ws} \times \frac{R_h}{100}\right)}{P_b} \tag{A.1}$$

As an example, $\%O_2$ in air is calculated underneath at given humidity (45%) and barometer pressure ($P_b = 1032.6\,\mathrm{mbar} = 774.25\,\mathrm{mmHg}$). Bear in mind that the saturated

water vapour (P_{ws}) is a function of the ambient temperature (T_a), it is given as 17.535 mmHg when the ambient temperature is 20 ℃.

$$\%O_2 = 20.95\% \times \frac{\left(774.25 - 17.535 \times \frac{45}{100}\right)}{774.25} = 20.7365\% \quad \text{(A.2)}$$

If the AFRecorder does not display the correct $\%O_2$ value, the measurement should be adjusted until the actually $\%O_2$ in the air is displayed by the AFRecorder.

The lambda sensor has claimed accuracies as shown in Table A.1. It only has 2 dp output display, which adds an extra error of $\pm$ 0.005.

Table A. 1 Specified Accuracy of the ECM AFRecorder Lambda Sensor for Different Lambda Ranges

λ	Accuracy
1	$\pm$ (0.006 + 0.005)
0.8 – 1.2	$\pm$ (0.008 + 0.005)
Elsewhere	$\pm$ (0.009 + 0.005)

A.2.1 Lambda Sensor Calibration with Gas Mixtures

The lambda sensor was calibrated with lab air, nitrogen and two calibration gases (Cal Gas). The first Cal Gas consists of 6.29% oxygen in nitrogen, with a 2% tolerance. This is used to test the lean condition. The lambda value for this gas was calculated based on the theory of partial pressures:

$$\mathrm{CH_y} + \lambda\left(1 + \frac{\mathrm{y}}{4}\right)(\mathrm{O_2} + 3.76\mathrm{N_2}) = \mathrm{CO_2} + \frac{y}{2} \cdot \mathrm{H_2O} + (\lambda - 1)\left(1 + \frac{\mathrm{y}}{4}\right)\mathrm{O_2} + 3.76\lambda\left(1 + \frac{\mathrm{y}}{4}\right)\mathrm{N_2} \quad \text{(A.3)}$$

The H / C ratio (y) is 1.8 and oxygen concentration is 6.29%, atom balance gives:

$$\%\mathrm{O_2} = \frac{(\lambda - 1) \cdot \left(1 + \frac{\mathrm{y}}{4}\right)}{1 + \frac{y}{2} + (\lambda - 1) \cdot \left(1 + \frac{\mathrm{y}}{4}\right) + 3.76 \cdot \lambda \cdot \left(1 + \frac{\mathrm{y}}{4}\right)} \quad \text{(A.4)}$$

$$\lambda = \frac{-\%O_2 \times \frac{\mathrm{y}}{4} - \left(1 + \frac{\mathrm{y}}{4}\right)}{\%O_2 \times \left(1 + \frac{\mathrm{y}}{4}\right) + \%O_2 \times \left(1 + \frac{\mathrm{y}}{4}\right) \times 3.76 - \left(1 + \frac{\mathrm{y}}{4}\right)} \quad \text{(A.5)}$$

Substitution of $\%O_2 = 6.29\%$ and y = 1.8 into equation (A.5) will yield $\lambda = 1.4552$.

The second Cal Gas mix contains 1965 ppm C_3H_8, 3.52% CO and 14.02% CO_2, balance is again nitrogen. The tolerance on each of the constitutes is 1%, which leads to a maximum error in lambda of 0.12%. This is used to test the rich condition. The Lambda value calculation is illustrated as follow:

$$C_xH_y + z(O_2 + 3.76N_2) = a \cdot CO_2 + b \cdot CO + c \cdot C_3H_8 + d \cdot N_2 + e \cdot H_2O \qquad (A.6)$$

Substitution of a = 14.02%, b = 3.52%, c = 0.1965% and d = 82.2635% for 100 kmol of dry products into Equation (A.6), atom balance gives:

x = 18.1295, y = 25.96636, z = 21.87859, e = 12.19718.

For this hydrocarbon, stoichiometric reaction gives $z = x + \frac{y}{4} = 24.62109$. Hence:

$$\lambda = \frac{21.87859}{24.62109} = 0.88861 \qquad (A.7)$$

The results from these tests are given in Table A.2.

Table A. 2 Comparison of the ECM AFRecorder Lambda Sensor against Four Calibration Gases

Gas	$\%O_2$		λ	
	Nominal	Measured	Nominal	Measured
Lab Air	20.95	21.05	-	-
Nitrogen	0	0.11	-	-
Cal Gas	6.29 ± 0.13	6.09	1.442-1.469	1.42
MOT mix	-	-	0.8874-0.8898	0.93

Appendix B Optical Ray Tracing Using Matrices

Ray tracing technique is employed in the design of the optical system. In computer graphics, ray tracing is a technique for generating an image by tracing the path of light through pixels in an image plane and simulating the effects of its encounters with virtual objects. This chapter gives an introduction of ray tracing algorithm with matrices. It also involves the construction of ray transfer matrices which describe the optical system, and the calculation of the most restricting ray angles used in the current optical model.

B.1 Ray Transfer Matrix Algorithm

Geometric ray tracing specifies the propagation of light rays through an element in an optical system. It based on the paraxial approximation. An optical ray at any point can be defined uniquely by a two-element column vector, in which the upper element is the small distance (y) from the optical axis (x-axis) in the system and the lower element is the small angle (θ). Two-by-two matrices operating on this column vector then describes how the ray changes when it crosses through the optical system. Without loss any of generality, the relationship between the exit plane (output vector) and entrance plane (input vectors) is given by the 2-by-2 matrix of the form:

$$\begin{pmatrix} y_2 \\ \theta_2 \end{pmatrix} = \begin{pmatrix} A & B \\ C & D \end{pmatrix} \begin{pmatrix} y_1 \\ \theta_1 \end{pmatrix} \tag{B.1}$$

where:

$$A = \frac{y_2}{y_1}\Big|_{\theta_1=0}, B = \frac{y_2}{\theta_1}\Big|_{y_1=0}, C = \frac{\theta_2}{y_1}\Big|_{\theta_1=0}, D = \frac{\theta_2}{\theta_1}\Big|_{y_1=0} \tag{B.2}$$

This represents the optical system between the input and output optical elements. The paraxial approximation expresses the angle θ equals the slope of the ray. For example, inspection of length d in free space gives:

$$\begin{pmatrix} y_2 \\ \theta_2 \end{pmatrix} = \begin{pmatrix} 1 & d \\ 0 & 1 \end{pmatrix} \begin{pmatrix} y_1 \\ \theta_1 \end{pmatrix} \tag{B.3}$$

For thin lens of focal length *f*, there is negligible distance between the entrance plane and the exit plane. Thus no matter what the slope of the incoming ray, the output position is always equal to the input position, hence *A=1* and *B=0*. For a special case that the input slope $\theta_1 = 0$, yet it is obviously that $C = -\frac{1}{f}$. In other case, light ray comes through the centre of the lens yields *D=1*. Therefore the ray transfer matrix of a thin lens is given by:

$$\begin{pmatrix} y_2 \\ \theta_2 \end{pmatrix} = \begin{pmatrix} 1 & 0 \\ -\frac{1}{f} & 1 \end{pmatrix} \begin{pmatrix} y_1 \\ \theta_1 \end{pmatrix} \tag{B.4}$$

To describe an optical system combining different optical elements, ray transfer matrices can be multiplied to obtain a single matrix for the system.

B.2 Application in the Optical Model

The current narrow field of view optical model is developed by means of ray tracing algorithm, which assesses what fraction of the light rays can reach the photomultiplier tube detector. For the current optical geometry, Figure B.1 illustrates the simplified 2D arrangement, of the optical elements along optical axis.

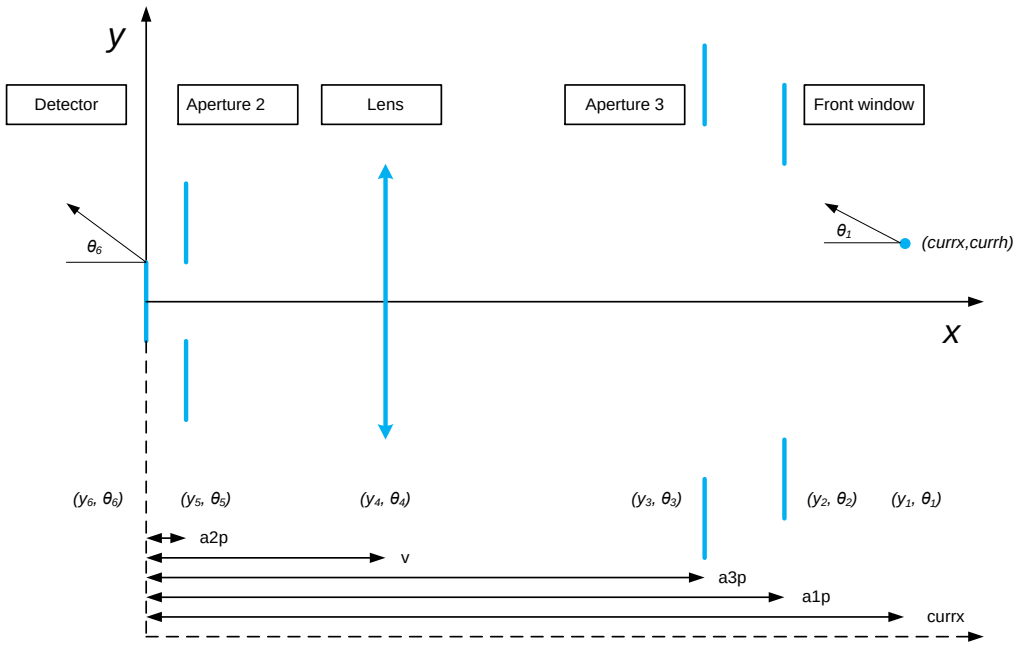


Figure B. 1 Simplified 2D arrangement of the optical elements.

The 2D spatial collection efficiency at location (*currx*, *currh*) inside the combustion vessel is obtained by looking at the maximum up and down angles that just passes each element, and choosing the most restricting element as the required case. Taking the detector to be a typical example, according to Figure B.1, the underlying equation, which comes from the series of ray transfer matrices for the system, governs the maximum up and down ray angles, e.g.

$$\begin{pmatrix} y_6 \\ \theta_6 \end{pmatrix} = \begin{pmatrix} 1 & v \\ 0 & 1 \end{pmatrix} \begin{pmatrix} 1 & 0 \\ -1/f & 1 \end{pmatrix} \begin{pmatrix} 1 & (currx - v) \\ 0 & 1 \end{pmatrix} \begin{pmatrix} y_1 \\ \theta_1 \end{pmatrix} \tag{B.5}$$

Bear in mind that the meanings of each parameter can be found in Table 3.1. Equation (B.5) then leads:

$$y_6 = \left(1 - \frac{v}{f}\right)[y_1 + (currx - v) \cdot \theta_1] + v \cdot \theta_1 \tag{B.6}$$

To get maximum ray angles (up and down), $y_6 = \pm\frac{det}{2}$ is chosen respectively. Hence

$$\theta_{1 \to det_{toplim}} = \frac{\frac{det}{2} - currh + currh \cdot \frac{v}{f}}{(currx - v)\left(1 - \frac{v}{f}\right) + v} \tag{B.7}$$

$$\theta_{1 \to det_{botlim}} = \frac{-\frac{det}{2} - currh + currh \cdot \frac{v}{f}}{(currx - v)\left(1 - \frac{v}{f}\right) + v} \tag{B.8}$$

where y_6 is the distance from the axis at the detector that the ray which leaves (x_1, h_1) at angle θ_1 strikes. Similar relationships are found for other elements and the up and down limits are obtained by choosing the most restricting ones, i.e.

$$\theta_{1_{top}} = \min(\theta_{1 \to ap1_{toplim}}, \theta_{1 \to ap3_{toplim}}, \theta_{1 \to lens_{toplim}}, \theta_{1 \to ap2_{toplim}}, \theta_{1 \to det_{toplim}}) \tag{B.9}$$

$$\theta_{1_{bot}} = \max(\theta_{1 \to ap1_{botlim}}, \theta_{1 \to ap3_{botlim}}, \theta_{1 \to lens_{botlim}}, \theta_{1 \to ap2_{botlim}}, \theta_{1 \to det_{botlim}}) \tag{B.10}$$

Finally the 2D spatial collection efficiency η at location (*currx*, *currh*) is calculated using the following formulae:

$$\eta = \left(\theta_{1_{top}} - \theta_{1_{bot}}\right)/2\pi \tag{B.11}$$

A full 3D spatial collection efficiency analysis using ray tracing matrix method begins in the same manner as before, i.e. for each position (*currx*, *currh*) inside of the bomb vessel, determining the limits in θ for each optical element, and then choosing the most restricting case overall. It discretises θ into n steps between $-\frac{\pi}{2}$ and $\frac{\pi}{2}$. For each θ value which lies between the 2D θ limits, it is then calculate the most restricting angle in the ϕ direction (i.e. the angle in a perpendicular plane). ϕ is calculated using the same strategy as θ in 2D modelling. Figure B.2 shows the simplified 3D geometric arrangement with optical elements sitting on the optical axis in a (x, z) plane, where z-axis is perpendicular to (x, y) plane in Figure B.1.

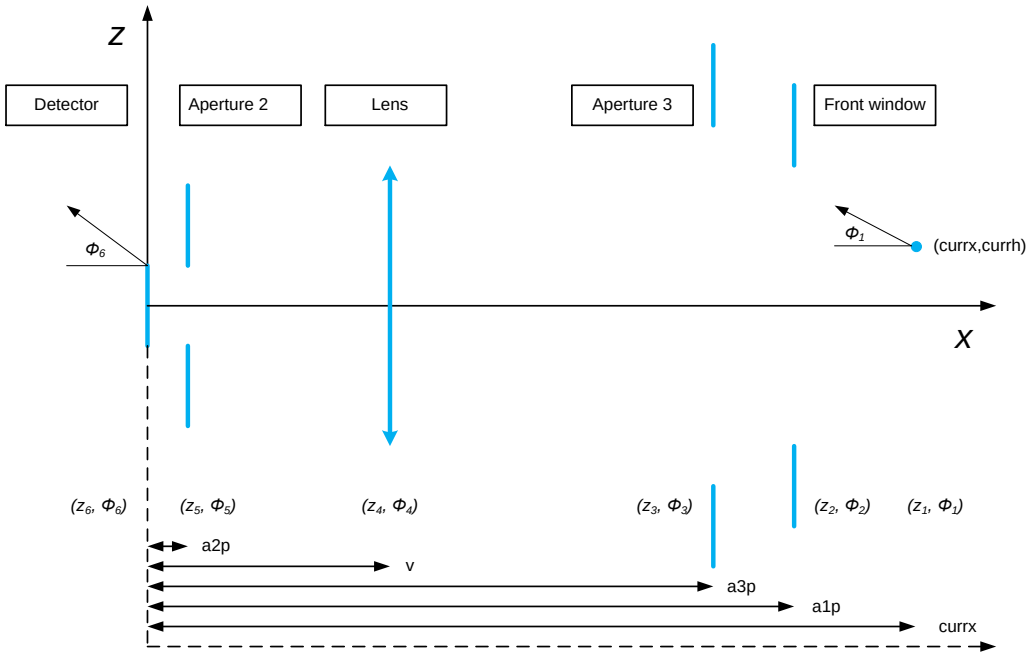


Figure B. 2 Simplified 3D geometric arrangement of the optical elements.

Taking the detector as an example, the ray transfer matrix method gives the following governing equation for a quantised θ value within the up and down limits:

$$\begin{pmatrix} z_6 \\ \phi_6 \end{pmatrix} = \begin{pmatrix} 1 & v \\ 0 & 1 \end{pmatrix} \begin{pmatrix} 1 & 0 \\ -1/f & 1 \end{pmatrix} \begin{pmatrix} 1 & (currx - v) \\ 0 & 1 \end{pmatrix} \begin{pmatrix} z_1 \\ \phi_1 \end{pmatrix} \tag{B.12}$$

To get a maximum up and down ϕ angle, $z_6 = \pm\sqrt{\left(\frac{det}{2}\right)^2 - \left(\frac{y_6}{2}\right)^2}$, and y_6 is given by Equation (B.6) with known θ. These lead to Equation (B.13) and (B.14):

$$\phi_{1\to det_{toplim}} = \frac{z_6}{(currx-v)-(currx-v)\cdot\frac{v}{f}+v} \tag{B.13}$$

$$\phi_{1\to det_{botlim}} = \frac{-z_6}{(currx-v)-(currx-v)\cdot\frac{v}{f}+v} \tag{B.14}$$

Similar procedures are implemented for other optical elements and the most constraining ϕ limits can be found as follow:

$$\phi_{1_{top}} = \min(\phi_{1\to ap1_{toplim}}, \phi_{1\to ap3_{toplim}}, \phi_{1\to lens_{toplim}}, \phi_{1\to ap2_{toplim}}, \phi_{1\to det_{toplim}}) \tag{B.15}$$

$$\phi_{1_{bot}} = \max(\phi_{1\to ap1_{botlim}}, \phi_{1\to ap3_{botlim}}, \phi_{1\to lens_{botlim}}, \phi_{1\to ap2_{botlim}}, \phi_{1\to det_{botlim}}) \tag{B.16}$$

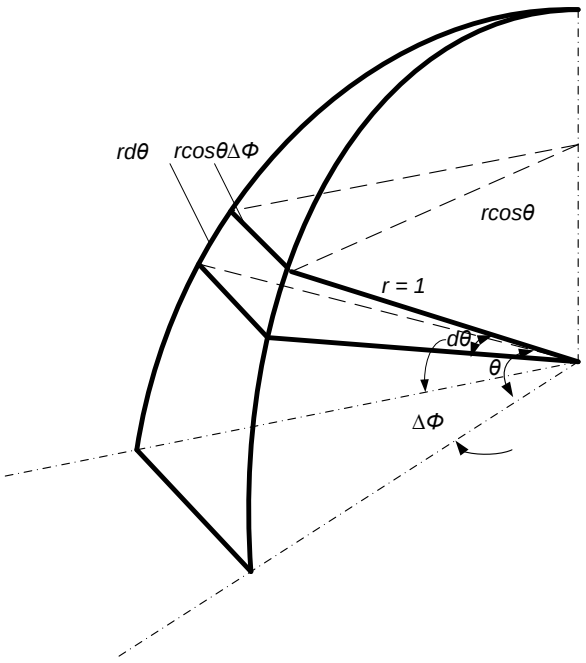


Figure B. 3 Collection-area subtends at a point.

Next, as shown in Figure B.3, with the limits in ϕ known, the surface area of the current ring section can be found by considering Equation (3.10).

$$collarea(\theta) = \left(\frac{\pi}{n}\right) \times \left(2\pi cos\theta \times \frac{\Delta\phi}{2\pi}\right) \tag{3.10}$$

where $\frac{\pi}{n}$ is the element of arc length in the θ direction, $2\pi cos\theta \times \frac{\Delta\phi}{2\pi}$ is the arc length around the ϕ direction that is within the limits in ϕ. The product of these is a small area.

Lastly the total spatial collection efficiency at the current position (*currx*, *currh*) is now obtained by summing up the ring areas of each θ and dividing by the total surface area of a unit sphere 4π.